Design, microfabrication and characterization of alkali vapor cells for miniature atomic frequency references

Vincent Maurice

SPIM

Thèse de Doctorat

Design, microfabrication and characterization of alkali vapor cells for miniature atomic frequency references

Vincent Maurice

SPIM
Thèse de Doctorat

école doctorale **sciences pour l'ingénieur et microtechniques**
UNIVERSITÉ DE FRANCHE-COMTÉ

UFC

N° | X | X | X |

THÈSE présentée par

Vincent Maurice

pour obtenir le

Grade de Docteur de
l'Université Bourgogne Franche-Comté

Spécialité : **Sciences pour l'ingénieur**

Design, microfabrication and characterization of alkali vapor cells for miniature atomic frequency references

Soutenue publiquement le 7 juillet 2016 devant le Jury composé de :

Noël Dimarcq	Rapporteur	Directeur de Recherche CNRS, LNE - SYRTE, France
Jan Dziuban	Rapporteur	Professeur, École polytechnique de Wrocław, Pologne
Pierre-André Farine	Examinateur	Professeur, École polytechnique fédérale de Lausanne, Suisse
Serge Galliou	Examinateur	Professeur, FEMTO-ST/ENSMM, France
Jean-Marc Lesage	Examinateur	Ingénieur, Direction Générale de l'Armement, France
Christophe Gorecki	Directeur de thèse	Directeur de Recherche CNRS, FEMTO-ST, France
Rodolphe Boudot	Co-encadrant	Chargé de Recherche CNRS, FEMTO-ST, France
Nicolas Passilly	Co-encadrant	Chargé de Recherche CNRS, FEMTO-ST, France

À la mémoire
de Simone Viard
et Marie Rose Maurice

Remerciements

Résumé

Introduction. La mesure précise du temps est cruciale pour de nombreuses applications et chaque avancée dans ce domaine apporte de nouvelles possibilités techniques. Les horloges atomiques primaires sont particulièrement stables, exactes et permettent de maintenir les échelles de temps internationales. Même s'il en existe des déclinaisons relativement compactes, celles-ci restent très imposantes. A l'opposé, les oscillateurs à quartz sont à la fois petits, peu coûteux et économes en énergie, mais ils présentent des stabilités bien moindres. Il existe donc un besoin pour des horloges avec des stabilités accrues par rapport aux oscillateurs à quartz actuels, mais conservant les caractéristiques de taille, de coût et de consommation de ces derniers.

Depuis une quinzaine d'années, plusieurs groupes de recherche développent des horloges atomiques miniatures présentant des stabilités de fréquence inégalées, de l'ordre de 1 µs/jour, avec des volumes de quelques centimètres cubes et des consommations inférieures à 100 mW. Parmi les applications visées, on peut noter l'amélioration de la navigation par satellite et les télécommunications. Contrairement aux oscillateurs disciplinés sur GPS, dont les signaux sont falsifiables et sensibles au brouillage, ces horloges apportent une autonomie essentielle à de nombreux systèmes tels que les réseaux de distribution d'énergie, les réseaux informatiques ou de nombreux systèmes embarqués.

L'émergence de ces horloges a été possible grâce à trois éléments principaux :

– la mise en évidence du phénomène de piégeage cohérent de population (CPT), qui permet d'interroger la transition hyperfine de l'état fondamental de l'atome (transition d'horloge) uniquement avec un champ lumineux composé de deux fréquences,

– le développement de diodes laser de type VCSEL (laser à cavité verticale émettant par la surface) modulables pour générer ce champ lumineux de façon efficace,

– l'utilisation des techniques de microfabrication pour réaliser des cellules de taille millimétrique, à partir de substrats de silicium et de verre, pour contenir les atomes.

Le schéma d'une horloge basée sur le CPT est montré en Fig. 1.8 (p. 12).

Contexte. Le NIST fut le premier à mettre en œuvre ces éléments et à réaliser un prototype d'horloge atomique basé uniquement sur des composants sous forme de puces (Knappe *et al.*, 2004b, Fig. 1.9, p. 13). Les développements entrepris par Microsemi ont récemment mené à l'apparition du premier produit commercial en 2011 : le modèle CSAC SA.45s. Après le développement d'une technologie de cellule originale à FEMTO-ST, le projet européen MAC-TFC a été initié en 2008 pour réaliser l'ensemble des briques nécessaires à l'horloge, en particulier une diode VCSEL résonnante avec la raie D_1 du césium (Université d'Ulm, Allemagne), un ASIC basse consommation intégrant une synthèse de fréquence (EPFL, Suisse) et un module physique intégré (VTT, Finlande). La technologie de cellule était alors basée sur un dispenser stable et solide de césium fabriqué par SAES Getters, introduit dans la cellule avant la fermeture par soudure anodique. Le césium est ensuite libéré par échauffement local à l'aide d'un laser de puissance. La structure de cette cellule est illustrée en Fig. 3.1 (p. 37). Les efforts ont été poursuivis à travers plusieurs projets français qui ont constitué le cadre des travaux présentés dans cette thèse :

– le projet ISIMAC, en partenariat avec le LNE-SYRTE, vise à étudier une nouvelle architecture de cellule, déjà esquissée pendant le projet MAC-TFC, et à appliquer des matériaux anti-relaxants dans les cellules,

– le projet HABAC, ayant pour but de transférer le savoir-faire développé à FEMTO-ST vers l'industrie,

– le project SCP-Time regroupe plusieurs partenaires industriels et académiques pour former un réseau de distribution du temps, sécurisé et précis.

Objectifs. Cette thèse vise à étudier les différents paramètres concernant la conception et la fabrication des cellules à vapeur de césium ainsi qu'à envisager des solutions pour pallier à certaines limitations telles que la plage de température opérationnelle, le coût de fabrication du dispositif, l'encombrement et la facilité d'assemblage du module physique.

Mélange de gaz. La largeur du signal de résonance CPT et la stabilité de fréquence qui en découle sont déterminées par le temps de relaxation des atomes alcalins à partir de l'état cohérent vers leur état fondamental non-cohérent. Ce temps est notamment déterminé par les collisions des atomes de césium avec les parois de la cellule, qui entrainent la perte de cette cohérence. Ainsi, une atmosphère, dite *tampon*, est généralement adjointe à la vapeur alcaline pour confiner les atomes et ralentir leur diffusion vers les parois de la cellule. Cette atmosphère tampon peut être composée d'un ou de plusieurs gaz.

Les niveaux énergétiques des atomes de césium sont toutefois perturbés par la présence du gaz tampon et la fréquence d'horloge subit un *déplacement collisionnel* qui dépend de la pression de gaz tampon et de la température de la cellule. Les variations de température auxquelles est soumise la cellule se traduisent alors par des variations de la fréquence d'horloge. Pour s'affranchir de cette sensibilité indésirable, une atmosphère tampon pour laquelle cette dépendance présente un point d'inversion (annulant la dépendance au premier ordre) autour de la température de fonctionnement de la cellule doit être utilisée.

Généralement, cette dépendance thermique peut être annulée à la température souhaitée en combinant deux gaz ayant des effets opposés sur la fréquence d'horloge. Cependant, le mélange d'azote et d'argon qui est généralement utilisé n'est pas compatible avec la technologie basée sur les dispensers car ils comportent un matériau qui absorbe l'azote.

Au cours du projet MAC-TFC, il a été montré qu'une atmosphère tampon composée uniquement de néon, inerte vis-à-vis du dispenser, présente un point d'inversion autour de 80 °C. Une telle atmosphère permet donc un fonctionnement de l'horloge dans un environnement dont la température est inférieure à 80 °C car la contrainte sur la consommation permet seulement de chauffer la cellule et proscrit le refroidissement thermoélectrique. Cette température est trop faible pour la plupart des applications industrielles qui imposent des températures opérationnelles plus élevées.

Au cours de ces travaux, des cellules avec une atmosphère composée de néon et d'hélium ont été réalisées grâce à la mise en place d'un équipement de soudure anodique dédié disposant de deux lignes de gaz. Il a été montré que ce mélange permet d'étendre la plage de fonctionnement au-dessus de 90 °C, en adéquation avec les besoins industriels. En revanche, une dérive de la fréquence d'horloge de l'ordre de $-2\,\mathrm{Hz\,h^{-1}}$ (soit -5×10^{-9} /j en terme de fréquence relative) a été observée. Cette dérive est associée à la perméation de l'hélium à travers les fenêtres en verre borosilicaté de la cellule et, bien qu'elle soit déterministe, elle est trop importante pour être compensée électroniquement. D'autres matériaux sont à l'étude pour empêcher la perméation.

Techniques de remplissage alternatives. La technique de remplissage basée sur des dispensers solides est avantageuse par sa robustesse et sa simplicité de mise en œuvre car elle permet l'utilisation d'équipements de soudure anodique standards. En revanche, si elle simplifie la fabrication, la présence d'un dispenser dans chaque cellule est contraignante. D'une part, elle limite la densité de cellules réalisables sur un wafer, ce qui augmente le coût de production par cellule. D'autre part, elle augmente la taille de la cellule et, par conséquent, celle du module physique qui l'intègre. Cette cellule pâtit également d'une dissipation thermique plus importante qu'une cellule composée d'une seule cavité. Par ailleurs, l'utilisation d'un dispenser par cellule impose un coût fixe non négligeable et leur manipulation reste délicate.

Ici, des solutions alternatives ont été étudiées pour tenter de pallier à certains de ces problèmes. En premier lieu, des dispensers sous forme de pâte, qui peuvent être déposés collectivement dans les cellules, ont été étudiés. Un échantillon de pâte fournie par SAES Getters a été introduite dans deux lots de cellules avec, pour la première fois, des taux de remplissage par wafer approchant les 100 %. Des mesures long terme en absorption linéaire valident la bonne stabilité de la densité atomique obtenue. Cette méthode permettra de réduire drastiquement les coûts associés aux dispensers et à leur manipulation. Par ailleurs, il a été observé que, malgré un volume de pâte bien plus petit qu'un dispenser solide, de grandes quantités de césium peuvent être obtenues, laissant entrevoir une potentielle diminution du volume de la cavité dispenser et de l'encombrement associé. Des mesures de vieillissement de fréquence en condition d'horloge sont en cours pour valider pleinement la stabilité de l'atmosphère.

D'autre part, une méthode de remplissage hybride, inspirée des méthodes de fabrication des cellules en verre centimétriques, a été proposée. Celle-ci fait appel à des vannes microfabriquées permettant d'isoler ou de

faire communiquer différentes cavités. Des cellules composées d'une seule cavité sont initialement connectées à un réservoir de césium commun par des canaux. Après la migration de la vapeur de césium dans les cavités, des vannes fermantes peuvent être actionnées pour sceller individuellement chaque cellule. Cette vanne est simplement constituée d'une membrane en verre qui est défléchie par échauffement local jusqu'à venir obstruer l'embouchure d'un canal, également en verre. La fusion locale des deux surfaces assure l'herméticité du scellement. A terme, cette méthode devrait lever plusieurs limitations, en autorisant d'utiliser de l'azote dans l'atmosphère tampon, en réduisant la taille des cellules et en minimisant les étapes de manipulation de la source de césium.

Des premiers essais ont été réalisés et ont permis de valider la méthode d'échauffement par laser CO_2. Des structures de test complètes doivent être fabriquées prochainement.

Architecture réflective. Un design original de cellule combinant des réseaux de diffraction à une cavité en silicium réflective formée par gravure anisotrope a été proposée durant le projet MAC-TFC. Cette architecture est montrée en Fig. 3.24 (p. 60). Dans cette structure le faisceau est routé dans une cavité orientée dans le plan du substrat grâce aux parois inclinées à 54,74° de la cavité et aux réseaux de diffractions qui corrigent l'angle pour que les faisceaux d'entrée et de sortie aient une incidence normale. Parmi les avantages apportés par cette solution, on peut noter la possibilité d'allonger la cavité optique tout en réduisant son diamètre sans avoir recours à des substrats plus épais, plus difficiles à graver et à assembler. Un faisceau laser plus étroit est propice à l'utilisation de composants optiques microfabriqués plus facilement intégrables au niveau wafer. Le faisceau étant réfléchi du coté du laser, la photodiode peut être placée sur le même substrat électronique facilitant également l'assemblage du module. Une des dimensions du module physique peut ainsi être réduite, en particulier sa hauteur, favorisant un montage en surface compacte sur le circuit électronique. Dans le cadre de ces travaux, plusieurs lots de cellules avec différentes longueurs de cavité ont été caractérisés. Malgré des largeur de raies relativement grandes, des contrastes CPT remarquables, jusqu'à 17 %, ont été obtenus. Un facteur de mérite de 1,25 % kHz^{-1} a été obtenu pour une cavité longue de 7 mm et une pression de néon de 200 Torr. Cette valeur est le double des valeurs observées dans les cellules transmissives classiques malgré un volume de cavité réduit de moitié. Cette architecture semble ainsi prometteuse pour réaliser un module physique particulièrement compact.

Revêtements anti-relaxants. La réduction de la taille des cellules a pour effet d'augmenter le taux de relaxation due aux collisions des atomes de césium sur les parois. Afin de miniaturiser davantage les cellules et d'améliorer les caractéristiques du signal CPT issu de la cellule, un revêtement anti-relaxant peut être déposé sur ses parois internes pour limiter cette décohérence. Cette méthode est, par exemple, utilisée dans les masers à hydrogène qui utilisent des revêtements de paraffine. Ces revêtements présentent d'autres avantages potentiels comme la possibilité de moyenner des inhomogénéités des champs lumineux ou magnétiques perçues par les atomes sur leur trajet balistique, rendant la conception du module physique plus tolérantes aux gradients de champs dans la cellule.

Cette étude, en collaboration avec le LNE-SYRTE à Paris, a été réalisée en deux temps : d'abord en développant des procédés de dépôt dans des cellules centimétriques en s'affranchissant des contraintes liées à la microfabrication, puis en adaptant le procédé à des cellules microfabriquées.

Des revêtements d'octadécyltrichlorosilane (OTS) ont été sélectionnés pour leur résistance aux températures élevées. Des procédés en phase vapeur et en phase liquide ont été mis en œuvre dans des cellules centimétriques scellées par les techniques classiques. Un effet anti-relaxant marqué par un signal formé d'une double structure lorentzienne a été observé. Le nombre de rebonds moyen des atomes sur la paroi avant relaxation est estimé à 12. La qualité du signal obtenu reste inférieure à une cellule avec gaz tampon et d'autres essais combinés avec un gaz tampon sont envisagés.

Des essais de dépôt d'OTS dans des microcellules ont également été réalisés. Les surfaces couvertes de condensation métallique et la section du canal séparant la cavité principale de la cellule de la source de métal alcalin se comportent comme des zones sans revêtement et dégradent les performances. Ainsi, un design spécifique avec une section de canal réduite a été utilisé. Ce canal est structuré en méandres pour limiter la migration de la condensation de césium dans la cavité optique lors de l'activation. Étant donné que l'OTS a tendance à gêner la soudure anodique, un procédé UV-O a été utilisé pour retirer sélectivement l'OTS sur les surfaces de scellement après le dépôt. Un effet anti-relaxant a été observé avec une largeur de raie 15 fois plus fine que pour une cellule de césium pur sans revêtement. Cependant, l'absence d'un gaz tampon résiduel doit encore être vérifiée pour démontrer pleinement l'effet anti-relaxant du revêtement.

Caractérisation et mesures long terme. Pour valider les performances des cellules, deux bancs de caractérisation ont été assemblés. Le premier fait appel à des composants intégrables directement dans une horloge miniature, en particulier un laser de type VCSEL, pour mesurer les performances court terme atteignables par le dispositif final. Le second utilise un laser DFB modulé par un modulateur électrooptique (EOM) et vise à estimer les performances long terme propres aux cellules en se plaçant dans les meilleurs conditions, sans contraintes sur les équipements utilisés.

La détermination des paramètres opérationnels optimaux nécessite de faire varier certains paramètres tels que la puissance optique et la température de la cellule, et ce pour chaque nouvelle cellule. D'autre part, leur caractérisation sur le long terme est délicate et nécessite de conserver des configurations constantes sur des temps longs. Dans le cadre de cette thèse, des moyens de caractérisation ont donc été développés davantage pour automatiser ces tâches.

Pour déterminer la pression de gaz tampon idéale, des cellules avec différentes pressions de néon ont été caractérisées par spectroscopie CPT avec le banc DFB. Il a été remarqué que les cellules avec une pression faible présentent des signaux avec des contrastes plus importants, au détriment de largeurs plus grandes. Le contraste diminue a mesure que la pression augmente mais cette diminution est compensée par une réduction de la largeur du signal. Ainsi, le facteur de mérite, proportionnel au rapport contraste/largeur, est quasiment constant pour une pression comprise entre 60 et 240 Torr. La stabilité de fréquence court terme relative limitée par le bruit de grenaille sur cette plage se situe autour de $4 \times 10^{-12}\,\tau^{-1/2}$ et est optimale pour des puissances optiques de l'ordre de 20 µW. Le choix de la pression ne semble donc pas critique à cet égard.

La mesure de la fréquence propre à l'atmosphère de la cellule nécessite de s'affranchir des autres perturbations, en particulier le déplacement lumineux dû à l'effet Stark dynamique. Ceci est fait en mesurant la fréquence de la résonance à différentes puissances optiques et en extrapolant la valeur à puissance nulle. Des mesures de vieillissement de fréquence préliminaires ont permis d'estimer une dérive relative inférieure à $-3{,}8 \times 10^{-12}$ /j, compatible avec les spécifications visées. Cette mesure confirme la mesure précédente réalisée au cours du projet MAC-TFC.

Prototype de module physique. Les premières étapes vers un module physique microfabriqué, réalisées dans le cadre de plusieurs collaborations, sont ensuite présentées. Des résistances chauffantes et thermométriques ont été intégrées à la surface des cellules au niveau wafer. Les tracés résistifs en platine ont été déposés sur un wafer de verre par pulvérisation et *lift-off* avant d'assembler ce wafer par soudure anodique.

Après découpe, les cellules ont été montées sur des supports en époxy pour les isoler thermiquement et reliées électriquement par *wire bonding*. Cette structure a été intégrée dans un module physique compact avec une diode VCSEL, une photodiode, des composants optiques et une bobine d'Helmotz.

Dans la configuration actuelle, sans isolation par le vide, la consommation nécessaire pour maintenir la cellule à 85 °C dans un environnement à 22 °C s'élève à 180 mW.

Les atomes étant sensibles au champ magnétique à travers l'effet Zeeman, il est important que le courant traversant ces résistances ne génère pas de champ magnétique parasite. Les résistances déposées ont ainsi été agencées en aller-retour pour compenser les contributions de chaque flux. Le comportement magnétique des résistances a été caractérisé par spectroscopie CPT, en observant le déplacement de fréquence des transitions Zeeman sensibles au champ magnétique au premier ordre, avec et sans courant de chauffe. La résolution de cette mesure est suffisante pour en déduire que l'effet de ce champ sur le transition d'horloge, avec une sensibilité quadratique au champ magnétique, est compatible avec la stabilité de fréquence visée.

Conclusions et perspectives. Les horloges atomiques miniatures offrent des perspectives à de multiples applications et leur développement reste un sujet d'actualité. Pour preuve, le nombre de brevets déposés sur ce sujet n'a jamais été aussi grand qu'en 2015. Le travail de cette thèse s'inscrit dans la continuité de nombreux efforts, en particulier du projet MAC-TFC, dont certains axes d'étude sont ici poursuivis. Ces travaux ont d'abord porté sur l'augmentation de la température opérationnelle et le développement de méthodes de fabrication alternatives, plus adaptées à l'industrialisation. La caractérisation d'une architecture réflective propice à la réalisation d'un module physique compact a été présentée ainsi que le développement de dépôts anti-relaxants applicables aux cellules microfabriquées. Enfin, un premier prototype compact a été présenté.

Les points restants à étudier sont mentionnés à plusieurs occasions. Si les mesures en cours des cellules avec dispensers sous forme de pâte sont concluantes, les dispensers solides pourront rapidement être remplacés. De même, la perméation de l'hélium pourrait être réduite en utilisant d'autres types de verre tels que les aluminosilicatés. La technique de remplissage par vannes nécessite plus d'efforts car certains procédés de

fabrication doivent encore être développés. A terme, cette méthode rendrait possible l'utilisation d'autres gaz tampon, dont l'azote, et d'autres sources de métal alcalin. La miniaturisation du module physique est en cours et une version intégrant des composants au niveau puce est à l'étude.

Au-delà des horloges, ces dispositifs atomiques miniatures ont également permis la réalisation de capteurs particulièrement sensibles tels que des gyroscopes et des magnétomètres avec des architectures similaires. Ces derniers ont d'ailleurs déjà montré des performances remarquables, ouvrant la voie aux premières applications in vivo en magnétoencéphalographie et magnétocardiographie.

Contents

Acronyms

AHM active hydrogen maser. 9

ASG aluminosilicate glass. 31, 102, 150

ASIC application-specific integrated circuit. ix, 1, 13

CBS cesium beam frequency standard. 9

CPT coherent population trapping. ix–xii, 1, 2, 8, 9, 12, 17, 22–25, 27, 29, 30, 33, 39, 58, 70, 87, 88, 103–107, 110, 135, 136, 141, 143–145, 148, 150

CSAC chip-scale atomic clock. 1–3, 8, 9, 12–16, 28–31, 58, 87, 151, 174

DARPA Defense Advanced Research Projects Agency. 1, 4, 12

DBR distributed Bragg reflector. 68

DFB distributed feedback. xii, 54, 68, 87–89, 95, 96, 99, 107, 150

DGA Direction Générale de l'Armement. 13, 149

DRIE deep reactive ion etching. 33, 39–42, 59, 62, 74, 83, 84, 126, 135

EOM electro-optic modulator. xii, 88, 89, 95

EPFL École polytechnique fédérale de Lausanne. 13

FWHM full width at half maximum. 24, 30, 80, 89, 93, 94, 96, 100, 117, 131, 132, 135, 141, 144

GNSS global navigation satellite system. 15

GPS global positioning system. ix, 1, 9, 15, 16

GPSDO GPS disciplined oscillator. 9

GUI graphical user interface. 89, 91, 92

HM hydrogen maser. 9

IMPACT Integrated Micro Primary Atomic Clock Technology. 4

ISIMAC Innovative Solutions for Improved Miniature Atomic Clocks. 1, 149

ITO indium tin oxide. 137

LILN laser-induced line narrowing. 25, 131

LTCC low temperature co-fired ceramic. 13, 14

MAC miniature atomic clock. 4, 8, 16

MAC-TFC MEMS Atomic Clocks for Timing, Frequency control and Communications. ix–xii, 1, 13, 14, 37, 41, 48, 66, 68, 87, 102, 136, 149

MEMS microelectromechanical systems. 33, 58, 77

NEG non-evaporable getter. 66

NIST National Institute of Standards and Technology. ix, 12, 13

NMR nuclear magnetic resonance. 31

OCXO oven-controlled crystal oscillator. 8, 15

OTS octadecyltrichlorosilane. xi, 2, 109–111, 135, 136, 150, 174

PBS polarizing beam splitter. 89

PCB printed circuit board. 54, 138, 139, 141, 142

PECVD plasma-enhanced chemical vapor deposition. 64

QMP quadrupole mass spectrometer. 66

QWP quarter-wave plate. 58, 59, 87, 89, 95, 140

RAFS rubidium atomic frequency standard. 8, 9, 15, 33

RGA residual gas analysis. 66, 67, 131, 133, 135

RIE reactive ion etching. 41, 64

SEM scanning electron microscope. 40–43, 65, 83, 84, 147

SQUID superconducting quantum interference device. 151

SYRTE Systèmes de Références Temps-Espace. 13, 71, 111, 112

TCXO temperature compensated crystal oscillator. 8, 9

UTC Coordinated Universal Time. 9

VCO voltage-controlled oscillator. 9, 12

VCSEL vertical cavity surface-emitting laser. ix, xii, 1, 8, 9, 12, 13, 30, 33, 58, 59, 87–89, 93, 103, 107, 140–142, 147, 150

VLBI very-long-baseline interferometry. 1

XO quartz oscillator. 8

Introduction

Accurate timekeeping has allowed tremendous progress on both scientific and technological grounds. Every improvement made in this field brought its share of new possibilities.

Navigation probably provides the most eloquent examples of those possibilities. In the 18th century, John Harrison's maritime chronometer allowed navigators at sea to keep track of time and derive their longitude from the position of stars with unprecedented accuracy. Nowadays, a global positioning system (GPS) receiver determines its position by comparing differences in propagation times between radio waves coming from different satellites. In order to allow a localization within a few meters, each satellite has to carry a set of synchronized atomic clocks accurate to within a few nanoseconds. On a broader scale, atomic clocks are also used to track objects in outer space through very-long-baseline interferometry (VLBI). It consists in aggregating data from multiple telescopes at different locations on Earth or in space to improve the resolution that a single telescope would have.

Today's most accurate clocks achieve such stabilities that it would take at least fifteen billion years before they loose or gain a second. This may seem more accurate than needed but pursuing efforts toward better timekeeping is actually essential in numerous ways. Since Einstein's theory of special relativity abolished the idea of a unique and absolute time, measuring it has become even more fundamental. Physicists are now using the most accurate clocks to test the fundamental laws of nature such as general relativity (Cacciapuoti and Salomon, 2009), look for potential drifts of fundamental constants (Guéna *et al.*, 2012, Godun *et al.*, 2014), and to observe signatures of gravitational waves (Taylor, 1994).

Many applications impose more drastic constraints on size, weight, power consumption and cost, particularly for telecommunication systems, improved GPS receivers and underwater applications. Over the past decade, chip-scale atomic clocks (CSACs) have appeared in the frequency reference spectrum. They benefit from the development of vertical cavity surface-emitting lasers (VCSELs) and exploit the coherent population trapping (CPT) phenomenon to probe alkali atoms contained in a microfabricated vapor cell.

Their development has been driven by the CSAC program initiated by the Defense Advanced Research Projects Agency (DARPA) around 2002, and led to the arrival of the first commercial product on the market in early 2011. At the time of writing, the cost of a CSAC remains in the order of $700, which is still about seven times too expensive for a wide market acceptance.

After preliminary studies done at FEMTO-ST, the European-wide project MEMS Atomic Clocks for Timing, Frequency control and Communications (MAC-TFC) allowed developing the key components of CSACs. Among them, a VCSEL resonant with the D_1 line of cesium was developed at Ulm University (Germany), along with a low power microwave synthesizer embedded in an application-specific integrated circuit (ASIC) at EPFL (Switzerland) and an integrated physics package at VTT (Finland). Furthermore, a robust alkali vapor cell technology based on solid dispensers was demonstrated at FEMTO-ST. A novel cell architecture, based on a folded light path, was also proposed with the potential to drastically reduce the physics package assembly costs thanks to a wafer-level approach.

On this basis, the research project Innovative Solutions for Improved Miniature Atomic Clocks (ISIMAC) was proposed to study further original solutions, including this novel cell architecture. The industrial transfer project HABAC began in the meantime. This project was the occasion to study and improve the robustness of the current cell technology, in particular regarding the laser activation process, whose repeatability was still somehow unsatisfactory. This work was mainly performed in the framework of those two projects. It focuses primarily on the optimization of microfabricated alkali vapor cells and their fabrication process. Several limitations, regarding the fabrication costs, the operating temperature or the device footprint could be identified and solutions were proposed to address them. Optimizing the cell requires a broader understanding of the CPT phenomenon and the different effects that may limit the clock performances. Constraints on the physics package such as ease of integration, power consumption and footprint also need to be kept in mind.

This thesis is structured as follows:

- Chapter 1 introduces the basics of frequency standards metrology, in particular the Allan deviation, which is commonly used to rate short and long-term frequency stabilities. After a brief description of their working principle, the context in which miniature atomic clocks are being developed is presented and the initial developments, notably done during the CSAC program, are retraced. Some applications that could greatly benefit from these devices are detailed and their targeted specifications are compared to other frequency standards.

- Chapter 2 covers basics on spectroscopy and describes the CPT phenomenon. The relaxation mechanisms are described mathematically or qualitatively, as functions of other parameters, in order to evaluate their impact on the clock performances. Thereby, this chapter aims at providing guidelines for the design of cells and physics packages complying with the targeted specifications.

- Chapter 3 details the vapor cells microfabrication processes and presents the reflective architecture, which have been proposed prior this work. The different fabrication steps are described in details, and we propose several improvements to raise the yield of the process. Paste-like dispensers, which could be collectively deposited to drastically lower the production costs, are studied further. A filling method inspired from the legacy of glass-blowing techniques is also proposed and early experiments are exposed.

- Chapter 4 reports the CPT metrology methods and results. The implementation of the characterization benches used for CPT spectroscopy and long-term aging measurements are described. The characterization results of transmissive cells with different buffer gas pressures is discussed. Results for reflective cells are also presented and compared to transmissive cells. In order to assess the adequacy of the cell technology with the stability specification, long-term frequency measurement are finally performed.

- Chapter 5 describes investigations conducted on octadecyltrichlorosilane (OTS) wall-coatings, performed both in centimeter and in millimeter-scale cells. We detail the coating procedures and the characterization results.

- Chapter 6 presents preliminary work on the development of a physics package compliant with collective fabrication. Cells with integrated heating and temperature sensing resistors are presented. A physics package integrating those cells was constructed and characterized thanks to several contributions.

Chapter 1

Atomic clocks

Time and frequency standards rely on a periodic phenomenon that repeats itself at a constant rate. The apparatus providing this periodic phenomenon is called a resonator. It is embedded in a system providing power to sustain the resonance and delivering a practical periodic signal, forming an oscillator. A clock finally integrates this oscillator and counts the periods of the signal it delivers to keep time. Although not strictly identical, the terms oscillator, frequency reference, frequency standard and clock may be used interchangeably in the following.

From the rotation of the earth to the vibration of quartz crystal, various phenomena have been employed over time with increasing performances. The use of atoms as resonators, previously proposed by Maxwell in 1873 (Thomson and Tait, 1879), was finally applied to clocks in the 50's. With the advances on quantum mechanics and spectroscopy techniques, atomic clocks soon became the most stable clocks. In 1967, the 13th General Conference of Weights and Measures redefined the second as:

> *the duration of* 9 192 631 770 *periods of the radiation corresponding to the transition between two hyperfine levels of the ground state of the cesium-133 atom (at rest and in a null magnetic field).*

Because the second is the most precisely measured unit, other units have been redefined to be derived from the second by conceptual methods, rather than to depend on physical artifacts. The meter has been redefined in 1983 in terms of the length traveled by light in a given duration. Likewise, the kilogram, which still relies on a physical artifact, will probably be redefined in the coming years, according to the definitions of the meter and the second (Lan *et al.*, 2013). As applications have become more and more diverse, various types of atomic clocks with different stability performances, sizes and costs have been developed. The recent development of CSACs aims to bridge the gap between compact atomic standards and quartz crystal oscillators, by improving the frequency stability while reducing the cost, volume and power consumption.

In this chapter, the tools for the characterization of oscillators are first presented. The working principle of atomic clocks is described and we bring the focus on miniature atomic clocks. In particular, their development, their applications and their place in the spectrum of frequency standards are described.

1.1 Characterization of frequency standards and clocks

1.1.1 Definitions

The signal delivered by a frequency reference can be described by the equation:

$$\text{V}(t) = V_0 \cos(2\pi\nu_0 t + \varphi(t)), \tag{1.1}$$

where V_0 is the amplitude, ν_0 is the unperturbed clock frequency and φ denotes the phase noise (amplitude modulation noise is neglected). For an ideal frequency reference, this phase noise is null. In reality, various effects disturb the frequency, as we shall see.

The instantaneous frequency is then:

$$\nu(t) = \nu_0 + \frac{1}{2\pi}\frac{d\varphi(t)}{dt} = \nu_0 + \Delta\nu(t), \tag{1.2}$$

We define the dimensionless frequency deviation (or fractional frequency) as:

$$y(t) = \frac{\nu(t) - \nu_0}{\nu_0} = \frac{1}{2\pi\nu_0}\frac{d\varphi(t)}{dt}, \tag{1.3}$$

1.1.2   Accuracy, stability, precision

In the following we should try to avoid any ambiguity between accuracy, stability and precision. The proper terminology defined by Rutman and Walls (1991), Vig (1992), Lombardi (2002) can be recalled:

Accuracy represents the degree of conformity of a measurement to the definition of the quantity being measured or a specified value.

Precision describes how close different measurements of the same measurand are.

Stability refers to how much the measurement is affected by the evolution of an other parameter such as time or temperature. For short, we will replace the term *time stability* with *stability*.

Hence, a stable clock is not necessarily accurate if the period of the signal it delivers does not translate into seconds without an initial calibration. A clock implementing a measurement method complying with the present definition of the second based on unperturbed cesium-133 is called a primary frequency standard. As correspondences with the energy level transitions of other atoms have been drawn, secondary representations of the second have been established. This allows so-called secondary standards to provide an accurate frequency (which is ultimately limited by the uncertainty of this correspondence). In principle, primary and secondary standards do not require an initial calibration.

The frequency delivered by atomic standards usually differs from the unperturbed atomic transition. Indeed, both the environment and the interactions required to probe this transition induce shifts on its frequency. Those are called systematic effects. We can split the constant part of the clock frequency ν_0 by defining the offset ϵ from the "accurate" frequency:

$$\nu(t) = \nu_{at}(1 + \epsilon) + \Delta\nu(t), \tag{1.4}$$

The uncertainty of ϵ indicates the clock "inaccuracy".

For applications where calibration and repeated synchronization are allowed, an inaccurate clock can still make a good working standard, provided that it is sufficiently stable. As we will see, miniature atomic clocks (MACs) are rather inaccurate compared to other atomic standards even if cesium is employed because they suffer from many systematic effects and a calibration step is required to account for them. Those effects will be described in Chapter 2. Intrinsic accuracy can be important in some field applications and, for this reason, the DARPA has recently proposed the Integrated Micro Primary Atomic Clock Technology (IMPACT) project, which is still ongoing.

Figure 1.1 provides four schematic cases of an oscillator frequency evolution through time. We can see that stability is not per se a quantitative characteristic as it depends on the time window during which it is assessed. Indeed, looking at the first data points of plots (a) and (c), it seems that (a) is more stable than (c). It is therefore relevant to distinguish different "degrees" of stability. (a) may be said to have a better short-term stability than (c) but a worse long-term stability. In order to quantify properly the stability of oscillators, we introduce the Allan deviation.

1.1.3   Allan deviation

The Allan variance is a statistical estimator particularly useful to characterize the frequency stability of a signal (Allan, 1966).

We denote by $\overline{y_k}$ the mean of the signal $y(t)$ on the interval $[t_k; t_{k+1}]$ such that $t_{k+1} - t_k = \tau$:

$$\overline{y_k} = \frac{1}{\tau}\int_{t_k}^{t_{k+1}} y(t)dt, \tag{1.5}$$
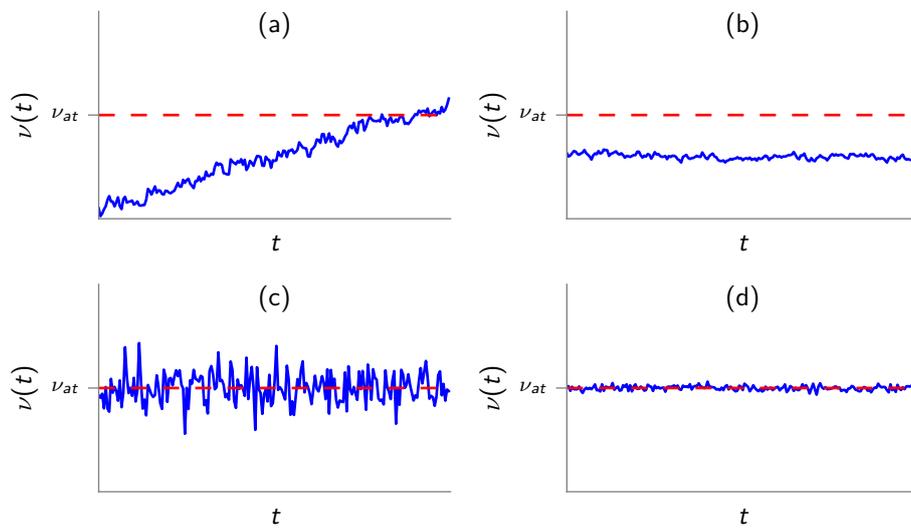
Figure 1.1: Time evolution of an oscillator frequency. In case (a), the frequency is neither stable nor accurate. On the contrary, (d) is both stable and accurate. (b) is rather stable but not perfectly accurate and (d) is accurate but not stable.
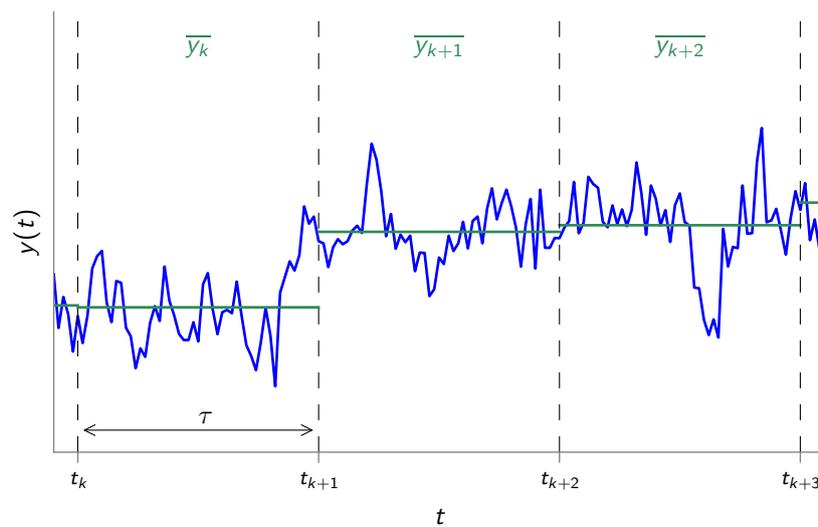
Figure 1.2: Computation of Allan variance.
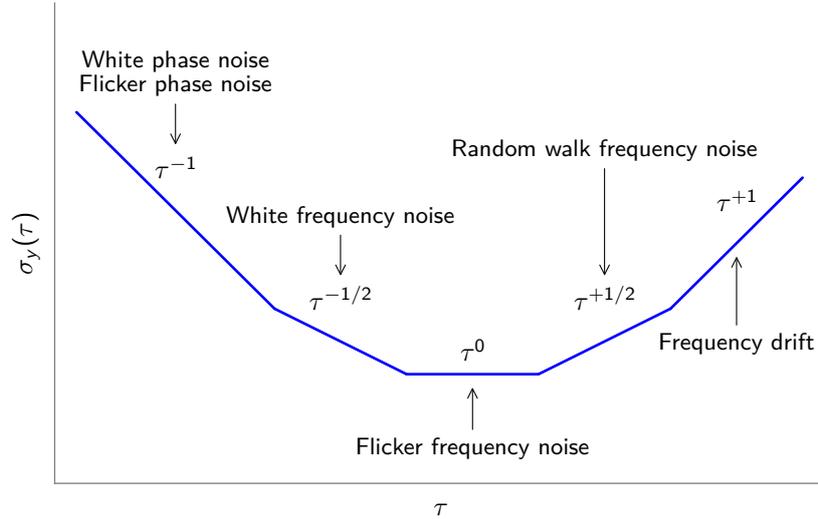
Figure 1.3: Log-log Allan deviation traces for different noise types.

$(\overline{y_k})$ is the sequence of average frequency samples as depicted on Fig. 1.2.

The Allan variance is expressed as:

$$\sigma_y^2(\tau) = \frac{1}{2}\big\langle\, (\overline{y_{k+1}} - \overline{y_k})^2 \,\big\rangle = \frac{1}{2}\lim_{n\to\infty}\left[\frac{1}{n}\sum_{k=1}^{n}(\overline{y_{k+1}} - \overline{y_k})^2\right]$$
$$\approx \frac{1}{2(N-1)}\sum_{k=1}^{N-1}(\overline{y_{k+1}} - \overline{y_k})^2 ,$$

(1.6)

The estimation of the Allan variance for a given τ gets better as the number of collected time samples gets larger. The Allan variance is particularly convenient to differentiate different noise types as they are translated into different slopes on the bi-logarithmic plot as shown on Fig. 1.3.

Figure 1.4 shows the relative frequency of three hypothetic signals with different characteristics and their respective Allan deviation plots. We can see that signal (a) is more stable for integration times smaller than $20\,\mathrm{s}$. The linear drift translates into an asymptotic limit of equation $0.1\times\tau$ on the stability plot. The stability of signal (b) suffers from a flat τ^0 limit due to flicker frequency noise. On long integration times, its stability is also limited by a frequency drift ($0.01\times\tau$). Signal (c) is essentially a white frequency noise. The Allan deviation follows a $7\times\tau^{-1/2}$ limit. The uncertainty is reduced as the frequency is averaged over several hundreds of seconds until the drift limit is reached ($0.001\times\tau$).

1.2   Description of atomic clocks

1.2.1   Basic concept

An atomic clock essentially consists in a feedback loop which constantly compares and corrects the frequency of a macroscopic oscillator against the frequency of an atomic transition. The macroscopic oscillator (also called local oscillator - LO) oscillates at a useful frequency ν_{osc} in the megahertz range (typically $10\,\mathrm{MHz}$). This local oscillator confers its short-term stability and its phase noise characteristics to the clock while the atomic transition provides mid and long-term stability. In order to probe the atomic transition whose frequency ν_{at} lies in the gigahertz range, ν_{osc} is frequency-multiplied using a microwave frequency synthesis. An electromagnetic field oscillating at this frequency is then emitted and the response of the atoms is detected. A synchronous detection is performed to generate an error signal and tune the frequency of the local oscillator, closing the feedback loop. A schematic of an atomic clock is shown on Fig. 1.5.

The short-term fractional frequency stability provided by the atomic clock can be approximated by:
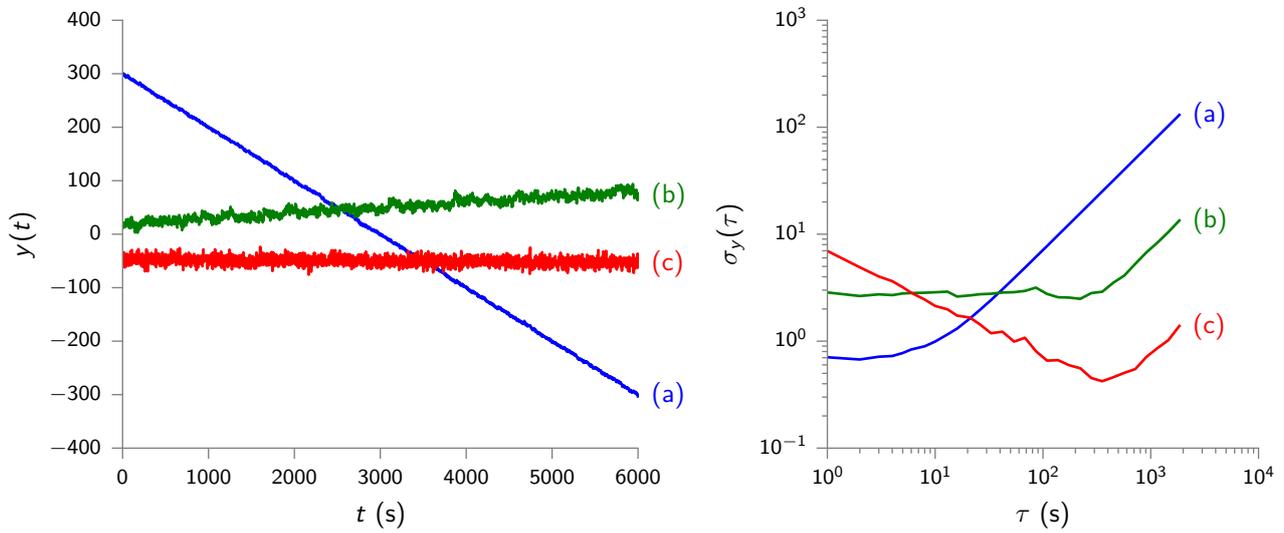
Figure 1.4: Allan deviation plots for three example signals (signal generation and Allan deviation computation performed using the AllanTools package for Python).
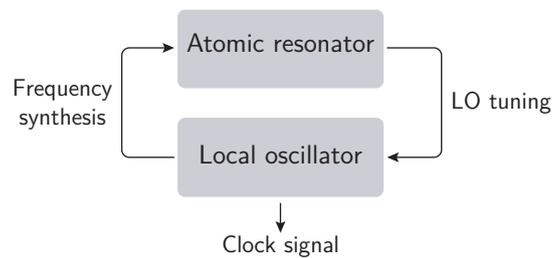
Figure 1.5: Working principle of an atomic clock.

$$\sigma_y(\tau) \approx \frac{\Delta \nu}{\nu_0} \frac{1}{S/N} \tau^{-1/2}, \tag{1.7}$$

where $\Delta \nu$ is the atomic resonance linewidth, ν_0 is the atomic resonance frequency and S/N is the signal to noise ratio of the detected resonance in a $1\,\mathrm{Hz}$ bandwidth.

Improving the stability boils down to reducing the resonance linewidth and increasing the resonance frequency while maximizing the signal to noise ratio.

1.3   Time and frequency standards spectrum

Cost, size, weight and power consumption, often referred to as the CSWaP, are critical parameters besides stability performances. Additional parameters include the warm-up time and the operating temperature range. Unlike the best atomic clocks used to define the international atomic time, which are being developed in a controlled environment with no restrictions on cost, volume or power consumption, those parameters need to be taken into account for most field applications. This section briefly details the different types of frequency standards that are available, from the least to the most stable, in terms of long-term stability.

Quartz oscillators.   Quartz oscillators (XOs) are the most common frequency references and equip most electronic devices. A quartz resonator relies on the strain generated by a piezoelectric crystal when a voltage is applied. The resonance frequency is the rate of expansion and contraction of the crystal. Quartz oscillators exhibit excellent short-term stabilities but their frequency changes over time owing to aging processes. Aging may occur due to material build-up or changes to the crystal itself. Additionally, they are sensitive to environmental factors such as vibration, pressure and temperature. Temperature compensated crystal oscillators (TCXOs) diminish this sensitivity by measuring the quartz resonator temperature and correcting the output frequency according to foreknowledge on this dependency. In an oven-controlled crystal oscillator (OCXO), the temperature of the resonator is maintained constant. Short and mid-term stabilities of OCXOs are better than TCXOs by several orders of magnitude. They are however bulkier and more power-intensive. High-end OCXOs actually compete with compact atomic references.

Thermal atomic vapor frequency references.   When long-term stability is required, an atomic resonator can be used to discipline the frequency of a local oscillator (often a quartz oscillator). Slow variations due to the quartz oscillator aging are then averted while still benefiting from the short-term performances of the quartz. The atomic resonator employed in most compact atomic standards comprises a glass cell containing a thermal vapor of alkali atoms, the alkali vapor cell.

Rubidium atomic frequency standards (RAFSs) have long been the most common and affordable compact atomic standards. In this case, a ^{87}Rb vapor is interrogated in a double resonance scheme. The vapor is illuminated by a ^{87}Rb discharge lamp filtered by a ^{85}Rb cell. Benefiting from the partial overlapping of ^{85}Rb and ^{87}Rb spectra, only one of the two hyperfine spectral lines emitted by the lamp is transmitted. As a result, the atoms in the cell are unevenly populated between the two hyperfine energy levels through optical pumping. A microwave field with a frequency resonant with the hyperfine splitting transition is emitted in the cell. When the microwave frequency is resonant with the hyperfine splitting of rubidium atoms, the absorption of the vapor is increased because the optically pumped level is repopulated by the microwave transition, providing atoms that absorb light.

Lasers are now replacing consuming discharge lamps in most frequency standards based on optical pumping. With the narrow spectral width provided by lasers, pumping a single level is easier and no longer requires additional filtering as in a RAFS. Moreover, the alkali vapor employed is not limited to rubidium anymore. In addition, the CPT phenomenon has revealed a way to interrogate an alkali vapor with an optically carried microwave signal, which sidesteps the need for bulky microwave cavities. The recent development of efficient VCSELs providing high modulation capabilities enabled further miniaturization. Small scale atomic references are referred to as CSACs or MACs.

Since the mid- and long-term stabilities are brought by the atomic resonator, the constrains on the local oscillator are relaxed. Hence, a smaller, cheaper and more power efficient local oscillator can be used. In the end, CSACs achieve unprecedented long-term stabilities with power consumptions drastically reduced. The developments of CSACs will be detailed later. Larger clocks based on CPT or double resonance and thermal vapor cells with short and mid-term stabilities reaching the performances of hydrogen masers are also being

developed (Bandi *et al.*, 2014, Danet *et al.*, 2014, Abdel Hafiz and Boudot, 2015). Unfortunately, various phenomenons including aging still degrades the long-term performances of vapor cell standards (Riley, 1992).

Cesium beam standards. For applications demanding better accuracy and long-term stability, and where more space and power can be provided, a cesium beam frequency standard (CBS) is adequate. It does not suffer from aging and is accurate without calibration. A beam of ^{133}Cs atoms is emitted from an oven at one end of a vacuum tube. The atoms are evenly distributed among the two hyperfine states. A first magnetic gate deflects atoms that are in a specific hyperfine state toward a microwave cavity. If the frequency of the microwave field matches the hyperfine splitting of the atoms, their state changes. A second magnetic gate then deflects the atoms whose state have changed toward a detector. The signal is fed back to the local oscillator, from which the microwave frequency is generated, in order to constantly maximize the number of atoms whose state changes in the microwave cavity. The accuracy of CBS depends on the length of tube and their miniaturization is therefore impossible. While some commercial devices still use magnetic deflection, most recent cesium standards employ optical pumping to prepare and detect atomic states (de Clercq *et al.*, 1984).

Hydrogen masers. In an hydrogen maser (HM), a beam of hydrogen atoms is generated, passes through a state selecting magnet and enters a quartz bulb. The inside of the cell is covered with an anti-relaxation fluorocarbon coating. The bulb is surrounded by a microwave cavity. In passive hydrogen masers, the cavity is powered by an external signal tuned at the resonance frequency of the atoms while in an active hydrogen maser (AHM), the cavity oscillates by itself. HM are more expensive and bigger than CBS but they provide improved short and mid-term stabilities.

GPS disciplined oscillators. The GPS satellites delivers signal containing accurate timing information from their on-board atomic clocks (3 or 4 Cs and Rb standards), which are regularly synchronized to an atomic time scale close to Coordinated Universal Time (UTC). Those signals are exploited in GPS disciplined oscillators (GPSDOs) to steer the frequency of a local oscillator. The resulting long-term stability is excellent. The local oscillator can be a quartz oscillator or a CSAC. GPSDOs provide inexpensive alternatives to the frequency references presented previously. However, they rely on external signals, which are not available in some applications (e.g. underwater) or not reliable enough. In addition, GPS signals are subject to jamming or even falsification (spoofing).

Cold atoms. Compact standards based on cold atoms recently emerged. For instance, the Muquans clock (MuClock) relies on the manipulation of cold rubidium atoms with lasers to prepare them in a cloud, where a clock transition can be probed (Muquans, 2016). This device could compete with hydrogen masers on the long-term with similar or slightly smaller form factors.

Figure 1.6 compares typical frequency stabilities and specifications achieved by different types of frequency standards. The dimensions of some relatively compact standards are compared in Fig. 1.7, which also displays the relevant characteristics such as operating temperature range, power consumption and cost.

1.4 Miniature atomic clocks

1.4.1 Principle

Miniature atomic clocks are rather similar to RAFS as they rely on a thermal vapor of alkali atoms. Although different miniature atomic clock architectures exist, the most typical is shown on Fig. 1.8. It comprises a microfabricated alkali vapor cell, which is interrogated by the light emitted from a VCSEL. The box embedding those components is called *physics package*, as in many sensors requiring to measure a physical quantity.

The transmission of light through the cell is measured by a photodiode. The VCSEL is modulated at half the hyperfine frequency of the alkali atoms, so that the frequency difference of the two first-order sidebands exactly equals the hyperfine transition. The CPT phenomenon, which will be detailed later, induces a transmission peak around the resonance. The signal is detected and used to correct the frequency of a local oscillator. This local oscillator can be a simple voltage-controlled oscillator (VCO) oscillating directly at the VCSEL modulation frequency, or a better performing oscillator such as a TCXO in the megahertz range. In the latter case, a frequency synthesizer needs to multiply the TCXO frequency in order to provide a modulation signal
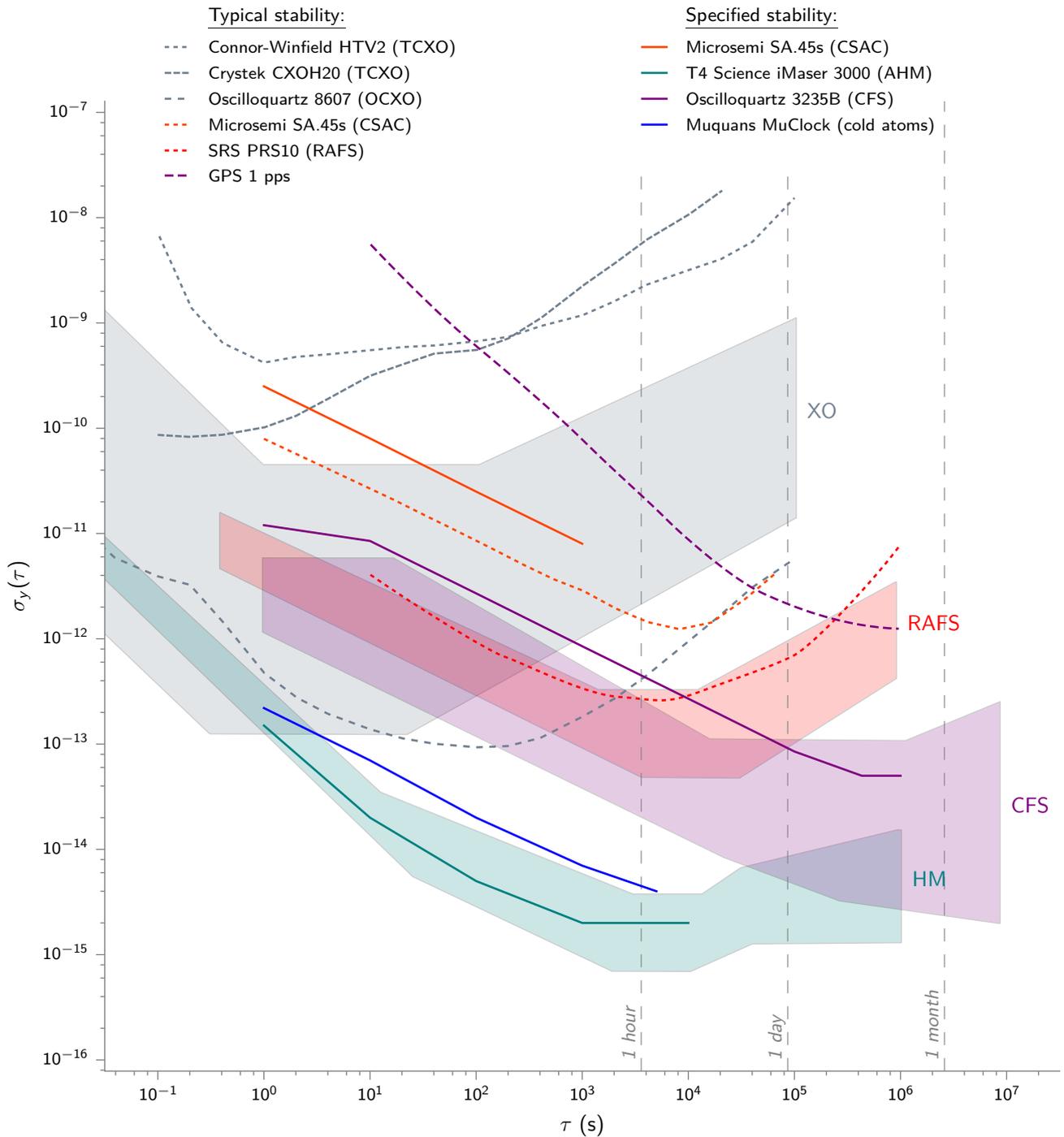
Figure 1.6: Frequency stabilities of different commercial frequency standards (Allan deviations).

Underlays from Allan *et al.* (1997). Oscilloquartz 8607 and Connor-Winfield HTV2 data from Van Baak (2015). Microsemi SA.45s data from Lutwak (2011). SRS PRS10 and GPS data from Stanford Research Systems (2016). MuClock specification from Muquans (2016). The comparison is only indicative as the measurement conditions and Allan deviation computation methods may differ.

TOP VIEW

OCXO
Oscilloquartz
8607

RAFS
SRS
PRS10

Miniature
Atomic Clock

Microsemi
SA.35m

CSAC
Microsemi
SA.45s

35.31 mm

TCXO
Crystek
CXOH20

40.6 mm

SIDE VIEW

-10°C to +75°C
5 W (14 W @ warm-up)
$ 1500

-20°C to +65°C
14 W (50 W @ warm-up)
$ 1500

11.4 mm

-10°C to +60°C
100 mW
$ 30

-10°C to +35°C*
120 mW (140 mW @ warm-up)
$ 1000 ?

-10°C to +75°C
5 W (14 W @ warm-up)
$?

Figure 1.7: Comparison of the dimensions and some characteristics of several compact frequency references.
Life-size dimensions if printed on A4 format.
* At the time of writing, the operating temperature range of the SA.45s has been reduced due to a technical problem limiting the product lifetime. It is expected to be solved soon and this range extended back to its original specification: −40 °C to 85 °C.
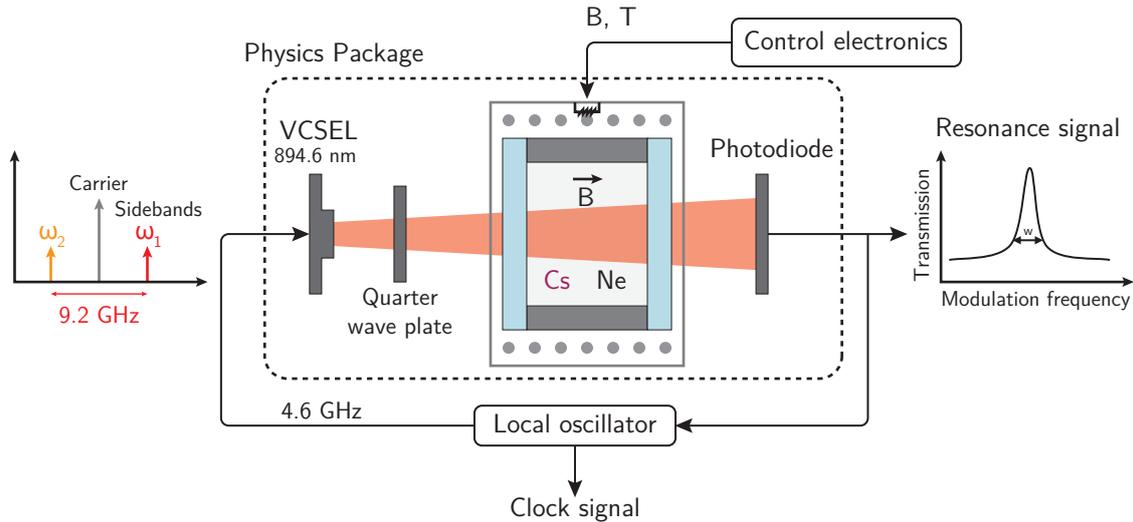
Figure 1.8: Schematic of a miniature CPT atomic clock.

in the gigahertz range to the VCSEL, whereas in the former case the frequency of the VCO is divided to the megahertz range to provide a convenient clock signal to the user. The package embeds several optical components. A quarter-wave plate confers a circular polarization to the light entering the cell. A neutral density filter adjusts the optical power. In the physics package, the cell is heated to provide enough atomic density. Since the cell temperature generally affects the clock frequency, it must be thermally isolated and finely regulated. In addition, a static magnetic field must be provided to raise the Zeeman degeneracy. The physics package is driven by the control electronics. It drives all the sensors and current sources and performs various computations, in particular, to detect and lock on the appropriate resonance signals during the start-up sequence. Knappe (2008) wrote a rich review article on miniature atomic clocks. This reference work covers most aspects.

1.4.2   Emergence of miniature atomic clocks

Cyr *et al.* (1993) first proposed to probe the clock transition of alkali atoms using a purely optical interrogation scheme. Using the phenomenon of CPT, it was suggested that smaller atomic references could be achieved by removing the microwave cavity commonly found around the vapor cell in rubidium oscillators. VCSELs were later found suitable to generate the optical fields in the CPT scheme (Affolderbach *et al.*, 2000). VCSELs are particularly appropriate for collective fabrication and vertical integration. In addition, they are power-efficient and allow direct modulation with bandwidths in the gigahertz range.

A first remarkably compact atomic clock was prototyped at the National Institute of Standards and Technology (NIST) by Kitching *et al.* (2001), who concluded that the volume could be shrunk further if components at the chip level were used instead of packaged components. Soon after, Kitching *et al.* (2002) also proposed to use micromachining technology rather than glass-blowing techniques to fabricate small-scale and inexpensive alkali vapor cells. DARPA started to fund extensively this topic through the CSAC program from that year. The use of a stack of silicon and glass wafers was outlooked by Knappe *et al.* (2003b) and demonstrated by Liew *et al.* (2004). Parallelepipedic cells compliant with a wafer-level integration solved the last barrier and a complete microfabricated physics package was finally reported by Knappe *et al.* (2004b). It is the first prototype assembling bare chip-level components and its utterly small volume of $9.5 \, \text{mm}^3$ is often compared to a grain of rice (see Fig. 1.9). The stability wa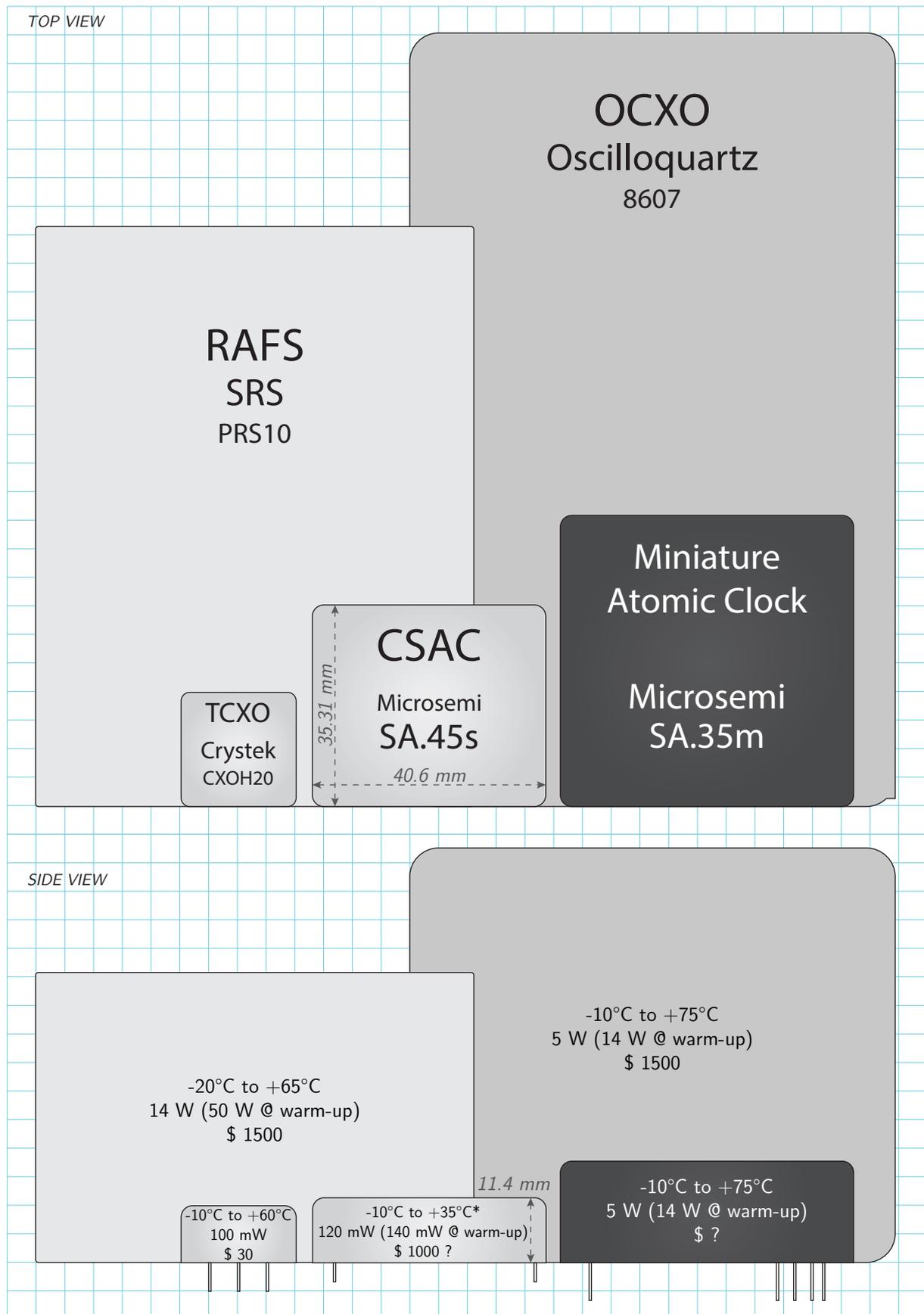s gradually improved over the following years by using lasers tuned on the alkali D_1 lines and a cell with a more stable inner atmosphere (Knappe *et al.*, 2005b,a).

Soon after this first demonstration, Symmetricom unveiled its first prototype in which the cell, the VCSEL and the photodiode are suspended between polyimide frames, providing an efficient thermal insulation (Lutwak *et al.*, 2004). VCSELs emitting at $894 \, \text{nm}$, resonant with Cs D_1 lines were developed at Sandia National Laboratories while the cell and the physics package were fabricated at the Draper Laboratory. The design provides high thermal decoupling allowing remarkable power-efficiency. Several prototypes from other institutes and companies were demonstrated, including Honeywell (Youngner *et al.*, 2007), Sarnoff (Braun *et al.*, 2007)
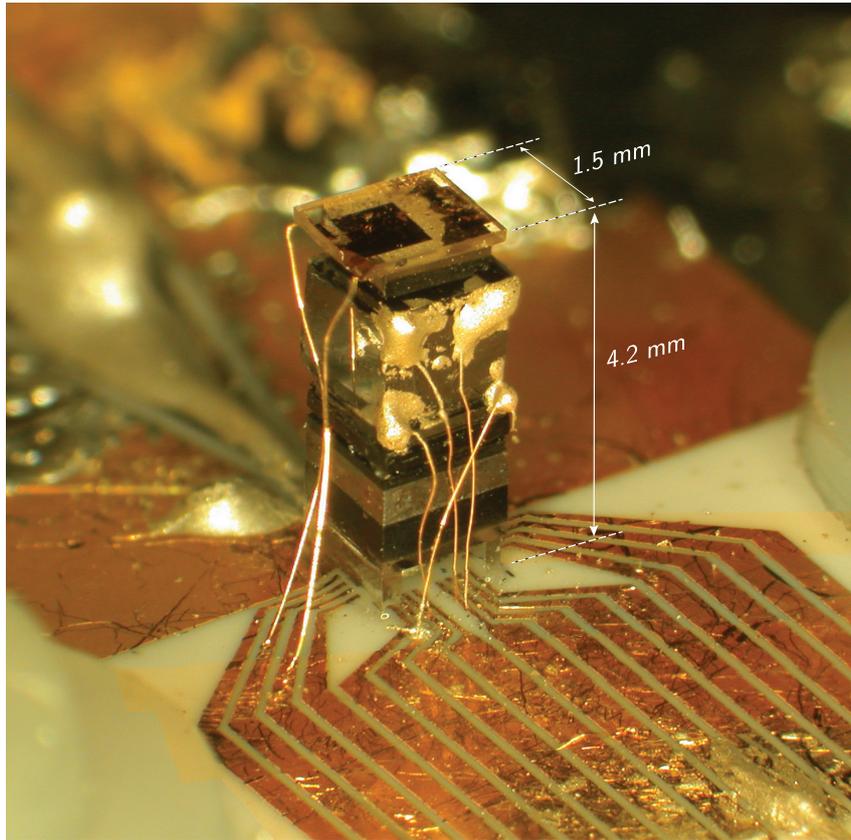
Figure 1.9: Microfabricated CSAC physics package developed at NIST.

and Teledyne (DeNatale *et al.*, 2008). After further developments, Symmetricom, acquired by Microsemi, announced the availability of the first commercial product in early 2011: the SA.45s (Lutwak, 2011). It only consumes 120 mW and fits in 16 cm^3. Initially priced around \$1500, a government funded program aiming at reducing its cost down to \$100 is underway.

Funded by the European Union, the MAC-TFC project started in 2008, shortly after the demonstration at FEMTO-ST of a new filling approach for microfabricated cesium vapor cells (Douahi *et al.*, 2007, Nieradko *et al.*, 2008). This project allowed the development of VCSELs resonant with the Cs D$_1$ line at Ulm University (Al-Samaneh *et al.*, 2012) and a robust cell fabrication process at FEMTO-ST (Hasegawa *et al.*, 2011b) based on custom solid cesium dispensers from SAES Getters. A frequency synthesizer ASIC was developed at the École polytechnique fédérale de Lausanne (EPFL) featuring a power consumption of 15 mW (Zhao *et al.*, 2014). A physics package, based on a low temperature co-fired ceramic (LTCC) assembly, was designed and constructed by the VTT Technical Research Center of Finland (Chutani *et al.*, 2012, Karioja *et al.*, 2014). It is shown in Fig. 1.10.

Haesler *et al.* (2013), Shao-Liang *et al.* (2014) and Shi *et al.* (2015) recently reported CSAC prototypes.

Figure 1.11 gathers Allan deviation plots of different CSAC prototypes and tabletop setups.

1.4.3 Context of this work

After the MAC-TFC project, several French projects were granted, mostly funded by the Direction Générale de l'Armement (DGA). The work reported in this manuscript was performed in the frame of these projects:

ISIMAC. In partnership with the Systèmes de Références Temps-Espace (SYRTE) laboratory of the Observatoire de Paris, this project aimed at developing further pumping schemes, examine the adequacy of wall-coatings and study novel and original cell architectures, best-suited for microfabrication and wafer-level production processes.
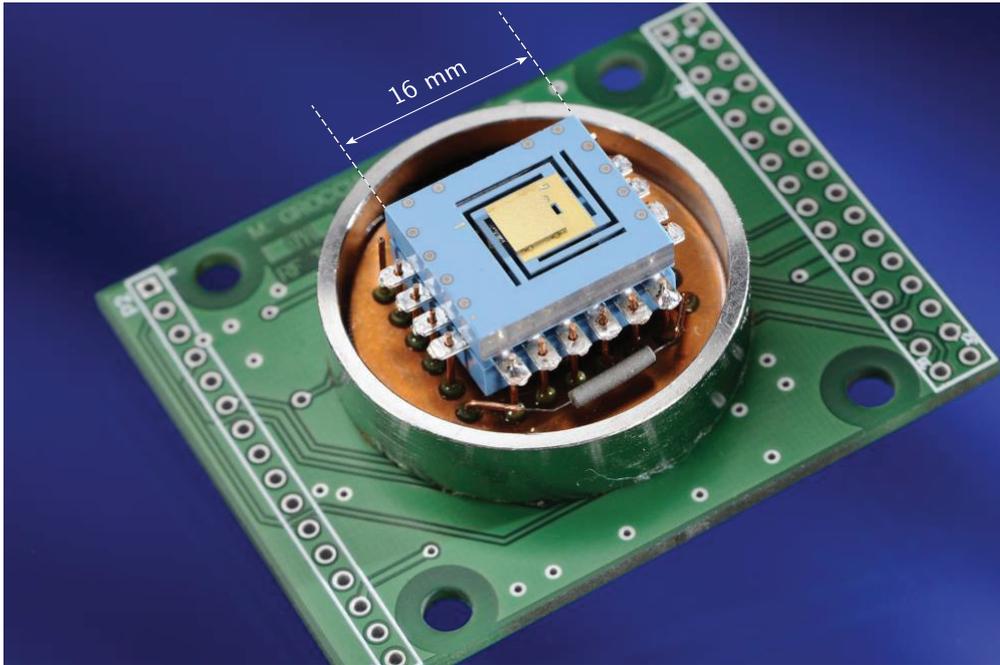
Figure 1.10: Physics package fabricated during MAC-TFC. The coil generating the magnetic field is integrated in the LTCC structure.
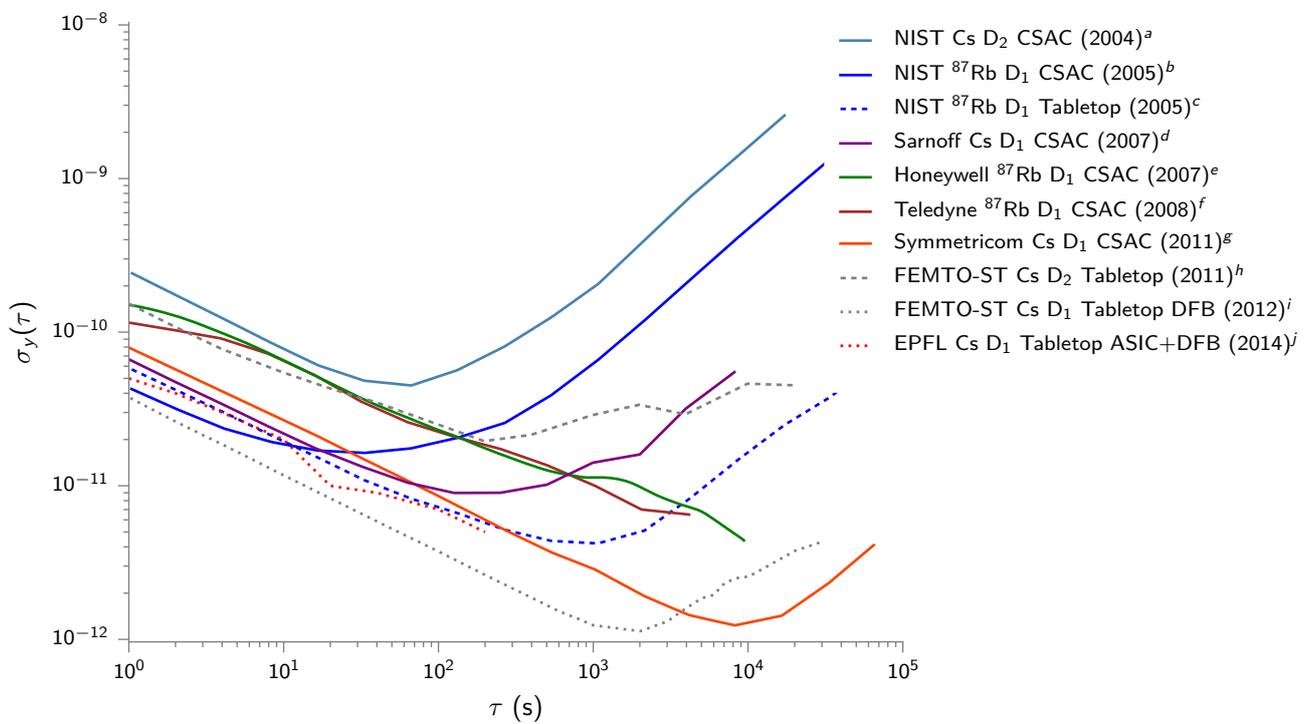
Figure 1.11: Frequency stability comparison of CSAC prototypes and tabletop setups based on millimeter-scale cells.

Data from [a] Knappe *et al.* (2004b), [b] Knappe *et al.* (2005b), [c] Knappe *et al.* (2005a), [d] Braun *et al.* (2007), [e] Youngner *et al.* (2007), [f] DeNatale *et al.* (2008), [g] Lutwak (2011), [h] Boudot *et al.* (2011b), [i] Boudot *et al.* (2012) and [j] Zhao *et al.* (2014).

HABAC. Gathering two industrial partners, the purpose of this project was to design a preliminary physics package of a miniature atomic clock with its electronics and transfer the technological knowhow developed at FEMTO-ST.

SCPTime. This consortium intend to develop a secure and precise time delivery network. This project mixes industrial partners and institutions contributing at different levels of this architure. In this network, the miniature atomic clock would mainly ensure holdover on a local server.

1.4.4 Applications

Telecommunications. Wireless communications have been increasingly demanding for accurate and stable frequency standards to comply with transmission channel separation requirements and offer constantly increasing data rates.

In order to avoid interferences and handle communications handovers between adjacent cells, the base stations of cellular networks need to be synchronized. Even if they are still costly, high-end OCXOs disciplined to GPS are often preferred to atomic standards for their lower cost. The holdover capability of a station describes its ability to function without access to the timing source, e.g. in case of GPS blackout. Because of the limited long-term stability of OCXOs equipping base stations, the holdover period is typically not longer than 24 hours after the timing source fails. This implies expensive emergency repairs. CSACs are particularly appealing since they could extend the holdover period to several days and still reach lower prices than high-end OCXOs or atomic references. CSACs are expected to be massively adopted as soon as their price is reduced to $300. Beyond base stations, any systems relying on an external timing source may require some level of holdover capability.

Power grids. The management of power grids relies on distributed and synchronized phasors, which remotely measure several electrical quantities across the network. Future power distribution networks, known as smart-grids, aim at more efficiency in complex architectures where power sources, storage and consumers are distributed over the entire network. In such complex grids, one may expect an increased demand on the number and the reliability of phasors. Presently, global navigation satellite system (GNSS) synchronized clocks are employed, making the system dependent on the availability of those signals. Here again, CSACs could diminish this dependency and secure the system.

Underwater sensing. When electromagnetic signals are out of reach, long-term frequency stability becomes especially critical. In particular, geophysical research and fossil fuels prospective make use of matrices of underwater sensors to probe the ocean floor with acoustic waves. Time-synchronized data from the sensors are then processed to produce maps or cross-sectional views of the floor. OCXOs are mostly employed for this task. They are synchronized before being immersed. With better long-term stability and power efficiency, CSACs can significantly extend the mission duration.

Navigation. GPS receivers could greatly benefit from more stable clocks. A regular receiver requires at least 4 satellites to compute its position and GPS time, but for a receiver equipped with a stable clock, after synchronization, 3 of them are sufficient as it benefits from the foreknowledge of the time variable (Sturza, 1983). In addition, the reacquisition time after a signal outage can be significantly reduced and the shorter warm-up time brought by CSACs makes the time to first fix much shorter. Compared to OCXOs and RAFSs, the power efficiency of CSACs extends appreciatively the battery life (Vig, 1993).

Jamming resistance and spoofing detection. GPS signals and telecommunication signals are subject to intentional or unintentional jamming. Secured military communications use spread spectrum techniques, which also require synchronized receivers and transmitters. In the frequency hopping technique, both have to switch to a common frequency on defined time slots. Confidentiality and jamming resistance is improved as the hopping rate is increased since it becomes harder for an eavesdropper or a jammer to detect and switch to the new frequency fast enough. However, this technique then requires superior time accuracy in a context were GNSS timing is not reliable. On the other hand, jammers are employed to prevent improvised explosive devices to be remotely detonated. Those jammers are synchronized to allow friendly communications.

Beyond jamming, GPS signals can be falsified to induce positioning or timing errors (spoofing). Those attacks can be detected thanks to a stable and accurate local clock along with inertial sensors as they provide a reference for observing potential anomalous steerings of GPS position or time.

Event tracking and data time-stamping in networks. In a network, tracking events or data exchanges require that all nodes are accurately and persistently synchronized. For instance, time-stamping and keeping track of the transactions in a financial network is essential to security and tamper detection.

Chapter conclusion

In this chapter, the context in which miniature atomic clocks are being developed has been presented. Some applications have been exposed along with the targeted specifications. It is worth keeping them in mind in order to make relevant choices during the device design. Achieving long-term frequency stabilities below 1×10^{-11} per day, ensuring sufficiently high operating temperatures and lowering the overall device cost are particularly critical issues, which are investigated throughout this thesis. After having described their basic working principle, the following chapter details further the physical phenomena behind CSACs and attempts to provide guidelines for designing an alkali vapor cell and a physics package meeting the desired specifications.

Chapter 2

Absorption and CPT spectroscopy

This chapter covers basics on atomic and CPT spectroscopy. The CPT phenomenon is described and the sources of broadening and shift of the dark resonance are studied. We attempt to provide guidelines regarding the specifications of the vapor cell and the design of the physics package.

2.1 Absorption spectroscopy

2.1.1 Atomic density

The alkali vapor cell contains a thermal vapor of an alkali metal. As long as a pure condensed phase (liquid or solid) of metal is present in the cell, the vapor phase is saturated and its pressure at thermal equilibrium depends on the temperature. For cesium, this vapor pressure is given by Steck (2003):

$$\log_{10} P_v = \begin{cases} -219.482\,00 + \frac{1088.676}{T} - 0.083\,361\,85\,T + 94.887\,52\,\log_{10} T, & T < 301.6\,\mathrm{K}. \\ 8.221\,27 - \frac{4006.048}{T} - 0.000\,601\,94\,T - 0.196\,23\,\log_{10} T, & T > 301.6\,\mathrm{K}. \end{cases} \tag{2.1}$$

where P_v is the vapor pressure in Torr and T is the temperature in K.

The number of atoms per unit volume n, called number density, is then deduced from the ideal gas law:

$$n = \frac{P_v}{k_\mathrm{B} T}, \tag{2.2}$$

where k_B is Boltzmann's constant. The number density against temperature is shown on Figure 2.1. Compared to other elemental metals, alkali metals have particularly low melting points and high vapor pressures. Centimeter scale cells only need to be heated slightly above ambient temperature to provide a practical optical density for absorption spectroscopy. In millimeter-scale, this temperature is increased higher to compensate for the shorter optical depth. At $80\,^{\circ}\mathrm{C}$, the atomic density of cesium in the volume of the vapor cell is around $4 \times 10^{12}\,\mathrm{cm}^{-3}$.

2.1.2 Energetic structure of alkali atoms

Fine structure. The valence electron of alkali atoms has a *spin* $S = 1/2$. In its ground state, the electron is in the s shell and the atom has an *orbital angular momentum* $L = 0$. In the standard spectroscopic notation, this state is written $^2S_{1/2}$. In the first excited state, the outer electron is uplifted to a p shell and its orbital angular momentum is brought to $L = 1$. A first coupling occurs between L and S limiting the number of configurations the atom can be found in. Since some configurations are more energetic, this coupling results in a splitting called the *fine structure*. The *total angular momentum* of the atom J is given by $J = L + S$. A p shell only provides 2 configurations with the spin and orbital angular momentum lying anti-parallel or parallel, resulting in two fine levels, where $J = 1 - 1/2 = 1/2$ and $J = 1 + 1/2 = 3/2$, respectively. Those states are written $^2P_{1/2}$ and $^2P_{3/2}$ and the transitions linking the ground state to those states are called D$_1$ and D$_2$ transitions, respectively. For cesium both D$_1$ and D$_2$ lines are in the near infrared range ($\lambda = 894.6\,\mathrm{nm}$ and $852.3\,\mathrm{nm}$, respectively). The ground state has no fine splitting as $L = 0$ and $J = S$.
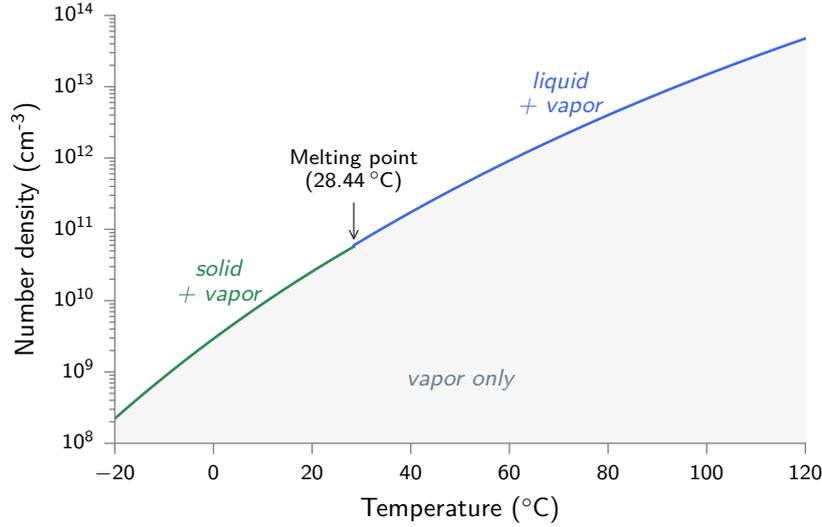
Figure 2.1: Atomic density of saturated cesium vapor. If condensed cesium (liquid or solid) is present at thermal equilibrium, the atomic density in the cell should theoretically be on the line.

Hyperfine structure.   Besides, alkali atoms possess a non zero *total nuclear angular momentum I*, which couples with the total angular momentum J to give rise to the *hyperfine structure*. The *total atomic angular momentum F* is given by $F = J + I$. The $^2S_{1/2}$ and $^2P_{1/2}$ states split into 2 hyperfine levels where $F = I - 1/2$ and $F = I + 1/2$, while the $^2P_{3/2}$ state is subdivided into 4 hyperfine levels $F = \{I - 3/2, I - 1/2, I + 1/2, I + 3/2\}$. Cesium has a total nuclear angular momentum $I = 7/2$. We often use F' to denote the total atomic angular momentum of the level toward which the atom is being excited, while F is the total atomic angular momentum of the level from which the atom is excited. Figure 2.2 represents the energy levels of the ground and excited states of cesium.

Zeeman structure.   The hyperfine energy levels are composed of $2F + 1$ magnetic sublevels of magnetic quantum number m_F, also called Zeeman levels, which are degenerate when the atom is not subject to an external magnetic field. In the presence of an external magnetic field, this degeneracy is lifted and an energy splitting depending on the magnitude of the magnetic field occurs. This dependence is given by the Breit-Rabi formula:

$$E(F = I \pm 1/2, m_F) = -\frac{\hbar\omega_{\text{hfs}}}{2(2I + 1)} + g_I \mu_B m_F B \pm \frac{\hbar\omega_{\text{hfs}}}{2}\sqrt{x^2 + \frac{4m_F x}{2I + 1} + 1}, \tag{2.3}$$

where $x = (g_J - g_I)\frac{\mu_B B}{\hbar\omega_{\text{hfs}}}$, B is the applied magnetic field, g_I is the nuclear g-factor, g_J is the fine structure Landé g-factor, μ_B is the Bohr magneton and ω_{hfs} is the hyperfine splitting frequency.

2.1.3   Absorption cross-section

The absorption spectrum of cesium is composed of Voigt line shapes. The absorption cross-section can be expressed as: (Seltzer, 2008)

$$\sigma(\nu) = \pi r_e c f \sum_{F,F'} A_{F,F'} \mathcal{V}(\nu - \nu_{F,F'}), \tag{2.4}$$

where r_e is the classical electron radius, c is the speed of light and f is the oscillator strength, which depends on the alkali atom and the considered transitions: for Cs D_1 and D_2 transitions, $f \approx 0.347$ and 0.721, respectively (Migdalek and Kim, 1998). $A_{F,F'}$ is the relative strength of the transition ($\sum_{F,F'} A_{F,F'} = 1$) and can be expressed with the Wigner 6-j symbol:

$$A_{F,F'} = \frac{(2F + 1)(2F' + 1)}{2I + 1} \left\{ \begin{array}{ccc} J & J' & 1 \\ F' & F & I \end{array} \right\}^2. \tag{2.5}$$

The Voigt profile can be computed from its complex expression:
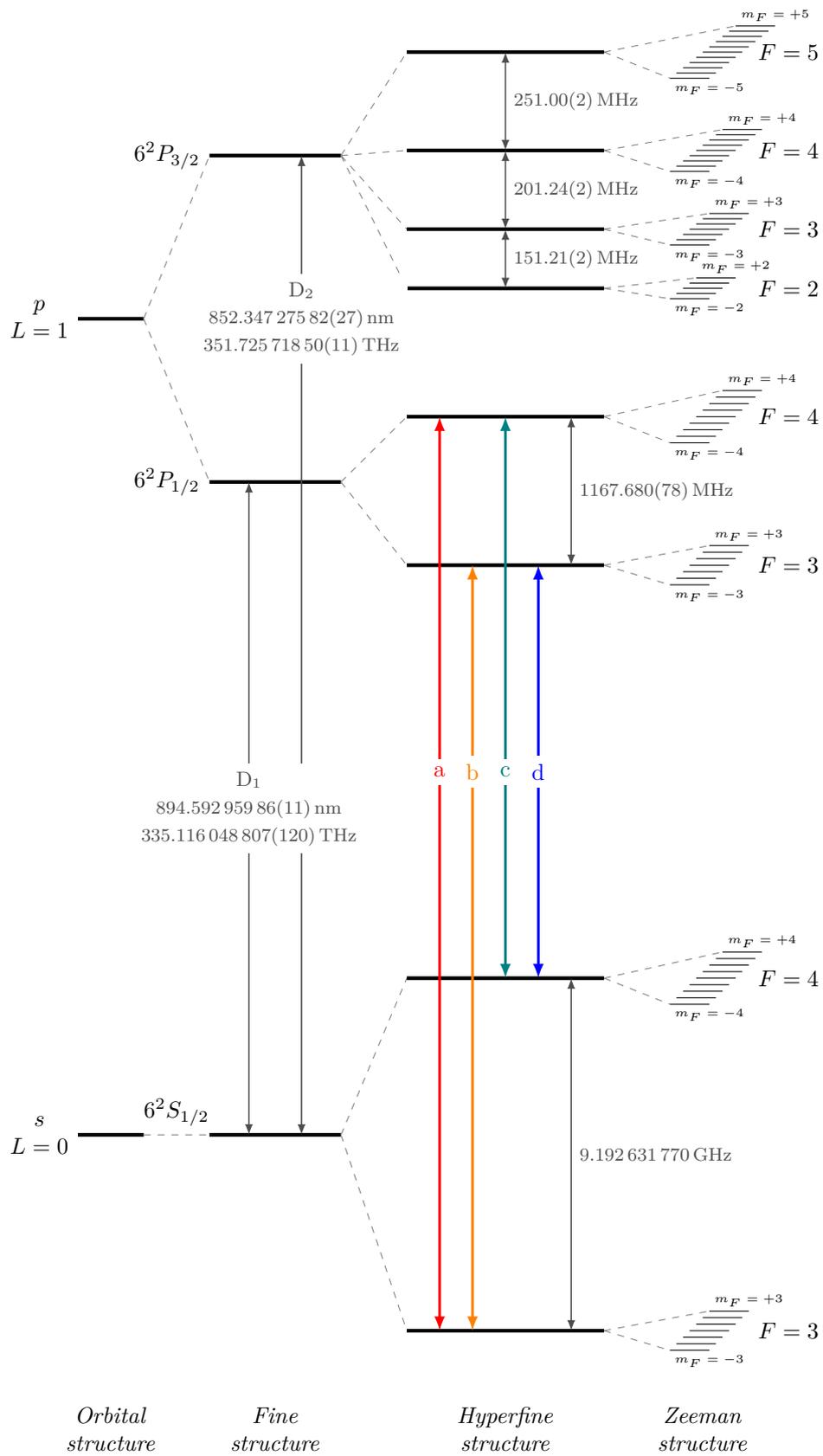
Figure 2.2: Energy levels of the D$_1$ and D$_2$ transitions of cesium (adapted from Steck, 2003).

$$\mathcal{V}(\nu - \nu_{F,F'}) = \frac{2\sqrt{\ln 2/\pi}}{\Gamma_{\mathrm{G}}} \, \mathrm{Re}\left[w \left(\frac{2\sqrt{\ln 2}(\nu - \nu_{F,F'} + i\Gamma_{\mathrm{L}}/2)}{\Gamma_{\mathrm{G}}} \right) \right], \tag{2.6}$$

where w is the Faddeeva function such that $w(z) = e^{-z^2}(1 - \mathrm{erf}(-iz))$. This lineshape is the convolution of a Lorentzian profile, which results from the lifetime of the excited state, and a Gaussian profile, owing to the Doppler effect. Γ_{L} and Γ_{G} are the linewidths of the Lorentzian and Gaussian components, respectively.

Natural lifetime.   The lifetimes τ of the excited states $6^2P_{1/2}$ and $6^2P_{3/2}$ of cesium atoms are about $34.9\,\mathrm{ns}$ and $30.5\,\mathrm{ns}$, respectively (Steck, 2003). Such short-lived states have large energy uncertainties as required by the uncertainty principle ($\Delta E \Delta t \sim \hbar$). It translates in frequency uncertainties: $\Delta\nu = \Delta E/2\pi\hbar \sim 1/2\pi\Delta t$. For instance, the limited natural lifetime of the $6^2P_{1/2}$ excited state causes a broadening $\Gamma_{\mathrm{nat}} = \Delta\nu = 4.56\,\mathrm{MHz}$.

Collisional broadening and shift.   The collisions of alkali atoms with other atoms shorten the excited state lifetime. In presence of a buffer gas, the Lorentzian linewidth is therefore broadened further by an amount proportional to the buffer gas pressure P so that:

$$\Gamma_{\mathrm{L}} = \gamma P + \Gamma_{\mathrm{nat}}, \tag{2.7}$$

In addition to this broadening, the collisions produce a shift adding to the "unperturbed" optical lines resonance frequency $\nu_{0F,F'}$. This shift depends on the nature of the gas and is also proportional to the pressure:

$$\nu_{F,F'} = \delta P + \nu_{0F,F'}. \tag{2.8}$$

It provides a simple method to evaluate the buffer gas pressure in a cell by linear absorption spectroscopy. The shift rates δ and the broadening rates γ have been reported for various alkali metals and gases in several publications (Bernabeu and Alvarez, 1980, Andalkar and Warrington, 2002, Rotondaro and Perram, 1997, Couture *et al.*, 2008, Pitz *et al.*, 2009, 2010, Zameroski *et al.*, 2011).

Doppler broadening.   In the vapor, atoms move at different speeds and the wavelength they experience depends on their speed along the laser's propagation direction. The Doppler broadening $\Delta\nu_{\mathrm{D}}$ results from the distribution of velocities, which follows a Maxwellian distribution. This effect determines the Gaussian component of the Voigt profile, whose linewidth Γ_{G} is given by:

$$\Gamma_{\mathrm{G}} = \Delta\nu_{\mathrm{D}} = \nu_{0F,F'} \sqrt{\frac{8k_{\mathrm{B}}T}{mc^2} \ln 2}, \tag{2.9}$$

where m is the mass of the atom and T is the temperature.

The absorption cross-section computed from Eq. (2.4) without pressure broadening is plotted in Fig. 2.3. The profile is almost exclusively defined by the Gaussian components since the natural lifetime broadening is small compared to Doppler broadening ($\Gamma_{\mathrm{G}} \approx 432\,\mathrm{MHz}$ and $\Gamma_{\mathrm{L}} \approx 4.57\,\mathrm{MHz}$). Likewise, Fig. 2.4 shows the computed absorption cross-section for a neon buffer gas of $100\,\mathrm{Torr}$, pressure at which Γ_{L} is significant ($1090\,\mathrm{MHz}$).

2.1.4   Optical absorption and fluorescence

Assuming a monochromatic probing light, the intensity of the light at the output of the cell is given by Beer-Lambert's law:

$$I(\nu) = AI_0 e^{-nL\sigma(\nu)}, \tag{2.10}$$

where A accounts for absorption unrelated to the vapor, I_0 is the incident intensity, n is the atomic density from Eq. (2.2), L is the cell length and σ_ν is the absorption cross-section from Eq. (2.4). The transmittance $t(\nu) = e^{-nL\sigma(\nu)}$ is plotted in Fig. 2.5 for different temperatures. This spectrum is slightly different from what is obtained in real spectroscopy experiments, when the laser frequency is tuned by changing its injection current. In this case, the intensity I_0 slightly varies with the frequency ν.

A part of the light that is absorbed is remitted by the excited atoms through radiative decay. This *fluorescence* light is unpolarized and is emitted isotropically, which makes the beam passing through a vapor cell
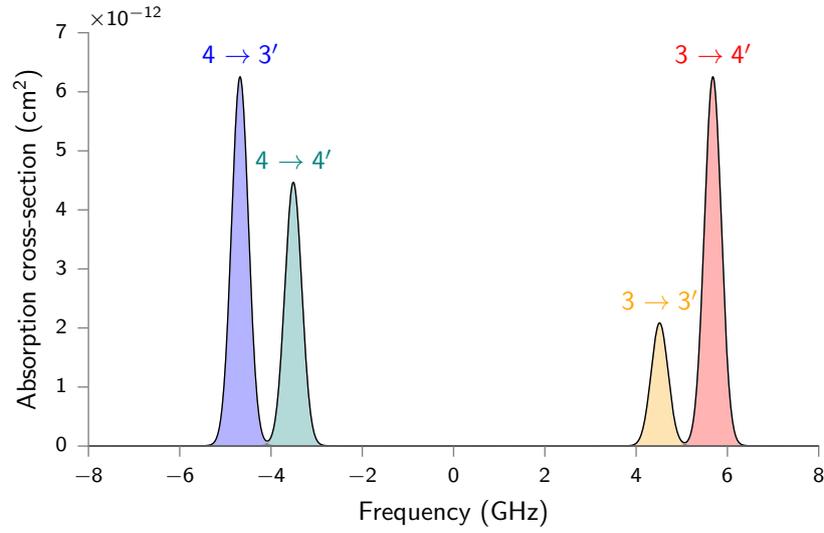
Figure 2.3: Absorption cross-section of the D_1 transitions without buffer gas computed at a temperature of 25 °C ($\Gamma_G \approx 432\,\mathrm{MHz}$ and $\Gamma_L = 4.56\,\mathrm{MHz}$). The x coordinate is the frequency detuning from 335.116 THz ($\approx 894.6\,\mathrm{nm}$). Since we refer to D_1 transitions, $4 \to 4'$ implicitly denotes the transition $|6S_{1/2}, F = 4\rangle \to |6P_{1/2}, F = 4\rangle$.
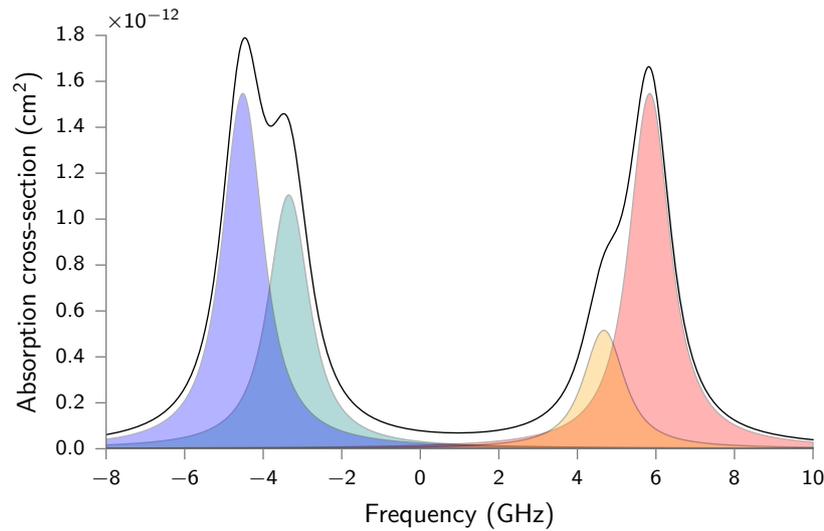

Figure 2.4: Computed absorption cross-section of the D_1 transitions with a neon buffer gas of 100 Torr (at 25 °C $\Gamma_G \approx 432\,\mathrm{MHz}$ and $\Gamma_L \approx 1090\,\mathrm{MHz}$). The x coordinate is the frequency detuning from 335.116 THz ($\approx 894.6\,\mathrm{nm}$).
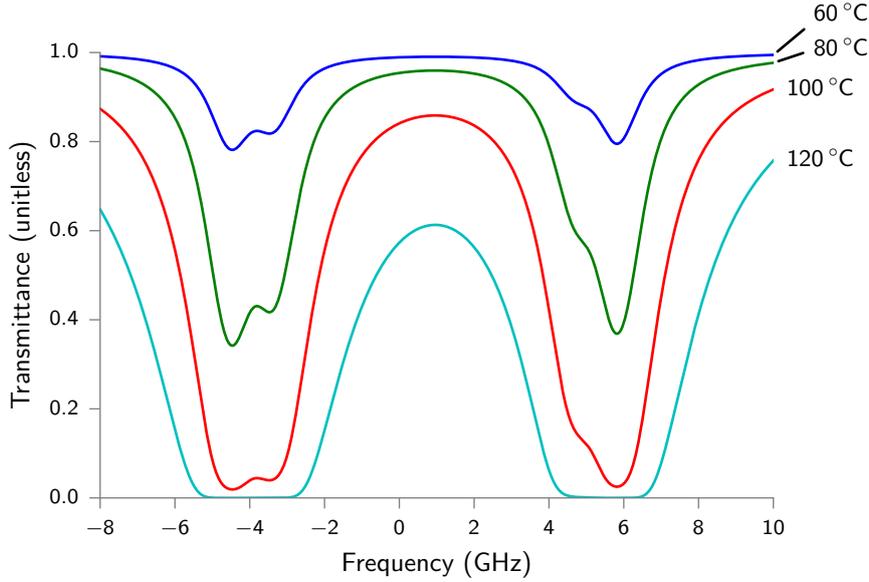
Figure 2.5: Transmittance computed at different temperatures for a $1.5\,\mathrm{mm}$ long cell with a neon buffer gas pressure of $100\,\mathrm{Torr}$. The x coordinate is the frequency detuning from $335.116\,\mathrm{THz}$ ($\approx 894.6\,\mathrm{nm}$).

clearly visible.[1] In some cases, this emission can inauspiciously interact with the atoms. This effect called *radiation trapping* can be mitigated by adding a quenching gas,such as N_2, that promotes non-radiative decay (Franz, 1968, Vanier *et al.*, 2003). However, this effect has not yet been studied in microfabricated cells to our knowledge. On the other hand, Yudin *et al.* (2013) proposed to use this spontaneous emission to achieve better contrasts in CPT.

2.2   Coherent population trapping

2.2.1   Description

The CPT phenomenon occurs when two coherent light fields address simultaneously two transitions connecting two distinct ground levels to a common excited level. This so-called Λ-system is represented in Fig. 2.6. The $|1\rangle$ and $|2\rangle$ levels are typically hyperfine sublevels of the ground state, while $|3\rangle$ refers to one of the excited levels. δ_R denotes the Raman detuning between the light fields frequency difference and the hyperfine splitting frequency: $\delta_\mathrm{R} = (\omega_1 - \omega_2) - \omega_\mathrm{hfs}$.

In the rotative wave approximation, the total Hamiltonian $\hat{H}$ of this system is written as the sum of the unperturbed Hamiltonian $\hat{H}_0$ and the interaction Hamiltonian $\hat{H}_\mathrm{int}$: (Kozlova, 2012)

$$\hat{H} = \hat{H}_0 + \hat{H}_\mathrm{int}, \tag{2.11}$$

$$\hat{H}_0 = E_1 |1\rangle \langle 1| + E_2 |2\rangle \langle 2| + E_3 |3\rangle \langle 3| , \tag{2.12}$$

$$\hat{H}_\mathrm{int} = -\frac{\hbar}{2}\Big[\Omega_1\big(|3\rangle \langle 1| + |1\rangle \langle 3|\big) + \Omega_2\big(|3\rangle \langle 2| + |2\rangle \langle 3|\big)\Big], \tag{2.13}$$

From the states $|1\rangle$ and $|2\rangle$, we can compose a *coupled* state vector $|C\rangle$ and a *non-coupled* state vector $|NC\rangle$, in order to form a new orthogonal basis $\{|C\rangle , |NC\rangle , |3\rangle\}$:

$$|C\rangle = \frac{1}{\sqrt{\Omega_1^2 + \Omega_2^2}} \left(\Omega_1 e^{-iE_1 t/\hbar} |1\rangle + \Omega_2 e^{-iE_2 t/\hbar + i(\varphi_2 - \varphi_1)} |2\rangle\right) \tag{2.14}$$

$$|NC\rangle = \frac{1}{\sqrt{\Omega_1^2 + \Omega_2^2}} \left(\Omega_2 e^{-iE_1 t/\hbar} |1\rangle - \Omega_1 e^{-iE_2 t/\hbar + i(\varphi_2 - \varphi_1)} |2\rangle\right) \tag{2.15}$$

The probability for atoms in the $|C\rangle$ and $|NC\rangle$ states to be excited to the $|3\rangle$ is defined by their transition

---

[1]provided that an adequate beam viewer is used for invisible wavelengths, which is the case of Cs D lines.

Figure 2.6: Interrogation of a three level system with bichromatic light in a Λ-scheme. Ω_1 and Ω_2 are Rabi frequencies. Γ_{31} and Γ_{32} are the relaxation rates from the excited state to each states. Δ_0 is the optical detuning and δ_R is the Raman detuning.
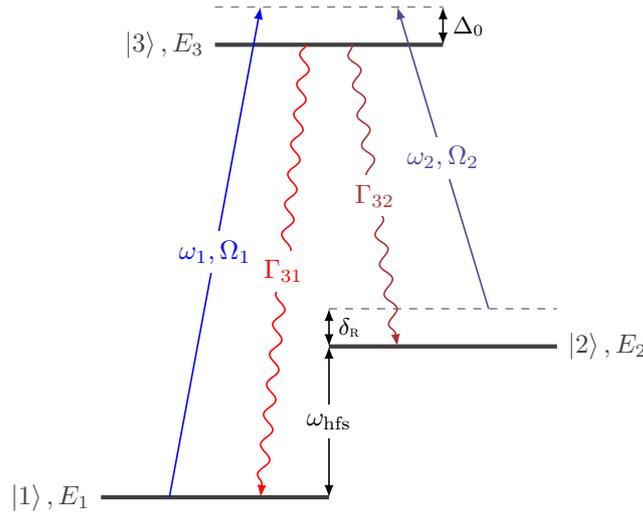
amplitudes:

$$\left\langle 3 \left| \hat{H}_{\text{int}} \right| C \right\rangle = \frac{\hbar}{2\sqrt{\Omega_1^2 + \Omega_2^2}} e^{-i(E_1/\hbar + \omega_1)t + i\varphi_1} \left(\Omega_1^2 + \Omega_2^2 e^{i\delta_R t + i\delta_\varphi} \right), \tag{2.16}$$

$$\left\langle 3 \left| \hat{H}_{\text{int}} \right| NC \right\rangle = \frac{\hbar \Omega_1 \Omega_2}{2\sqrt{\Omega_1^2 + \Omega_2^2}} e^{-i(E_1/\hbar + \omega_1)t - i\varphi_1} \left(1 - e^{i\delta_R t - i\delta_\varphi} \right), \tag{2.17}$$

where $\delta_\varphi = \varphi_2 - \varphi_1$ is the difference between the light fields phase.

If $\delta_\varphi = n\pi, n \in \mathbb{Z}$ and $\delta_R = 0$, the probability for the transition from the $|NC\rangle$ state to the $|3\rangle$ state to occur is zero. At resonance, this $|NC\rangle$ state is indeed uncoupled from the light fields. On the other hand, atoms in the coupled state $|C\rangle$ can still be excited to $|3\rangle$. Because atoms in the state $|3\rangle$ have equal probabilities of relaxing in either of those states, they are gradually pumped into the uncoupled state after several excitation/relaxation cycles, increasing the population of atoms trapped in this state, which is what the term *coherent population trapping* refers to. Since atoms stop absorbing light, the optical transmission through the vapor is increased and the spontaneous emission (fluorescence), decreases because the $|C\rangle$ and, by extension, the $|3\rangle$ states are depopulated. For this reason, the uncoupled state is also called *dark state*.

Scanning the frequency detuning around δ_R reveals a positive transmission peak with a Lorentzian form on transmitted light signal, as represented in Fig. 2.7. The phenomenon was first observed by Alzetta *et al.* (1976) who reported the presence of "narrow black lines" in the fluorescence pattern observed in a sodium vapor cell pumped by a multi-mode dye-laser and subject to a magnetic field gradient.

From the amplitudes A and B marked in Fig. 2.7, we distinguish the absorption contrast $C_A = A/B$ and the transmission contrast $C_T = A/(1 - B)$ (Shah and Kitching, 2010). In the following, we employ the term *contrast* to denote the transmission contrast.

2.2.2 Signal characteristics and relaxation mechanisms

Amplitude. The amplitude of the CPT signal is proportional to the number of atoms interacting with the field and therefore to the atomic density n and to the volume V of the cell. This amplitude can be expressed as: (Kozlova, 2012)

$$A \propto nV \frac{\Omega_R^4}{\Gamma^{*2}} \frac{1}{\left(\frac{\Gamma^*}{2}\right)^2 + \Delta_0^2} \frac{1}{\gamma_2 + \frac{\Omega_R^2}{\Gamma^*}}, \tag{2.18}$$

where $\Omega_R = \Omega_1 = \Omega_2$ is the Rabi frequency (we assume equal field intensities), Γ^* is the excited state relaxation rate, Δ_0 is the optical detuning and γ_2 is the relaxation rate of the hyperfine coherence. γ_2 is also called *transverse relaxation rate*. This expression is only valid for an optically-thin medium. In practice, the amplitude of the CPT signal increases with atomic density up to a maximum before decreasing because of the increased optical thickness (Knappe *et al.*, 2002). Experimentally, the amplitude is generally maximized when the optical
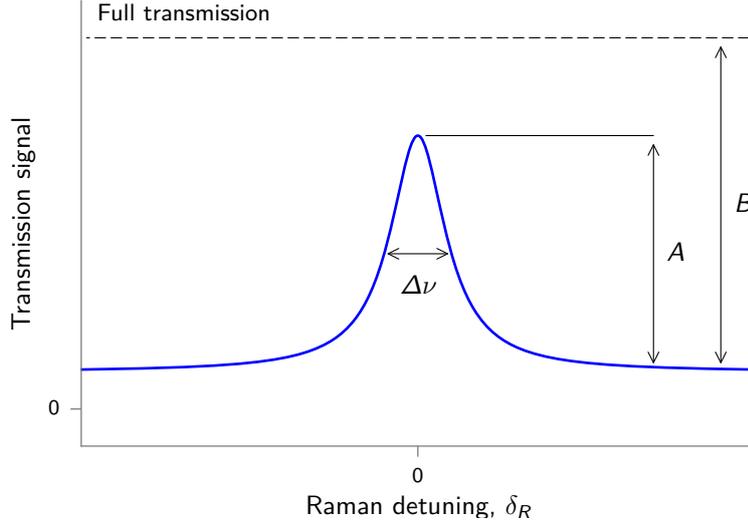
Figure 2.7: A Lorentzian CPT resonance signal. The full transmission level corresponds to the transmission obtained far from the optical transitions, i.e. when the optical detuning Δ_0 is large (out of the absorption peak). $\Delta\nu$ is the FWHM of the Lorentzian. A is the amplitude of the CPT signal. $A/B = C_A$ stands for the absorption contrast.

transmission is around $50\,\%$. Accordingly, cells exhibit an optimal temperature regarding the transmission contrast and the resulting short-term stability. Gornyi *et al.* (1989), Godone *et al.* (2002) and Barantsev *et al.* (2015) have developed models for optically-thick media, which would have to be considered to predict more accurately this behavior according to the buffer gas pressure, the temperature and the cell length.

Linewidth. The width of the CPT resonance depends on the time during which cesium atoms remain in the coherent dark state before relaxation. In an optically thin medium, the FWHM of the resonance is given by: (Vanier, 2005)

$$\Delta\nu = \frac{1}{\pi}\left(\gamma_2 + \frac{\Omega_1^2 + \Omega_2^2}{2\Gamma^*}\right) = \frac{1}{\pi}\left(\gamma_2 + \frac{\Omega_R^2}{\Gamma^*}\right). \tag{2.19}$$

The term Ω_R^2/Γ^*, also called *pumping rate*, is responsible for the broadening due to optical power (power broadening). It is proportional to the incident light intensity and depends on the relaxation rate of the excited state Γ^*, which can be approximated by: (Zanon-Willette, 2005)

$$\Gamma^* \approx \Gamma_L + \Gamma_G \approx \Gamma_{\text{nat}} + \gamma P + \Delta\nu_D. \tag{2.20}$$

Measuring $\Delta\nu$ for different optical intensities and extrapolating at null intensity is a common method to cancel power broadening and evaluate γ_2.

Rabi frequency. Kozlova (2012) recalls the expression of Rabi frequency for the transition $|F, m_F\rangle \rightarrow |F', m_F'\rangle$:

$$\Omega^2 = s^2 C I, \tag{2.21}$$

where s is the dipole matrix element associated with the transition (values tabulated by Steck, 2003) and I is the light field intensity. The quantity C is given by:

$$C = \frac{2J_e + 1}{2J_g + 1}\,\frac{3\lambda_{eg}^3}{2\pi hc}\,\Gamma_{\text{nat}}, \tag{2.22}$$

where J_g and J_e are the total angular momenta of the ground and excited states, λ_{eg} is the wavelength of the transition, h is the Planck constant and c is the speed of light.
For cesium D_1 transitions: $C = 4.945 \times 10^{13}\,\text{m}^2\,\text{J}^{-1}\,\text{s}^{-1}$ and for a simple Λ-system, Rabi frequencies for the D_1

σ^+ transitions $|F \in \{3, 4\}, m_F = 0\rangle \to |F' \in \{3, 4\}, m'_F = 1\rangle$ are obtained by:

$$\Omega^2 = \begin{cases} \frac{1}{8} \ 4.945 \times 10^{13} \ I, & \text{for } F' = 3, \\ \frac{5}{24} \ 4.945 \times 10^{13} \ I, & \text{for } F' = 4, \end{cases} \tag{2.23}$$

where Ω is in rad s^{-1} and I is in W m^{-2}.

As the coherent dark state is long-lived, the relaxation rate of the hyperfine coherence γ_2 is mainly defined by external factors such as the atom-light interaction time and collisions with the cell walls or other atoms.

2.2.2.1 Evacuated cell

Doppler effect. In a cell containing only an alkali vapor, the width of the CPT resonance is subject to Doppler broadening expressed similarly as in Eq. (2.9):

$$\gamma_D = \omega_{\text{hfs}} \sqrt{\frac{8k_B T}{mc^2} \ln 2}. \tag{2.24}$$

Time-of-flight. In evacuated cells, atoms move ballistically between each collision with the cell walls. It is assumed that atoms bouncing on bare glass tend to stick to the wall long enough to lose its coherent state. Between collisions, the atom interacts with a light beam for an average time t_t, which limits the resonance linewidth to:

$$\gamma_{\text{TOF}} = \frac{1}{t_t} = \frac{v}{\ell}, \tag{2.25}$$

where $v = \sqrt{8k_B T/\pi m}$ is the mean atomic velocity and ℓ is the mean free path between two wall collisions. ℓ depends on the geometric configuration. In a cylindrical cell of radius R and length L, $\ell \approx 2/(1/R + 1/L)$ (Vanier and Audoin, 1989). ℓ can also be computed for any shape by Monte Carlo simulations (Graf *et al.*, 2005). We assume that the light beam covers completely the section of the cell. This is the dominant broadening contribution in evacuated cells of small dimensions.

Spin-exchange. Collisions between alkali atoms broaden the resonance due to spin-exchange with a relaxation rate:

$$\gamma_{\text{SE}} = \frac{6I + 1}{8I + 4} \overline{v}_r n \sigma_{\text{SE}}, \tag{2.26}$$

where I is the nuclear spin, n is the atomic density and σ_{SE} is the cross section of the spin-exchange collision. $\overline{v}_r = \sqrt{8k_B T/\pi\mu}$ is the average relative velocity of the colliding atoms and μ is the reduced mass of the system ($\mu = m_1 m_2/(m_1 + m_2)$ for two bodies of mass m_1 and m_2, yielding $\mu = \text{m}/2$ for two atoms of mass m). This phenomenon is dominant at high temperatures.

Narrowing mechanisms. Doppler broadening can be inhibited by Dicke narrowing (Dicke, 1953), which arises when the mean free path of the alkali atoms becomes much shorter than the frequency difference between the two fields ω_{hfs} (Firstenberg *et al.*, 2007). Hence, Doppler broadening in millimeter scale evacuated cells is rather low. Besides, in a Doppler-broadened system, Javan *et al.* (2002) and Radonjić *et al.* (2009) have shown that the resonance linewidth does not linearly depend on laser intensity as in Eq. (2.19), but instead, presents a square root dependency at low field intensities. This effect is similar to the laser-induced line narrowing (LILN) effect investigated theoretically by Feld and Javan (1969) and Kazakov *et al.* (2007), in which the spectral width of the light field affects the resonance signal. Ramsey narrowing has been observed in evacuated cells when two (or more) spatially separated beams are used (Zibrov and Matsko, 2001, Failache *et al.*, 2010, Radojičić *et al.*, 2015).

Total relaxation. With those dominant relaxation mechanisms, we can write the total relaxation γ_2 for an evacuated cell:

$$\gamma_{2,\text{EV}} = \gamma_{\text{TOF}} + \gamma_{\text{SE}}. \tag{2.27}$$

In alkali vapor cells, two main techniques are used to reduce the relaxation rate γ_2. The first method is to dilute the alkali vapor in a buffer gas. The second consists in coating the cell walls with a coating that prevents the relaxation of the atoms upon collisions.

2.2.2.2   Buffer gas cell

A buffer gas contributes to the reduction of the relaxation rate in two ways: by canceling the Doppler effect and by confining atoms in the light field, which limits wall induced relaxations and lengthens the interaction time. On the other hand, the time-of-flight broadening as expressed in Eq. (2.25) is suppressed since the atoms no longer have ballistic trajectories but follow a diffusive motion.

Wall collisions.   Atoms confined in a buffer gas diffuse to the walls and eventually cause a relaxation whose rate can be estimated by:

$$\gamma_{\mathrm{W}} = \left[\left(\frac{2.405}{r} \right)^2 + \left(\frac{\pi}{L} \right)^2 \right] D_0 \frac{P_0}{P} \left(\frac{T}{T_0} \right)^{\frac{3}{2}}, \tag{2.28}$$

where r and L are the cell radius and length respectively (a cylindrical cell is assumed), D_0 is the diffusion coefficient of alkali atoms in the buffer gas atoms, P_0 and T_0 are the reference pressure and the cell temperature. For cesium in neon, $D_0 = 0.153 \, \mathrm{cm^2 \, s^{-1}}$ (Beverini *et al.*, 1971), $P_0 = 101\,325 \, \mathrm{Pa}$ and $T_0 = 273 \, \mathrm{K}$.

Buffer gas collisions.   In spite of reducing the Doppler effect and the relaxation due to transit time, collisions between alkali atoms and buffer gas atoms add a relaxation rate, which can be significant at high pressures:

$$\gamma_{\mathrm{BG}} = \overline{v}_{\mathrm{r}} n_{\mathrm{BG}} \sigma_{\mathrm{BG}}, \tag{2.29}$$

where $\overline{v}_{\mathrm{r}}$ is the relative mean speed of alkali and buffer gas atoms (same expression as in Eq. (2.26) but with μ computed for the system composed of an alkali atom of mass m_1 and a buffer gas atom of mass m_2), n_{BG} is the number density of buffer gas atoms and σ_{BG} is the cross section of the collision.

Narrowing mechanisms.   In a buffer gas cell whose volume is not completely illuminated, some atoms that have diffused out of the light beam are likely to reenter the interrogation region after having evolved coherently in the dark and before having lost their coherent state. Atoms actually experience various sequences out or in the light field, as they would in Ramsey spectroscopy. Summing the contributions from all atoms results in a Lorentzian signal with a narrower linewidth and a sharper tip depending on the configuration. This effect is referred to as diffusion-induced Ramsey narrowing (Xiao *et al.*, 2006, 2008).

Total relaxation.   In the case of a buffer gas cell, the relaxation rate γ_2 is mainly limited by spin exchange, wall collisions and buffer gas collisions:

$$\gamma_{2,\mathrm{BG}} = \gamma_{\mathrm{SE}} + \gamma_{\mathrm{W}} + \gamma_{\mathrm{BG}}. \tag{2.30}$$

2.2.2.3   Wall coated cell

A buffer gas broadens the optical resonance signal and degrades the optical pumping efficiency, which in turn requires higher light intensities. These drawbacks are particularly critical in chip-scale atomic devices where high buffer gas pressures (up to 700 Torr) are required in order to minimize the wall-induced relaxation. Instead, the glass walls of a cell can be coated with an anti-relaxation material in order to decrease the probability for the atoms to relax from their coherent state during each collision with the walls.

Wall collisions.   In the case of a cell with a wall coating for which atoms have a probability P of relaxing at each collision (inelastic collision), the relaxation induced by wall collisions can be estimated by: (Graf *et al.*, 2005)

$$\gamma_{\mathrm{WC}} = P \frac{v}{\ell}, \tag{2.31}$$

where v is the mean atomic velocity and ℓ is the mean free path between two wall collisions, as in Eq. (2.25).

Phase dispersion. Elastic (or adiabatic) collisions preserve the state of the atom but may still induce a phase shift ϕ between hyperfine states due to the interaction with the wall (Budker *et al.*, 2005). A dispersion exists in the phase shift accumulated by the atoms, leading to a shift and a broadening of the CPT signal. Budker *et al.* (2005) have shown that the contribution of the phase dispersion to the line width of a "classical" microwave transition is:

$$\gamma_\phi = \phi^2 \frac{v}{\ell}. \tag{2.32}$$

ϕ depends notably on the nature of the coating and the temperature of the cell.

Stem effect. A thin capillary connects the volume of a cell to the stem, where alkali condensation remains. The section of this capillary can be seen as an uncoated area: all polarized atoms reaching this area are lost for the signal and "replaced" by unpolarized one. This yields the following relaxation rate, which depends on the ratio of the capillary outlet area to the total inner area of the cell:

$$\gamma_{\mathrm{ST}} = \frac{r^2}{2R(L+R)} \frac{v}{\ell}, \tag{2.33}$$

where r is the radius of the capillary outlet section, R and L are the radius and length of the cell, assumed cylindrical. This effect can be critical in coated cells when the coatings reach particularly high performances. Balabas *et al.* (2010b) implemented a stem locking mechanism to prevent this effect.

Narrowing mechanisms. The shape of the resonance in a wall-coated cell is often different from a simple Lorentzian profile. It typically exhibits a dual structure composed of a broad pedestal shape with a narrow central peak at its center. The broad structure is generally attributed to atoms passing through the light beam only once before decoherence, while the narrow structure is the addition of coherent contributions from atoms experiencing multiple elastic bounces (Gateva *et al.*, 2011). Those atoms see sequences of time in the dark and in the light field, which yields a Ramsey narrowing effect (Breschi *et al.*, 2010, Klein *et al.*, 2011, Kazakov *et al.*, 2012, Nasyrov *et al.*, 2015). The broad structure is dominantly broadened by the limited time-of-flight of atoms (Eq. (2.25)).

Total relaxation. We can assume that the relaxation rate γ_2, characterizing the narrow structure in a wall-coated cell, can be approximated by:

$$\gamma_{2,\mathrm{WC}} \approx \gamma_{\mathrm{SE}} + \gamma_{\mathrm{WC}} + \gamma_\phi + \gamma_{\mathrm{ST}}. \tag{2.34}$$

2.2.3 Frequency shifts

The frequency of the hyperfine transition is mainly affected by the buffer gas collisions, the light intensity and the static magnetic field:

$$\nu = \nu_0 + \Delta\nu_{\mathrm{BG}} + \Delta\nu_{\mathrm{LS}} + \Delta\nu_{\mathrm{MAG}}. \tag{2.35}$$

2.2.3.1 Buffer gas collisional shifts

Buffer gases provide a convenient way of narrowing the CPT resonance, but they also introduce a shift $\Delta\nu_{\mathrm{BG}}$ to the clock transition frequency. This shift arises from the modification of the atoms wave function due to van der Waals interactions and repulsive exchange interactions that take place to keep atoms apart (Pauli exclusion principle). What is more, this shift depends on the cell temperature, which inflicts to the clock frequency an additional sensitivity to temperature variations and can impair its stability. This frequency shift is called *collisional frequency shift* and can be approximated in a limited temperature range by: (Vanier and Audoin, 1989)

$$\Delta\nu_{\mathrm{BG}} = P\left[\beta + \delta\left(T - T_0\right) + \gamma\left(T - T_0\right)^2\right], \tag{2.36}$$

where P is the total buffer gas pressure at the reference temperature T_0 (273 K), T is the cell temperature, β is the pressure coefficient, δ is the linear temperature coefficient and γ is the quadratic temperature coefficient.

Values of β, δ and γ can be found in the literature and have been summarized by Kroemer (2015) for cesium.
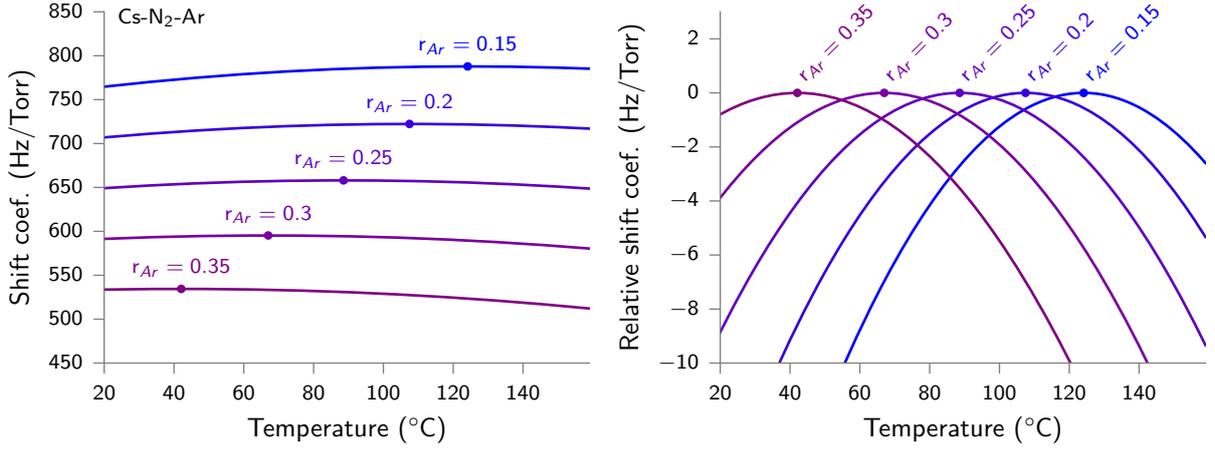
Figure 2.8: Total collisional shift coefficient against temperature $(\beta + \delta\,(T - T_0) + \gamma\,(T - T_0)^2)$ for different buffer gas mixtures of N_2 and Ar. r_{Ar} is the partial pressure proportion of Ar so that $r_{Ar} + r_{N_2} = 1$. On the right graph, the value of the shift at the inversion temperature is subtracted for each curve to reveal more clearly the quadratic dependencies and the inversion points (marked by a dot). The inversion temperature is shifted from $124\,°C$ for $r_{Ar} = 0.15$ to $42\,°C$ for $r_{Ar} = 0.35$.

Mixture. The equivalent coefficients for a mixture of two gases can be expressed by a weighted arithmetic mean of each gas coefficients:

$$\beta = \sum_i r_i \beta_i, \quad \delta = \sum_i r_i \delta_i, \quad \gamma = \sum_i r_i \gamma_i, \tag{2.37}$$

where r_i are the ratio of each buffer gas partial pressure to the total pressure in the cell, such that $\sum_i r_i = 1$. β_i, δ_i and γ_i are the pressure, linear and quadratic coefficients of each gas.

Inversion temperature. When the quadratic temperature coefficient γ is not zero, an inversion exists at the temperature T_{inv} given by:

$$T_{\text{inv}} - T_0 = -\frac{\delta}{2\gamma} \tag{2.38}$$

For a mixture of two buffer gases, the temperature dependence of the frequency shift vanishes at the inversion temperature T_{inv} for the pressure ratio $a = P_2/P_1$ such that: (Kozlova *et al.*, 2011)

$$a = -\frac{\delta_1 + 2\gamma_1(T_{\text{inv}} - T_0)}{\delta_2 + 2\gamma_2(T_{\text{inv}} - T_0)} \tag{2.39}$$

Choice of the buffer gas composition. Any thermal control inevitably keeps a degree of fluctuations around a temperature setpoint, depending on its performances. Canceling the clock frequency temperature dependence around the working point of the cell is therefore necessary in order to reduce this sensitivity at a reasonable level and relax the constraints on the physics package thermal management.

The working point in millimeter-scale cells usually lies between $80\,°C$ and $120\,°C$ to provide enough atomic density. In most CSAC designs, thermoelectric coolers, which would allow cooling the cell when the ambient temperature is higher, are consistently avoided because of their excessive power consumption. It is actually more power efficient to keep the cell at a temperature higher than the maximum ambient temperature at all time, provided that the cell is sufficiently thermally isolated. In this design, the cell temperature consequently defines the upper limit of clock operating temperature range.

Using a buffer gas composed of Ar and N_2 is particularly convenient because the inversion temperature of N_2 at $164\,°C$ can be shifted down to any practical temperature by admixing Ar, which presents a negative linear temperature coefficient. Figure 2.8 shows how the inversion temperature in a N_2-Ar cell is shifted towards lower temperature as the ratio of Ar is increased. This mixture has been broadly adopted in CSACs (Braun *et al.*, 2007, Lutwak *et al.*, 2007b).

The microfabricated cell developed at FEMTO-ST employs a cesium dispenser that contains a getter material, which absorbs most gases aside noble gases. For this reason, N_2 is incompatible with the current technology.
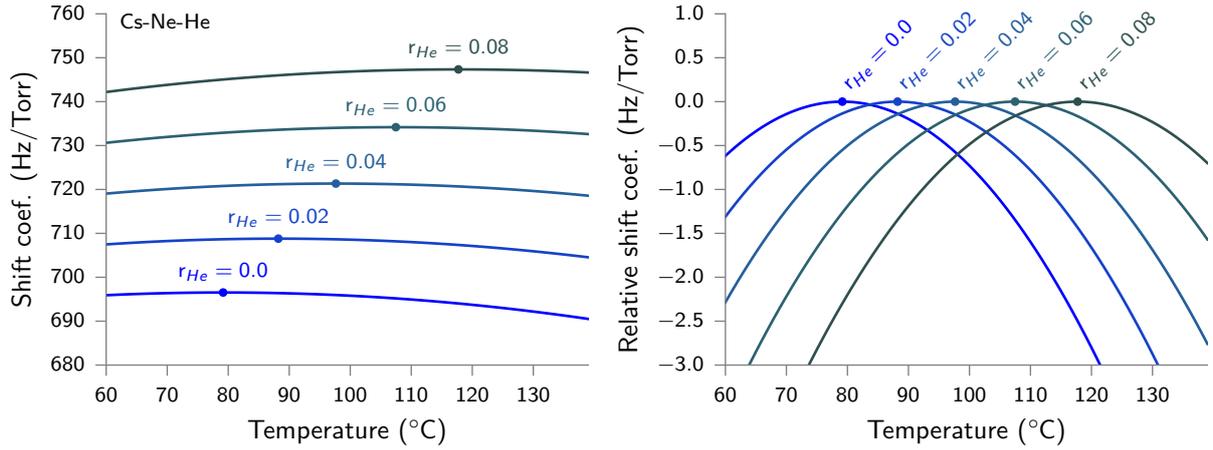
Figure 2.9: Total collisional shift coefficient against temperature for different buffer gas mixtures of Ne and He. r_{He} is the partial pressure proportion of He so that $r_{\text{He}} + r_{\text{Ne}} = 1$. On the right graph, the value of the shift at the inversion temperature is subtracted for each curve to reveal more clearly the quadratic dependencies and the inversion points (marked by a dot). The inversion temperature is shifted from $79\,°\text{C}$ for $r_{\text{He}} = 0$ to $118\,°\text{C}$ for $r_{\text{He}} = 0.08$.

Fortunately, a neon atmosphere has been found to present a quadratic dependency with an inversion temperature around $80\,°\text{C}$, close to the desired working temperature (Miletic *et al.*, 2010, Kozlova *et al.*, 2011). In this case, it has been reported that the inversion temperature point does not depend on the buffer gas pressure (Boudot *et al.*, 2011a).

However, this solution is not well-adapted for CSACs devoted to operate in environments with elevated temperatures and current industrial standards often impose an operating temperature range up to $85\,°\text{C}$. In practice, a margin must be kept between the cell temperature and the maximum ambient temperature to account for thermal dissipation from the surrounding electronics. We assume that the cell must be around $95\,°\text{C}$ to safely operate in a $85\,°\text{C}$ environment.

The inversion temperature of neon can be shifted to higher temperatures by admixing helium, whose temperature dependency is positive and almost linear, as shown in Fig. 2.9. We investigated the potential of a mixture of neon and helium in microfabricated cells in Section 4.3.2. A mixture Ar-Ne could also be envisioned to obtain a flatter shift coefficient on a larger temperature range. However, as discussed in the following, helium is particularly difficult to contain within usual materials and larger atoms such as xenon, for instance in a Ne-Xe mixture, deserve to be studied. Kroemer (2015) has indeed observed peculiar dependences in Cs-Xe cells, with an inversion of the collisional shift around $40\,°\text{C}$, above which, the coefficient is positive. However, xenon atoms are expected to increase unfavorably the relaxation due to buffer gas collisions.

2.2.3.2 Magnetic field

A static magnetic field is established in the cell to lift the Zeeman degeneracy and address specific transition between Zeeman sublevels of the ground state hyperfine splitting, in the case of cesium, the transition $|F = 3, m_F = 0\rangle \leftrightarrow |F = 4, m_F = 0\rangle$. This transition is convenient because it is independent of the magnetic field in first order. This dependency is derived from the Breit-Rabi formula given in Eq. (2.3):

$$\Delta\omega_{\text{clock}} = \frac{(g_J - g_I)^2 \mu_{\text{B}}^2}{2\hbar \Delta E_{\text{hfs}}} B^2 \tag{2.40}$$

For cesium, $\Delta\omega_{\text{clock}} = \beta B^2$ with $\beta = 427.45\,\text{Hz}\,\text{G}^{-2}$. Hence, the static magnetic field must be sufficient to separate the Zeeman sublevels, but low enough to limit the sensitivity to parasitic magnetic field fluctuations. The typical magnetic field magnitude is around $10\,\mu\text{T}$.

If the applied magnetic field is not uniform enough, atoms from different areas of the cell will not experience the same Zeeman shift. As a result, the overall lineshape arising from the contributions of all atoms, will be broadened.

In addition, the magnetic field direction should be aligned with the light propagation direction as the amplitude of the CPT is proportional to the square cosine of the angle between the two directions.

2.2.3.3   Light shift

In addition to power broadening, described earlier, the light field causes the clock transition frequency to shift. This effect is called *light shift*. This shift is primarily due to the *AC-Stark shift*, which results from the interaction of the atomic dipole moment with the radiating electromagnetic field (Levi *et al.*, 2000). Additional effects contribute to this apparent shift without necessarily shifting the energy levels of the atom, but also by inducing asymmetries in the resonance signal shape, which can introduce a frequency offset depending on the center detection method. In a nutshell, different parameters affect the CPT resonance frequency including: the optical detuning Δ_0, the ratio between each light field intensities (i.e. between the sidebands of a modulated laser), the hyperfine coherence relaxation rate or the pressure broadening of the optical lines (Kozlova, 2012, Danet, 2014).

At low laser powers, the light shift evolves linearly with the incident intensity and we note α the light shift coefficient:

$$\alpha = \frac{d\nu}{dI}, \tag{2.41}$$

where I denotes the laser intensity, in a given configuration where the other parameters are fixed.

Light shift is often the dominant limit to the mid and long-term frequency stabilities of CPT clocks based on vapor cells. With a VCSEL for instance, the light shift coefficient α is typically in the order of $1\,\mathrm{Hz\,\mu W^{-1}}$ (Knappe *et al.*, 2001).

For the characterization of cells or the observations of frequency aging phenomena, the frequency of the CPT resonance can easily be extrapolated linearly at null power to cancel the light shift contribution. However, in clock configurations, where no external frequency reference can be used, the light shift impact must be minimized through other means. In practice, with a modulated VCSEL, the light shift can be minimized or canceled at specific working points, by adjusting the RF modulation index (Boudot *et al.*, 2011a) or the cell temperature (Miletic *et al.*, 2012). The VCSEL temperature and injection current can also be adjusted together to find a zero light shift point while remaining at the right frequency.

Shah *et al.* (2006) proposed a method to continuously adapt the modulation index to a value where the light shift vanished. However, this method requires an additional liquid crystal modulator to modulate the light intensity, which is not convenient in a CSAC.

Like magnetic gradients, light field intensity gradients may induce a broadening to the CPT resonance signal through the light shift. For this reason, the laser beam must be adequately shaped to provide a sufficiently homogeneous intensity. Nikolić *et al.* (2013) analyzed the effect of different intensity profiles on the resonance signal characteristics.

2.3   Short-term stability estimation

The short-term relative frequency stability of an atomic clock, in terms of Allan deviation $\sigma_y(\tau)$, is given by:

$$\sigma_y(\tau) \approx \frac{\Delta\nu}{\nu_0}\frac{1}{S/N}\tau^{-1/2}, \tag{2.42}$$

where ν_0 is the clock transition frequency ($9.192\,631\,770\,\mathrm{GHz}$ for Cs atom), $\Delta\nu$ is the resonance FWHM, S/N is the signal-to-noise ratio of the detected resonance in a $1\,\mathrm{Hz}$ bandwidth, and τ is the averaging time of the measurement. Assuming that detection is limited by photon shot noise, it can be written that: (Shah and Kitching, 2010)

$$S/N = C_{\mathrm{T}}\sqrt{\frac{P_{\mathrm{out}}}{2h\nu}}, \tag{2.43}$$

where P_{out} denotes the laser power at the output of the cell and $h\nu$, the thermal energy of a single photon and C_{T}, the transmission contrast.

2.4   Frequency aging and equilibration

Thermal vapor cell references suffer from long-term frequency drifts. The mechanisms responsible for this *frequency aging* are not well understood and difficult to investigate. Literature on this subject is rather scarce. Helium permeation into the cell was proposed as an explanation to slow frequency shifts observed in rubidium

vapor cell clocks (Herbulock *et al.*, 2004, Camparo, 2004, Bloch *et al.*, 2002). Another explanation is the outgassing of frequency shifting byproducts due to the reaction of rubidium with the inner surface of the cell (Vanier *et al.*, 2004). It is typically found that cells that have been throughly outgassed exhibit lower drift rates (Vanier and Audoin, 1989). The frequency variations tend to diminish over time. This behavior was also observed by Kozlova (2012), who found that a baking step of a few weeks in an oven between $150\,°C$ and $180\,°C$ could help stabilizing the frequency of new cells. Lutwak *et al.* (2007b) also reported similar behaviors in CSACs, with an early fractional frequency drift rate of $-1.2 \times 10^{-10}\,\mathrm{d}^{-1}$, lowered to $3 \times 10^{-12}\,\mathrm{d}^{-1}$ after an equilibration period of 200 days.

In addition, the reaction of alkali atoms (surface or volume) can induce variations of the vapor density which can also affect the clock stability. Such density variations are typically observed during the curing process of freshly sealed off cells but may continue to evolve slightly on the long term. Patton *et al.* (2007) notably observed the contamination of cesium cells by oxygen impurities through nuclear magnetic resonance (NMR) measurements. Density variations (due to temperature fluctuations in this case) may convert to frequency shifts through the process of spin-exchange (Micalizio *et al.*, 2006).

Neon causes a collisional shift on the clock frequency on the order of $686\,\mathrm{Hz\,Torr}^{-1}$. For the atomic clock to reach a fractional frequency stability around 1×10^{-11} at $1\,\mathrm{d}$, the pressure fluctuation must be lower than $1.5 \times 10^{-4}\,\mathrm{Torr\,d}^{-1}$. In a recent article, Abdullah *et al.* (2015) observed a frequency drift in Cs-Ne microfabricated cells very similar to the ones developed at FEMTO-ST. Those cells feature identical dimensions and also comprise a neon buffer gas, a cesium pill dispenser from SAES Getters and Borofloat33 windows. For a cell heated at $81\,°C$ and neon pressure of $62\,\mathrm{mbar}$, a frequency drift of $-5.2 \times 10^{-11}\,\mathrm{d}^{-1}$ was measured over one year and was attributed to the permeation of neon through the glass windows. Considering solely a neon leak, this drift is equivalent to a leak of $-0.9\,\mathrm{\mu bar\,d}^{-1}$. A second cell heated at $150\,°C$ with a neon pressure of $77\,\mathrm{mbar}$ had a drift rate of $-4.5 \times 10^{-10}\,\mathrm{d}^{-1}$. However, measurements have been initiated at FEMTO-ST to verify this permeation rate and we observed that frequency drifts are typically lower by, at least, an order of magnitude (see Section 4.4). In microfabricated cells, if permeation is found to limit the clock performances, we could envision using other glass types such as aluminosilicate glass (ASG) (Scholes, 1993), which could greatly reduce this effect.

Dellis *et al.* (2015) recently reported aging measurements of Rb-He microfabricated cells with two types of glass: Borofloat33 and a type of ASG. Their experiment consisted in placing a cell in a chamber pressurized with helium. The sign of the drift rate was consistent with the pressure difference between the cell atmosphere and the chamber atmosphere, which confirms a permeation phenomenon through the cell windows. The "intrinsic" drift rate for the borosilicate glass is measured around $1 \times 10^{-8}\,\mathrm{h}^{-1}$. The drift rate increases from $7.6 \times 10^{-9}\,\mathrm{h}^{-1}$ at $96\,°C$ to $1.5 \times 10^{-8}\,\mathrm{h}^{-1}$ at $116\,°C$. With aluminosilicate glass, this drift is reduced by three orders of magnitude, reaching $3.7 \times 10^{-11}\,\mathrm{h}^{-1}$ at a temperature of $90\,°C$. This remarkable results suggest that permeation phenomenons can be significantly reduced with aluminosilicate glass.

Chapter conclusion

The physics of CSACs has been described and the parameters of interest, determining the expected performances, have been identified. The main relaxation and shift mechanisms have been mathematically expressed or qualitatively described, allowing us to evaluate their impact. These parameters notably include the cell dimensions, the choice of the buffer gas mixture and pressure and the cell operating temperature. Wall coatings have been presented as an interesting alternative to buffer gases. The alkali vapor cells and physics packages featuring appropriate characteristics can now be designed. In the next chapter, we describe the fabrication process of miniature alkali vapor cells, which necessarily introduces additional concerns, in particular regarding production costs and lifetime.

Chapter 3

Microfabrication of vapor cells

In this chapter, we recall the legacy fabrication techniques used for centimeter-scale cells and we present different approaches undertook to miniaturize alkali vapor cells. The current fabrication process developed and employed at FEMTO-ST is then described in details, along with several improvements brought through this thesis. An original cell architecture proposed prior this thesis work is then presented. As the cell technology based on dispensers still suffers from several limitations, a novel filling method is proposed, inspired by the legacy of glass-blowing techniques.

3.1 Review of fabrication techniques

Alkali vapor cells used in RAFS have been fabricated using glass-blowing techniques for decades.

The fabrication of classical glass-blown cells requires skillful glass work and handling pure alkali metals, which is challenging as they are highly reactive and oxidize rapidly in contact with ambient air. The cells, fabricated either by glass-blowing or by mold casting, are connected to a common glass tube, called *manifold*. This manifold is connected to a pump, a gas source and an alkali metal source, typically a glass ampoule containing pure alkali metal. After outgassing the manifold and the cells, alkali metal condensation is driven from the ampoule to each cell by establishing temperature gradients, for instance with a propane torch. After introducing the buffer gas, each cell is successively sealed off by melting the narrow glass tube, through which it is connected to the manifold. By doing so, the cell is removed from the manifold without exposing its content, or the content of the manifold, to the ambient air.

Once the possibility to miniaturize atomic clocks thanks to CPT and VCSELs had been envisioned, achieving reliable and inexpensive millimeter-scale cells became the last piece of the puzzle. Early attempts to fabricate millimeter-scale cells were logically inspired by glass-blowing techniques. Knappe *et al.* (2003a,b) demonstrated the use of a hollow-core fiber, sealed at both ends by a CO_2 laser, which allowed to melt the glass locally with precision. Alkali metal and buffer gas were then introduced in this structure using the same techniques as classical glass cells.

Microelectromechanical systems (MEMS) fabrication techniques were foreseen to simplify and lower dramatically their cost by adopting a collective fabrication approach (Kitching *et al.*, 2002). Structuring cells by forming cavities in a silicon wafer by deep reactive ion etching (DRIE) or KOH etching and sandwiching it between two glass wafers, assembled by anodic bonding, became the method of choice, but a relatively wide variety of solutions remains for the introduction of the alkali metal and the buffer gas.

An hybrid approach where microfabricated cells are connected to a glass manifold and filled by the classical method has been proposed (Lutwak *et al.*, 2004), but most developments have later been oriented on solutions in which alkali metal filling is also performed collectively. The method used for filling the cell is often constrained by the sealing technology and vice versa. Table 3.1 summarizes several filling and sealing techniques for microfabricated cells reported in the literature.

Liew *et al.* (2004) initially proposed two methods. In the first solution, a mixture of barium azide (BaN_6) and cesium chloride (CsCl) diluted in water is pipetted into the cell, which is then baked to evaporate the water before anodic bonding is performed at $200\,°C$. At this temperature, the compound is decomposed and elemental cesium is released. However, the stability of the atmosphere is compromised by the recombination of nitrogen, used as buffer gas, with barium residues, inflicting a fractional frequency drift of $-2 \times 10^{-8}\,d^{-1}$. Besides, the amount of nitrogen trapped in barium depends on temperature, inducing an additional frequency

shift (Knappe *et al.*, 2005a). To avoid this phenomenon, a buffer gas composed of noble gases, which are not absorbed by barium, was preferred (Knappe *et al.*, 2005b), but the stability of the atmosphere remained unsatisfactory (fractional frequency drift of $-5 \times 10^{-9}\,\mathrm{d}^{-1}$) because of residual nitrogen (Knappe *et al.*, 2005a).

The second solution proposed by Liew *et al.* (2004) uses directly elemental cesium from a glass ampoule, which is pipetted in the cell, so that no precursors are left in the cell after bonding. Kwakernaak *et al.* (2004) also applied this technique, but cesium was inserted by pin transfer in the cells. The method was later improved by transferring alkali metal by evaporation from a small ampoule placed on top of the cell preform (Knappe *et al.*, 2005a). The ampoule containing barium azide and rubidium chloride is heated at 180 °C, initiating the diffusion of elemental rubidium in the cell. As a result, the fractional frequency drift rate was reduced to $5 \times 10^{-11}\,\mathrm{d}^{-1}$, and probably below since this measurement was limited by the accuracy of the measurement setup. This process was notably adopted by Pétremand *et al.* (2012), but a commercial wire dispenser[1] of natural rubidium was used instead of the $\mathrm{BaN_6}$+RbCl mixture. Yet, unlike the dispensers currently available, $\mathrm{BaN_6}$+RbCl can provide isotopically selected ^{87}Rb, which improves short-term frequency stability performances (Stähler *et al.*, 2002).

Still, the method described by Knappe *et al.* remains slow as cells are processed one at a time. Based on the same technique, Perez *et al.* (2010) envisioned to speed up the process by filling the cells in parallel thanks to an array of micromachined nozzles aligned with the cell array, instead of a single ampoule. Although a stable atmosphere can certainly be obtained, it can be argued that the setup remains rather complex because filling and bonding operations have to be performed in the same vacuum chamber.

Liew *et al.* (2006, 2007) demonstrated a wafer-level technique based on cesium azide ($\mathrm{CsN_3}$). The compound, initially in powder form, is deposited by evaporation through a shadow mask, forming a thin layer in all the cells at once. After anodic bonding, UV radiation is used to decompose the compound into elemental alkali metal and nitrogen. Compared to previous solutions, this solution is claimed to improve the windows transparency as no bulk oxides or residues are present after the process, except the remaining precursors. As the thermal evaporation of $\mathrm{CsN_3}$ is rather difficult to control, Woetzel *et al.* (2011) modified this technique and diluted $\mathrm{CsN_3}$ in deionized water, which could then be pipetted into the cells and dried. Overstolz *et al.* (2014) adopted and automated this process to fill cells with $\mathrm{RbN_3}$. However, the long-term stability obtained with this technique has not yet been clearly reported. Overstolz *et al.* suggested a fractional frequency drift rate close to $3 \times 10^{-12}\,\mathrm{d}^{-1}$ (1×10^{-10} per month) and Liew *et al.* observed no significant changes in the absorption linewidth after one year.

Gong *et al.* (2006) reported an original solution benefiting from the ability for alkali elements to migrate through hot glass. Here, a fragment of cesium-enriched glass acts as alkali metal source. It is placed in a regular Pyrex/silicon preform and allows anodic bonding sealing at standard temperatures. The fragment is then melted to the Pyrex substrate to ensure good contact and cesium is released from it by flowing on electrolytic current and injecting Na^+ through the outer side of the Pyrex substrate. This technique has apparently not been studied further and the electrolytic migration may be difficult to implement at the wafer-scale as it requires heating the glass substrate at 540 °C.

Because anodic bonding requires relatively high temperatures, keeping alkali metal from evaporating out of the preform and inserting the buffer gas can be tricky. Other bonding techniques have therefore been studied instead of anodic bonding but, to our knowledge, none of them were successful in demonstrating a stable atmosphere on the long-term. In particular, Radhakrishnan and Lal (2005)[2] proposed enclosing pure rubidium in wax-micropackets, which are then bonded to a cell preform, separated with a silicon nitride layer. Laser ablation allows to ablate the separation layer and part of the wax to free rubidium. However, we can suspect that wax is not able to retain the cell atmosphere on long time scales (note that only one side of the cell is bonded by anodic bonding).

Epoxy sealing has been tried by Post *et al.* (2004) and, more recently by Hulbert *et al.* (2011), but, for the latter, the cells only lasted for a few days at high temperatures (typically 3 days at 90 °C).

A solution based on a metallic interlayer may seem suitable since some metals are known to be both hermetic and resistant to alkali vapors, in particular copper, used in cold weld sealing. Pétremand *et al.* (2010) reported a thermocompression sealing process with relatively thick (125 µm) indium rings performed at low temperature (140 °C), but the lifetime was limited to approximately 4 days at high temperature (between 65 °C and 85 °C). Later, Straessle *et al.* (2013) refined this process using thinner indium rings and bonded at a temperature lower than 140 °C. Here again, cells did not last longer than a few days, typically 15 days at 80 °C (Straessle,

---

[1]from SAES Getters, Inc.

[2]better illustrations can be found in the associated patent (Lal and Radhakrishnan, 2010).

2013). SnBi eutectic solder bonding reported by Vecchio *et al.* (2011) can also be mentioned but it remains unsuccessful with lifetimes under 10 days.

Since the sealing solution must be both hermetical and chemically compatible with alkali vapor, Youngner *et al.* (2008) suggested in a patent combining metal sealing, to provide hermeticity, with a polymer layer acting as a chemical protection. However, no experimental implementation has been reported.

Interestingly, the classic cell fabrication techniques have inspired other hybrid solutions in which channels are used to feed several cells from an alkali metal source present in the wafer after sealing. The channels, fabricated at the wafer-level, are then sealed individually, isolating each cell from the alkali source. Lee *et al.* (2004)[3] proposed to seal such channels with wax, but the hermeticity and alkali metal resistance provided by this material is doubtful.

Finally, sealing channels with glass frit was proposed by Tsujimoto *et al.* (2013a,b) and Sato *et al.* (2013). However, glass frit reflow requires high temperature (over 400 °C) and glass tends to absorb alkali metals at high temperature (Brossel *et al.*, 1955, Woetzel *et al.*, 2011). This solution could therefore be demonstrated in centimeter-scale cells, where heat can be applied locally to seal the channels, while another part of the cell is kept cold to host the alkali metal without absorbing it. This solution has not yet been demonstrated in millimeter-scale cells, and establishing such a high temperature gradient across small cells at the wafer-level may be difficult.

A solution benefiting from the long-term stability provided by anodic bonding and the ease of implementation of stable alkali compounds was developed at FEMTO-ST over the past years. This solution, relying on embedded alkali dispensers, is described in more details in the next section.

---

[3]according to the short description of Tsujimoto *et al.* (2013b), as we could not obtain this paper.

Alkali source	Transfer method	Sealing	Post-sealing alkali release	Buffer gas fill.	Reference	
CsCl+BaN$_6$	Dilution in H$_2$O + liquid pipetting + baking	AB at 200 °C	Heating at 200 °C (along AB)	BF	Liew *et al.* (2004)	🟧
Pure Cs	Liquid pipetting from an ampoule of pure Cs (GB)	AB at 250 °C		BF	Liew *et al.* (2004) Kwakernaak *et al.* (2004)	🟩
Pure Rb	Local evaporation from a small ampoule of RbCl+BaN$_6$ (HVC)	AB at 300 °C		BF	Knappe *et al.* (2005a)	🟩
Pure Rb	Local evaporation from a wire dispenser (HVC)	AB at 300 °C		BF	Pétremand *et al.* (2012)	🟩
CsN$_3$	Wafer-level evaporation through a shadow mask (HVC)	AB at 200 °C	UV radiation (8 h-10 h)	RBP	Liew *et al.* (2006, 2007)	🟦
CsN$_3$	Dilution in H$_2$O + liquid pipetting + baking	AB at 300 °C	UV radiation (a few minutes)	RBP	Woetzel *et al.* (2011, 2013)	🟦
RbN$_3$	Dilution in H$_2$O + liquid pipetting + baking	AB at 280 °C	UV radiation (50 h)	RBP	Overstolz *et al.* (2014)	🟦
Cs-enriched glass	Manual pick and place of glass fragments	AB (500 °C ?)	Melting with gas flame and migration by electrolytic current	BF	Gong *et al.* (2006)	🟦
Cs wire/pill dispenser	Manual pick and place	AB (350 °C - 450 °C)	Local IR laser heating (≈ 700 °C)	BF	Nieradko *et al.* (2007) Hasegawa *et al.* (2011a)	🟩
Rb wax-micropackets	Rb packeting in GB + bonding to preform by wax heating	Wax bonding	Si$_x$N$_y$ layer and wax laser ablation	BF	Radhakrishnan and Lal (2005)	🟧
Pure Cs	Liquid pipetting (GB)	Epoxy sealed hole		BF	Post *et al.* (2004)	🟧
Pure Rb	Liquid pipetting in dodecane pool	Eutectic SnBi soldering (≈ 150 °C)		BF	Vecchio *et al.* (2011)	🟧
Pure Rb	Local evaporation from a wire dispenser (HVC)	Indium bonding by thermocompression (140 °C, 1 - 4 bar)		BF	Pétremand *et al.* (2010) Straessle *et al.* (2013)	🟧
KCl+BaN$_6$ in solid alumina tablet	Pick and place + baking to release elemental K while N$_2$ is evacuated	Glass-frit reflow across microchannels		BF	Tsujimoto *et al.* (2013a,b)	🟧

AB = anodic bonding, GB = glove box, HVC = high-vacuum chamber, RBP = reaction by-products, BF = back filled.

🟧 = atmosphere instabilities reported or very likely, 🟩 = atmosphere stability demonstrated or expected, 🟦 = unknown atmosphere stability.

Table 3.1: Summary of different alkali metal filling and sealing techniques in microfabricated vapor cells.
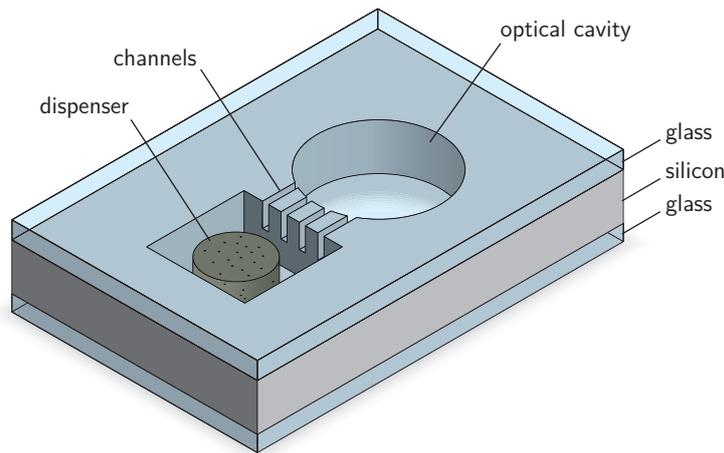
Figure 3.1: The transmissive cell

3.2 Transmissive cell technology

3.2.1 Overview

The current cell microfabrication process employed at FEMTO-ST results from contributions by Nieradko *et al.* (2008), Douahi (2009), Hasegawa *et al.* (2011b) and Chutani (2011). The cells are made of a stack of a structured silicon wafer sandwiched between two glass wafers, like most solutions reported in the literature. Its originality lies in the filling technique, which is based on a solid cesium dispenser specifically designed by SAES Getters (trade name Cs/AlkaMax/Pill/1-0.6).

This dispenser takes the form of a pill and is obtained by aggregating a zirconium-aluminum alloy powder and a stable cesium chromate (Cs_2CrO_4) by mechanical pressing. The two compounds represent around $83\,\%$ and $17\,\%$ in mass, respectively. The alloy, composed of Zr at $84\,\%$ and Al at $16\,\%$, acts as reducing agent and is also used alone as a non-evaporable getter (trade name St 101).

Before this product with a pill form became commercially available, this dispenser used to be obtained by dicing a piece of a wire alkali metal dispenser (Douahi *et al.*, 2007). This wire essentially consists of the same material but is embedded in a metallic enclosure made of Ni/Cr. In its usual operating mode, a current is flown through the wire, which heats up by Joule effect. When the temperature is high enough, cesium chromate decomposes and lets pure cesium evaporate while other by-products are sorbed by the getter. Such dispensers have been used to prepare photosensitive surfaces in phototubes (Succi *et al.*, 1985). Nowadays, they are notably used to adjust the work function of electrodes in OLED displays (Cattaneo *et al.*, 2004). Experiments performed during MAC-TFC tended to show that cells with raw pills exhibit longer lifetimes than slices from the wire dispenser as cesium condensation subsisted longer (Douahi, 2009). In addition, the metallic enclosure tended to form short-circuits and impend the anodic bonding. Nowadays, raw pills have completely replaced wire dispensers in cells fabricated at FEMTO-ST.

The cell design includes a dedicated cavity to host the dispenser. Thin channels ensure that the alkali vapor diffuses to the optical cavity while preventing its obstruction by particles that may detach from the pill, as shown in Fig. 3.1.

The pill is stable up to $500\,°C$ and can be handled in air unlike pure cesium, which is highly reactive and oxidizes rapidly with the water vapor present in the ambient atmosphere. Thanks to this stability, the anodic bonding step can be performed in conditions ensuring a strong sealing (typically $350\,°C$). The flow chart of the fabrication process is summarized in Fig. 3.2. Once the cell is hermetically sealed, the dispenser is locally heated at a temperature above $600\,°C$ with a high-power laser, starting the reduction reaction of the cesium chromate and releasing cesium vapor. The temperature in the rest of the cell remains low so that cesium is not significantly absorbed by hot glass. The complete fabrication process is described in more details in the following.
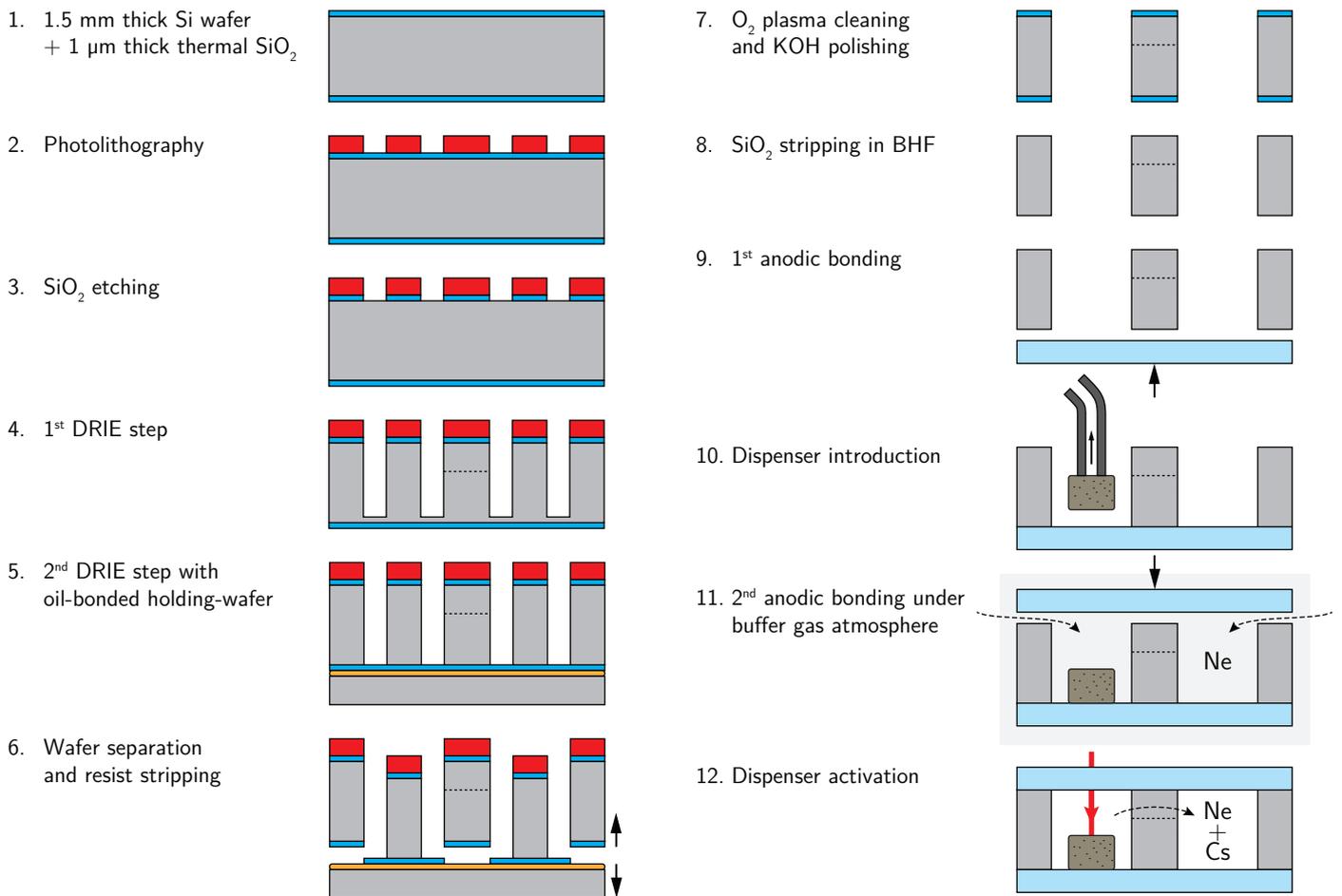
1. 1.5 mm thick Si wafer
   + 1 µm thick thermal SiO_2

2. Photolithography

3. SiO_2 etching

4. 1st DRIE step

5. 2nd DRIE step with
   oil-bonded holding-wafer

6. Wafer separation
   and resist stripping

7. O_2 plasma cleaning
   and KOH polishing

8. SiO_2 stripping in BHF

9. 1st anodic bonding

10. Dispenser introduction

11. 2nd anodic bonding under
    buffer gas atmosphere

12. Dispenser activation

Figure 3.2: Fabrication process of transmissive cells.

1.   Dehydration baking (120 °C, 10 min)
2.   Adhesion promoter spin coating and baking (Ti Prime)
3.   AZ9260 resist spin coating (900 rpm, 3000 rpm/s, 30 sec, ≈ 15 μm)
4.   Soft baking (105 °C, 12 min)
5.   UV exposure (1500 mJ cm^{-2})
6.   Development (AZ400K, DIW, 1:3)

Table 3.2: Details of the photolithography procedure.

3.2.2   Photolithography

The fabrication process starts by structuring a 1.5 mm thick, 100 mm, p-type silicon wafer (resistivity 1-10 Ω cm). To this end, a 15 μm thick photoresist layer of AZ 9260[4] is deposited by spin coating on the wafer and is photolithographically patterned by exposing it to UV light through a mask. Only the areas exposed to light are dissolved by the developer. This resist is particularly suitable for very thick layers and it can be used directly as an etching mask for the following etching process. The photolithography procedure is detailed in Table 3.2.

3.2.3   Mask layout

An example of mask layout is shown in Fig. 3.3. While previous layouts did not use all the available space, the cell number has been increased to its maximum (215 cells on a 100 mm wafer) to evaluate the scalability of the process. The margin width between cavities and dicing paths were kept at 1 mm so that the outer dimensions comply with the existing characterization physics packages and leave room for a visible identification mark. However, this margin could reasonably be reduced to a few hundred micrometers to achieve a higher density and a smaller physics package. For instance, a 350 μm margin would allow to fit 440 cells on the same area. Mask layouts are generated in the GDS format by parametric scripting[5] with the Python package gdsCAD[6] and KLayout [7] is used for visualizing the masks.

3.2.4   Etching

The DRIE process is a method of choice for etching deep cavities in a silicon substrates with vertical sidewalls. It consists in alternating between two gas compositions in a plasma reactor. The first step uses a SF_6 plasma, which etches isotropically unprotected areas and tends to attack vertically fluorocarbon layers. In the second step, a C_4F_8 plasma covers all surfaces with a fluorocarbon layer. This layer effectively protects sidewalls but surfaces oriented toward the plasma, like the bottom of cavities, still get attacked during the etching step. By this alternation of etching and passivation, the etching process is made anisotropic and high aspect ratio structures can be patterned.

This technology is well established for depths up to 500 μm, however, at millimeter-scale depths, the result is challenged by the formation of "grass" on the lower part of the sidewalls, increasing the roughness of inner surfaces. Figure 3.4 shows grass on the sidewalls of cavities after DRIE.

A reduced surface roughness is not expected to improve the CPT signal quality factor, in particular in buffer gas cells (Knappe, 2008). However, it may affect their performances in several respects. First, minimizing the area of the internal surfaces can help to reduce the amount of cesium consumed during the curing process of the internal surfaces (see Section 3.2.8.2). Besides, when antirelaxation coatings are used, surface roughness should be as low as possible to avoid imperfections in the formation of the coating (Stephens *et al.*, 1994). From a practical standpoint, excessive grass can complicate wafer cleaning and drying, and compromise the bonding cavity. On the other hand, rough surfaces may help preventing fluorescent light from getting reflected back toward the vapor by silicon sidewalls, which would adversely contribute to radiation trapping. Furthermore, as explained in Section 3.2.8.1, rough sidewalls may promote the condensation of the alkali metal away from the optical windows in order to prevent their obstruction (Nakajima and Maki, 2015).

Ensuring that the sidewalls are vertical and minimizing surface defects require optimizing the recipe on the DRIE equipment. Two equipments are available at FEMTO-ST's clean room (MIMENTO). Chutani *et al.* (2014) reported the optimization performed on the Alcatel A601E. Similar optimization was performed on the

---

[4]from MicroChemicals, GmbH
[5]source code at http://github.com/mv20100/phd_code_mask_layout
[6]http://pythonhosted.org/gdsCAD/
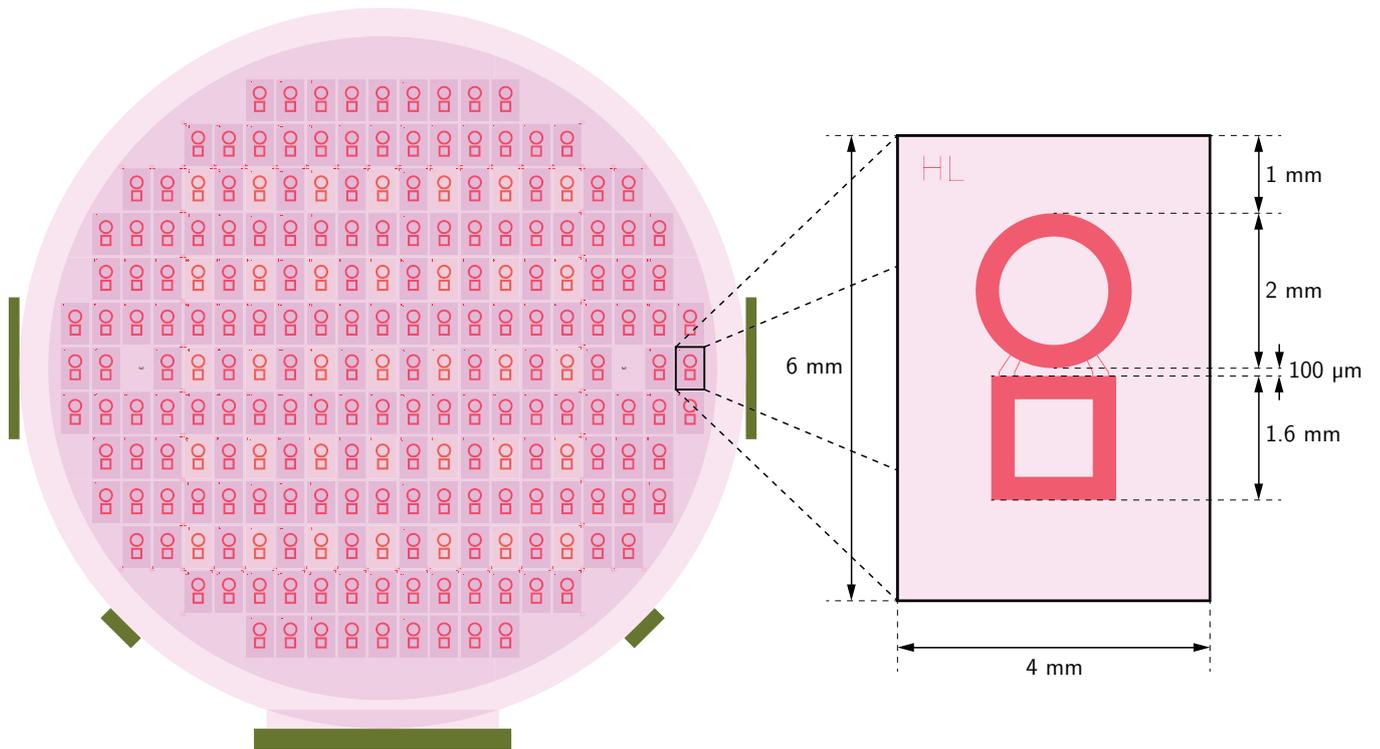[7]http://www.klayout.de/

Figure 3.3: Photolithography mask layout used to pattern 215 cells on a 100 mm wafer. Cells in light orange corresponds to the previous layout. This mask ensures compatibility with the existing mask for getter deposition (see Section 3.4).
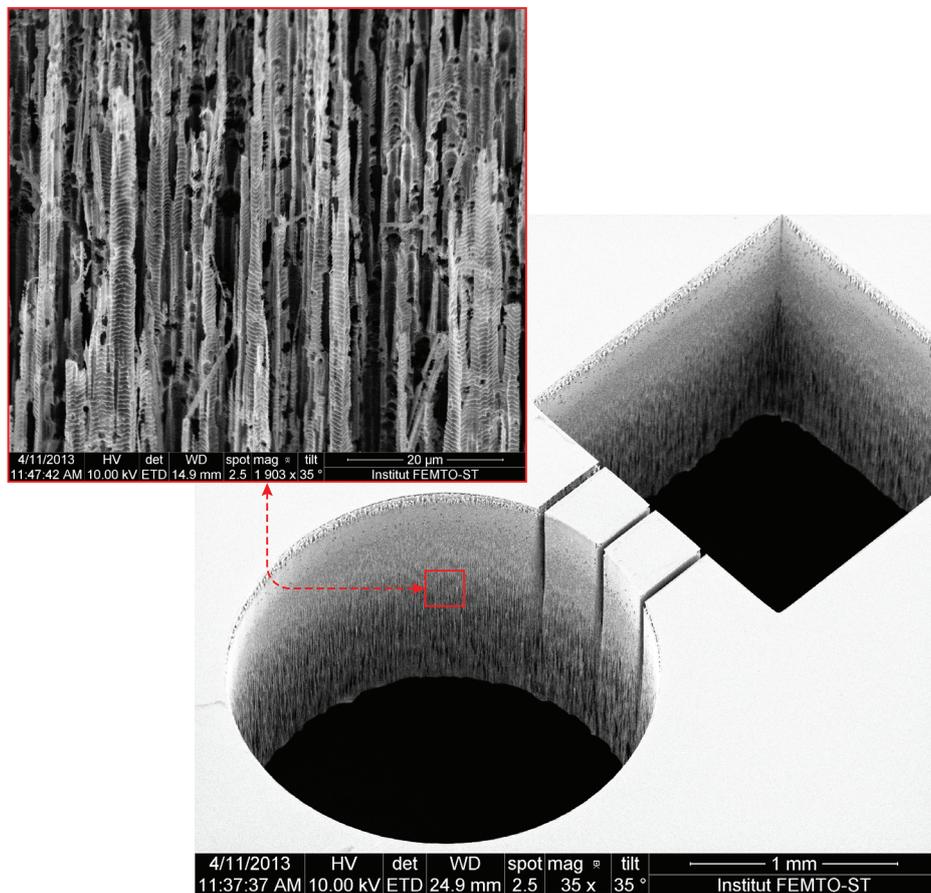

Figure 3.4: Scanning electron microscope (SEM) image of grass on the sidewalls of cavities etched by DRIE.
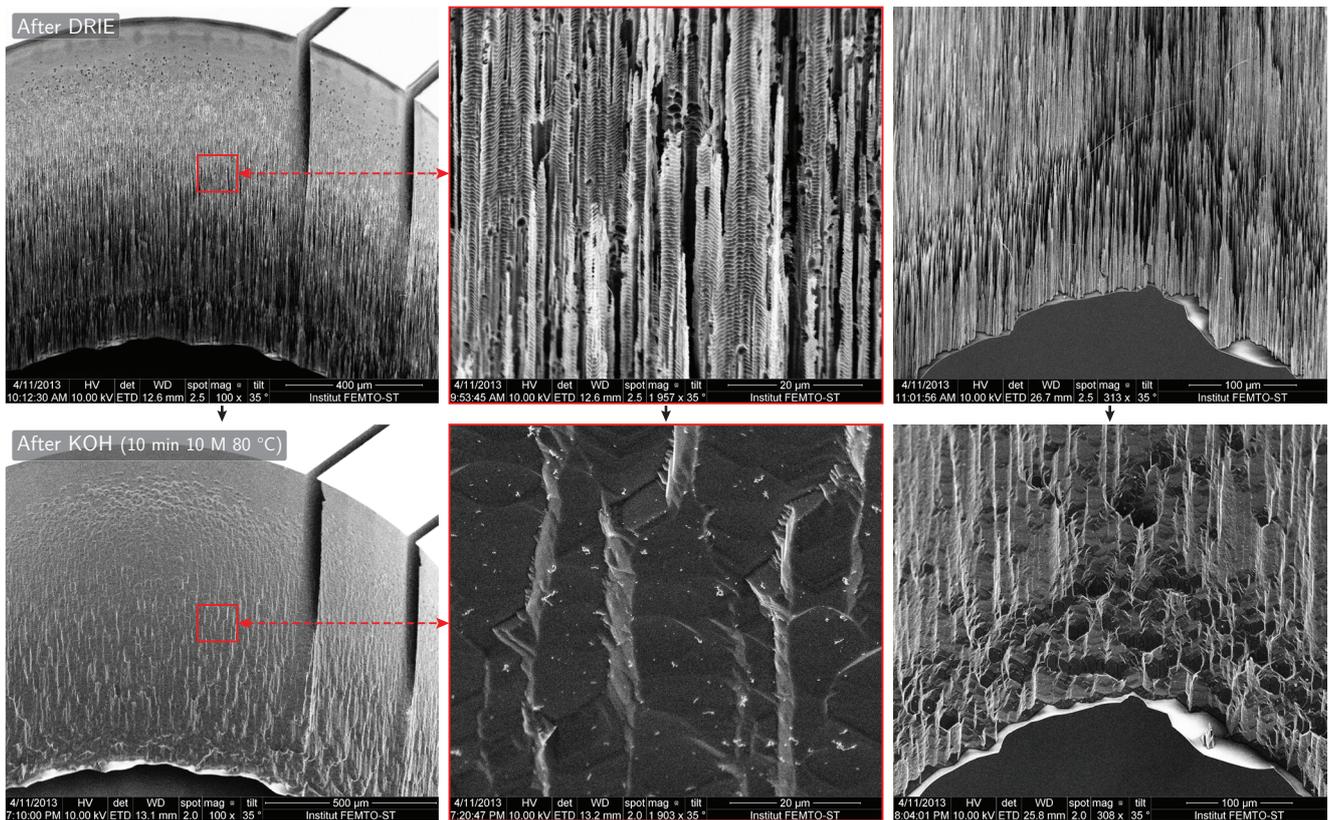
Figure 3.5: SEM images before and after KOH polishing (10 min, 10 M at 80 °C). Grass is effectively removed by this process. Images on the right are taken in the angle at the bottom of the dispenser cavity, where grass is usually more present.

SPTS Pegasus Rapier more recently installed at MIMENTO (this optimization was notably done by Sylwester Bargiel). The duration to etch through a 1.5 mm thick wafer is reduced to 2 hours compared to the previous process developed on the Alcatel, which typically lasted around 6 hours (mostly due to cooling steps). With the SPTS, we prefer using silicon wafers with a 1 µm thick thermal SiO_2 layer to protect its backside from plasma lapping during DRIE, otherwise the plasma tends to etch unprotected surfaces once the backside is reached through the cavities.

DRIE tends to etch faster larger openings. This process benefits from this effect, called aspect ratio dependent etching, to etch shallower channels between cavities in a single process just by making the channels line width thinner in the mask. On the other hand, if one wants to etch areas of different sizes at the same rate, a halo mask design can be necessary. It consists in etching only the outlines of cavities so that the line width remains uniform on the wafer.

Ultrasonic drilling has also been employed to etch vapor cell cavities by Woetzel *et al.* (2011) and, at FEMTO-ST, by Douahi (2009), but DRIE may be faster and more convenient to use in a large-scale production context. KOH etching is also very frequently employed for this purpose (Knappe *et al.*, 2004a, Post *et al.*, 2004, Straessle *et al.*, 2014). This solution was also used at Wrocław University of Technology during MAC-TFC.

3.2.5   Sidewall polishing

Several polishing methods have been experimented to smooth etching defects. Polishing by KOH etching has been proposed by Hasegawa *et al.* (2011b) and is used on a regular basis at FEMTO-ST. Etching is anisotropic and crystallographic planes are revealed. A 10 min etching in a 10 M solution heated at 70 °C usually gives satisfactory results. Figure 3.5 shows images of cavity sidewalls before and after this process.

Other isotropic etching methods were also investigated: reactive ion etching (RIE) (SF_6 plasma) and $HF/HNO_3/CH_3COOH$ wet etching. Pictures of the sidewalls obtained after a SF_6 plasma process are shown in Fig. 3.6. This process was performed on the Plassys RIE equipment for 25 min at a pressure of 280 µbar, with a SF_6 flow of 15 sccm and a power of 80 W. Different process durations have been tried by covering the cells with a physical mask after 5 min lapses. The evolution of grass removal by this process is illustrated in
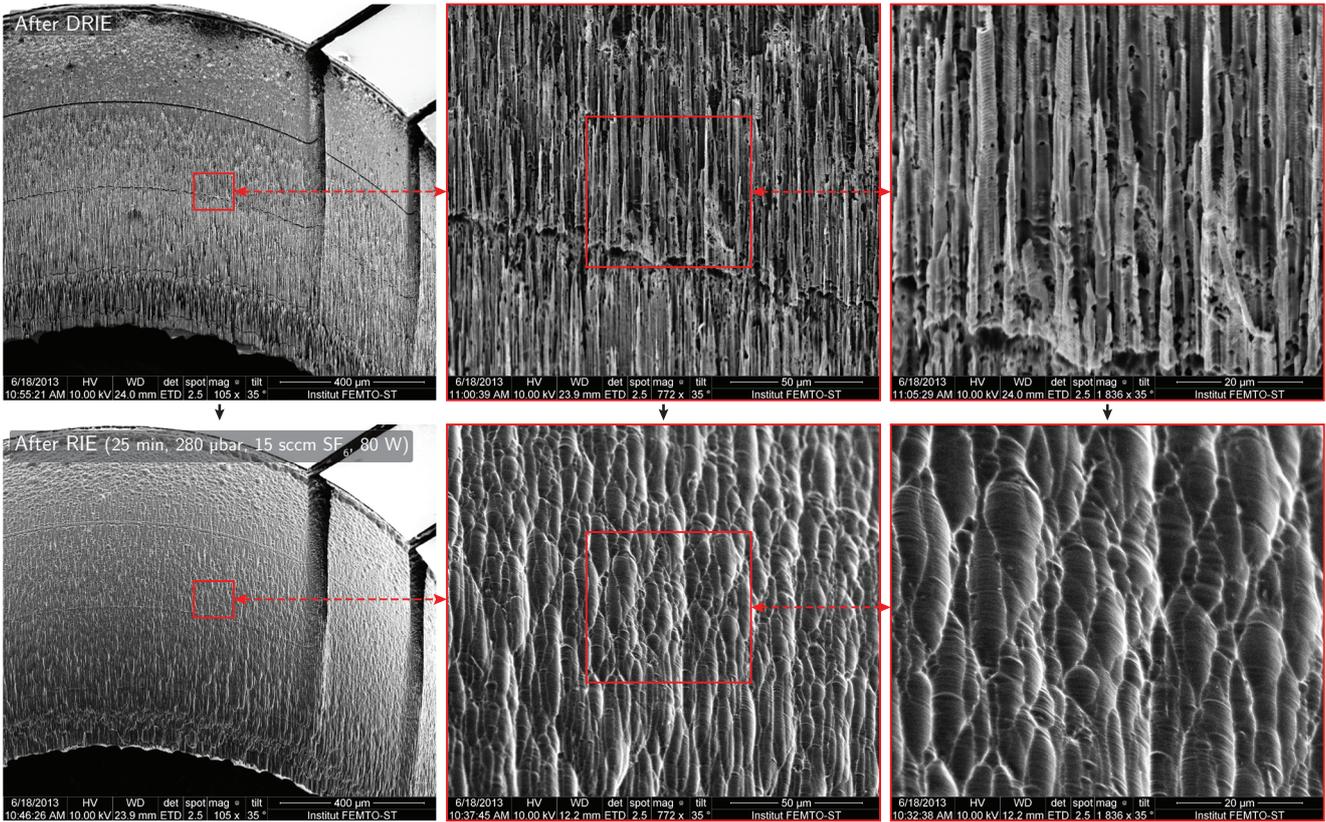
Figure 3.6: SEM images before and after RIE polishing (25 min, 15 sccm of SF_6 at 80 W and 280 µbar).

Fig. 3.7.

Polishing by $HF/HNO_3/CH_3COOH$ wet etching has been used for wall coated cells and the achieved surfaces are shown in Section 5.3.1. All three methods seem to remove grass and large defects, and are therefore appropriate for buffer gas cells. Note that those trials were performed before the DRIE process optimization. The necessity to reduce further the roughness for wall coated cells remains unclear and, to our knowledge, no quantitative analysis of the impact of roughness on their performances have been done. We can expect a mirror-like surface to favor specular atomic collisions. Thereby, atoms transiting diametrically through the cell, which is the ideal case (maximum transit time to collision rate ratio), can persist with the same surface incidence angle after several collisions. On the other hand, an atom colliding at normal incidence on a very rough surface has less chances of bouncing back along the same direction, and, in the worse case, can stay trapped in the vicinity of surface defect.

3.2.6   Dispenser introduction

The introduction of dispensers in the cells before sealing remains a critical step. Indeed, after cleaning the preform (silicon/glass stack), dispensers are introduced manually in each cavities. This step is rather delicate because the bonding surface must be kept clean throughout the process in order to avoid bonding defects, which can cause nonfunctional cells.

In order to place the dispensers faster and more precisely, a custom-made vacuum pen is employed. In practice, the dispensers are unpacked from the cans provided by SAES Getters and a number of dispensers are placed in a glass cup on a hot plate around 80 °C. As they are handled under the clean room aerobic environment, we expect that heating their container help reducing their humidity absorption. Indeed, in a few dozen minutes in ambient air, dispensers start disaggregating and their surface becomes sticky.

In principle, using a glove box would solve this issue. However, the manual dexterity required for this process is difficult to achieve with such equipment because of the stiffness and thickness of the gloves. We typically introduce around 20 dispensers per wafer, as we rarely need more. For small dispenser numbers, this process is not critical but introducing a few hundred of them at once would require the development of a specific setup.
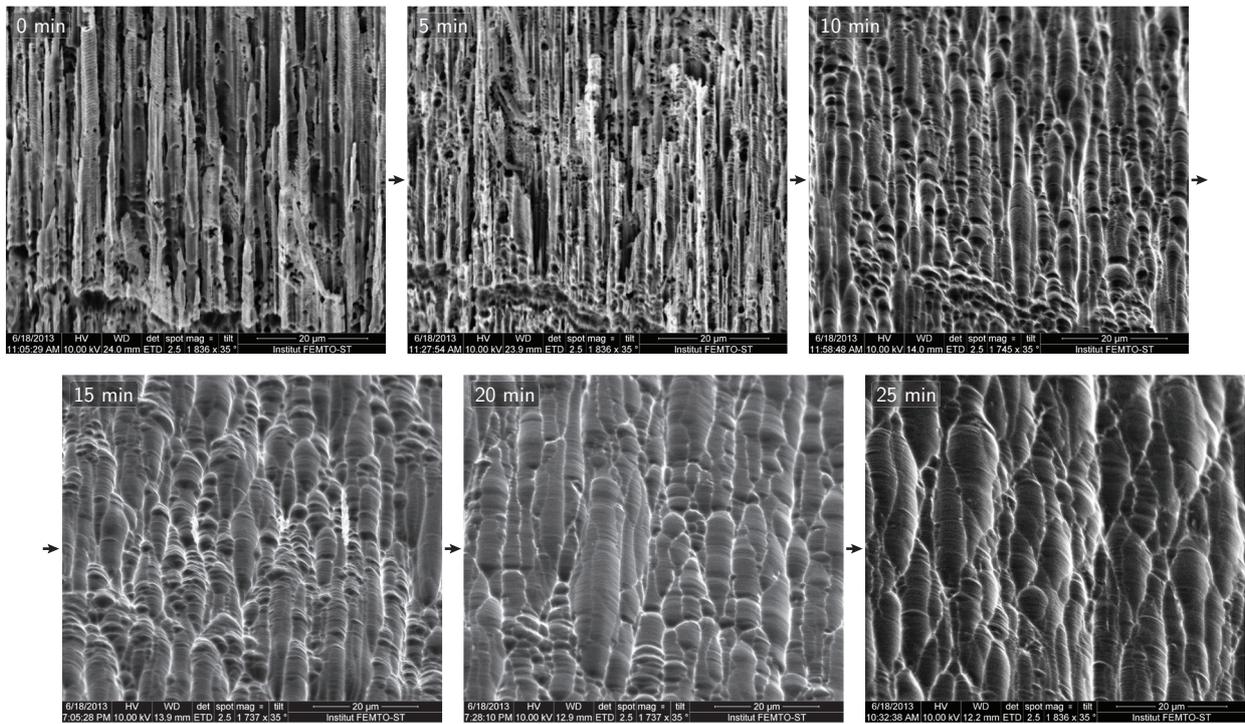
Figure 3.7: SEM images of the cavity sidewalls as grass is being removed through the RIE polishing process (15 sccm of SF_6 at 80 W and 280 µbar).

3.2.7 Anodic bonding

Anodic bonding is particularly convenient to bond glass and silicon substrates. In this process, the substrates are put in contact, heated between 250 °C and 450 °C and a high voltage is applied to the stack. The borosilicate glass, which is typically employed in anodic bonding, is able to conduct electrical charges at high temperatures through the migration of sodium cations and oxygen anions. Oxygen ions migrate from glass bulk to the interface between glass and silicon, where they form silicon oxide as they bond to hydroxyl groups initially present on the silicon surface. The electrostatic attraction is sufficient to bring the substrates in close contact so that bonding occurs but a moderate additional force is usually applied to the stack. The resulting sealing is hermetical and mechanically resistant.

Since its first application to microfabricated vapor cells demonstrated by Liew *et al.* (2004), this technology has been widely used for this purpose. Hasegawa *et al.* (2011b) has described the anodic bonding process employed at FEMTO-ST, on the EVG 501 equipment available at MIMENTO.

In 2013, an novel anodic bonding equipment (AML AWB-04) was installed at MIMENTO and has since been used to perform all the bonding steps of our cells. This equipment allows to perform in situ alignments before bringing the substrates in contact. In addition, the separation distance between the wafers can be kept large (around 1 cm), which is favorable for the outgassing step preceding bonding. On the EVG machine, this separation was ensured by 400 µm thick flags. Outgassing on the AML is also more efficient since it can easily reach vacuum levels on the order of 8×10^{-6} mbar, whereas the EVG hardly reaches 1×10^{-4} mbar.

In early experiments, gases were introduced in the bonder chamber through flexible polyurethane tubes and manual pneumatic valves, whose permeability is rather high and cannot preserve the gas purity. This configuration was not very practical because the pressure reading from the pressure gauge installed on the AML was not directly accessible on the AML software and its resolution was limited. Besides, the gas bottles were not ideally secured and the gas lines had to be purged before each use.

Therefore, a gas distribution setup with stainless steel tubes was installed[8] and interfaced with the AML equipment. The setup includes, for each of the two gas lines, a pressure reducing valve, a mass flow controller and a pneumatic valve. An additional pressure sensor with a 0.1 mbar resolution was installed. A separated pressure display unit can automatically stop the pneumatic valves once the specified pressure is reached. The gas bottles are fixed in a closed box, which complies with security standards. Room remains for an optional

---

[8]The fabrication and the installation were outsourced to a subcontractor.

Figure 3.8: Pictures of the AML anodic bonding equipment without gas lines (left) and the dedicated gas lines added thereafter (right).

1. SiO_2 stripping in buffered HF
2. Cleaning in H_2O_2/H_2SO_4 (piranha solution) or hot H_2O_2 (both wafers)
3. Drying with N_2
4. Evacuation of the bonder chamber ($< 1 \times 10^{-5}$ mbar)
5. Heating at $350\,°C$
6. Wafers in contact with a force of $200\,N$
7. Voltage set to $1000\,V$ (until a total charge above $1500\,mC$ is obtained)
8. Cooling and venting

Table 3.3: Details of the first anodic bonding procedure.

third gas line. Pictures of the AML equipment and the additional gas lines are shown in Fig. 3.8. A synoptic diagram of setup is given in Fig. 3.9.

3.2.7.1 First anodic bonding (preform assembly)

A first anodic bonding step is used to bond the glass wafer and the patterned silicon wafer, forming the preform. This process is straightforward since no buffer gas is introduced. It is generally performed within 1 hour (in addition to the wafer preparation time). The steps are summarized in Table 3.3.

3.2.7.2 Second anodic bonding (sealing)

After cleaning the preform and the second glass wafer, the dispensers are introduced into the cavities and the cells are sealed by a second anodic bonding process. This process is more delicate than the previous one.

A deported electrode is used to short-circuit the glass wafer already bonded, which would otherwise impede the current flow. This electrode consists in a flat metallic spring screwed to the lower platen and bent to reach the lower side of the silicon wafer, made accessible by the flat of the glass wafer (this electrode is depicted in Fig. 3.9). This method is rather standard to make glass/silicon/glass assemblies.

Besides, the presence of a buffer gas such as neon limits the voltage that can be applied during bonding. Indeed, depending on the pressure, the nature of the gas and the gap between the electrodes, an electrical
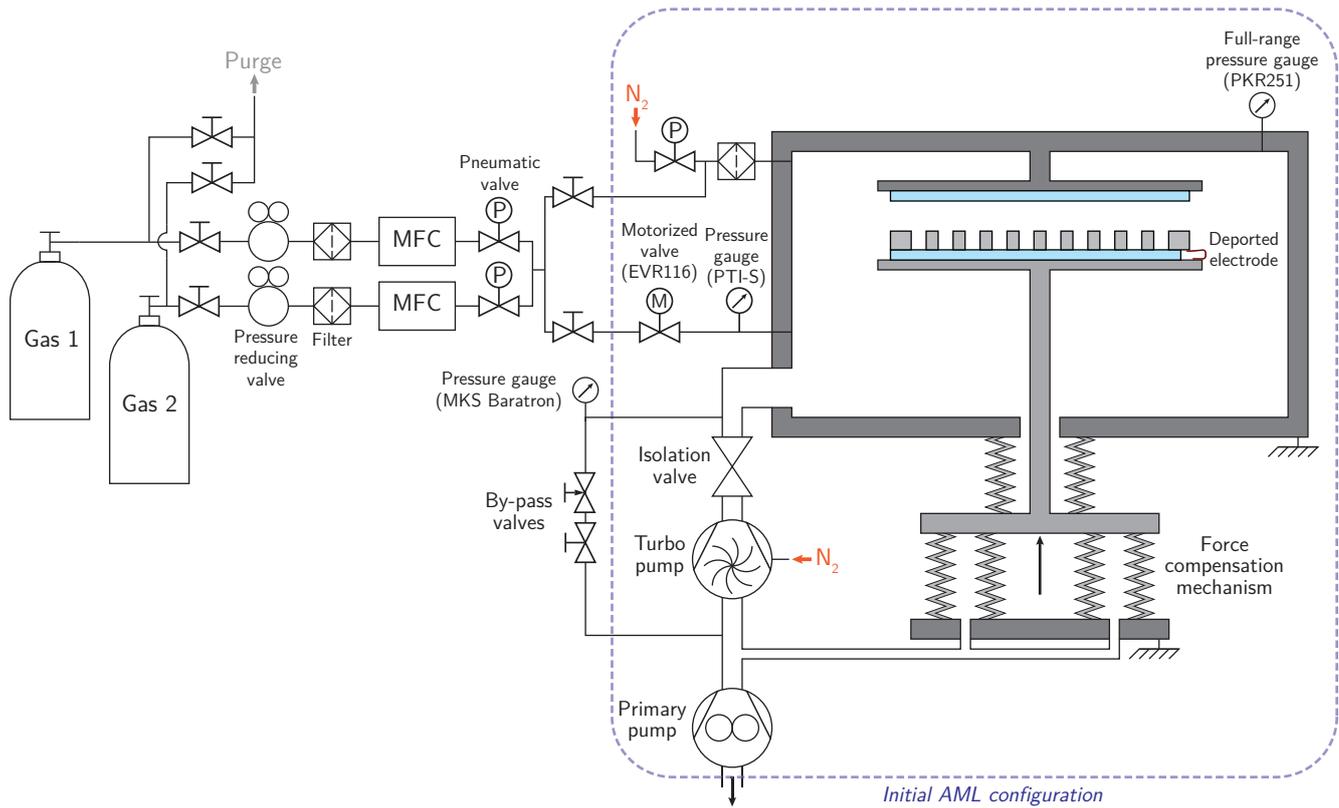
Figure 3.9: Synoptic diagram of the AML machine and the gas lines addition.

discharge through the gas occurs at the breakdown voltage (Paschen's law). For this reason, Hasegawa *et al.* (2011b) adopted a two-step process, in which the voltage is first set below the breakdown limit, under the buffer gas atmosphere, to perform a preliminary sealing. Air is then introduced in the chamber, which raises this limit and allows performing the following steps at 600 V and 900 V, ensuring a stronger and permanent sealing. This process is detailed in Table 3.4.

Several complications arose when we first attempted to perform bonding under a buffer gas atmosphere with the AML equipment. First, the pressure inside the chamber is limited to 700 mbar because the lid has no clamping mechanism to hold it closed (it is solely closed by the pressure difference between the inside and the outside of the chamber). In addition, AML advises against introducing air in the chamber when the platens are heated above 200 °C to avoid oxidizing and damaging some parts of the equipment. An acceptable process has been established accordingly and is detailed in Table 3.5. A first bonding step is performed at 220 V under a neon buffer gas atmosphere. Unlike the EVG, the AML allows to partially see the evolution of the process through two windows intended for in situ alignment. After this first step, the fringes, which reveal a gap between the silicon and the glass wafers, are no longer visible, suggesting that bonding is already well engaged.

1.	Outgassing under vacuum at 350 °C
2.	Cooling down
3.	Gas filling at low temperature (≈ 40 °C)
4.	Wafers in contact with a force of (500 N)
5.	Heating at 350 °C
6.	Voltage set to 250 V (just below the breakdown voltage)
7.	Introduction of air (atmospheric pressure)
8.	Voltage set to 600 V
9.	Voltage set to 900 V
10.	Cooling and venting

Table 3.4: Details of the second anodic bonding procedure performed on the EVG 501, as described by Hasegawa *et al.* (2011b).

1. Outgassing under vacuum at 350 °C (30 min)
2. Gas filling at high temperature
3. Wafers in contact with a force of 200 N
4. Voltage set to 220 V (just below the breakdown voltage)
5. Introduction of N_2 up to 700 mbar
6. Voltage set to 550 V (just below the breakdown voltage)
7. Chamber pumped out (after primary and secondary circuits pressure equilibration)
8. Voltage set to 900 V
9. Cooling and venting

Table 3.5: Details of the second anodic bonding procedure performed on the AML.
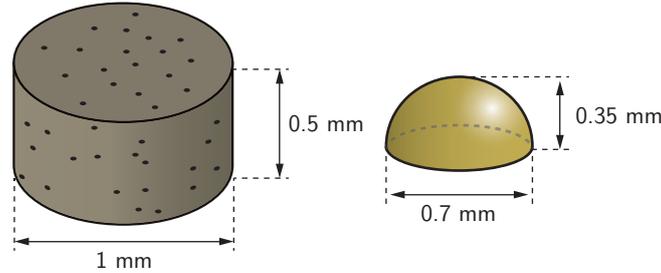
Figure 3.10: Estimation of the cesium quantity contained in a dispenser (left) represented in terms of volume of condensation (right).

In order to increase the voltage limit and consolidate the bonding, the chamber is filled with nitrogen up to a total pressure of 700 mbar. The breakdown voltage with the mixture of neon and nitrogen is typically increased above 550 V. The second bonding step is then done at this voltage. At this point, the only way to raise further the voltage limit is to pump out the chamber. The pressures between each sides of the isolation valve have to be equilibrated before opening it to avoid damages. The by-pass valves are therefore opened for a short time, the isolation valve is opened and the pumps are restarted. A last bonding step can finally be done at 900 V under a rough vacuum. Gases with higher dielectric strength, such as SF_6, could be used instead of N_2 to circumvent this last step.

The cooling step, used in the previous process, before filling the chamber with the buffer gas was removed, without compromising the pressure uniformity. This modification significantly reduced the process duration as cooling down the platens from 350 °C to 40 °C lasted several hours. Among the first batch of 10 cells fabricated according to this process, a pressure of 79 ± 7 mbar at 80 °C was observed (wafer T19). This pressure was estimated by linear absorption and the actual pressure dispersion could be smaller. Among the 6 cells of a second batch (wafer T18), the pressures were measured around 50.7 ± 2.6 mbar at 80 °C.

For gas mixes, gases are introduced in sequence. Mixing obtained by diffusive motion and inlet flow turbulences is expected to be sufficient to achieve proper homogeneity.

3.2.8   Activation and curing

After sealing, pure cesium is released from the dispenser by heating it with a high-power laser. This process, called *activation*, aims at providing the appropriate cesium quantity to ensure a saturated vapor over the cell's lifetime while preventing the optical cavity from being obstructed by condensation.

3.2.8.1   Condensation excess

The cesium quantity contained in each dispenser can roughly be evaluated from data provided by SAES Getters (2007). Assuming that all cesium is released, a dispenser of 0.4 mm^3 can supply around 150 µg of elemental cesium. The equivalent volume it represents in a condensed phase is shown in Fig. 3.10. When dispensers are excessively heated, such volumes can indeed be observed as can be seen in Fig. 3.11a.

Condensation gradually migrates toward cold areas of the cell. If the windows of the optical cavity happen to be colder than the rest of the cell and if too much condensation is present, the optical path can be severely obstructed as shown on Fig. 3.11b. In order to prevent this obstruction, the condensation volume should be
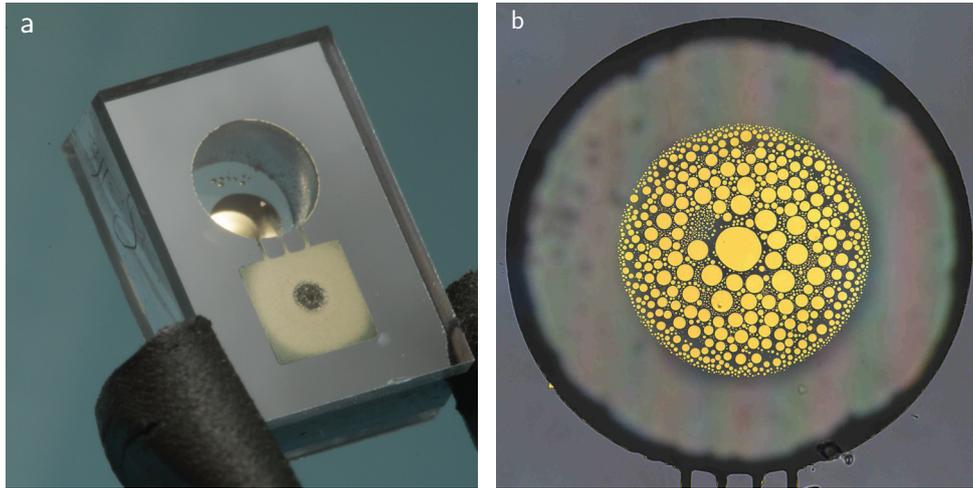
Figure 3.11: Picture and microscope image of cells with an excess of cesium condensation. On the microscope image, the cell was heated from backside on a hot plate after activation, resulting in a cold area at the center of the top window.

minimized. Additionally, the cell heating system of the physics package should be adequately designed to prevent cold spots on the windows as suggested by Knappe (2008). Transparent ITO resistive patterns have been used to apply heat directly on the windows (Schwindt *et al.*, 2007, Ruffieux *et al.*, 2014, Borwick *et al.*, 2012).

Other solutions have been proposed to manage an excess of condensation but not yet demonstrated. For instance, the use of electrodes to control the position of condensation through electrowetting was proposed by Davis *et al.* (2011), although not directly serving this purpose. Parsa and Hopper (2015), Parsa and French (2015) and Maki and Nakajima (2015) propose to form a sharp concave or convex corner next to the optical cavity to draw condensation at this site. Similarly, Nakajima and Maki (2015) describes ways to enhance the wettability of a holding portion formed by roughening the wall surface or using a porous membrane or trapping condensation in columnar or slit-shaped through holes. Nakajima (2015) intends to engineer the cell so that cold spots are obtained by favoring radiative losses at specific locations. A few additional solutions to prevent a condensation excess in cells with dispensers will be proposed in the following.

3.2.8.2 Curing process

On the other hand, alkali metals and cesium in particular are known to be consumed by hot glass surfaces and foreign pollutants in vapor cells, especially during their early life (Brossel *et al.*, 1955, Thomsen *et al.*, 1968, Patton *et al.*, 2007). This process is known as *curing* or *ripening* (often applied to wall-coated cells) and is not well understood. Bouchiat *et al.* (1999) observed that glass cell walls undergo a modification when exposed to dry cesium vapor, which causes them to become electrically conductive. This phenomenon has been studied by Ma *et al.* (2009) who found that Pyrex (similar to Borofloat33) absorbs about 3×10^{15} rubidium atoms per cm^2 at $94\,°C$. We can estimate the quantity of cesium required to establish a saturated vapor in a $9\,mm^3$ cell heated at $80\,°C$. Neglecting the curing process and any phenomenon that may consume cesium, a mass of $8 \times 10^{-6}\,\mu g$ would be sufficient. This would mean that a single dispenser could provide enough cesium for 20 million cells. In reality, the curing process consumes a significant quantity and it is the quantity in vapor that is negligible. Glass blown cell makers typically account for this by introducing more alkali metal before sealing (Straessle, 2013). A reserve of condensed metal ensures that the vapor pressure will remain saturated after the curing process and throughout the cell's lifetime.

The idea of using a passivation layer to prevent the reaction of alkali metals with glass windows in microfabricated cells was proposed by Lipp *et al.* (2008). Woetzel *et al.* (2013) showed that an Al_2O_3 layer deposited on the inner surfaces of the cell reduces the consumption of cesium at high temperature. A layer as thin as $6\,nm$ provides a 100 fold reduction in the cesium consumption rate compared to a bare borosilicate glass wafer. Besides, it does not prevent anodic bonding.
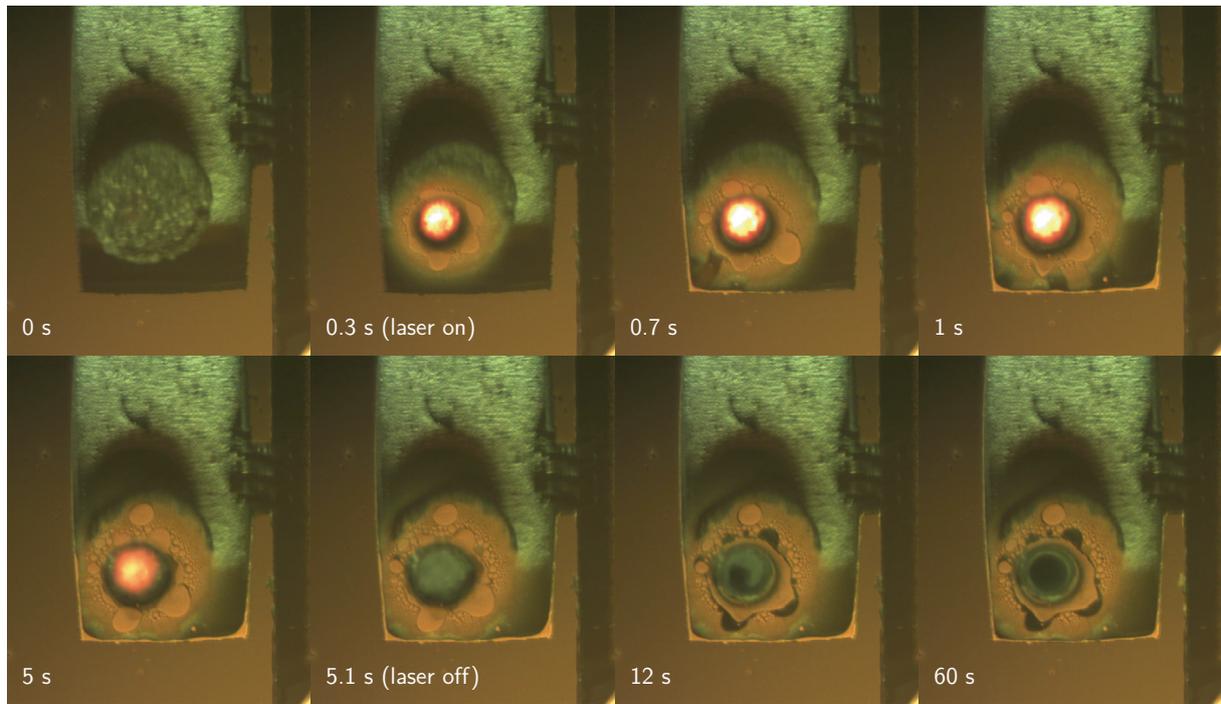
Figure 3.12: Observation of the activation process in a reflective cell.

3.2.8.3   Activation setup and procedure

The activation setup was initially assembled by Dziuban (2011) but major evolutions have since been brought to the setup in order to observe the activation process and to perform linear absorption spectroscopy characterization collectively.

The setup comprises an XY motorized stage[9], a fiber coupled laser diode[10] (7 W CW at 808 nm) powered by a laser diode driver[11]. At the fiber output, the beam is collimated and focalized on the dispenser with a beam size around 500 µm. A camera[12] allows to target the dispenser and observe the activation. The dispenser is first targeted at low laser power so that a spot can be seen on the camera and aligned on the dispenser. During the activation, reflections of the beam toward the camera tends to saturate it. To prevent this, a removable filter[13] was added to filter out light from the laser. This simple upgrade allows us to see and record directly the black body emission from the dispenser being heated (providing us with a rough estimation of its temperature) and the appearance of the condensation. Video snapshots acquired during the activation of a reflective cell are shown in Fig. 3.12. In practice, several cells are activated in a row by memorizing the positions of the stage during a targeting step, before activating them with the filter set. The optical power is calibrated with a thermal power meter[14]. Figure 3.13 shows its response curve.

A current is supplied to the laser following a gate function. The multiple activation experiments undertaken during MAC-TFC showed that a 1.2 W power for 60 s was generally sufficient to activate a buffer-gas filled cell (Dziuban, 2011, Rutkowski, 2010). However, it was observed that some cells seemed to require longer activation times and the process repeatability remained rather unsatisfactory. Without buffer gas, the activation seems much faster and durations shorter than 10 s were found sufficient.

Computations tend to show that this difference can be due the additional heat conduction that the buffer gas provides, which limits the dispenser temperature.

We attempted to study the optimal activation parameters depending on the buffer gas pressure. To this end, cells from 5 wafers sealed with different buffer gas pressures were fabricated and activated with the same parameters. Figure 3.14 shows images of the cells after activation. The amount of cesium indeed seems to decrease gradually as buffer gas pressure increases. Condensation was driven toward the top window by

---

[9]Thorlabs BSC201 and Thorlabs NRT150
[10]Oclaro BMU7-808/C
[11]Newport 560B
[12]Thorlabs DCC1645C
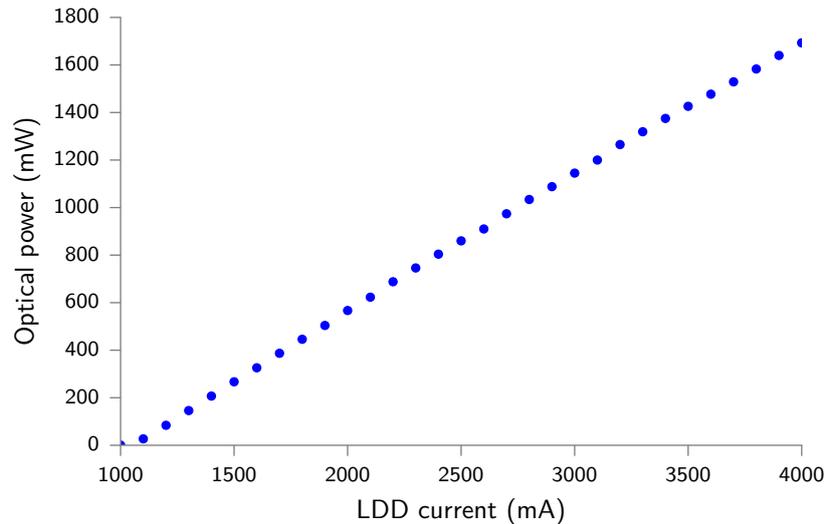[13]Thorlabs FES0700 and Thorlabs CFH2
[14]Thorlabs S310C

Figure 3.13: Power calibration of the activation laser.

heating them from behind on a hot plate at 80 °C for a few minutes. In this configuration, thermal losses due for instance to air convection on the top side of the cell result in cold spots on the top windows of the cavities, which is convenient for microscope observation.

3.2.8.4 Condensation observation

Figure 3.15 shows a cell at different time intervals after being put on a hot plate. Just after activation, condensation is mostly visible on sidewalls. After a few minutes, condensation has moved toward the center of the windows, clearing the sidewalls. When the amount of condensation is not too important, it seems that all condensation is effectively driven to the top windows since no condensation can be seen elsewhere. This method seems more relevant to assess the amount of condensation than a direct observation without condensation migration. After heating the cell for several hours, the amount of visible condensation reduces dramatically.

A first setup was assembled to get longer and more detailed observations of this phenomenon in multiple cells. It consisted in a custom made hot plate fitted on the XY stage of a microscope available at MIMENTO[15]. The hot-plate was designed to hold a 100 mm wafer. The Micro-Manager software[16] was used to acquire time-lapse sequences of several cells in parallel over several days. Videos were then generated from image sequences[17].

A first batch of 13 cells from a same wafer was observed after activation with the same parameters (10 s at 3 A).

Figure 3.16 shows the progression of cesium disappearance in 3 typical examples. In cell (a), condensation disappears after 36 h at 70 °C. In cell (c), this quantity is also reduced but less significantly. The acquisition time was insufficient to say if cesium would subsist longer. Conversely, cesium in cell (b) does not seem to be reduced significantly. On the contrary, condensation tends to migrate gradually in the optical cavity. Among this set of 13 cells, the behaviors of cells (a), (b) and (c) are found in 5, 6 and 2 cells, respectively. Reasons for this reduction in condensation are not yet clear and the curing process could hardly explain it on its own. The dispenser may also reabsorb a part of it by capillary action, as it is a granular solid, or by chemical recombination with a the by-products of cesium chromate decomposition. While capillary absorption would be beneficial to avoid obstructing the windows, chemical recombination would probably be more problematic and could jeopardize the saturated vapor regime over long time periods. We observed unexplained differences among cells concerning both the initial quantity of condensation and the condensation reduction rate. It appears unlikely that this phenomenon results from sealing defects as it usually leaves visible oxidation traces (Straessle, 2013). Other explanations could be differences in cell cleanness, positioning of the dispenser and activation beam or simply an inhomogeneous cesium quantity among the dispensers.

---

[15]Leica DM8000 M
[16]https://micro-manager.org/
[17]with FFmpeg (https://www.ffmpeg.org/)

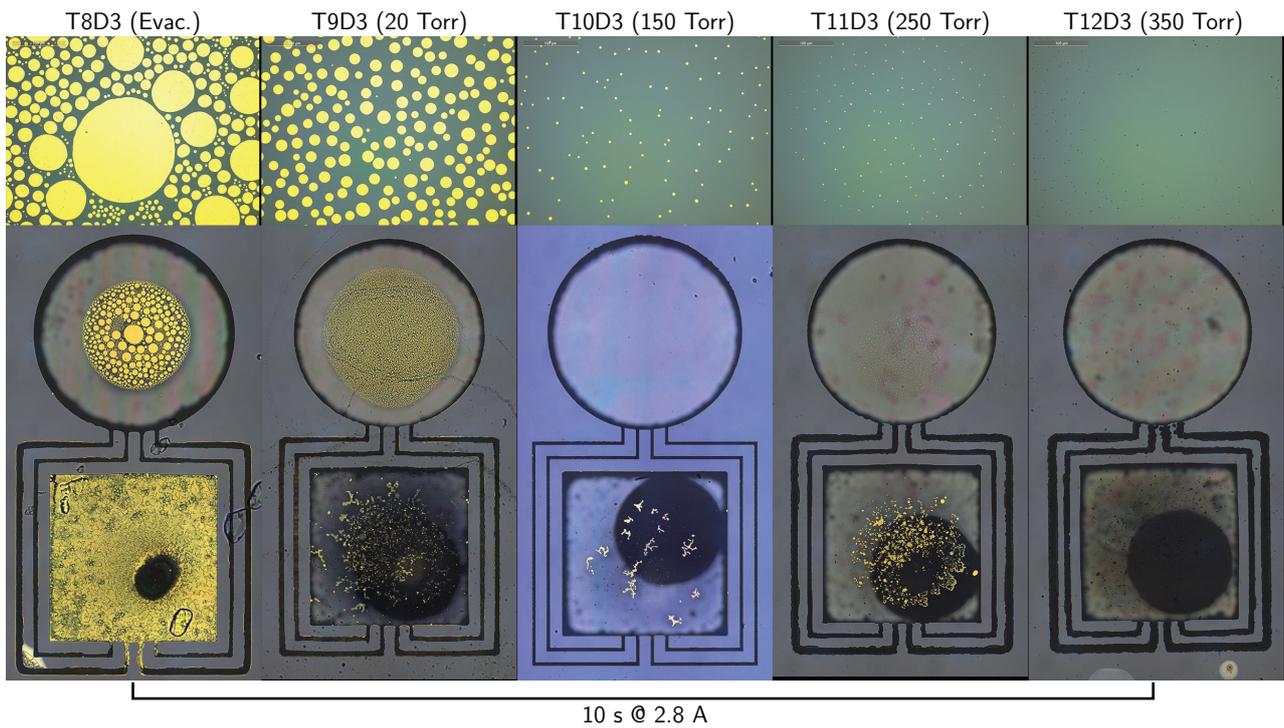| T8D3 (Evac.) | T9D3 (20 Torr) | T10D3 (150 Torr) | T11D3 (250 Torr) | T12D3 (350 Torr) |

10 s @ 2.8 A

Figure 3.14: Observation of the condensation in 5 cells with different buffer gas pressures after activation under the same conditions. Condensation was driven toward the top window by heating them on a hot plate at 80 °C for a few minutes.

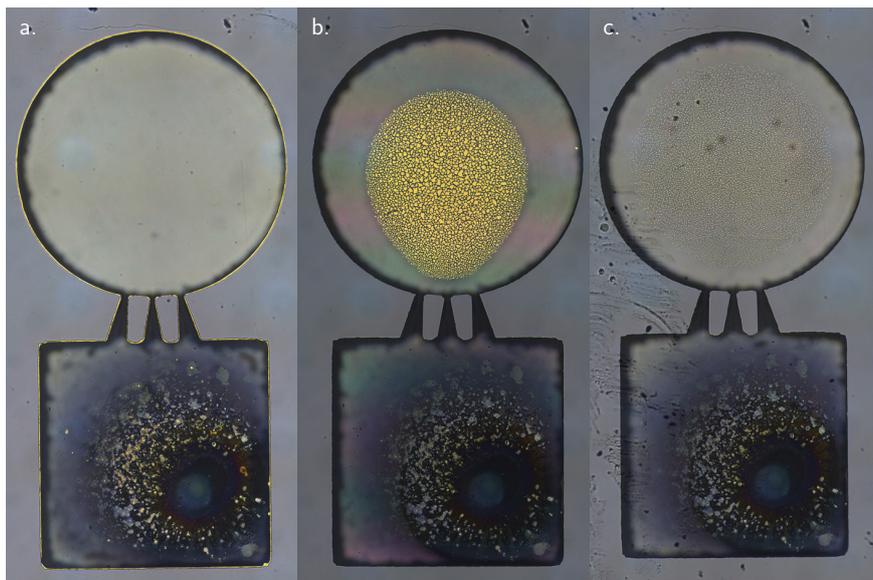Figure 3.15: Observation of the evolution of the condensation in a cell: just after activation (a), after a few minutes on the hot plate (b) and after a few hours on the hot plate (c).
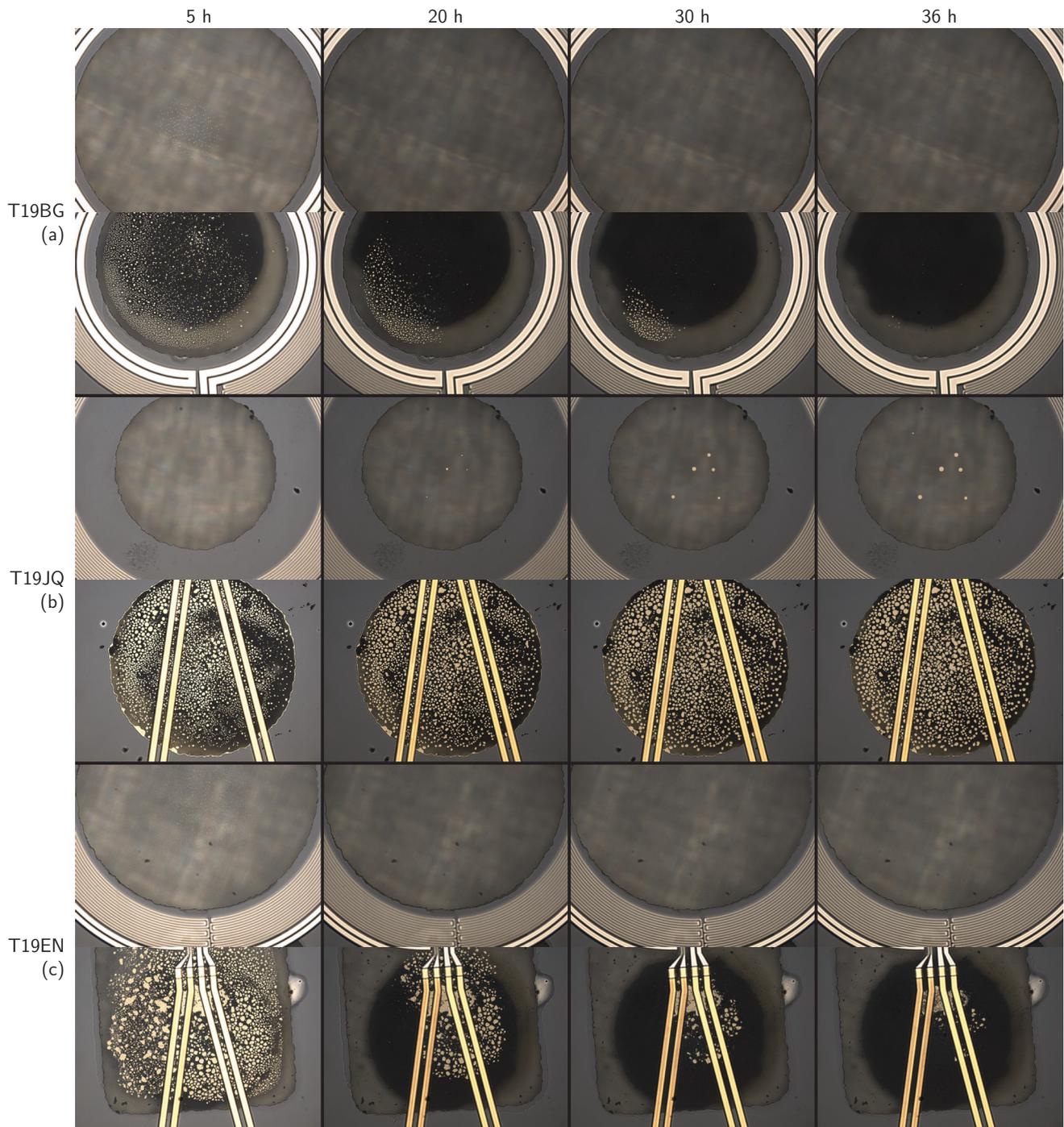
Figure 3.16: Evolution of cesium condensation in 3 cells heated from backside at 70 °C.
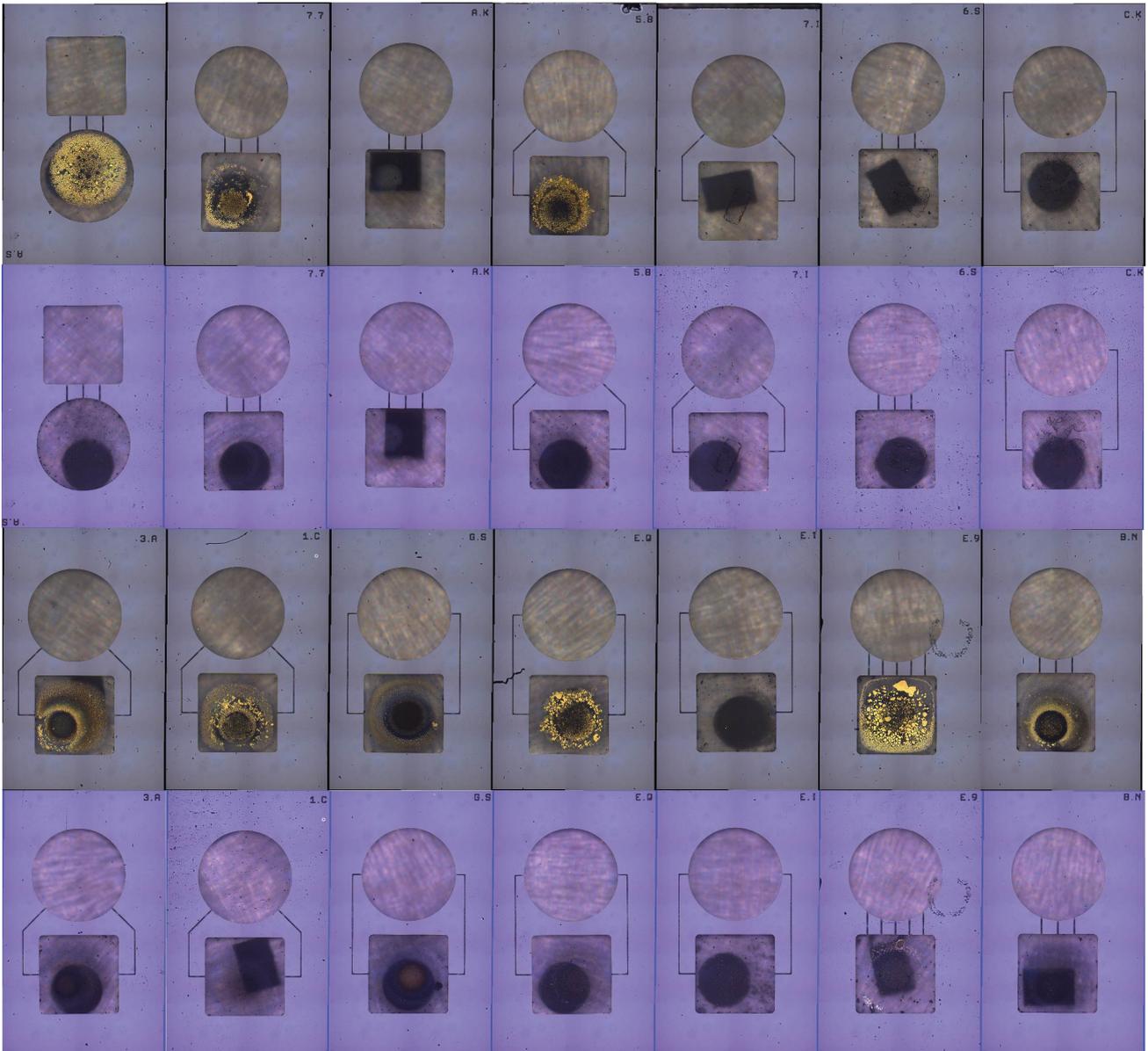
Figure 3.17: Comparison of cells after activation (rows 1 and 3) and after 27 days at 110 °C (rows 2 and 4).

We typically observe solid deposits on the top window of the dispenser cavity after activation of evacuated cells (Fig. 3.18). At the center of this image, a dark spot can be seen, marking the laser beam path. We suspect that it results from the reaction of cesium with the heated glass. This darkening seems to occur gradually after the laser is switched off as can be seen on Fig. 3.12 between 5 s and 60 s. The cesium-colored deposits around this dark spot seem solid and do not evaporate or flow elsewhere when a temperature gradient is applied. Although this deposit can cause initial cesium consumption, it does not seem to evolve over time and should not be the reason for long-term cesium losses. Those deposits are far less visible in buffer gas cells.

A set of 14 cells were activated at 1.4 W for 10 s. All cells were successfully activated as they all showed an absorption signal. However, the quantity of condensation was large enough to cause obstruction issues. Yet, after baking them at 110 °C for 27 days, it had drastically reduced (Fig. 3.17). Condensed cesium did not seem to have oxidized because no oxide traces were observed on the windows. Oxide traces are usually clearly visible in cells with a bonding defect. Here again, we suspect that the dispenser reabsorbs the condensation. Despite the fact that no condensation could be seen in most cells after baking, those cells still showed absorption signals. Consequently, this baking step may be a solution to remove an excess of condensation, which would be less constraining than other solutions. Longer tests are ongoing to verify that the atomic density is sustained even in cells where no condensation is visible.

Throughout these experiments, we noticed that baking cells for a few hours (typically 3 h at 110 °C) was
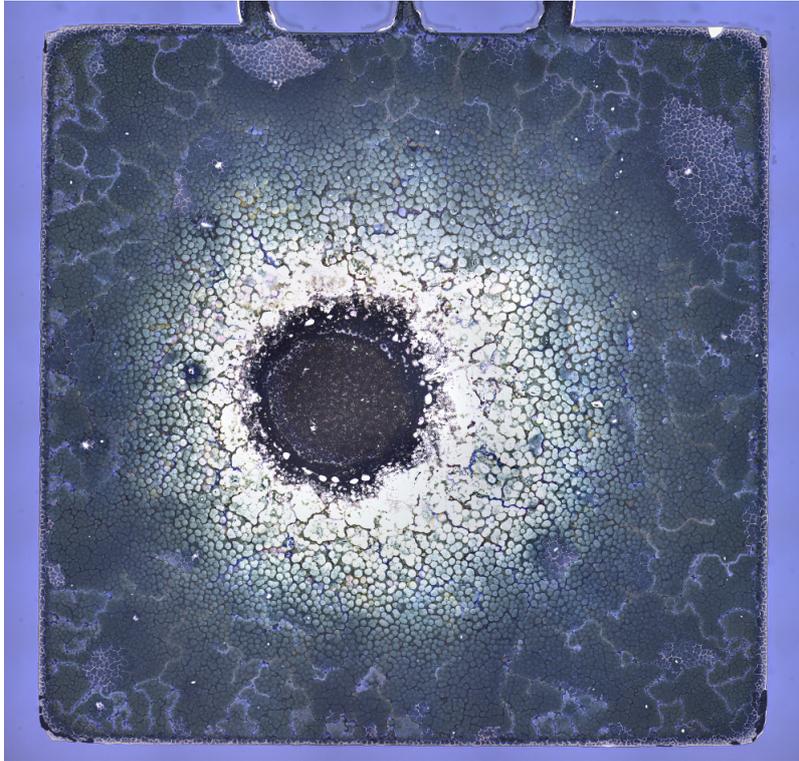
Figure 3.18: Traces observed on the top window of the dispenser cavity after activation of an evacuated cell.

necessary for stabilizing the atomic density. The linear absorption characterization just after activation without baking is misleading. In the past, this step was not systematically performed and some of the cells were wrongfully considered as defective or requiring a reactivation.

The modifications brought to the bench now aim at observing how the atomic density evolves over time following the activation.

3.2.8.5 Optimal parameters

Several sets of cells have been activated to determine optical activation duration and intensity. However, because of the variabilities, finding unique activation parameters ensuring both saturated vapor pressure on the long-term and no condensation excess for all the cells of a batch seems difficult. Indeed, for a given set of parameters, some cells exhibit a condensation excess whereas others do not show a significant absorption spectrum.

Several approaches can be envisioned to consistently activate cells with a high yield and without condensation excess. First, we can heat dispensers with a high laser intensity to make sure that a large quantity of cesium is released. In this case, one of the solutions described earlier to drive condensation excess away from the optical cavity has to be employed, by heating the cell through the windows during operation or adding a relatively long baking step after activation.

Alternatively, we could use several activation steps of increasing intensity with intermediary linear absorption measurements and baking steps. With this method, the activation process can be stopped as soon as a saturated vapor is detected without releasing too much cesium. The modifications and additions brought to the activation bench described bellow will allow to implement this method.

3.2.8.6 Activation bench evolution

After the experiments described above had been performed, several improvements were brought to the setup to perform linear absorption spectroscopy in the cells. An opaque box was constructed around the setup to avoid perturbations from the ambient light and improve laser safety. The setup was mounted on an optical breadboard and the various equipments were put on a rack (Fig. 3.19a). A breadboard mounted vertically makes it easier to attach the various components (Fig. 3.19b). Some space was reserved to host a CO_2 laser for the experiments on the microfabricated make-seal components described later. In order to perform spectroscopy in parallel, a

distributed feedback (DFB) laser at 852 nm was deported on the optical table. The beam is split in so that the first part propagates through a centimeter-scale glass-blown reference vapor cell while the second part of the beam is coupled into an optical fiber. The probing beam is brought next to the activation beam by the fiber (Fig. 3.20). A custom heating cell holder was designed and fabricated by Jarosław Rutkowski. It consists of a stack of two printed circuit boards (PCBs) interleaved by a 3D printed alumide spacer openworked to host up to 97 cells. The copper of the PCBs was patterned to make resistive traces. Traces were designed to be driven by a MPT 5000 temperature controller with 12 V. Three thermistors are soldered on the plate. The cell holder was mounted on a platform attached to the XY translation stage leaving room for the photodiode under the cell holder, facing the spectroscopy beam. The laser current is modulated with a function generator. Signals are acquired with a PicoScope. The camera can take images of cells at regular intervals to observe the evolution of the condensation. A control software[18] was developed to ease the activation and characterization tasks. It employs the Python package PyQtGraph[19]. The graphical user interface for controlling and monitoring the activation bench is shown in Fig. 3.22.

3.2.9   Advantages and limitations

The main benefit of dispenser pills is their ease of use for small volumes. Indeed, they can be handled in ambient air and standard anodic bonding equipments can be used. Besides, the cell atmosphere remains stable over long time periods. After a short post-activation baking step, high yields are typically obtained and the method is robust. Faulty cells are mostly due to evident bonding defects, which rarely occur. Anodic bonding can be done in optimal conditions, at 350 °C, which ensures a high mechanical resistance.

However, despite these advantages , they still present several drawbacks. The manual insertion of dispenser pills in the preform before bonding remains a critical step. Indeed, they tend to pick up ambient humidity and disaggregate rather rapidly, as we have seen earlier. In addition, if their placement is not precise enough, particles can fall on the top surface of the wafer, around the cavity, leading to local bonding defects. Several steps can be taken to improve this issue. In particular, a masking plate can be used to protect the bonding area and this step can be performed under a controlled atmosphere. For large scale production, an automated pick and place equipment could be employed. However, it would ideally have to be placed under a controlled atmosphere, which makes the setup complex.

Even if those issues were solved, dispenser pills would still impose several restrictions.

As we have seen in Section 2.2.3.1, because nitrogen is absorbed by the getter material contained in pills, the convenient mixture of nitrogen and argon as buffer gas can not be used to shift the temperature insensitive working point toward higher temperatures (Braun *et al.*, 2007). Although an atmosphere composed of neon and helium can achieve the same purpose without being absorbed by the dispenser, it is difficult to contain helium hermetically.

In addition, the dispenser cavity, which occupies nearly half the cell volume, is cumbersome. However, dispenser pills can hardly be made smaller than 1 mm diameter. Indeed, they would be difficult to agglomerate and an homogeneous composition among dispensers would be harder to reach. This negatively affects the cell unit cost, compared to other single cavity designs as the number of cells per wafer is halved. Furthermore, the dispenser cost (around €5 each) must be added on top of that, compromising competitiveness.

The adverse effects of a larger cell on the physics package are numerous. First, it increases the physics package size. The larger the volume and the mass of the cell, the larger the heat capacity and the longer the delay to reach the temperature set point (warm-up time). An elevated weight requires stronger suspensions to endure shocks and vibrations, which go against the reduction of thermal conductivity. The larger radiative surfaces also tend to demand more heating power.

Finally, relying on a single supplier might represent a risk in an industrial context. Other filling solutions are described in Section 3.5 and Section 3.6, which could alleviate some of those drawbacks by either depositing collectively the dispensers or by separating the optical cavity from the dispenser cavity, once the cell has been filled with alkali metal.

---

[18]Source code available at http://github.com/mv20100/phd_code_activation
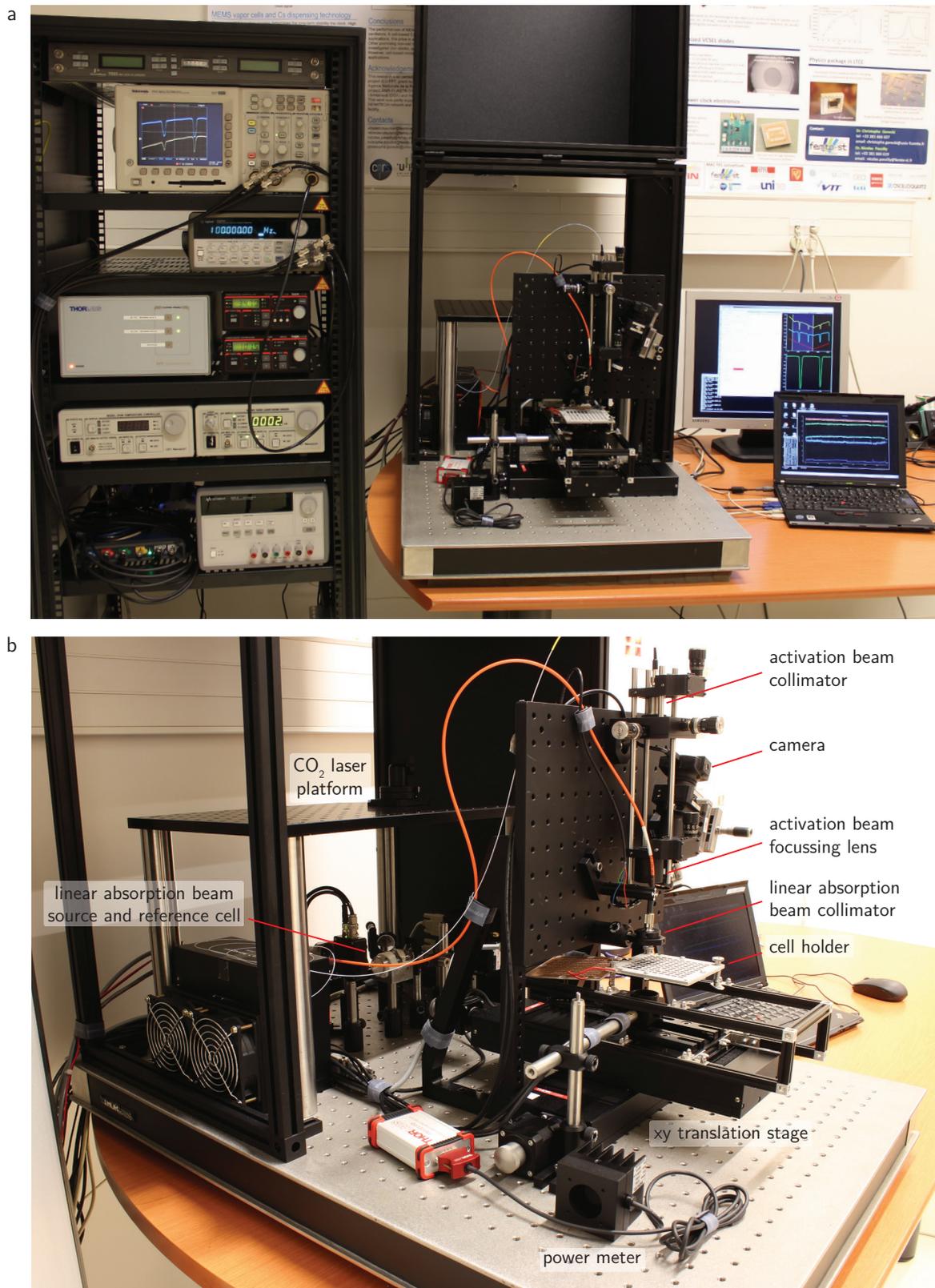[19]http://www.pyqtgraph.org/

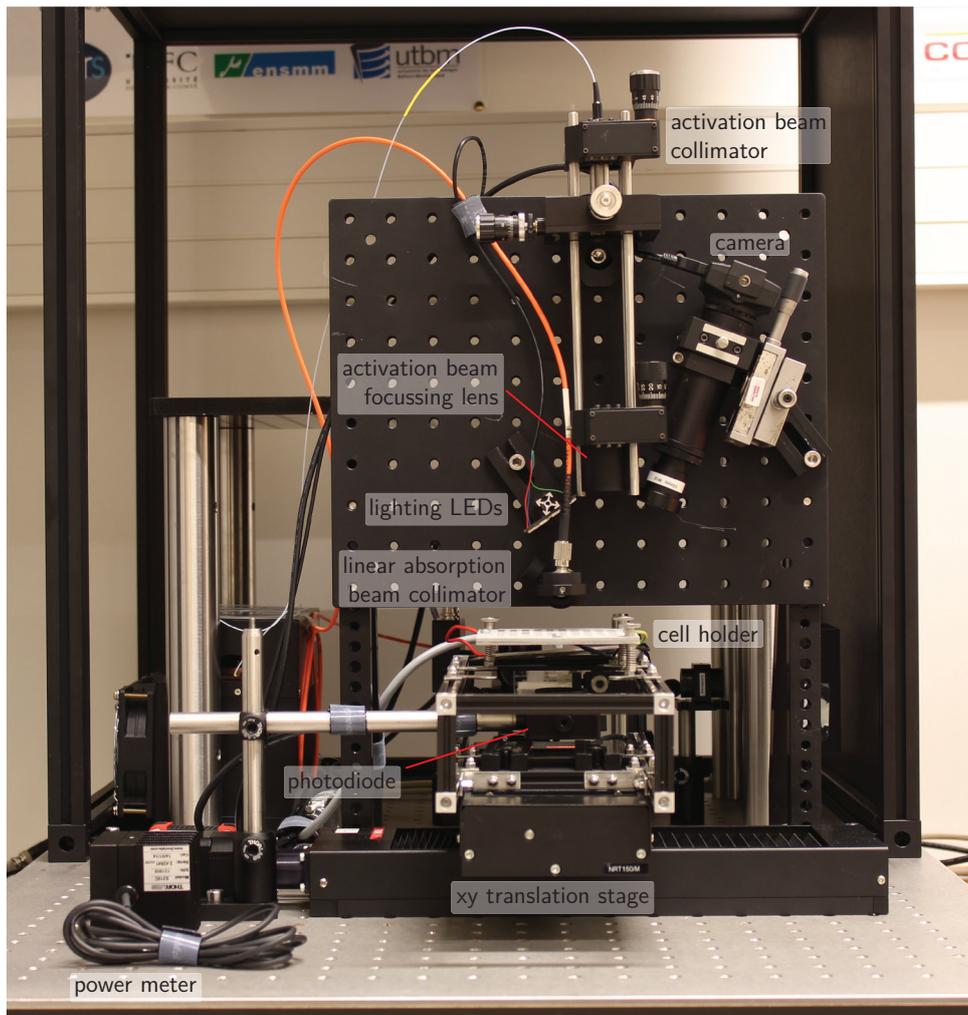Figure 3.19: Pictures of the activation bench.

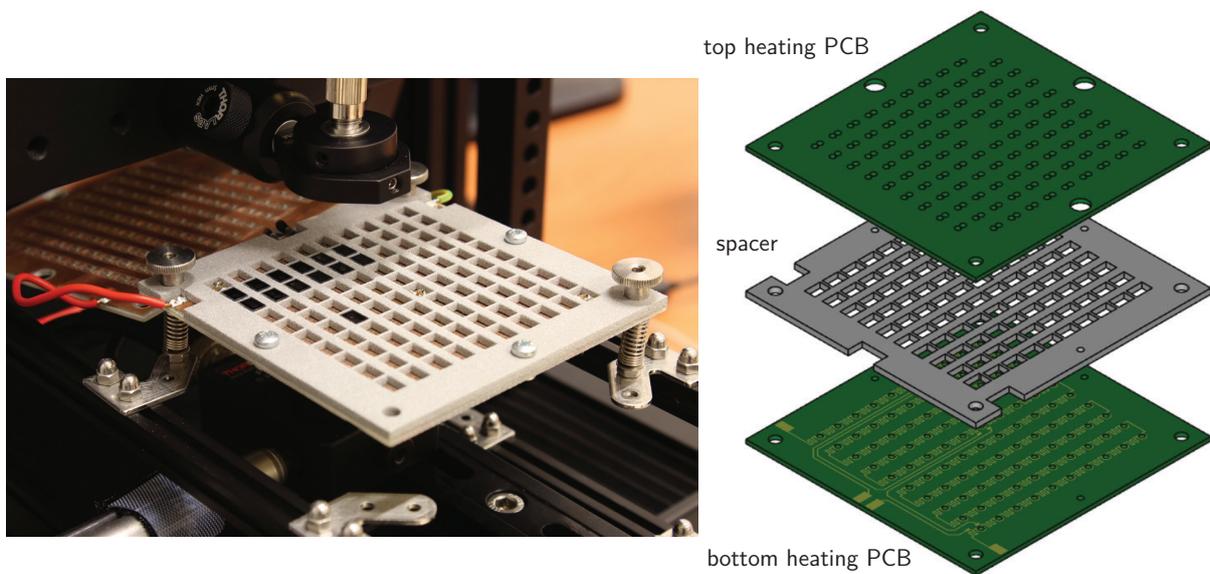Figure 3.20: Front view of the activation and characterization bench.

Figure 3.21: Picture and assembly of the heating cell holder (CAD image by Jarosław Rutkowski).
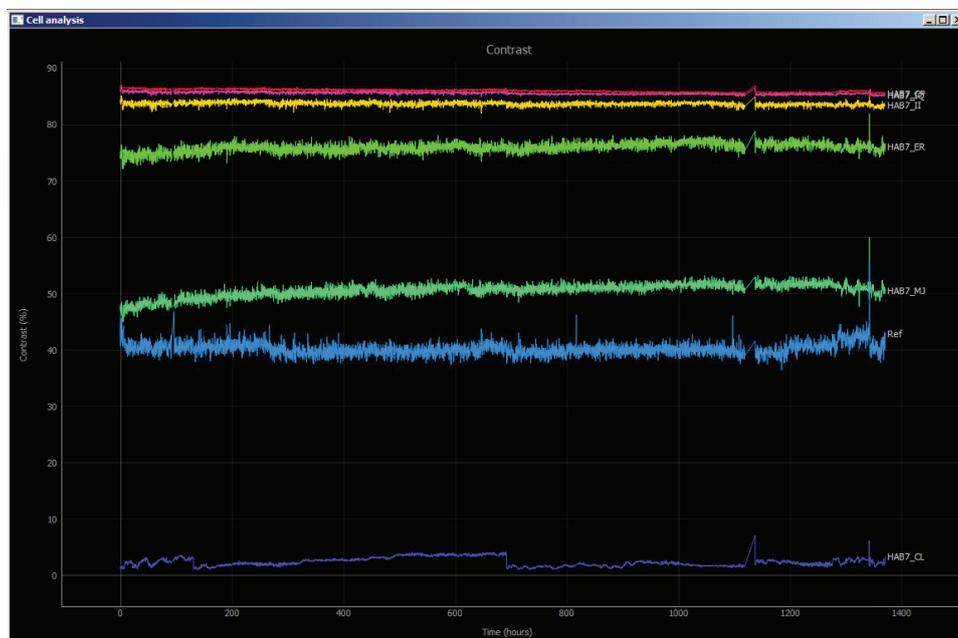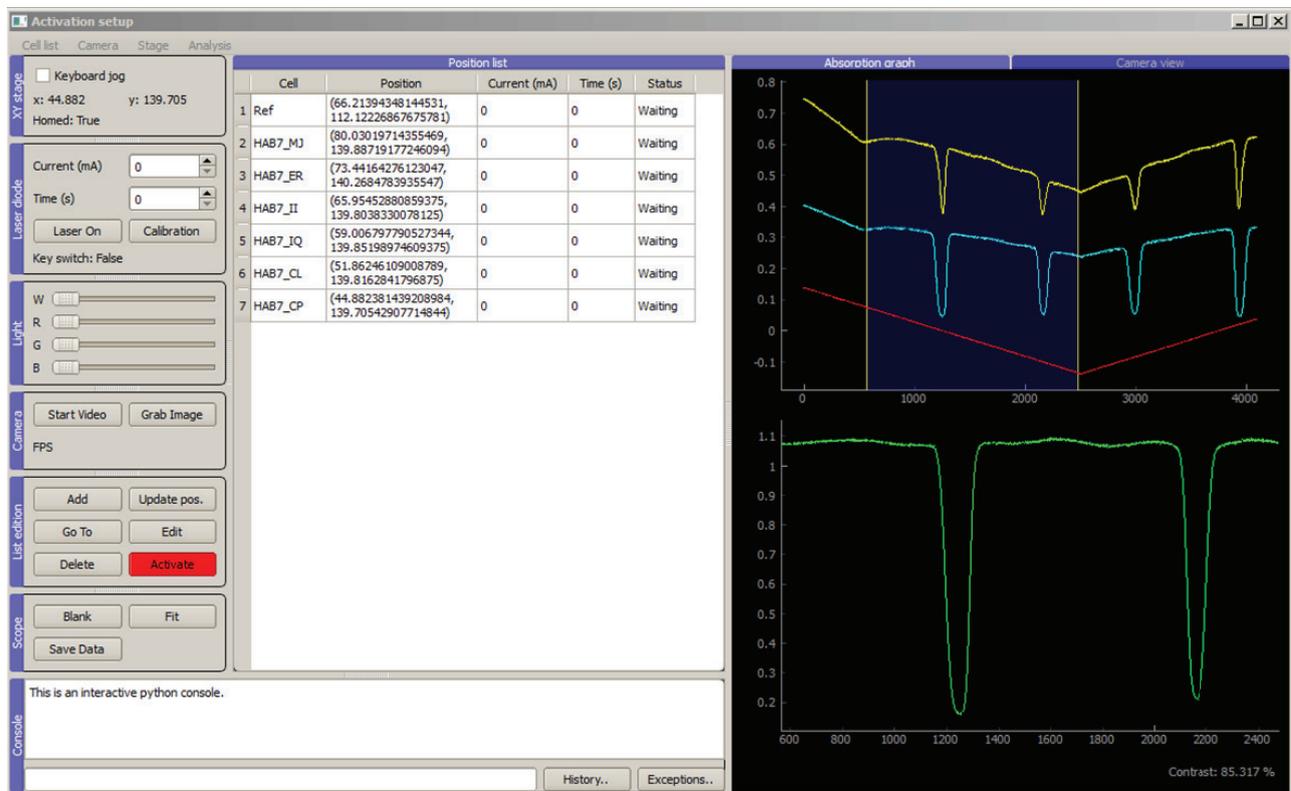
Figure 3.22: Graphical user interface for controlling and monitoring the activation bench.

3.3   Reflective cell

Reflective cells have been designed by Passilly *et al.* (2015) and fabricated prior this thesis work by Chutani (2011). This work has been published more recently (Chutani *et al.*, 2015).

3.3.1   Motivations

In its most basic configuration, a CSAC consists of a straight-lined arrangement in which a VCSEL beam is circularly polarized by a quarter-wave plate and illuminates one side of an alkali vapor cell. The transmitted light is then collected by a photodiode on the other side of the cell. In order to preserve the CPT signal quality and hence the resulting frequency stability, three main aspects regarding the illumination scheme should be addressed. Those aspects include a sufficient collinearity between the propagation direction of the probing light beam and the static magnetic field axis, a highly circular polarization state and a large and uniform illumination of the volume occupied by the alkali vapor so that most of the atoms are likely to contribute to the CPT signal. Nevertheless, fulfilling all these constraints can be difficult when it comes to miniaturizing the device down to millimeter scales. In addition to being compact and comply with those illumination requirements, the device must remain easy to assemble. As for many MEMS based products, the assembly can indeed be predominant in the overall cost. The integration of components at the wafer level rather than at the package level becomes necessary and can tip the balance in the compromise that is usually conceded between stability, compactness and integrability. Aiming at improving some of these aspects, alternative configurations using additional micro-optical elements such as reflectors or microlenses have been proposed. However, few of them actually address all those constraints.

Here, we propose an original architecture where laser light is routed in an alkali vapor cell with angled reflectors formed in a wet-etched silicon cavity and integrated diffraction gratings. This architecture, in accordance with the illumination requirements to improve the CPT signal quality, provides both compact beam shaping ability and a simpler integration of the laser and the detector which can be placed side by side on the same electronic plate. These features allowing an extensive wafer-level approach could answer the need for cost and size reduction. In addition, we show that an elongated geometry does not jeopardize the performances, quite the contrary, since the results exhibit a potential for stability improvement. Long and narrow cells find other applications, for instance in stored light experiments (Klein, 2009). This novel approach based on an elongated cell is not straightforward. Indeed, it does not allow the reduction of the CPT resonance linewidth because of the dominating sidewalls collision rate. But the contrast is significantly improved, balancing the use of both a tinier cavity and a smaller beam, and improving the figure of merit.

3.3.2   Review of optical architectures

The most basic optical assembly of a CSAC essentially consists of a VCSEL, an alkali vapor cell and a photodiode arranged so that the optical train is straight-lined (Fig. 3.23a). The natural divergence of the VCSEL allows to reach a sufficient beam diameter in the cell provided that the distance between them is long enough. This simple approach is particularly appealing since no optical element is added (except for a quarter-wave plate (QWP) and a neutral density, not shown in Fig. 3.23 because they do not have a beam-shaping function). This architecture was adopted by Lutwak *et al.* (2007a) in the first commercial device. However, depending
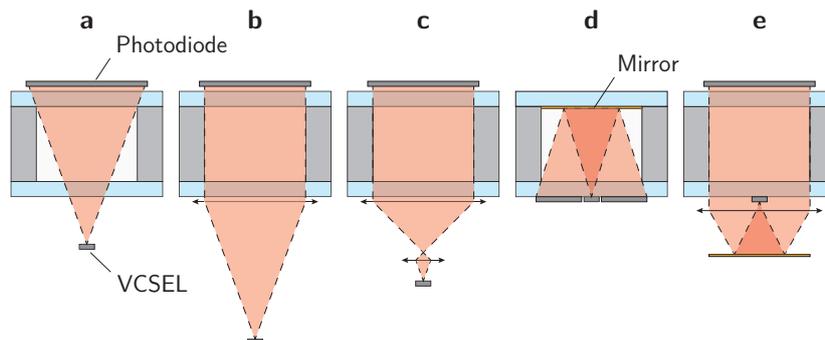

Figure 3.23: Different CSAC optical architectures.

on the cell diameter, several millimeters can be required to reach the desired beam width while reducing the light intensity inhomogeneity and ensuring collinearity between the light propagation and the magnetic field. Another approach involves a collimating lens located close to the entrance window of the cell (Fig. 3.23b). Even though it provides a beam collinear with the magnetic field, a large and uniform illumination still requires a long propagation distance. In order to shorten the beam shaping distance and thereby the assembly length, a lens can be added before the collimating lens to increase the divergence and form a beam expander (Fig. 3.23c). While this solution can collimate a large beam in a relatively tight space, it comes at the expense of constraining alignments during the assembly of the first high numerical aperture lens of the doublet (Chutani *et al.*, 2012, Karioja *et al.*, 2014). Configurations based on reflectors have also been proposed to reduce further the assembly size by folding the optical path. For instance, Riley and Lutwak (2006) also proposed a folded configuration in which the beam performs a round trip through the alkali vapor cell, with the addition of a mirror on the former exit window (Fig. 3.23d). In this case, the VCSEL can be placed at the center of a surrounding photodetector on the same electronic plate, offering a significant advantage regarding the assembly of the physics package. However, this specific configuration led to an inhomogeneous light shift due to a highly uneven illumination within the cell, both in direction and intensity. Moreover, it reduces significantly the density of VCSELs that can be fabricated on a wafer and thus the cost efficiency. The design was finally changed to a non-folded and non-collimated design (Fig. 3.23a) which provides better performances and reduces the cost of the optoelectronic components (Lutwak *et al.*, 2007a). Slightly later, DeNatale *et al.* (2008, 2009) proposed a design in which the VCSEL is oriented outward the cell. The beam is reflected back toward the cell with an additional mirror (Fig. 3.23e). In this design, a dual-focus optic allows to increase the divergence of the beam just emitted from the source and collimates the beam reflected by the mirror at the same time. This solution is similar to the configuration using a doublet (Fig. 3.23c) but in a folded arrangement where the two lenses are part of a single element. This component joining a Fresnel lens with a microlens at its center can be batch fabricated and is more compliant with wafer-level alignments. The common feature of the designs presented so far is a vapor cell fabricated by sandwiching a silicon wafer featuring a dry-etched through-cavity between two glass wafers. The resulting cell length is limited by the DRIE which can hardly reach 2 mm depths (Pétremand *et al.*, 2012, Chutani *et al.*, 2014). In order to overcome this limitation, the interrogation beam can instead be propagated in a cavity along the wafer surface. Even if the cell diameter is now limited by the wafer thickness, its length can be extended at will. The number of probed atoms can thus be increased while keeping a small beam diameter, which relaxes the beam shaping requirements. From the integration standpoint, it is desirable to keep the VCSEL emission direction and the detector orientation normal to the wafer plan, hence, the light beam should be folded accordingly.

Reflectors can be patterned on the angled sidewalls of a silicon cavity. The most appealing approach is to take advantage from the surface quality of (111) crystallographic planes revealed by the anisotropic wet etching of (100)-oriented silicon wafers. Unfortunately, because of the diamond structure of silicon, these crystallographic planes are oriented at 54.74° from the wafer surface which differs from the ideal 45° orientation. The angle of the input beam should therefore be corrected before the reflection. Based on such reflectors, Youngner *et al.* (2007) proposed a solution where the interrogation beam propagates along the wafer surface across a suspended cell (Lust and Youngner, 2008). This design uses prisms structured in glass to refract the beam and correct the angle of incidence on the reflector so that its reflection is in the wafer plane. However, the batch fabrication of such a refractive component is challenging. In addition, the vapor is contained in a smaller portion than the volume available between the two reflectors and the fact that the QWP is placed between the reflector and the vapor cell makes it difficult to integrate at the wafer level. Another solution based on refractive components could also rely on a misaligned microlens but its behavior would be very sensitive to alignments during packaging and the circular polarization state could be quite affected. In this work, we consider the integration of diffraction gratings on an alkali vapor cell in order to route the probing laser beam and perform the required angle correction. Unlike a microlens, the advantage is that gratings will perform the same optical function regardless of the incident beam lateral position. Concerning the cell, the whole cavity between the reflectors contains alkali vapor and its length can thus be freely extended. The circular polarization is preserved by the gratings which enable to integrate a QWP upstream at the wafer level since the incident beam remains under normal incidence. This solution provides both compactness and a simpler integration of the laser and the detector which can be placed side by side on top of the cell (Fig. 3.24).
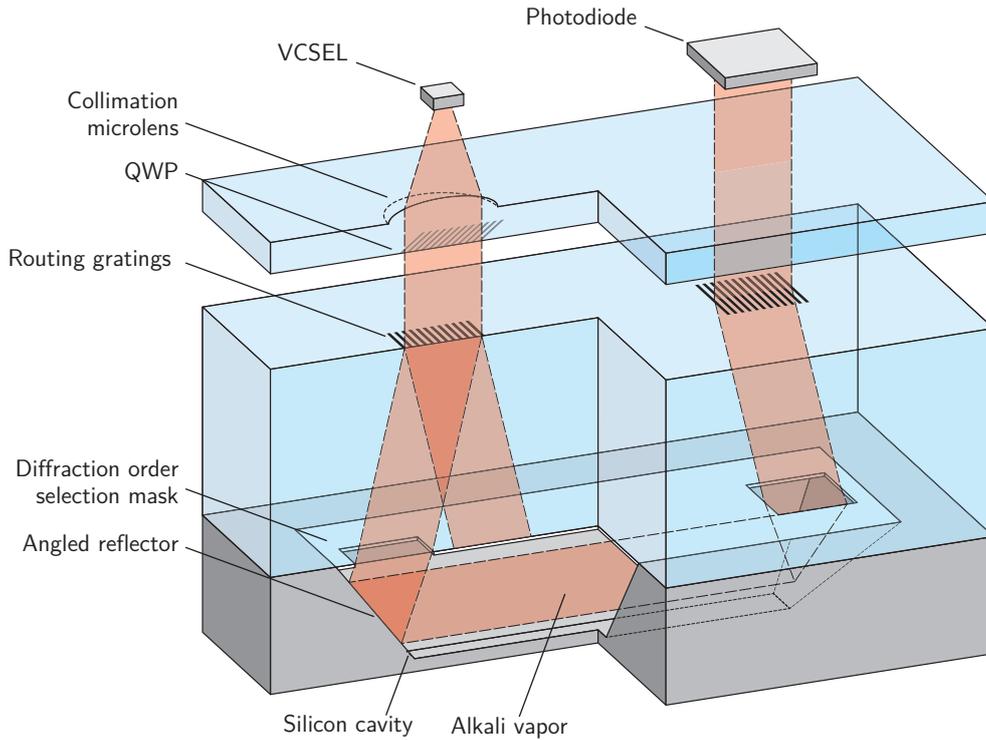
Figure 3.24: Architecture based on a reflective cell.

3.3.3   Gratings design and fabrication

The optical function of the diffraction gratings is to diffract most of the energy in the first diffraction orders. Their diffraction angle is fixed by the 54.74° orientation of the silicon planes used as reflectors. To ensure a beam propagation along the wafer, the incident angle on the reflectors should thus be 35.26°, which corresponds to an angle of 19.48° at the glass window exit (Fig. 3.25). The angle α of the beam within the glass window is deduced from Snell law. In our case, the cell is sealed with a borosilicate glass whose refractive index is $n = 1.4645$ at $\lambda = 894.6\,\text{nm}$. The angle α is then equal to 13.16°. The angles between the normal of the gratings and the propagation direction of the different diffraction orders obeys the grating equation. For the first diffraction order to be diffracted at $\alpha = 13.16°$, the period of the grating should be $d = \lambda/n \sin\alpha = 2683\,\text{nm}$. As electron beam lithography is used, the gratings period is controlled within a few nanometers.

Different types of gratings could perform this function. Blazed gratings appear as a suitable option as they diffract most of the energy into one diffraction order. However, for high diffraction angles, the efficiency drops down to ca. 65 % due to shadowing effects (Lalanne *et al.*, 1999). Furthermore, the energy is dissipated in various orders, especially the second and third ones. In order to increase this efficiency at higher angles, binary blazed gratings with sub-wavelength features are good candidates (Lalanne *et al.*, 1998). Nevertheless, they are characterized by high aspect ratios and are consequently challenging to fabricate. Geometries slightly easier to fabricate could be considered (Elfström *et al.*, 2006) but they also show sizable difference in efficiencies depending on the incident polarization orientation and might not be appropriate for the conservation of a circular polarization state. Indeed, the grating should also conserve the beam circular polarization state, as required for the CPT spectroscopy. For this purpose, polarization diffraction gratings (Gori, 1999) are very attractive, especially because they can break the efficiency of the scalar-domain limit and reach very high efficiencies (Tervo and Turunen, 2000). In here, theoretical 100 % diffraction efficiency of the first order where the incident circular polarization is conserved is achieved. Since the first demonstration based on liquid crystals by Davis *et al.* (2001), polarization gratings made for infrared light (Hasman *et al.*, 2002) and visible light were fabricated (Vartiainen *et al.*, 2010). Conservation of circular polarization was also shown recently based on twisted nematic liquid crystals (Honma and Nose, 2012). Unfortunately, despite this quasi-perfect behavior, polarization gratings require paraxial domain, which is no longer the case if the angle of diffraction is high. Indeed, enough sub-wavelength periods are required within each full-rotation period and, consequently, the latter cannot be as small as a few microns.

Lamellar gratings with binary corrugation were finally considered as they are easier to fabricate. First,
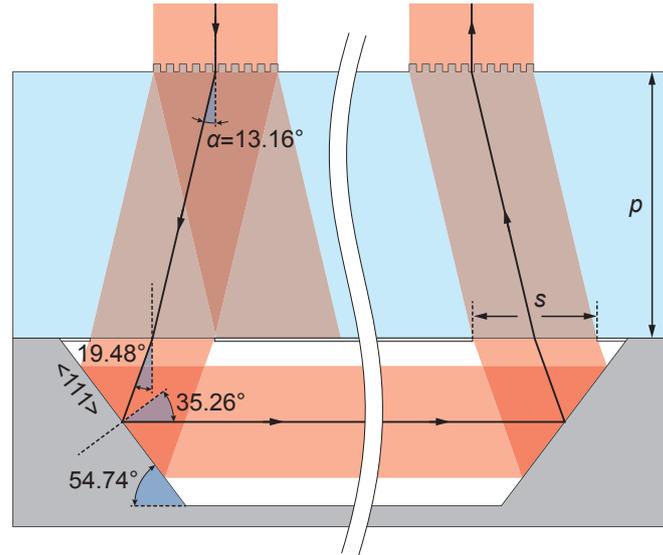
Figure 3.25: Routing of the beam in the cell.

the parameters maximizing the energy in the first order while minimizing it in the zeroth order had to be determined. Such type of gratings have been used e.g. as a phase mask to print periodic structures with characteristic dimensions of several tens of nanometers based on the interferences between the two $\pm 1^{st}$ transmitted orders (Bourgin *et al.*, 2010). In addition to the zeroth order cancellation, the incident circular polarization state should be preserved. All these conditions make it necessary to find the pair height (h) and fill factor (f) (corresponding respectively to the corrugation depth and the duty cycle) achieving the following characteristics: a canceled zeroth order considering incident polarizations both parallel (transverse-electric TE) and perpendicular (transverse magnetic TM) to the grating vector, a maximized first order while keeping both TE and TM-efficiencies equal and a minimized phase shift between the transmitted components in the first order. It can be noted that such a rather high period-to-wavelength ratio, imposed by the restricted angle of diffraction, implies that higher orders than the first one exist in the substrate (until $\pm 4^{th}$) although their amplitudes are kept low.

The gratings are made of Si_3N_4 stripes ($n = 2.0064$ at $\lambda = 894.6$ nm) on top of a borosilicate substrate in order to reduce the aspect ratio of the structure to be fabricated. The rigorous Fourier modal method is employed to compute the optimal parameters (Turunen, 1997). Figure 3.26a–c shows the efficiencies of the 3 first orders (0th, 1st and 2nd, respectively). Note that we consider on the plot the average values between the two polarization components. In addition, the ellipticity of the beam diffracted into the first order is shown in Fig. 3.26d. The ellipticity is simply defined as the ratio between the maximum and the minimum of the intensity that would be recorded after a rotating polarizer located on the optical path of the 1st order, i.e. as the ratio between the major and minor axis of an elliptical polarization. Therefore, a circular polarization corresponds to an ellipticity equal to unity.

As we can see from Figure 3.26, there are no ideal parameters. Indeed, the best extinction of the zeroth and second orders and the maximum of the 1st order along with the minimum of ellipticity do not match perfectly. Fortunately, a suitable trade-off is found for $f = 0.47$ and $h = 466$ nm for which the ellipticity is only 1.04, and the transmission efficiencies are 0.54 %, 38.05 % and 2.40 % for the 0th, and each of the 1st and 2nd orders, respectively. The slight ellipticity is mostly attributed to the difference between the transmission coefficients, although only equal to 0.7 %, rather than to the phase shift that is close to zero. Tolerances in the range of ± 20 nm on the height and ± 0.02 on the fill factor values (i.e. ± 53 nm on the linewidth) ensure an ellipticity better than 1.1 and a transmission over 36 % in each of the first orders.

Hence, in order to discriminate the two efficient first orders, a mask, whose apertures match the grating size, is added on the bottom side of the lid. Depending on the grating lateral size s, a sufficient distance of propagation is required before the discrimination aperture ($p \geq s/(2 \tan \alpha)$). In this work, we use commercially available borosilicate wafers whose thicknesses are fixed. The gratings size s was chosen to be 600 µm and $p = 1.3$ mm. Note that the alignment performed at wafer level between the cavity (reflectors), the aperture and the grating ensures that light normally incident to the grating will be routed inside the cavity. The orientation
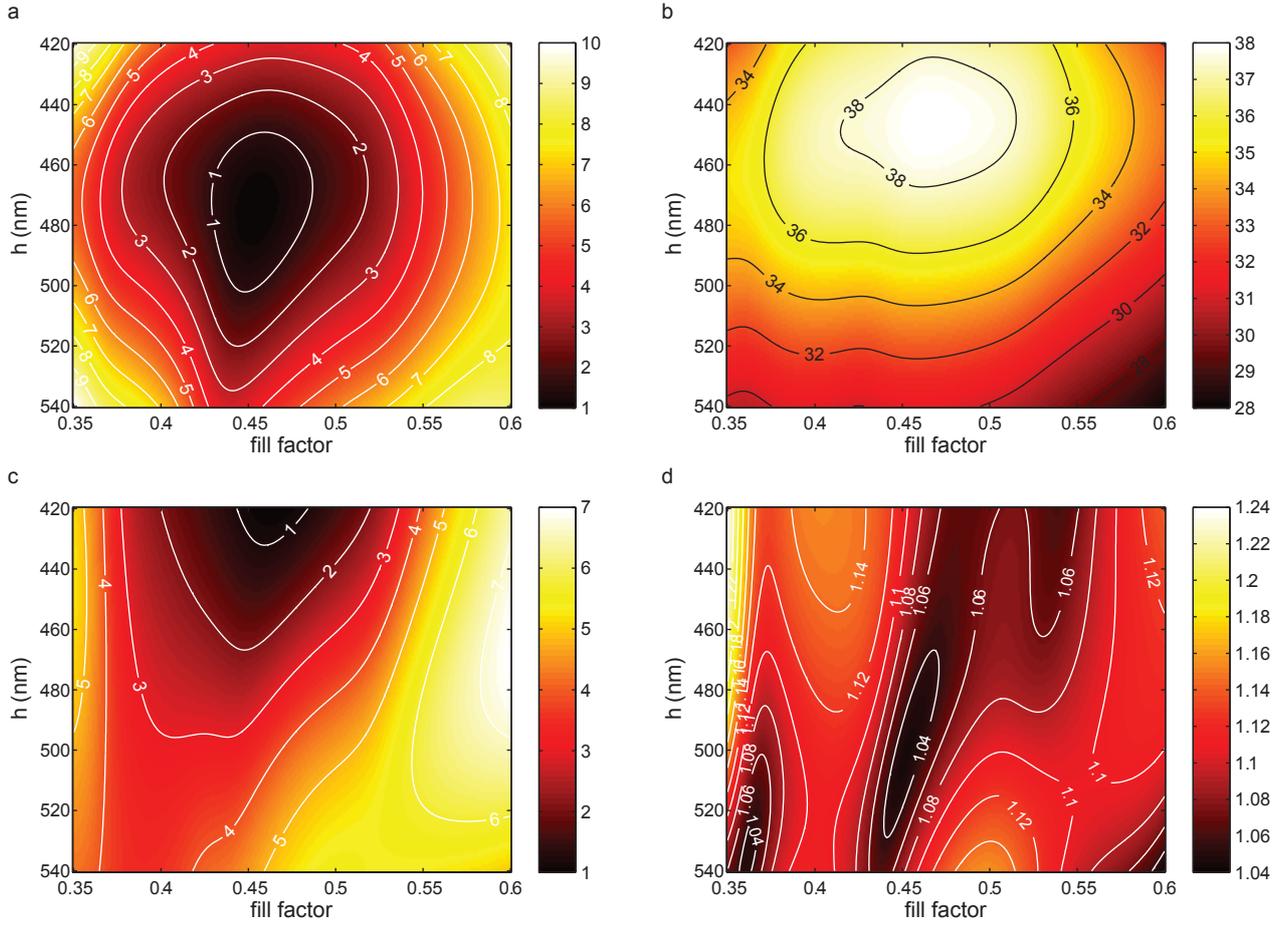
Figure 3.26: (a) Average of TE and TM efficiencies (%) in 0th transmitted order, (b) average of TE and TM efficiencies (%) in 1st transmitted order, (c) average of TE and TM efficiencies (%) in 2nd transmitted order. (d) Ellipticity of the beam diffracted into the 1st orders.

of the grating lines, perpendicular to the cavity axis, is also well controlled during fabrication.

A first set of gratings was actually designed and tested at 633 nm for optical characterization convenience. We employed electron beam lithography to fabricate 2 mm × 2 mm test structures. The latter behaved as expected and diffracted 37.7 % and 38.6 % in the two first orders oriented at 19.4(3)°. The ellipticity was measured to be 1.12 and 1.14, respectively. Note that the ellipticity of the incident beam was already 1.04. Meanwhile, the zeroth order was nearly suppressed (0.6 %) and the second orders efficiencies were reduced to 5.5 %. It has to be noted that the ellipticity in the zeroth and second orders was measured to be over 20 and 7, respectively, showing that the circular polarization conservation is only achieved in the 1st order. Once the process optimized, the parameters were transposed to 894.6 nm which is resonant with the D_1 line of cesium atoms.

3.3.4   Cell fabrication

The first step of the cell fabrication consists in patterning the silicon cavity, while ensuring that the obtained sidewalls are mirror-like. Generating flat, large and optically smooth surfaces by etching is not straightforward and it has been the subject of previous studies (Chutani *et al.*, 2013). A Cr/Au etch mask is patterned on a 100 mm silicon wafer with a 1.5 mm thickness and a (100) orientation. It is then immersed in a KOH solution at a concentration of 40 % and heated at 70 °C for several hours to obtain a 650 μm deep cavity (0.5 μm min^{-1}). This wet-etched cavity is referred to as the optical cavity. Next to the optical cavity, a second cavity is then etched using DRIE. This cavity aims at holding the cesium dispenser from which pure cesium vapor is released later on in the process. Channels connecting both cavities are patterned by DRIE along with the dispenser cavity. As a bare silicon surface absorbs around 68 % of the incident light at the considered wavelength, a coating should be deposited on the angled sidewalls to reach a high reflectivity and avoid deterioration of the
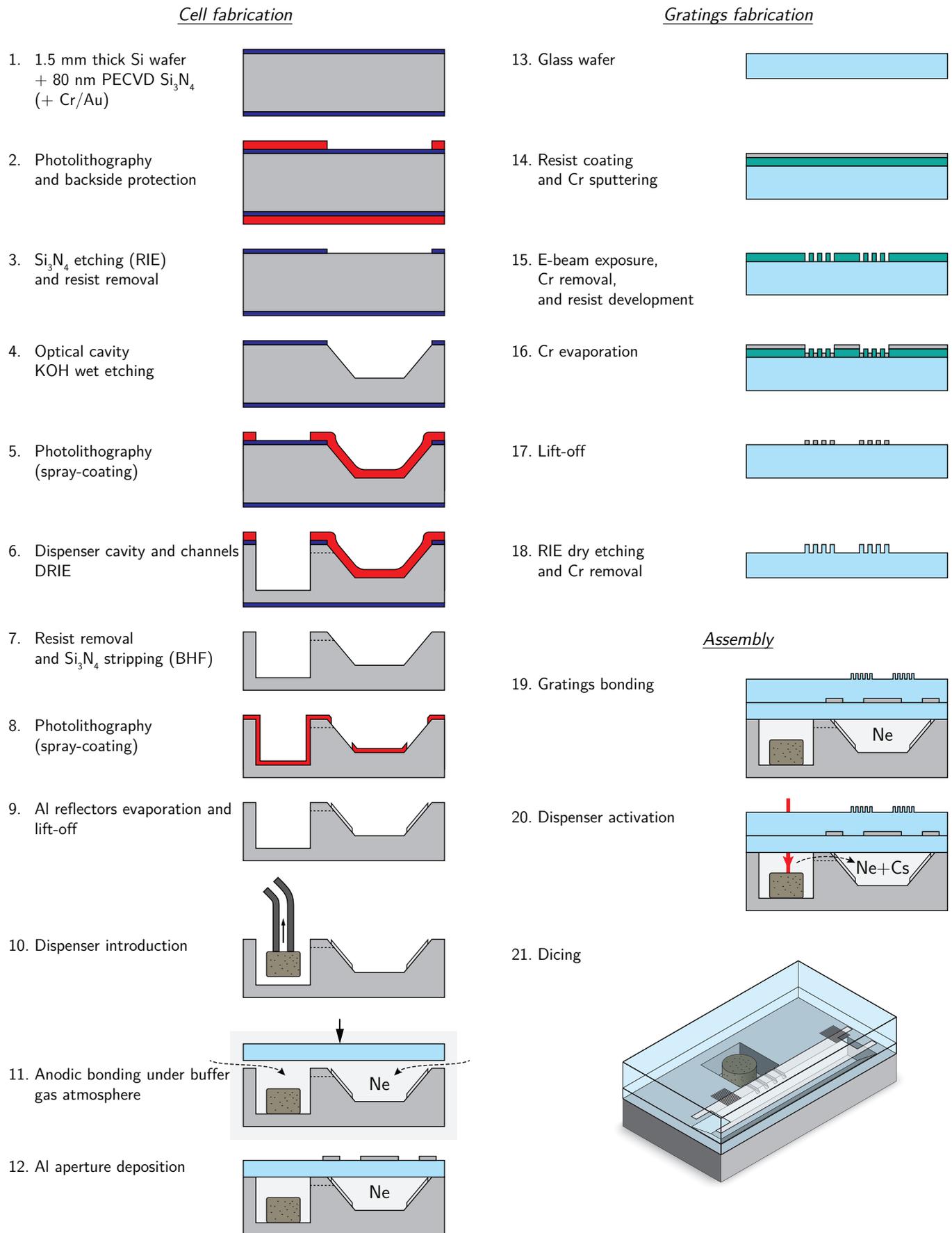
Cell fabrication

1. 1.5 mm thick Si wafer
   + 80 nm PECVD Si_3N_4
   (+ Cr/Au)

2. Photolithography
   and backside protection

3. Si_3N_4 etching (RIE)
   and resist removal

4. Optical cavity
   KOH wet etching

5. Photolithography
   (spray-coating)

6. Dispenser cavity and channels
   DRIE

7. Resist removal
   and Si_3N_4 stripping (BHF)

8. Photolithography
   (spray-coating)

9. Al reflectors evaporation and
   lift-off

10. Dispenser introduction

11. Anodic bonding under buffer
    gas atmosphere

12. Al aperture deposition

Gratings fabrication

13. Glass wafer

14. Resist coating
    and Cr sputtering

15. E-beam exposure,
    Cr removal,
    and resist development

16. Cr evaporation

17. Lift-off

18. RIE dry etching
    and Cr removal

Assembly

19. Gratings bonding

20. Dispenser activation

21. Dicing

Figure 3.27: Fabrication process of reflective cells.

polarization state due to dichroism (the ellipticity after one reflection under such incidence would be equal to 1.6). A solution based on silicon reflectors was also sought by Kitching *et al.* (2011a) to achieve a crossed beam configuration for an atomic magnetometer. A multilayer dielectric coating deposited on the silicon sidewalls to efficiently reflect circularly polarized beams was implemented by Perez *et al.* (2009). Indeed, dielectric mirrors are preferable over metallic mirrors since they do not affect the magnetic field and do not react with alkali metals. Although slightly less efficient, the reflectors of the cells presented here were coated with aluminum (the efficiency is reduced to 89 % instead of 98 % with dielectric multilayers and the ellipticity of the circular polarization is degraded to 1.2 after the first reflection). After inserting a dispenser in the second cavity, the cell was sealed with a borosilicate glass lid using anodic bonding. So as to operate in the Dicke regime, a buffer gas (neon) was introduced in the chamber during the bonding, following a procedure previously described.

After the bonding, the dispenser was locally heated with a high power laser diode focused through the glass window, which releases cesium vapor in the cell.

The gratings were patterned on a separate glass wafer. Two different processes were developed. The first approach consists in depositing a 470 nm thick Si_3N_4 layer using plasma-enhanced chemical vapor deposition (PECVD). A layer of resist is patterned using electron-beam lithography. The pattern is then etched with RIE defining stripes in the silicon nitride layer. In the alternative approach, the gratings are directly etched in a glass wafer. A chromium etching mask is evaporated after the lithography. A lift-off is performed, removing the resist. The remaining metal stripes are then used as a mask to etch directly 1 µm deep stripes in the glass wafer with RIE (Fig. 3.28a). The metallic aperture which selects the first diffraction order was deposited on top of the lid after the anodic bonding, although it could be integrated on the inner surface of the cell if accurate alignment can be performed during anodic bonding. The grating wafer is finally aligned and bonded to the cell wafer with UV-curable paste. The complete fabrication process flow chart is shown on Fig. 3.27. A picture of a cell after dicing is shown on Fig. 3.28b. The 1.3 mm propagation distance needed to screen the other diffraction orders is obtained using a thickness of 1.3 mm for the gratings wafer. The characterization of the cells is described in Section 4.2.2.
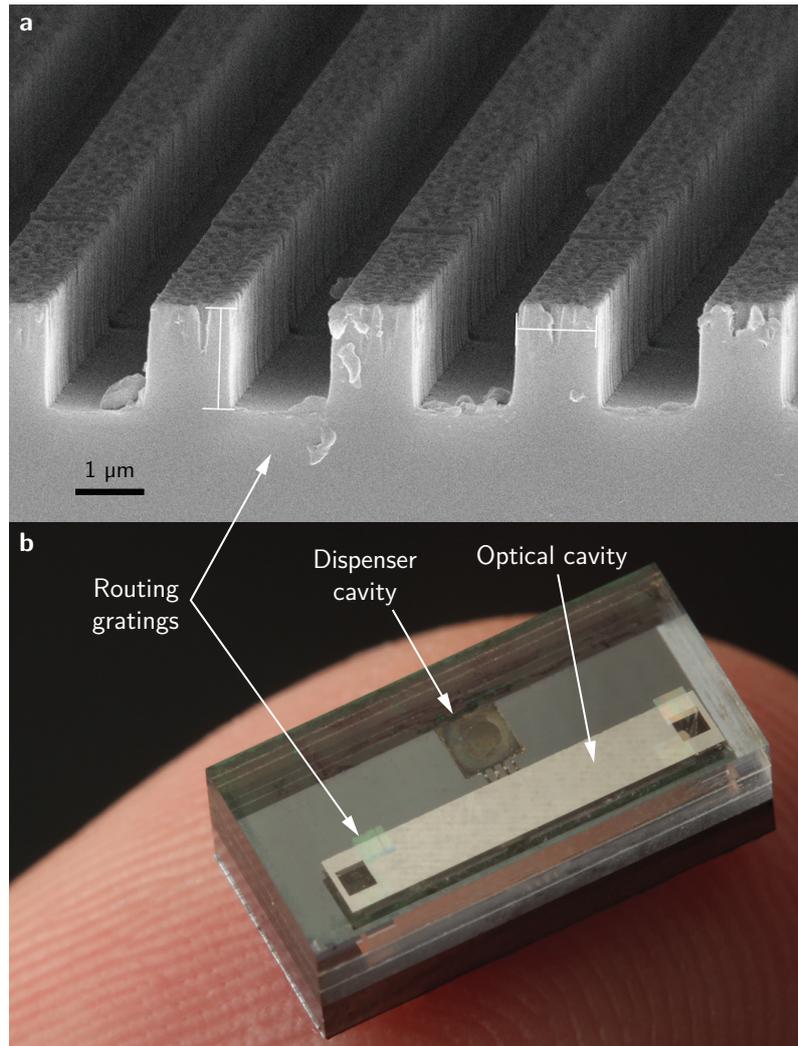
Figure 3.28: Picture of a reflective cell and SEM image of the integrated gratings.

3.4   Getters

Getter materials are used to absorb impurities in vacuum-sealed enclosures. Their absorption results from chemical reactions, therefore all noble gases present in the atmosphere are left unaffected.

Getters were used in wall-coated glass-blown cells by Bouchiat (1964) to ensure that the measured properties resulted solely from the action of the coating and not from a residual buffer gas. On the other hand, the use of getters in glass blown cells filled with buffer gas is unusual. Most atmospheres include nitrogen, which would be absorbed by the getter. Whereas great care is usually taken to provide excellent atmosphere quality in glass blown cells (baking until a pressure of 1×10^{-7} mbar is reached), the anodic process employed for miniature cells is known to release substantial amounts of residual gases (Mack *et al.*, 1997), in particular oxygen compounds. Therefore, we may wonder if those pollutants, whose partial pressure can easily reach 1×10^{-2} mbar, could affect the cell performances.

Knappe *et al.* (2007) reported using getters in evacuated microfabricated cells used for saturated absorption spectroscopy, but neither the nature of the getters nor their effect were mentioned.

During MAC-TFC, non-evaporable getters (NEGs) have been integrated at the wafer level in order to improve the quality of the inner atmosphere. Because the atmosphere is only composed of neon, the getter should not affect the neon partial pressure. The PageWafer solution from SAES Getters was used. It is based on a Zr-Al alloy. Getters proved to be successful in reducing the residual pressure after anodic bonding (Hasegawa *et al.*, 2013). A 50-fold improvement of the purity was observed (99.95 % for cells with getters against 98 % without getters). The purity was measured by residual gas analysis (RGA). It consists in breaking cells in an evacuated vacuum chamber and flowing the chamber content toward a quadrupole mass spectrometer (QMP). This analysis was performed by SAES Getters. Only cells without dispensers had been analyzed since cesium vapor could damage the QMP.

Frequency drifts of a few tens of hertz after 240 h at 110 °C were measured, but the measurement was limited by the resolution of the setup at the time. Getter free cells already showed good stability over a period of 500 h (3 weeks) at 125 °C with a clock frequency shift less than 3 Hz (Hasegawa *et al.*, 2011b). The benefit of getters regarding the long-term frequency aging remains therefore inconclusive.

However, dispensers contain a getter material, which is also supposed to improve the buffer gas purity (it is actually the reason why we can not use nitrogen in cells with dispensers). Cesium itself also plays the role of getter as it is very reactive. In order to compare the effect of dispensers and getters and conclude about its benefits, a new wafer has been fabricated combining cells with getters and cells without getters (Fig. 3.29), following a process similar to the one reported by Hasegawa *et al.* (2013) but with the anodic bonding equipment from AML where the large separation between the wafers during pumping should, in principle, help outgassing. Additionally, thanks to the in situ alignment, the getter lid could be integrated directly at the sealing stage. Cells with all possible configurations were obtained on a small portion of the wafer: (getter and dispenser), (getter but no dispenser), (no getter and dispenser) and (no getter and no dispenser). Dispensers were not laser activated.

Results of RGA performed on 4 cells are shown in Table 3.6. Even tough the number of tested cells is small, we can attempt to draw conclusions. Despite the absence of getter and dispenser in cell EN, a purity of 99.84 % is found, which is rather good compared to what was measured before (typically 98.75 %). The recent replacement of polyurethane tubing by stainless steel on the anodic bonding equipment, and better outgassing may explain this improvement. However, the effect of nearby getters on the wafer can not be excluded. Cell with a single getter (EO) exhibits a purity of 99.98 %, which is consistent with previous results (typically 99.97 %). Consequently, getters are rather effective in purifying the atmosphere within anodically bonded cells. However, results from cells with dispensers cast doubt on the benefit of an additional getter: EL cell with a dispenser only and EM with both a dispenser and a getter have similar purity (99.91 % and 99.93 %, respectively). A dispenser or a getter both seem to absorb significantly CO_2, O_2 and CO, which are the main contaminants released by anodic bonding. However, dispensers seem to introduce an additional CH_4 pollution not absorbed by the getter.

The early and long-term frequency aging behavior of those cells should be measured with better resolution soon.
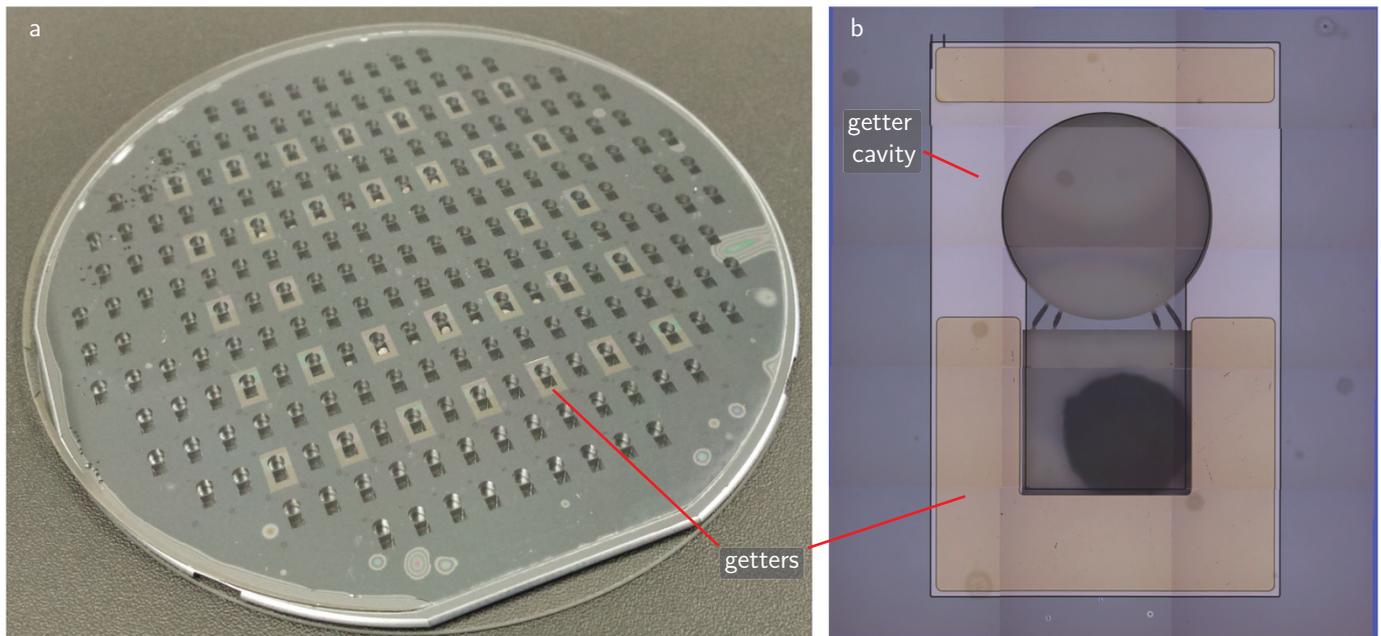
Figure 3.29: Wafer of cells with getters and microscope image of a cell integrating a getter.

Gas	EN no dispenser, no getter		EL dispenser, no getter		EO no dispenser, getter		EM dispenser, getter	
	Pressure (mbar)	Ratio (%)	Pressure (mbar)	Ratio (%)	Pressure (mbar)	Ratio (%)	Pressure (mbar)	Ratio (%)
H_2	-	-	-	-	-	-	-	-
He	1.6×10^{-3}	< 0.01	1.5×10^{-3}	< 0.01	2.9×10^{-3}	< 0.01	2.1×10^{-3}	< 0.01
CO	4.3×10^{-2}	0.06	4.2×10^{-3}	0.01	-	-	-	-
N_2	-	-	-	-	-	-	-	-
CH_4	6.6×10^{-3}	0.01	4.7×10^{-2}	0.07	1.2×10^{-2}	0.01	4.1×10^{-2}	0.06
H_2O	-	-	-	-	-	-	-	-
Ne	7.8×10^1	99.84	6.9×10^1	99.91	8.6×10^1	99.98	7.0×10^1	99.93
O_2	4.1×10^{-2}	0.05	-	-	-	-	-	-
HCs[*]	1.0×10^{-2}	0.01	8.1×10^{-3}	0.01	6.5×10^{-3}	0.01	8.8×10^{-3}	0.01
Ar	-	-	2.3×10^{-4}	< 0.01	-	-	1.2×10^{-4}	< 0.01
CO_2	2.0×10^{-2}	0.03	-	-	-	-	-	-
Total	7.8×10^1	100	6.9×10^1	100	8.6×10^1	100	7.0×10^1	100

[*] HCs = hydrocarbons.

Table 3.6: RGA results from 4 cells with different getter and dispenser configurations.
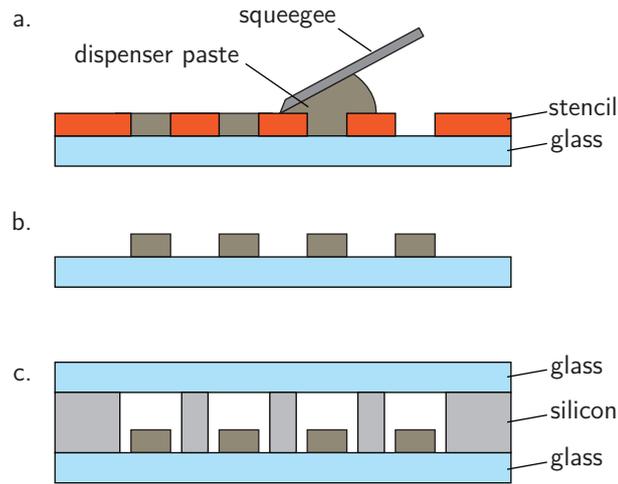
Figure 3.30: Deposition of getters by the stencil printing process.

3.5   Paste dispenser

As we have seen earlier, there are high incentives to overcome the drawbacks of dispenser pills. In the course of the MAC-TFC project, a dispenser taking the form of a paste was developed by Mauri *et al.* (2015) at SAES Getters. This paste can be deposited using conventional liquid dispensing techniques such as screen or stencil printing, spray coating, micro-drop dispensing or inkjet printing, which are much more suitable for large-scale wafer-level production than pick and place. Figure 3.30 illustrates a stencil printing process, which could be envisioned to deposit dispensers (not yet tested).

This organic-inorganic mixture contains a cesium compound (Cs_2MoO_4), a stabilizer, a reducing agent $(Zr-Al$ getter powder) and an amino-functional alkoxysilane binder (N-(3-(trimethoxysilyl)propyl)ethylene-diamine). Once deposited and dried at room temperature, the paste can be consolidated through a heat treatment (typically at $200\,°C$ for $1\,h$). Like dispenser pills, a high-power laser can be used to reach the temperature at which alkali vapor is released. In 2011, several batches of cells were fabricated with this paste at Wrocław University of Technology. After activation, cesium condensation could be seen and a proper absorption spectrum was measured. However, after a few months, the atomic density had vanished without adequate explanation. We have undertaken new experiments to pursue this study at FEMTO-ST.

A new paste sample was supplied by SAES Getters[20]. A first wafer was prepared and the paste was deposited manually in the dispenser cavity of the preform by contact transfer with a thin capillary. After a short baking step, the cells were sealed using the usual anodic bonding process. More than a hundred cells were filled in a single run. In order to evaluate the minimal quantity required, different amounts of paste were introduced among the cells. The quantity in each cell can roughly be estimated from a microscope observation on Fig. 3.31.

Among these cells, six have been activated with the same parameters in a single step and have been monitored through linear absorption spectroscopy since November 2015 on the bench described earlier. The cell holder is kept at $80\,°C$ and an absorption spectrum is recorded every $15\,min$. The absorption contrast evolution over 4 months in those 6 cells, with an additional reference cell from a previous batch (with buffer gas), is shown on Fig. 3.32. A saturated and rather stable atomic vapor is found in 5 of the 6 cells. Interestingly, the faulty cell contained a much larger quantity of paste and was not islanded on the glass like the other five. Instead, the whole cavity was filled and the paste was in contact with silicon all around the cavity. This cell could be activated once again with higher intensity. Variations among the cells are attributed to temperature gradient across the cell holder. Indeed, we noticed that the contrast is lower as the cell is farther from the center. The steep increase at $2500\,h$ is due to a replacement of the distributed Bragg reflector (DBR) laser, which was not convenient to use because of mode-hopping and the absence of integrated Peltier module. A DFB laser was used instead but the optical power may have been diminished meanwhile, affecting the contrast measurement. The bench was disturbed by the installation of a CO_2 laser, which required the box to be opened and produced the fluctuations around $2800\,h$. Those measurements are still ongoing and, after 4200 hours around $80\,°C$, the cells have not yet shown any failure or significant density diminution unlike what MAC-TFC's experiments

---

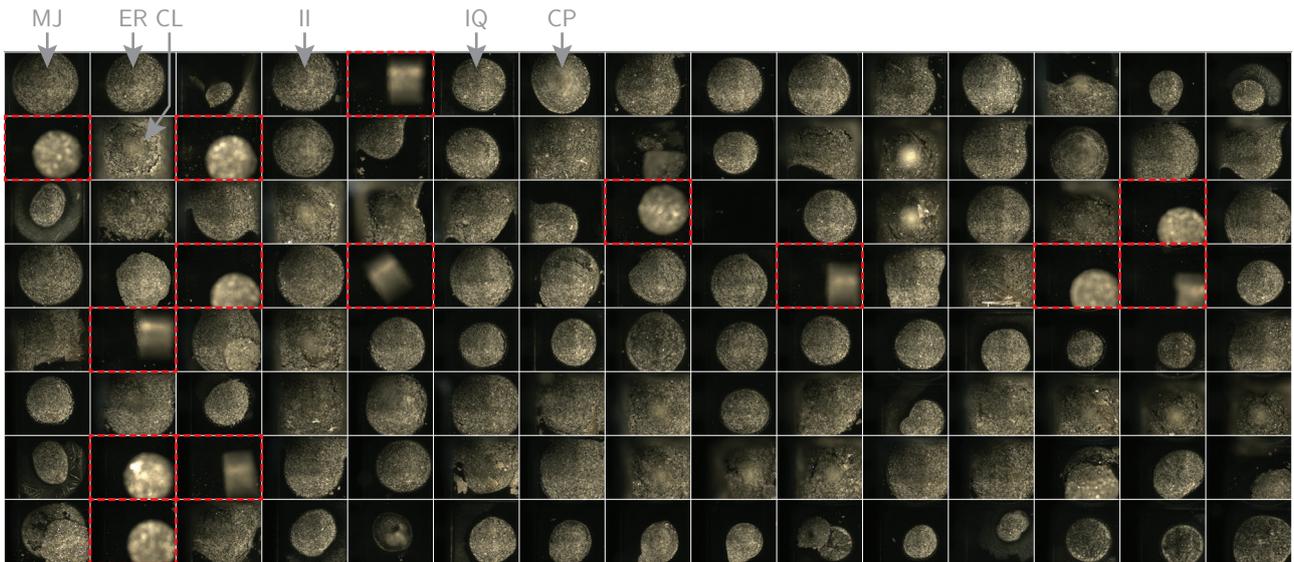[20]probably with a composition slightly different than before

Figure 3.31: Observation of paste dispensers after bonding. More than 100 cells contain paste dispensers and 14 have pill dispensers (circled in red).
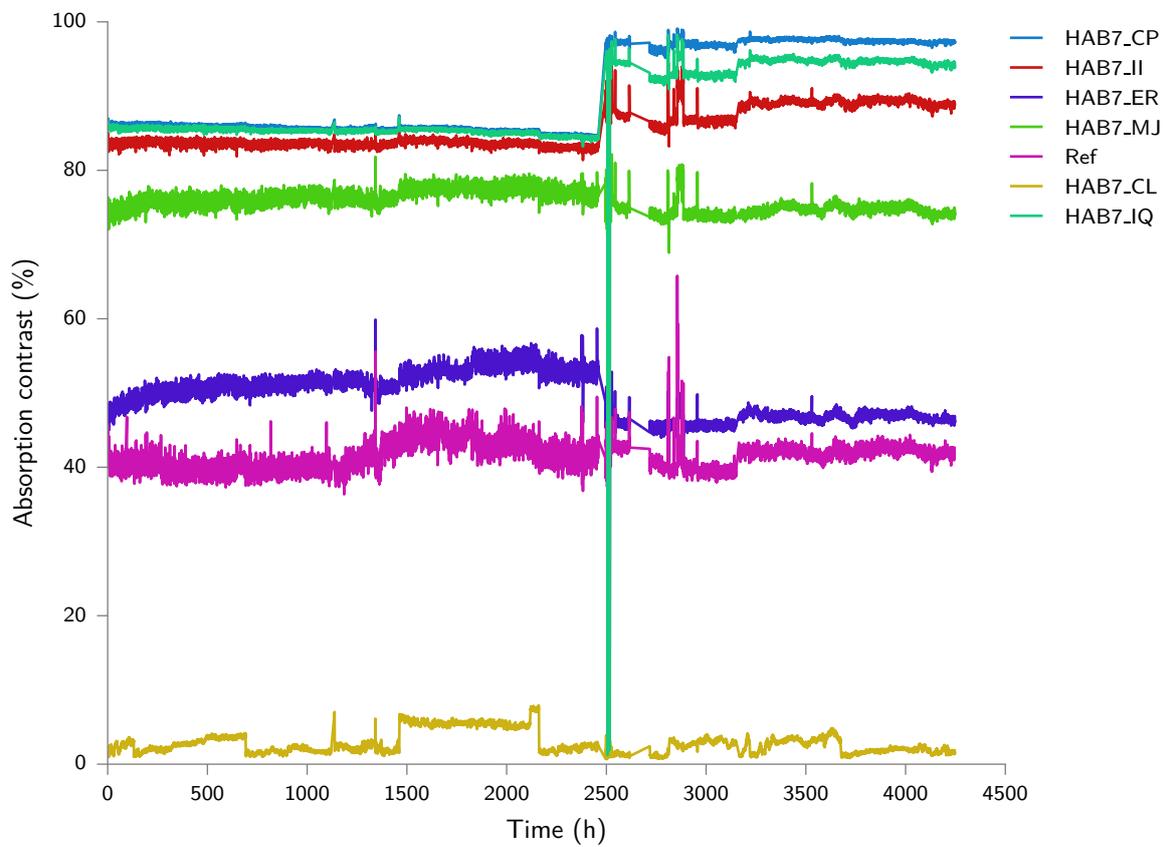

Figure 3.32: Evolution of the absorption contrast in cells with paste dispensers.

foreshadowed.

The remaining cells will soon be activated and monitored likewise. In addition, a second wafer will be fabricated, this time with a buffer gas so that frequency stability can be assessed with better resolution through CPT spectroscopy. Micro-drop dispensing or stencil printing will soon be tested.

Even though paste dispensers could dramatically reduce fabrication costs, they still impose some limitations in terms of footprint and potentially reacts with some buffer gases like nitrogen, which we explained in Section 3.2.9. An ideal cell would only contain a pure buffer gas and the minimal quantity of elemental alkali metal. Indeed, keeping the alkali metal source in the cell often disturbs the cell atmosphere. Solutions where pure alkali metal is directly introduced in the cells seem rather complicated to enforce since the bonding equipment and the dispensing setup should both be in an anaerobic atmosphere.

On the other hand, dispensers whether in the form of pills or paste, are rather convenient to handle and do not require particular care or sophisticated equipments. Dispensing and bonding can be done with independent equipments.

The method proposed in the following section, inspired from conventional glass-blown cell fabrication techniques, aims at allying those benefits.

3.6   Single use, zero leak, micro-valves

We proposed to produce microfabricated structures allowing to isolate or connect different cavities. Those structures are inspired from the methods typically used for filling centimeter-scale glass-blown cells. They can be combined to achieve various functions. One interesting way of using those structures could be to use a unique dispenser to fill several optical cavities. After cesium release and isolation of each cavities, they would form individual cells, detached from the common dispenser cavity. In addition, we can envision other use cases such as filling cells with different buffer gas ratios on a same wafer, evacuating cells at vacuum level below what is typically achieved by anodic bonding. This method also opens up the possibility of using different alkali metal sources, without the current restriction on the buffer gases, which bans the use of nitrogen, and provides a sealing process compliant with antirelaxation coatings.

3.6.1   Glass-blown cell filling methods

The fabrication and filling of glass-blown cells involves peculiar components made in glass and integrated to the glass manifold used to connect ("make-seal") or detach ("break-seal") different compartments of the glass vessel. Figure 3.33 shows a typical glass assembly used for filling cells including such components.

The first component called "make-seal" can hermetically close two compartments initially connected. It can be done by forming a bottleneck in a glass tube beforehand, which is heated by a flame. When the temperature is high enough for glass to be malleable, the bottleneck shrinks and eventually closes the channel under the action of surface tensions and the pressure difference between the inside and the outside. Cells are typically separated from the glass manifold by this technique, without any contact with the ambient atmosphere and preserving the vacuum established in the manifold (up to 1×10^{-9} mbar). This process is illustrated in Fig. 3.34.

Conversely, a component called "break-seal" is used to connect two initially separated compartments. It consists in a thin membrane sealing hermetically two parts of the manifold. In order to open the channel, this membrane is broken by hitting it with a magnetic ball, which has been previously inserted in one of the compartments (the magnetic ball is moved from outside with a magnet). This technique is often used to open the glass ampoule containing pure cesium after outgassing the manifold, which avoids exposing its content to the ambient aerobic atmosphere.

Those features can only be used once but they are hermetic with near zero leak rates compared to actuated valves. They can be used in series or in parallel to circumvent their single usability. Singh *et al.* (1972), Robinson (1986) show how those components are used in the making of glass blown cells.

3.6.2   Microfabricated make-seal

We propose to construct a make-seal structure similar in principle to the solution presented above, but adapted to microfabrication. It consists in deflecting and bonding a glass membrane against the outlet of a tubular channel. The general principle is shown in Fig. 3.35. In this case, the tubular channel is obtained by etching a cavity in a silicon substrate (Fig. 3.36a-c). Two glass substrates are bonded on each sides of the silicon wafer by
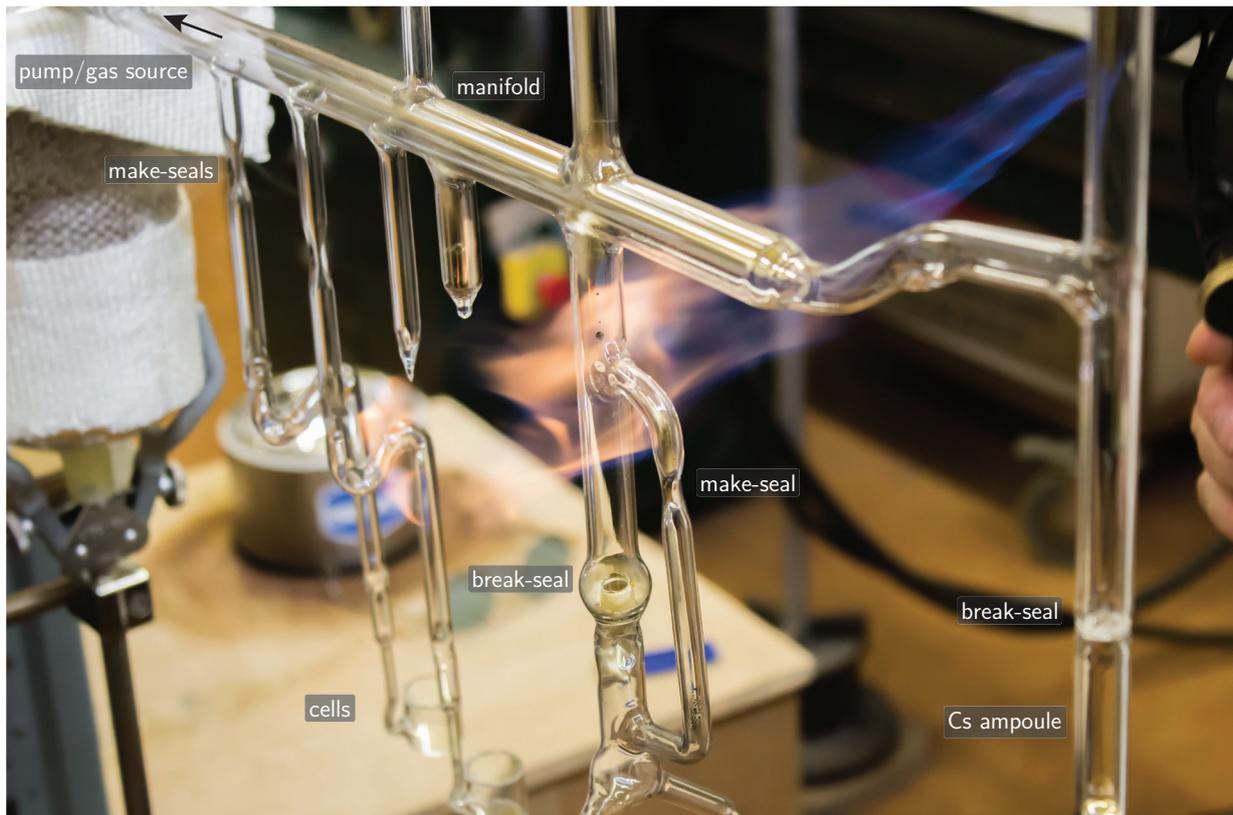
Figure 3.33: Picture of the glass assembly used to fill the wall-coated cells described in Section 5.2.1, taken at the SYRTE laboratory. This impressive glasswork was done by Pierre Bonnay and the overall process developed by Stéphane Guérandel (Observatoire de Paris).
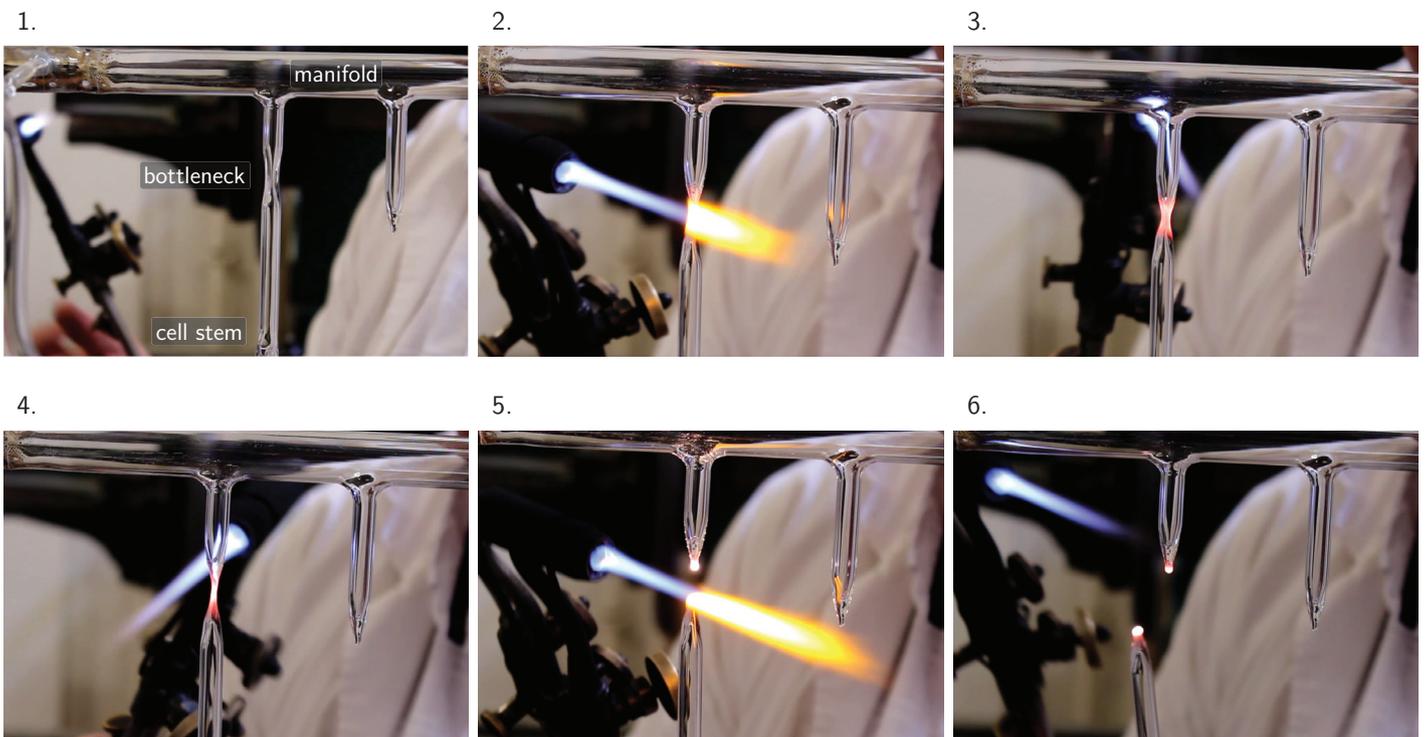

Figure 3.34: A glass cell being sealed off from a glass manifold. Images extracted from a video filmed at the SYRTE laboratory. Glasswork done by Pierre Bonnay.

anodic bonding and a heating resistor (or other heating means) can possibly be deposited in the outer surface of the glass membrane (Fig. 3.36d). To seal the channel, the membrane is heated at a temperature at which glass starts melting. The pressure difference between each side of the membrane drives its deformation inward until it touches the channel outlet. The annular contact area can eventually form an hermetical bond (Fig. 3.36f). In presence of alkali metal, heating the whole cell to deflect the membrane should be avoided since hot glass absorbs alkali metals (Woetzel *et al.*, 2013). Besides, the cell optical windows would also be deformed. Hence, only the membrane should be heated. Different solutions can be used to heat locally the membrane including:

- flowing a current through resistive traces patterned on the membrane,

- irradiating the top of the surface with a high power laser at a wavelength directly absorbed by glass such as a CO_2 laser ($\lambda = 10.6\,\mu m$),

- using a laser at a wavelength not absorbed by glass and patterning an additional layer absorbing this wavelength on the membrane.

If needed, the deflection of the membrane can be facilitated by:

- increasing the pressure difference by placing the whole wafer in a pressurized chamber in order to apply a larger force on the membrane,

- making the membrane thinner, either by grinding and polishing the glass substrate in which the membrane is patterned, or by etching locally the portion of the wafer defining the membrane. After sealing, if the thin membrane is excessively permeable to buffer or ambient gases, a thick metal layer could be deposited to prevent permeation through the membrane and protect it mechanically from subsequent processes like dicing (Bartek *et al.*, 1997). However, cells with wall thicknesses as low as $7\,\mu m$ have been demonstrated by Eklund and Shkel (2007) in wafer-level glass-blown cells, which suggests that even very thin membranes could be employed.

Alternatively, the tubular channel can be made of glass as shown in Fig. 3.37. A glass substrate is etched to form the channel cavities (Fig. 3.37a-c). A second substrate is bonded on top of it by fusion bonding thereby closing the cavities and forming a channel (Fig. 3.37d).

This wafer can then be polished so that the membrane is sufficiently thin (Fig. 3.37e), but wafers with the required thickness may also be commercially available. For instance, Eklund and Shkel (2007) used $100\,\mu m$ thick Pyrex 7740 wafers. If needed, a heating apparatus can be deposited on it (Fig. 3.37f). This stack can then be assembled to a preform by anodic bonding (Fig. 3.37g). The channel is sealed with the same techniques (Fig. 3.37h-i).

In this case, the two surfaces in contact are made of glass and can fuse together, which is likely to provide better hermeticity. In addition, the different CTEs of silicon and glass may induce stress and eventually break the membrane as it quickly cools down after bonding to silicon. Here, the membrane and the channel outlet are made of the same material, therefore this solution does not suffer from this problem.

Literature survey. Two recent patent applications have already proposed to achieve this technical function in microfabricated cells.

In the first one, a channel separating two cavities includes a solid piece of Au-St alloy placed so that the channel is not initially obstructed (Harasaka *et al.*, 2014). Alkali metal can then be generated in one cavity, for instance from a dispenser, and diffuse to the second. In order to seal the channel, the cell is heated at $280\,°C$. When melting, the alloy tends to spread over the complete cross-section of the channel by capillary action, hermetically sealing it. The wetting ability of the channel inner surfaces by the alloy is improved by coating them with a gold layer beforehand. In this process, the bonding of silicon and glass substrates is done by thermocompression at $200\,°C$ with an interleave layer of gold particles. Indeed, the anodic bonding typically requires a temperature over $280\,°C$. This solution aims at preventing changes in the buffer gases pressure due to their absorption by the dispenser. Filling multiple cavities from a single dispenser is also claimed. However, we are quite skeptical about it since gold is known to absorb cesium to form an Au-Cs alloy (Hirashima and Asano, 1966). If this solution may be used with rubidium, it might not be suitable for cesium.

Likewise, Sato *et al.* (2013) proposed to place glass frit in the channel. Glass frit is reflowed by a heat treatment ($20\,min$ at $470\,°C$ and $300\,kPa$), which seals the channel. The purpose is to avoid interactions of the alkali metal source with cell atmosphere and therefore improve the frequency stability. However, it is unlikely that pure cesium would actually withstand this temperature without reacting with glass.
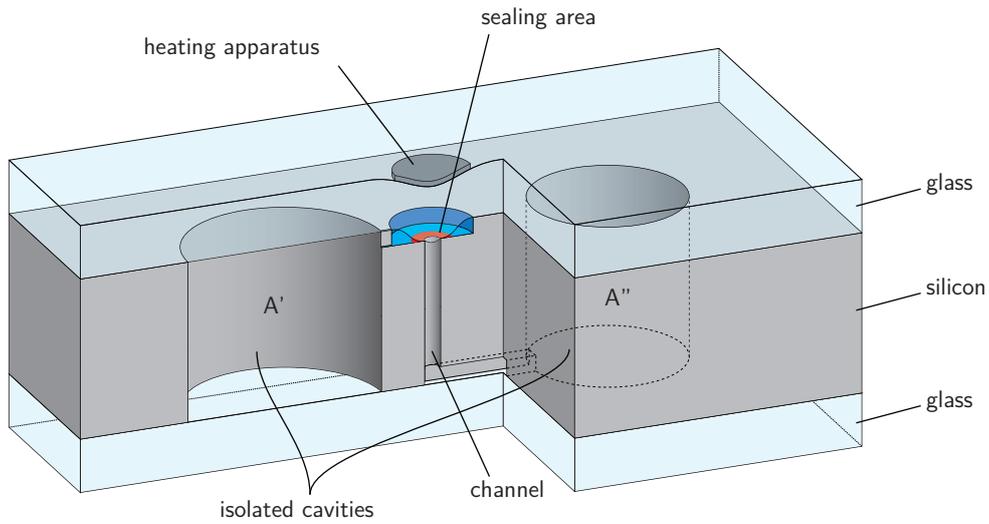
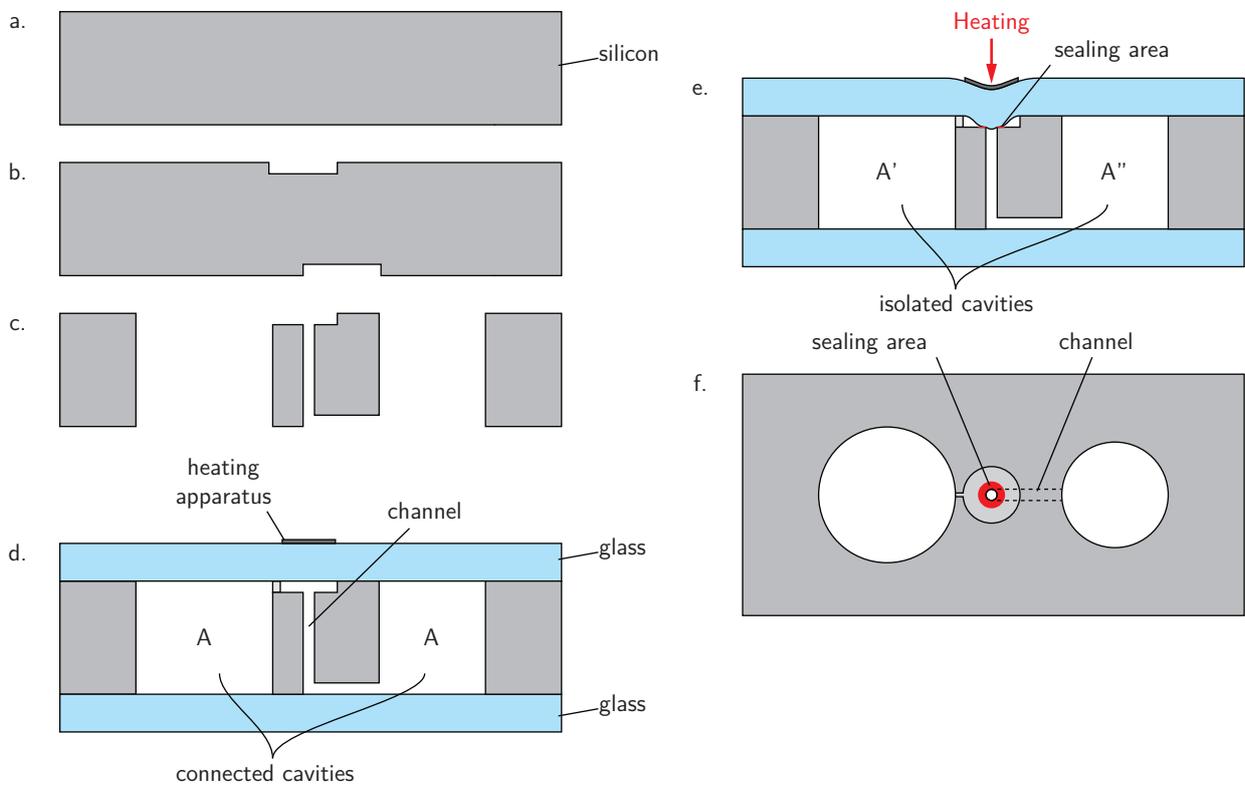Figure 3.35: Make-seal structure example in silicon and glass.

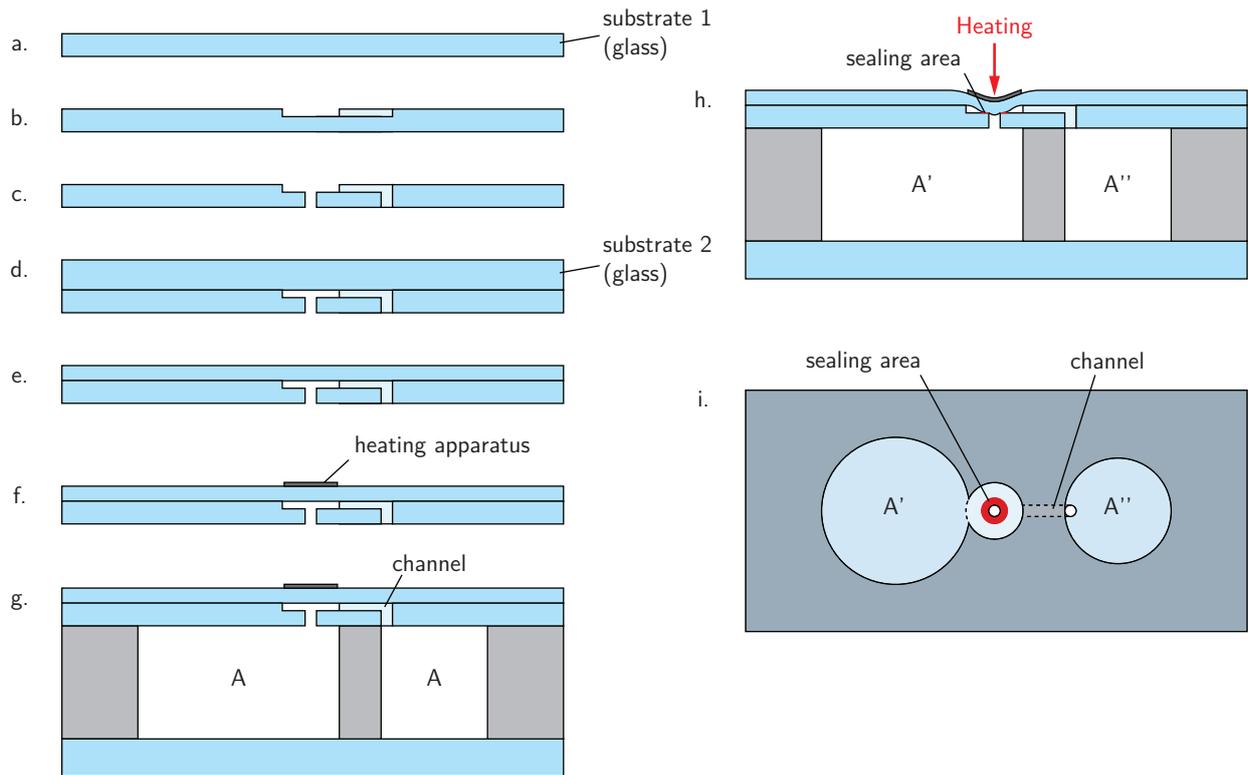Figure 3.36: Fabrication of a generic make-seal structure.

Figure 3.37: Fabrication of a generic glass-based make-seal structure.

Sealing sacrificial microchannels by glass frit reflow has also been proposed by Tsujimoto *et al.* (2013a) but seems unsuited for wafer-level fabrication because it would also require to overheat the cells.

In the early developments of microfabricated vapor cells, hybrid approaches were used to fill millimeter-scale cells (Lutwak *et al.*, 2003). In particular, Knappe *et al.* (2003a,b) demonstrated a cesium cell made from a glass fiber melted at both ends by a CO_2 laser. A cell without filling tube could be made. Losev *et al.* (2015) also demonstrated an hybrid approach where a CO_2 laser is used to bond the cap of small all-glass cells. Lipp *et al.* (2008) proposed to seal a channel linking the inner cavity of a cell to the ambient atmosphere by heating a bead of glass placed in the channel with a CO_2 laser. Ishihara (2015) took this idea and developed it further for wall coated cells. A microfabricated glass structure has been proposed by Ishihara (2016) to facilitate fusion sealing at the wafer level. According to these works, CO_2 laser seems to be the best candidate to locally melt and bond the glass structure. This method was therefore investigated further and preliminary experiments are reported below (Section 3.6.6).

3.6.3   Microfabricated break-seal

A break-seal structure can be done by forming a membrane isolating two cavities patterned in a silicon substrate. The fabrication process of a possible break-seal structure is shown in Fig. 3.38. The cavities can be etched by DRIE or KOH wet etching (Fig. 3.38a-b). The first cavity is not etched through and is sealed at the first anodic bonding step under an atmosphere A (Fig. 3.38c). The second cavity is etched-through and is sealed during the second anodic bonding under an atmosphere B (Fig. 3.38d). The membrane can then be broken to let the two atmospheres mix (Fig. 3.38e).

Different techniques can be envisioned to break locally the membrane. First, a high-power laser, preferably absorbed by the membrane material, can be used to heat the membrane and force it to break under the stress induced by its dilatation. The membrane could be patterned (angles and indents) to promote the stress in a specific rupture point. It could also be ablated with a pulsed laser or destroyed by a local electric discharge.

Literature survey.   The idea of breaking a membrane in a microfabricated cell has already been claimed by Kamada *et al.* (2014) but for a different purpose. Indeed, in order to generate a pure alkali metal, compounds such as rubidium chloride and barium azide can be used. When this mixture is heated, pure rubidium and
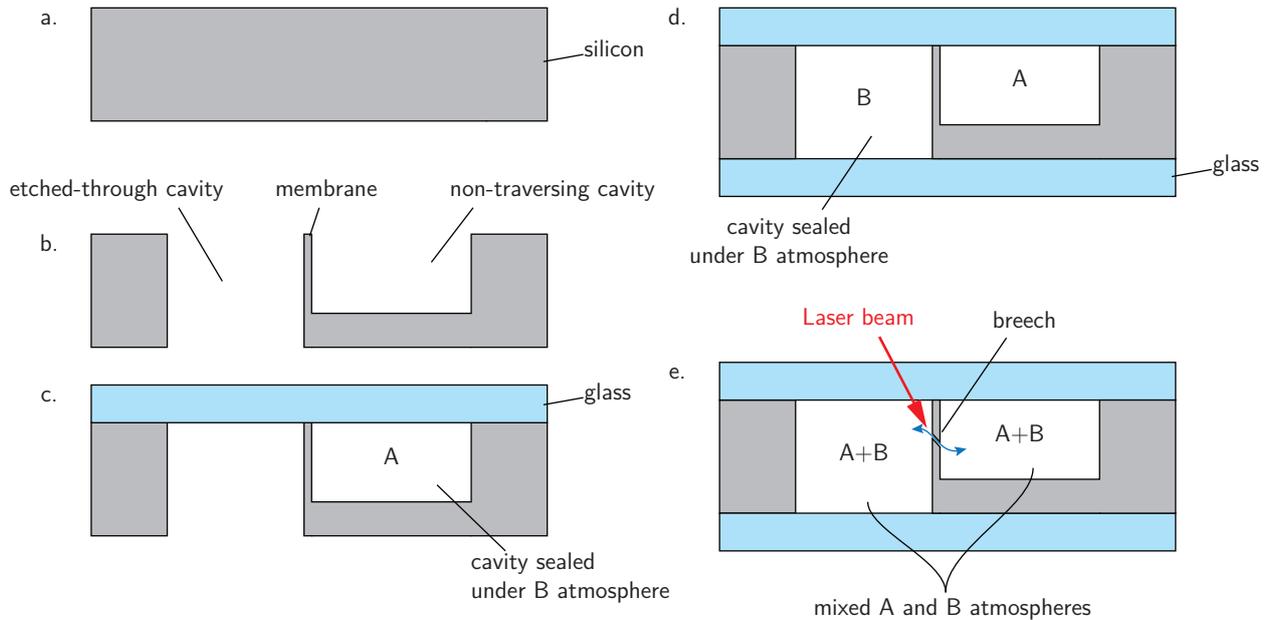
Figure 3.38: Fabrication of a generic break-seal structure.

nitrogen are released. The nitrogen quantity can be difficult to control. Kamada *et al.* proposed to observe the deflection or the rupture of the membrane to evaluate the pressure of nitrogen being generated. Using a high-energy laser such as a YAG laser to break the membrane is also claimed.

The concept of a zero-leak single-use normally-closed microfabricated valve was proposed by Mueller *et al.* (1999, 2001) for micro-propulsion in space applications. In this device, a membrane hermetically closing a channel is broken to release a propellant. The canal and membrane structures are patterned in a silicon substrate and closed by a glass substrate (Pyrex) anodically bonded. The canal is broken by an electric discharge applied through the membrane. The silicon surface in the sealing interface is doped to increase the conductivity locally and promote the destruction of the membrane at the interface.

Shah *et al.* (2012) shortly described a rubidium vapor source for a miniature cold atom clock in which the same function is realized. Here, a SiN membrane with resistive patterns is used to protect the rubidium source while the device is being outgassed at high temperatures. The membrane can then be broken by flowing a high current through the resistive patterns.

The approach we chose to realize this function consists in breaking the membrane with a laser, so that, the complete process (activation, make-seal and break-seal) would eventually rely on a set of lasers that could be installed on a single bench. Preliminary trials performed with a femtosecond laser are described in Section 3.6.7.

3.6.4 Applications

Cell size reduction. The most obvious use of make-seals is to dispose of the dispenser cavity to make smaller cells. Once the dispenser has been activated and the channel has been sealed, the optical cavity can be diced. The ability of this method to reduce the footprint depends on how small the make-seal valve can be made. The fabrication costs are diminished thanks to a denser implantation on the wafer and, especially, the reduced number of dispensers. The benefits for a smaller cell are recalled in Section 3.2.9.

Alkali metal dispatching. As we have seen in Section 3.2.8, the quantity of cesium in a dispenser is large enough for several cells. A single dispenser cavity could feed multiple cells through a network of channels ended by a make-seal valve before each optical cavity, forming the microfabricated equivalent of the glass manifold.

Figure 3.39 shows an example of reflective cells integrating make-seal valves. After the make-seal of each cell is sealed, they can be diced individually. In the case of reflective cells, the make-seal valve can be superposed over the optical cavity so that only the optical cavity contributes to the overall footprint ($\approx 1\,\mathrm{mm}$ wide).
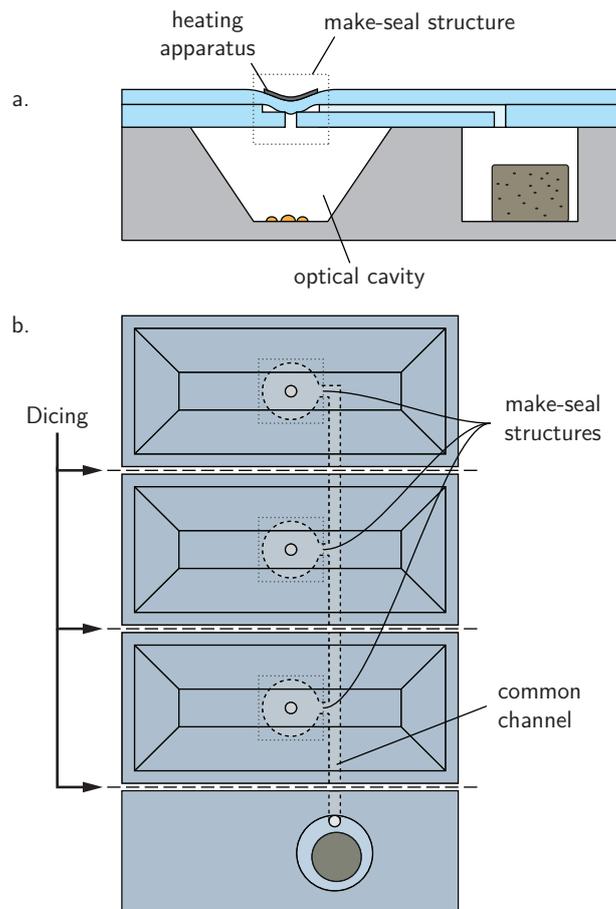
Figure 3.39: Make seal structure

Condensation control.   We could ensure that the appropriate cesium quantity is introduced in the cells. Indeed, cells can be sealed once the curing process is settled. Once the surfaces of the optical cavity are saturated with cesium, a small quantity of condensed cesium has been sufficient to ensure a saturated atomic density throughout the cell lifetime. This small quantity can be obtained by heating the wafer at a temperature superior to the operating temperature of the cell while the make-seal valves are sealed. Because the atomic density is increased at higher temperature, a larger number of atoms is trapped in vapor phase in the optical cavities. This excess condensates when the cell cools down to the operating temperature. The volume of condensation can be controlled and made very small so that it does not obstruct the optical path significantly. In this case, a temperature gradient would have to be established to prevent condensation in the optical cavities when sealing the cells.

Dispenser and buffer gases compatibility.   The absorption of the buffer gases by the dispenser can be prevented by combining make-seal and break-seal valves. In addition to the optical cavity and the dispenser cavity, a third non-etched-through cavity could be implanted and separated from the optical cavity by a break-seal membrane. The process is described in Fig. 3.40. This third cavity would be filled with a buffer gas at the first anodic bonding step. In a first step, the dispenser is activated and cesium is introduced in the optical cavity. The make-seal valve is then sealed (Fig. 3.40a-b). The buffer gas is released from the third cavity into the optical cavity through the break-seal membrane (Fig. 3.40c). The dispenser is no longer in contact with the atmosphere of the optical cavity and the absorption of the buffer gas therefore prevented. This allows to use buffer gases such as nitrogen along with dispensers. Like the previous example, several cells can be filled with a single dispenser using, for instance, the implantation of Fig. 3.40d.

The additional buffer gas cavity could be kept out of the cell die thanks to an additional make-seal disposed just after the common alkali source cavity. After the alkali metal release, this make-seal would be sealed, and the buffer gas cavity opened to fill several cells. Each cell would then be sealed by their individual make-seals before dicing.

Buffer gas total and partial pressures modulation.   When the break-seal is opened, the gas spreads in a larger volume resulting in a pressure reduction. A larger pressure should therefore be introduced in the anodic bonding chamber when encapsulating the buffer gas in its cavity, depending on the ratio of the optical cavity and the buffer-gas cavity. This enables to perform the anodic bonding at a chosen pressure, which can increase the anodic bonding voltage limit caused by electric discharge. If the layout includes cavities with different volume ratios, cells with different pressures can be obtained on a single wafer. This can be useful to compensate for systematic pressure inhomogeneities or when cells with different pressures are needed, for instance for optimization studies.

Likewise, if this additional non-etched-through cavity is sealed with a first gas and the etched-through cavities are sealed with a second gas, a mixture is obtained after opening the break-seal. Varying the volume ratios results in different partial pressure ratios, which can be beneficial in the search for appropriate buffer gas composition, or to provide cells with different operational temperatures on a same wafer.

Alkali source diversification.   We could envision to use different forms of alkali metal sources instead of pills dispensers. While CsN_3 and mixtures of CsCl and BaN_6 usually lead to stability issues due to slow buffer gas pressure changes, the make-seal valve would ensure that the alkali source does not interact with the optical cavity atmosphere. Besides, this method could give access to isotopically pure ^{87}Rb, which would provide better performance (Knappe *et al.*, 2005a). Indeed, pure ^{87}Rb dispenser pills are not yet commercially available (at present, only a natural mixture of ^{85}Rb and ^{87}Rb can be obtained).

Hybrid wafer filling with glass blowing techniques.   The wafer could be attached to an external filling station through a single port, allowing to use alkali metal from a glass ampoule and any buffer gases. Better vacuum conditions could be reached before sealing as the anodic bonding residual gases could be properly outgassed. Indeed, the atmosphere is often suspected to induce long-term fluctuations or drifts on the clock frequency. Associated with active getters, this solution may also be useful for magneto-optical trapping (Rushton *et al.*, 2014, Schwindt *et al.*, 2016). It could serve to reach a proper initial vacuum in a MEMS vacuum device without using a NEG getter (Grzebyk *et al.*, 2014).
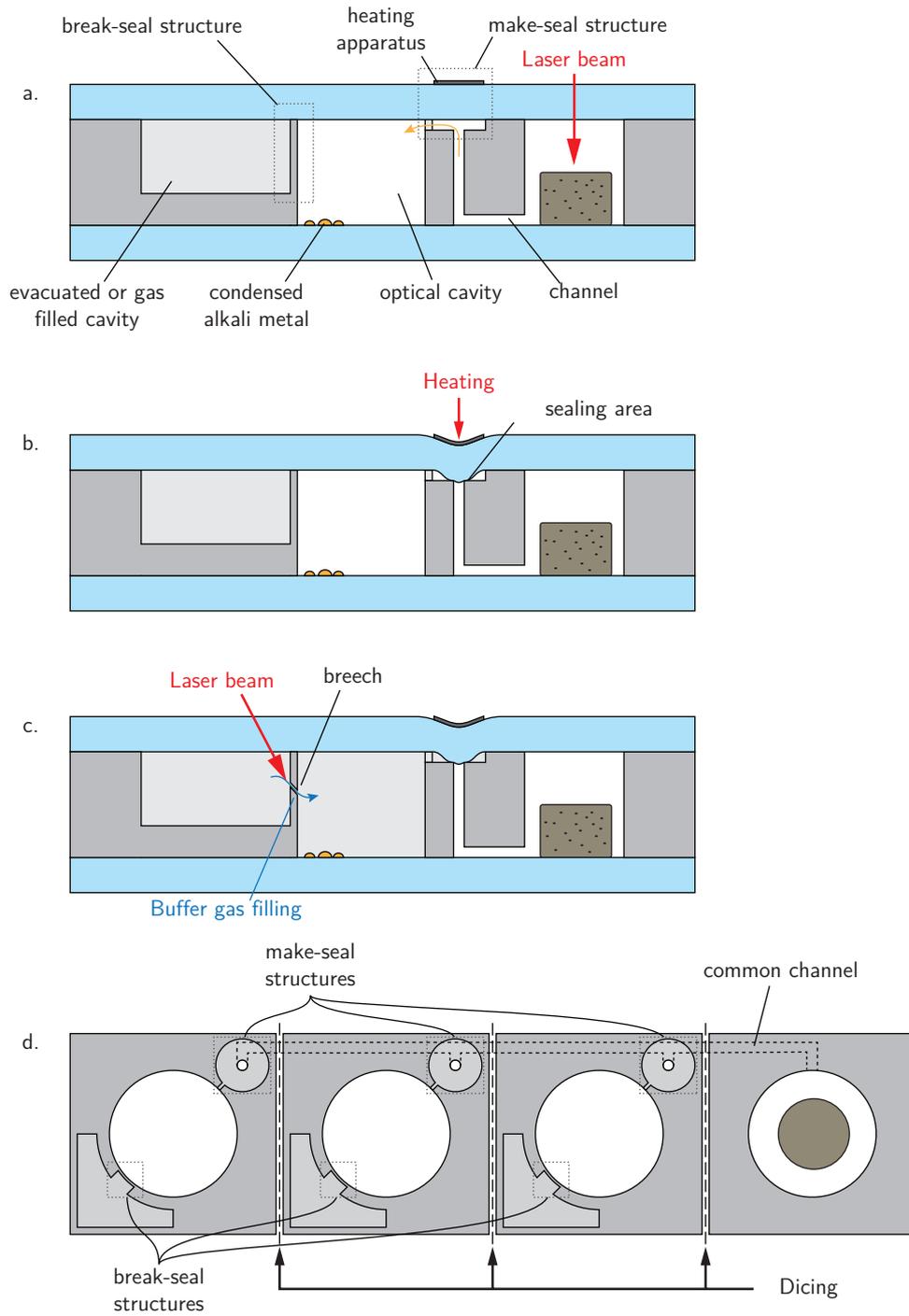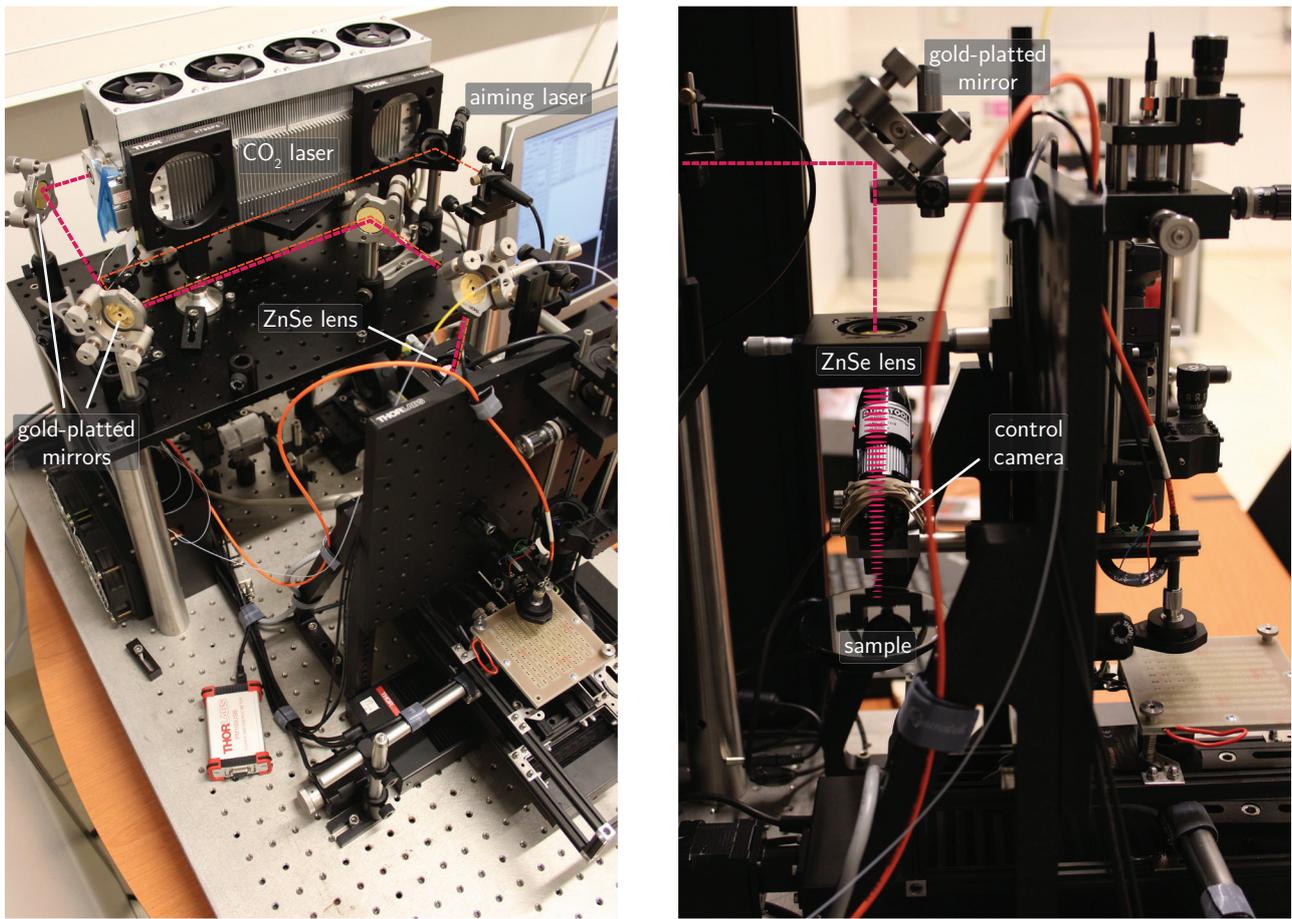
Figure 3.40: Make seal structure

Figure 3.41: Pictures of the activation bench temporarily mounted with the CO_2 laser.

Wall coatings compatibility. Some wall coatings can not withstand the temperature of anodic bonding. Since the make-seal technique only heats a small portion of the cell, a cell with a coating, deposited through a channel after anodic bonding, could be sealed without damaging it. Getters or external pumping (hybrid approach) could then be useful to pump out residual gases.

3.6.5 Preliminary experiments

3.6.6 Make-seal

First experiments have been conducted in order to evaluate the feasibility of microfabricated make-seals. The first point of concern was to demonstrate that a thin glass membrane can be adequately deflected under a pressure difference when it is heated without causing cracks.

As we have seen, CO_2 lasers are often used to machine glass. The absorption of light by glass in the UV spectrum range is dominated by electronic excitation of molecules, whereas it is dominated by molecular vibrations in the IR. In other terms, due to low photon energy of the CO_2 laser ($E_{ph} = 0.2$ eV compared to the Si-O bond energy of 4.60 eV), bonds cannot be broken. Instead, CO_2 laser radiation is strongly absorbed by Si-O vibrational mode and subsequently converted into thermal energy by excitation of lattice vibrations. Thus, in glass, the absorption depth is very small (a few tens of microns). Consequently, CO_2 laser machining is dominated by surface heating without significant absorption of the light into the bulk of the material.

Setup description and beam shaping. A 30 W CO_2 laser[21] has been installed on the activation setup, benefiting from the existing protection box and translation stages (Fig. 3.41). The operating frequency and duty cycle are adjustable from 0 to 25 kHz and from 0 to 100 %, respectively allowing to adapt the average power. The duty cycle is controlled by a 0 to 10 V signal. This signal was provided by a programmable voltage

---

[21]DIAMOND C-30, from Coherent, Inc.
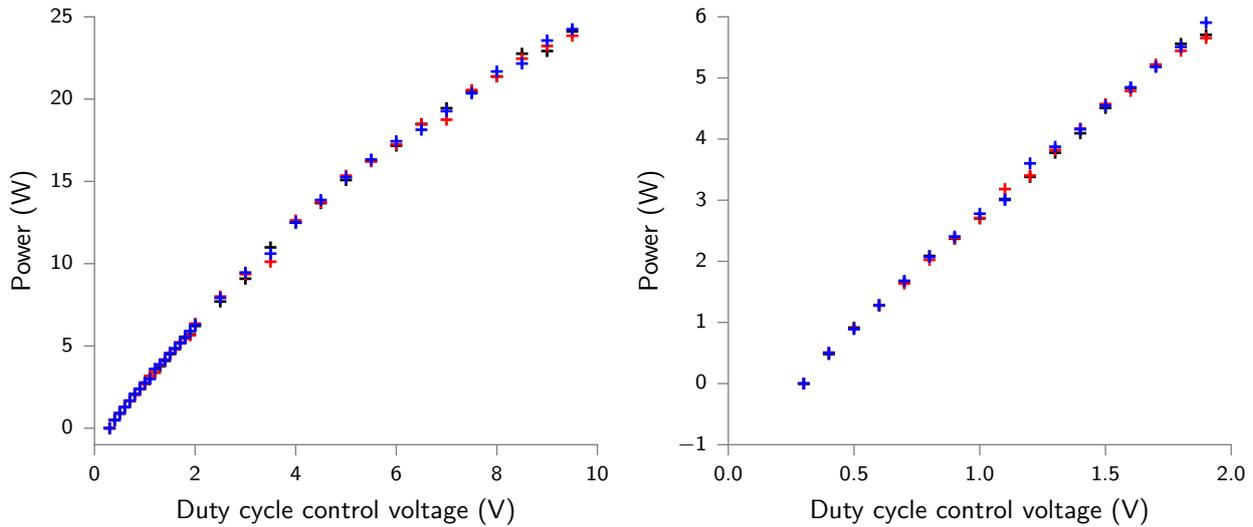
Figure 3.42: Calibration curve of the CO_2 laser.

supply[22] controlled over GPIB to control irradiation durations more accurately. After installing the laser, the correspondence between the optical power and the duty cycle control voltage was established with a thermal power meter[23]. The calibration curve is shown in Fig. 3.42.

Gold-platted copper mirrors and ZnSe lenses are typically used to route and shape CO_2 laser beams. We initially selected a ZnSe lens with a focal length of 150 mm located approximately at 700 mm from the laser exit. The computed intensity gradient in the region of the focal plane for an incident beam power of 1 W is illustrated in Fig. 3.43. Due to the long wavelength, the Rayleigh distance is rather short and even with this lens focal, the focal plane is well defined over a few millimeters only. Figure 3.44 displays the beam profile at the focal plane. Its width is around 230 μm (radius at $1/e^2$) or 270 μm (FWHM) in the lens focal plane.

In order to provide a reference point for aligning the samples under the invisible CO_2 laser beam, an additional laser diode ($\lambda \approx 640$ nm) was installed and aligned so that its beam is collinear with the one from the CO_2 laser.

Test structures fabrication.　Glass test structures have been realized from standard microfabricated evacuated cells where one side has been grinded and polished to obtain different thicknesses, namely 20, 50, 100, 200 and 500 μm. Hence, the generated membranes will be considered very large since we will use mostly the optical cavity footprint of 2 mm diameter. The membrane aspect ratios consequently range from 10 to 100. 20 μm thick membranes are quite fragile and some of them were damaged during polishing. In future experiments, we expect to overcome this issue by using commercially available wafers with the desired thickness (for instance, Schott, Inc. proposes on demand AF32 aluminoborosilicate glasses wafers with thicknesses down to 30 μm).

Pressure inside the cells is expected to be below a few millibars and allows to generate a pressure difference with the cell environment. Since the force applied over the window is proportional to the pressure difference, it is almost proportional to the atmospheric pressure as soon as the inner cell pressure is small enough.

Preliminary results.　For these preliminary series of test, about 60 membranes have been irradiated with different combinations of power and duration. In order to control the resulting deformations, the samples were then studied with an optical profilometer[24].

First observations show that due to low thermal conductivity of glass, the deposited energy over a few seconds is hardly evacuated and, consequently, the temperature rises quickly. For instance, for a power of 6 W, glass radiation turns white within 5 s irradiation, indicating that a high temperature is reached. In this particular case, a 500 μm membrane was opened with a hole of basically 3 times the beam size and without deformations of the rest of the membrane. In here, a large decrease of the viscosity is expected so that the liquid glass flows inside the cavity. Note that the deformations are mostly confined within the irradiated area.

---

[22]Agilent E3631A
[23]Thorlabs S314C
[24]White light interferometer MSA-500 from Polytec GmbH
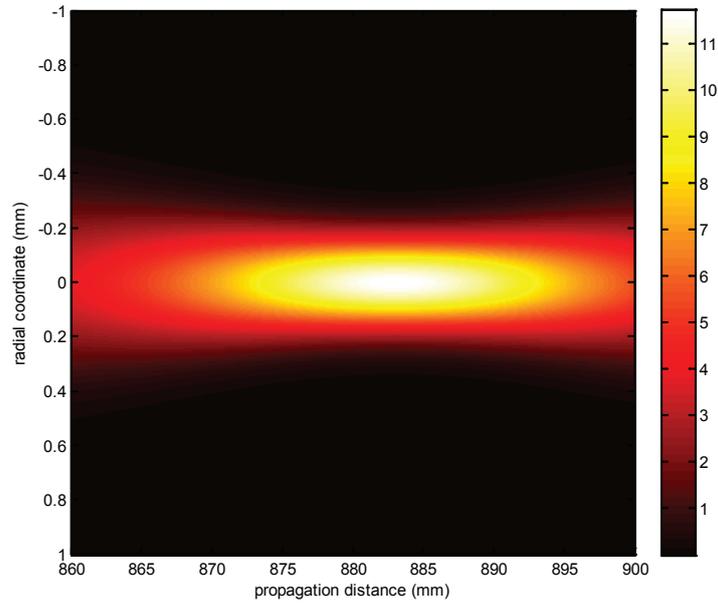
Figure 3.43: Intensity gradient $(\mathrm{W\,mm^{-2}})$ in the vicinity of the focal plane when the incident beam power is 1 W. This intensity map is computed from the laser specifications, assuming that the laser beam size at the laser exit is 1.8(2) mm with a full angle divergence of 7.5(5) mrad, and in the case where a ZnSe lens with a focal length of 150 mm is positioned at 700 mm from the laser exit.
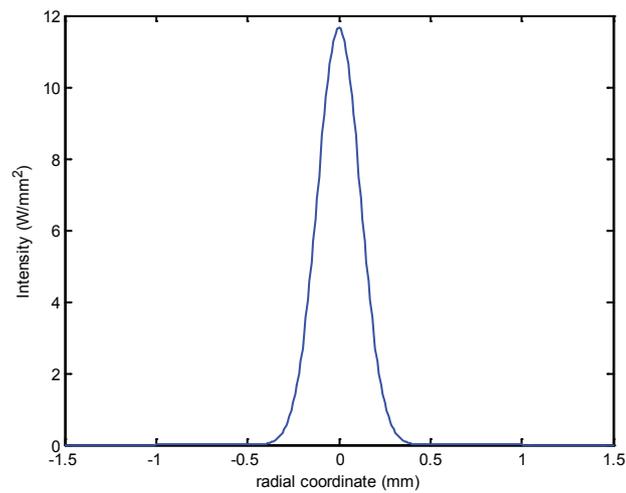

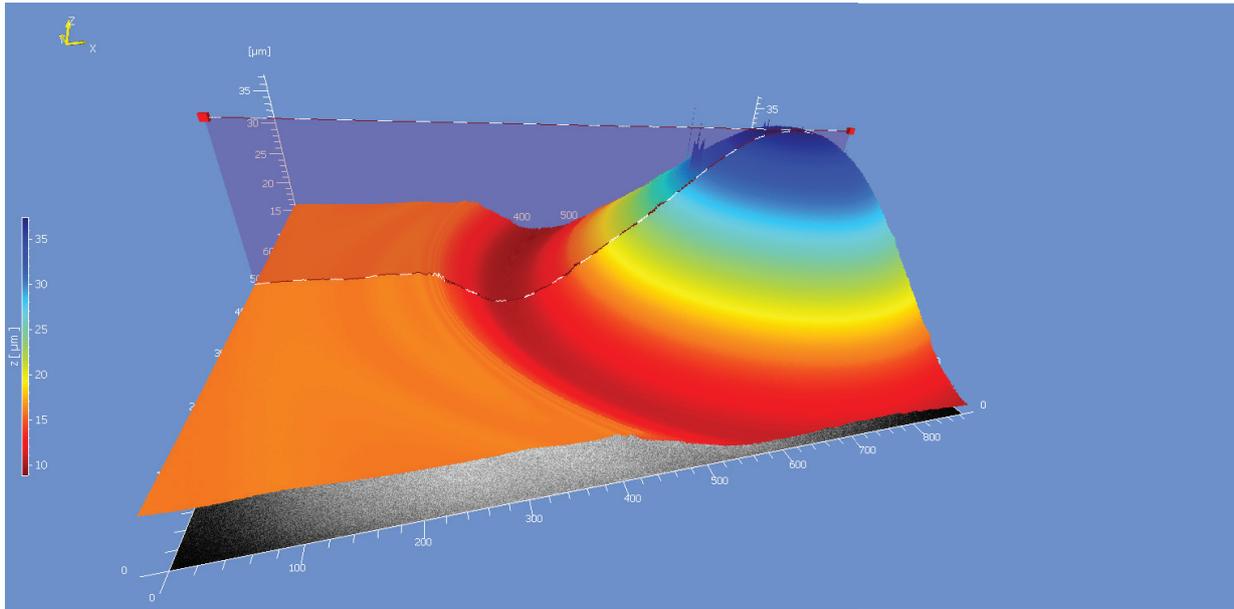Figure 3.44: Intensity profile of the beam in the focal plane.

Figure 3.45: Profile of a W-shaped deformation obtained on the surface of a 500 μm thick glass membrane irradiated at 3.5 W for 18 s.

Membrane thickness (μm)	50	100	200
Incident laser power (mW)	400 - 450	700 - 900	1250 - 1450
On-axis peak value laser intensity ($W\,mm^{-2}$)	4.7 - 5.3	8.2 - 10.5	14.6 - 17.6

Table 3.7: Summary of the adequate set of parameters for different membrane thicknesses.

When the power applied to 500 μm thick membranes is smaller (from 1 to 4 W), a deformation of the glass surface is observed in most cases. It can take the form of a bump, for instance, with a 8 μm sag over a 500 μm diameter for a 40 s long irradiation at 2.7 W, or a more complex W-shape (central bump surrounded by a lower circular lobe) depending on the energy deposited. Figure 3.45 displays such a shape observed at the surface of a membrane surface after a 18 s long irradiation at 3.5 W. This phenomenon, described by Wlodarczyk (2011), is attributed to a non-uniform distribution of surface tensions, due to the temperature gradient. However, with this set of parameters, the membrane is not deflected downward, as we would like it to be, because the viscosity is only lowered at its surface and the other side remains too cold for the whole membrane to deform.

Effects are much more interesting for us when dealing with thinner membranes. Bumps and W-shapes are still observed for large powers and rather short irradiation durations. For instance, we saw a W-shape profile with a central bump as high as 180 μm with a power of 1.6 W only and a duration of 60 s on a 100 μm thick membrane.

For 100 μm thicknesses, the whole membrane starts deflecting downward at powers around 700 mW and with durations in the order of a minute. Since the energy is mostly deposited at the surface (in a layer of approximately 10 μm), this relatively long time seems to be required to warm the membrane down to its other side so that it can deflect significantly toward the cavity. Deflections up to 160 μm were observed.

For 200 μm thicknesses, the power required to deflect the membrane is around 1.3 W and durations as long as 4 minutes have been tested. In this case, deflections up to 80 μm were observed. Figure 3.46 shows a 35 μm deep deflection on a 200 μm thick membrane after a 240 s long irradiation at 1.3 μW (the diameter of the deflected area is around 650 μm).

It can be noticed that using thicker membranes increases the tolerance on power instabilities, however, it also enlarges the deflected area.

Result summary and future work.   Discrepancies remain between the results obtained despite keeping the experimental conditions seemingly identical. But those experiments answer our initial concerns on the possibility to deflect a membrane very locally without breaking it, and allowed narrowing down the range of parameters yielding the most appropriate results. These parameters are summed up in Table 3.7. Further tests
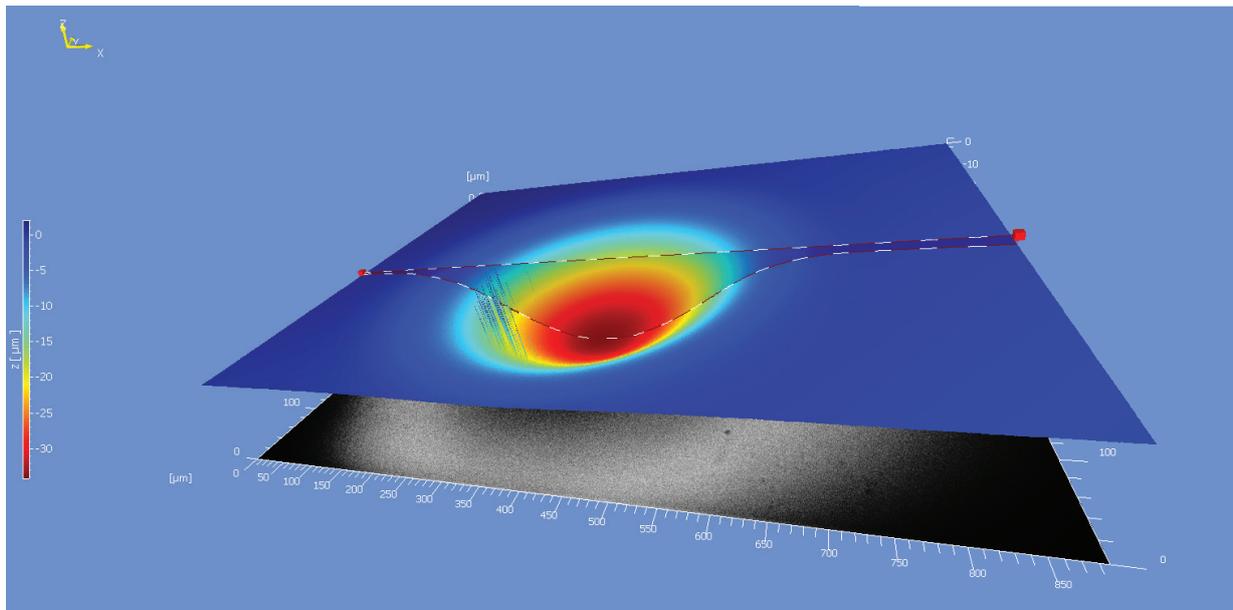
Figure 3.46: Profile of a 200 µm thick membrane after an irradiation at 1.3 W for 240 s. The deflection depth is 35 µm and the diameter of the deflected area is around 650 µm.

should be done to evaluate the process repeatability as a function of laser power, which should be monitored, and location of the irradiated area within the membrane, since both of those parameters are expected to be responsible for the observed discrepancies. The next experiments will be performed on complete structures as described earlier. In order to achieve the fabrication process described in Fig. 3.37, glass-glass bonding is being developed at MIMENTO notably by Florent Bassignot, Aurélien Hamzaoui and Sylwester Bargiel.

3.6.7 Break-seal

Connecting initially separated cavities within a hermetically closed structure seems easier than hermetically sealing a channel. Here again, a laser-based method appears to be a good candidate to achieve this remotely, without having to embed, for instance, an electrically actuated system as proposed by Mueller *et al.* (1999, 2001) and Shah *et al.* (2012). Picosecond or femtosecond laser micromachining has recently emerged and exhibits increasing agility and abilities (Mathis *et al.*, 2012).

Consequently, we began developing a solution in which a relatively thin vertical silicon membrane separating the cavities would be ablated through the top glass wafer, which should remain intact to ensure the cell hermeticity. If successful, this technique could be enforced without complicating significantly the microfabrication process. Achieving this purpose by ablating a glass membrane could also be done but we expect silicon ablation residues to be less disturbing than glass residues, in contact with alkali metals.

The following experiments were performed with Jassem Safioui, who is in charge of the femtosecond laser machining equipment available at FEMTO-ST. Femtosecond lasers can machine both opaque and transparent materials. Since, in our case, glass should ideally be preserved, an adequate set of parameters had to be found.

Our first experiment was performed directly on a glass/silicon/glass stack but in a region without cavities. Silicon was ablated from the top, at its interface with glass, along parallel lines. For each line, the parameters were varied to find appropriate laser power and focal point position. For each power, 50 lines were patterned, spaced by 100 µm and the position of the focal point was lowered by 20 µm between each lines, starting from the top glass surface down to 1 mm below this surface. Since the glass wafer is 500 µm thick, the focal point is thereby scanned across the glass/silicon interface. Dark marks are clearly visible at the interface, suggesting that it is affected. Figure 3.47 shows a cross-section image of the top glass surface after ablation and dicing (where the focal point is in the vicinity of the glass surface). Looking at the diced section, no significant change could be seen at the silicon/glass interface as the focal point was scanned across the interface, despite the fact that glass is indeed ablated when the laser is focused on the top surface.

Several test cell layouts have already been designed, where a non-etched-through cavity and an etched-through cavity are separated by a wall with various shapes and thicknesses. SEM images of the cavities after DRIE for different cell layouts can be seen in Fig. 3.48. The cells after the anodic bonding steps are visible
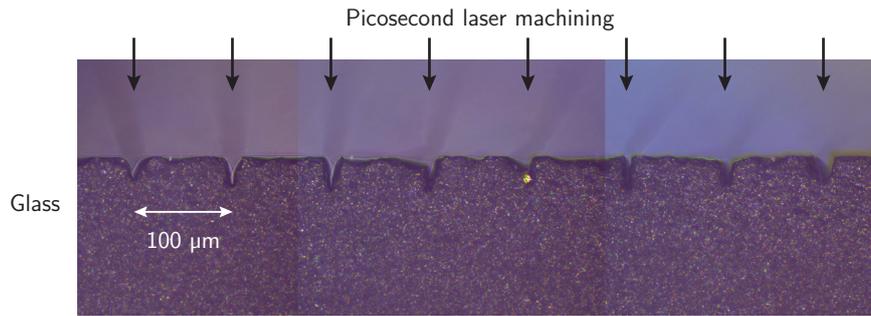
Figure 3.47: Microscope image of the top glass surface section after laser ablation and dicing. The visible channels are obtained for a power of $100\,\mathrm{mW}$, $3\,\mathrm{ps}$ pulses, $\lambda = 800\,\mathrm{nm}$, a line scanning speed of $1\,\mathrm{mm}$ and a 10X objective magnification.
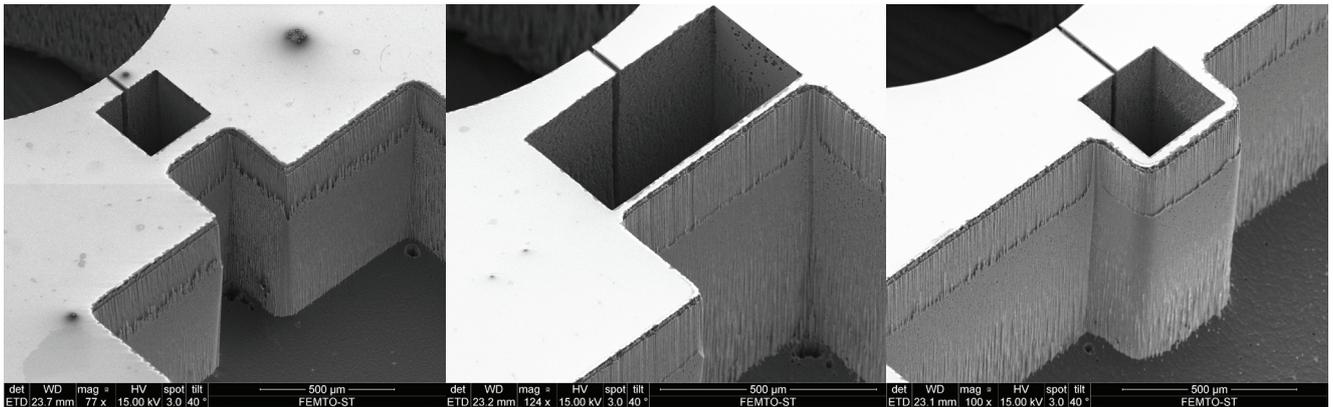

Figure 3.48: SEM images of cavities separated by a wall, obtained after two DRIE steps.

in Fig. 3.49.

Coming experiments will be conducted on those cells to verify if the hermeticity is broken between the cavities, as desired, and observe the impact of the ablation residues on the cell inner atmosphere.

3.6.8   Conclusion

In this section, a wafer-level approach was proposed to apply the classical glass cell fabrication techniques to microfabricated cells. As it only relies on well-known materials, essentially silicon and glass, and techniques whose reliability has been established, namely anodic bonding and local fusion bonding, a stable inner atmosphere can be expected. Besides, this solution would be relatively simple to implement. Indeed, the simplicity brought forth by dispensers is conserved and a standard anodic bonding equipment can be used. All subsequent operations could be done with a set of lasers disposed on a single setup in standard environment. In this scheme, the final cells are free of dispensers, which opens the path to smaller form-factors and the ability to introduce buffer gases, formerly incompatible with this technique. This solution was the subject of patent application and developments are ongoing.
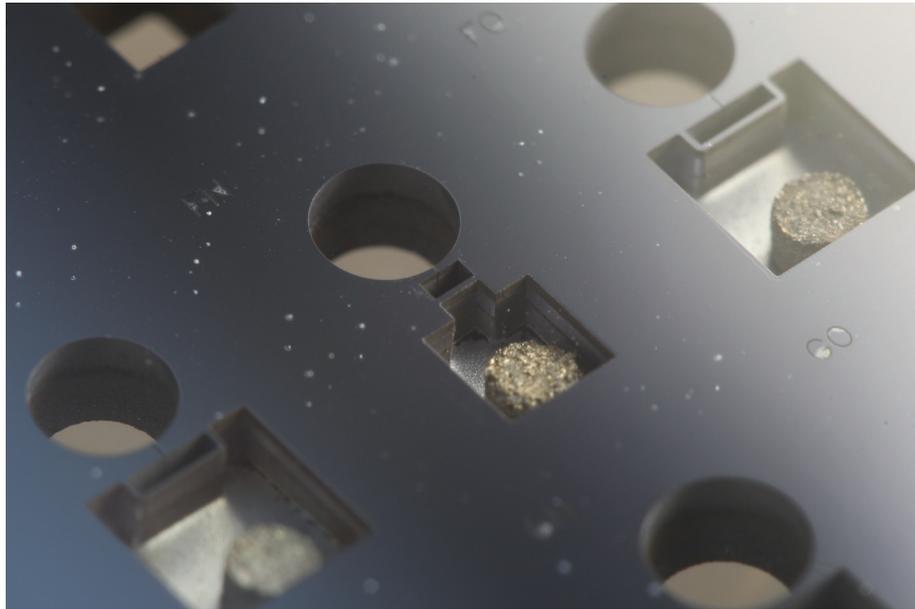
Figure 3.49: Pictures of the cells fabricated for the break-seal experiments.

Chapter conclusion

The fabrication process employed at FEMTO-ST has been developed over several years before this thesis began, and was pursued in this work. This process was described in details in this chapter. The reflective architecture, also proposed prior to this thesis, was presented. Compared to other methods, dispensers alleviate the need for complex vacuum chamber equipments and allow to control independently the quantity of alkali metal and the buffer gas pressure. The current process was scaled-up and accelerated. Besides, it was adapted to a bonding equipment to which dedicated gas lines were added, providing higher gas purity and better control over mixed atmospheres. After the addition of a final baking step, the activation process, which tended to yield uneven results, was found more robust than initially observed. Baking notably speeds up the establishment of a saturated vapor and reduces the condensation excess on the windows. A setup was assembled to activate and test cells through linear absorption spectroscopy in parallel and over long periods of time, which will be useful for future large-scale studies. Despite their benefits, dispensers remain bulky, expensive and inadequate for collective deposition. In addition, they limit the buffer gas atmosphere to noble gases. To address those drawbacks, paste-like dispensers were tried and have been exhibiting stable atomic densities for several months. In order to completely exclude the alkali metal source from the final cell, a solution based on make-seal and break-seal components, inspired from glass-blown cell fabrication techniques, was proposed and early experiments were performed. This technique could significantly reduce fabrication costs and allow the use of any buffer gas composition. The cell operating temperature could thereby be increased to any temperature. After fabrication, cells are characterized to evaluate their performances. This work is presented in Chapter 4.

Chapter 4

Metrology and characterization

This chapter describes the methods employed for characterizing microfabricated cells and presents their results. First, the characterization benches are detailed. In particular, a first table-top bench based on a VCSEL was assembled with components that could eventually be integrated in a small-size device. This bench allows us to measure the performances that could be achieved in a real CSAC configuration. The second bench benefits from higher contrasts provided by a DFB laser. It aims at evaluating rapidly the frequency stability limit resulting solely from the cell atmosphere evolution. The focus is then brought to the results of CPT spectroscopy and long-term frequency measurements in different cells. Transmissive cells with different buffer gas pressures are studied in order to identify an optimal pressure. Reflective cells of different dimensions are characterized and compared to the transmissive cells. Aiming at increasing the cell operating temperature over 80 °C, a buffer gas mixture composed of neon and helium is also analyzed.

4.1 Description of the characterization benches

4.1.1 VCSEL setup

This table top setup aims at measuring clock performances in an integrable system. It uses a VCSEL prototype resonant on the D_1 line of cesium from Ulm University made in the course of MAC-TFC (Gruet *et al.*, 2013). A schema of the setup is shown on Fig. 4.1. The injection current of the VCSEL is modulated at 4.596 GHz by microwave frequency synthesizer[1]. The synthesizer is referenced to a high-performance hydrogen maser available at the laboratory[2]. The output laser beam is collimated with a lens, reaching a 2 mm diameter. For some characterizations, the optical power has to be adjusted over a relatively large range. To accomplish this, a pair of polarizers is used. The light attenuation depends in the angle between the polarizers axes, which is changed by rotating one of them with a stepper motor controlled from the computer. The linearly polarized light is then converted into circular polarization with a QWP.

A physics package dedicated to microcells was designed and fabricated by Philippe Abbé. It consists of a metallic cylindrical core, featuring a rectangular slot to host the cell. To this core are attached heating resistors and a thermistor[3]. Helmholtz coils are preferred to keep access to the cell slot without disassembling the package, which is convenient to test several cells in a row. They are directly coiled in slots machined around the core. The core is held and thermally isolated by a shell made of Teflon. This assembly is fixed in a cylindrical magnetic shield with Teflon screws. The current of the Helmholtz coils is provided by a commercial laser driver. The temperature regulator was custom-made by Cyrus Rocher and can also be controlled through USB.

The optical power is measured continuously just before entering the physics package with a power meter[4]. The optical power is changed by rotating the polarizer with the motor until the power is close enough to the set point (typically within ±1 μW).

The signal from the photodiode is sampled by a data acquisition module[5]. The same module is used to generate ramp or sawtooth waveforms to sweep either the laser frequency for linear absorption spectroscopy or

---

[1] Rohde-Schwarz RS SMB100A
[2] T4 Science iMaser3000
[3] BetaTHERM BetaCURVE 10K3A1
[4] Thorlabs S130C
[5] NI USB-6259 BNC
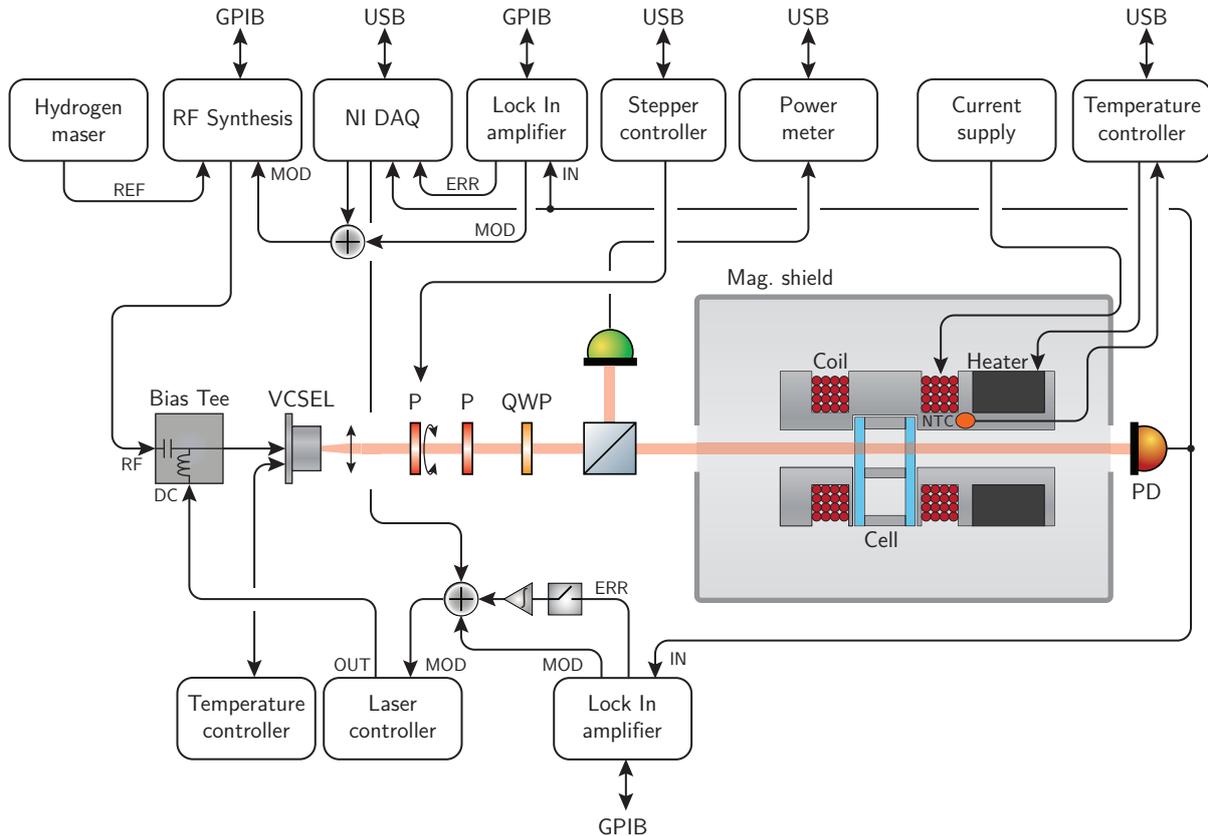
Figure 4.1: Schematic of the VCSEL setup.

the frequency synthesis for CPT spectroscopy.

The frequency of the laser is locked on the absorption peak by a lock-in amplifier[6] whose error output is fed back to the laser current supply[7] through an integrator, feeding the DC component of the VCSEL injection current.

A Python based control software[8] was developed to aggregate the parameters of the devices. This extensive control of the bench from the software helps to detect and solve potential failures remotely, and allows to perform characterization sequences automatically, including the extraction of CPT signal characteristics through Lorentzian fits. Moreover, it allows to systematically and automatically record all the parameters of an acquisition.

4.1.2   DFB + EOM setup

This setup initially aimed at characterizing the "intrinsic" performances of the cells. It is similar to the setup described by Liu *et al.* (2013b). Unlike the VCSEL based setup, it is not intended to be integrable in a small form factor but, instead, targets high stability performances. By doing so, we expect to reach a resolution sufficient to measure frequency drifts unambiguously within short time periods. This would allow to observe more easily phenomenons like frequency equilibration and aging. A schematic representation of the setup is shown in Fig. 4.2. The overall setup and the optical breadboard are shown in Figs. 4.3 and 4.4.

This setup uses a DFB laser diode[9] resonant on the D_1 line of cesium at 894.6 nm. D_1 transitions are known to provide larger CPT amplitudes than D_2 transitions (Stähler *et al.*, 2002, Boudot *et al.*, 2012). An optical isolator is placed at the output of the laser to prevent optical feedback. The laser beam is sent to a pigtailed Mach-Zehnder intensity electro-optic modulator (EOM)[10]. The later is driven at 4.596 GHz by a low-noise microwave frequency synthesizer[11] in order to generate two first-order optical sidebands separated by

---

[6]SRS SR830
[7]LaserLabs, France
[8]Source code available at http://github.com/mv20100/phd_code_characterization
[9]Eagleyard EYP-DFB-0895
[10]Photline NIR-MX800-LN-10
[11]Agilent E8254A

9.192 GHz. The synthesizer is referenced to the hydrogen maser. The operating point of the EOM tends to drift over time due to various factors, including temperature variations. In order to suppress the optical carrier from the output of the EOM, its bias voltage is regulated by a microwave synchronous detector described in more details by Liu *et al.* (2013b). The optical power at the EOM output is stabilized with a noise eater[12]. The noise eater attenuation can be tuned by an external signal, but it cannot cover a sufficiently large optical power range by itself. Therefore, the same system based on crossed polarizer as in the VCSEL bench is used to adjust coarsely the optical power over a wide range. Since the stepper motor used has a limited resolution, the optical power can be finely adjusted and actively regulated to reach the actual power set point by counteraction on the noise eater bias input voltage.

Push-pull optical pumping is performed by converting the amplitude modulation of the light field into a light field with alternating σ^+ and σ^- circular polarizations (Jau *et al.*, 2004). To this end, a setup arranged like a Michelson interferometer is used. In this setup a polarizing beam splitter (PBS) splits the beam in two arms, each of them containing a QWP and a mirror. The QWPs are adjusted so that beams of equal intensities and having linear polarizations with orthogonal orientations are obtained at the output of the PBS. One of the mirrors is placed so that the optical path difference between the two beams equals a half of the hyperfine frequency wavelength (16.3 mm), introducing a time delay of about 54.4 ps. A 180° phase difference between each beams modulation is thereby obtained. The beams recombine without interfering at the exit of the PBS and the orthogonal linear polarizations are converted into σ^+ and σ^- circular polarizations by a QWP. The optical power is measured continuously just before entering the physics package with a power meter[13].

The physics package containing the cell is identical to the one described on the VCSEL setup. The current of the Helmholtz coils is provided by a commercial laser driver[14], which can be controlled over USB.

Most equipments are controlled over GPIB or USB from the computer and can be parametrized remotely. As in the VCSEL bench, the signal from the photodiode is sampled by a data acquisition module[15], which also provides modulation functions for spectroscopy or synchronous detection.

The frequency of the laser is also locked on the absorption peak. A relay is used to activate or deactivate this correction signal from the computer.

The same software core is used for both the VCSEL and the DFB + EOM setups but it is adapted in each case for managing the associated devices. The graphical user interface (GUI) of the software was developed using PyQtGraph[16]. The GUI of the DFB setup is shown in Fig. 4.5 and Fig. 4.6.

The relationship between the coil current and the magnetic field generated in the cell can be established by ramping the current and measuring the $0 - 0$ (short for $|F = 3, m_F = 0\rangle - |F = 4, m_F = 0\rangle$) clock transition frequency. From Eq. (2.40), we expect $\Delta\omega_{\mathrm{clock}} = \beta B^2$ with $\beta = 427.45\,\mathrm{Hz\,G^{-2}}$. The clock transition frequency against coil current is shown in Fig. 4.7. The quadratic coefficient of $0.485\,\mathrm{Hz\,mA^{-2}}$ entails a conversion factor of $33.7\,\mathrm{G\,A^{-1}}$.

4.2 CPT spectroscopy

4.2.1 Transmissive cells

4.2.1.1 Impact of the buffer gas pressure

In order to determine the optimal buffer gas pressure in the case of a buffer gas composed only of neon, 5 wafers were fabricated with different neon pressures. Figure 4.8 shows the characteristics of the CPT signals at different optical powers for cells taken from these wafers. The CPT signals were measured with an early implementation of the DFB+EOM setup presented in Section 4.1.2, where the cell was probed with a circularly polarized beam (without push-pull). Signals were fitted with a Lorentzian function using the Python package Lmfit[17] (non-linear least-squares minimization). The dependence of contrast on the buffer gas pressure is evident: the lower the pressure, the larger the contrast. A 34 Torr cell exhibits a contrast up to 10 %, while it barely reaches 2 % in a cell with 240 Torr. In addition, the optical power that maximizes the contrast slightly decreases as pressure increases. On the other hand, the FWHM of the signal diminishes as pressure increases, namely from 8 kHz at 150 μW for a pressure of 34 Torr down to 1 kHz at 150 μW for 240 Torr. The shot noise limited short-term

---

[12]Thorlabs LCC3112
[13]Thorlabs PM16-120
[14]Newport 505B
[15]NI USB-6259 BNC
[16]http://www.pyqtgraph.org/
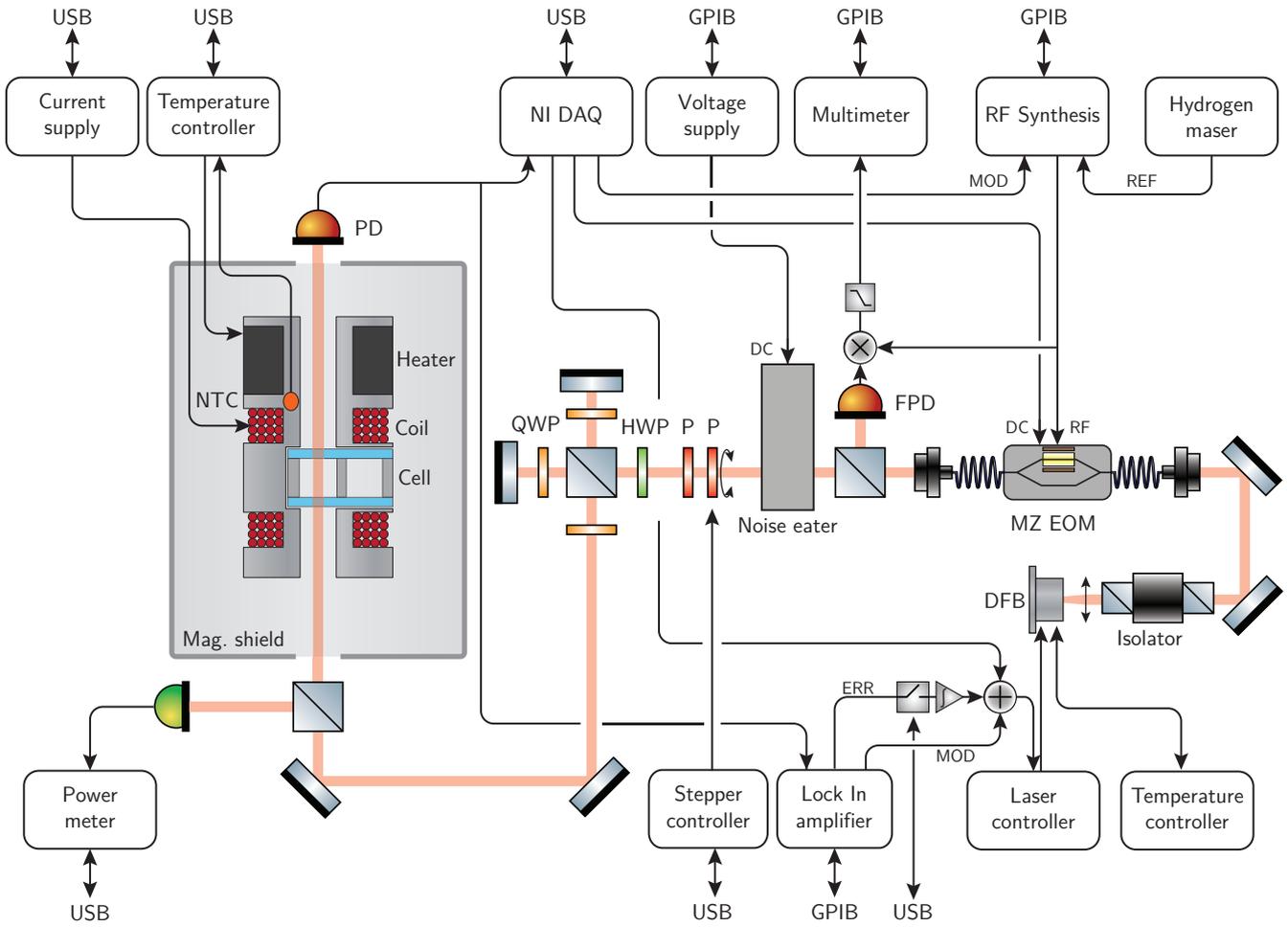[17]http://lmfit.github.io/lmfit-py/

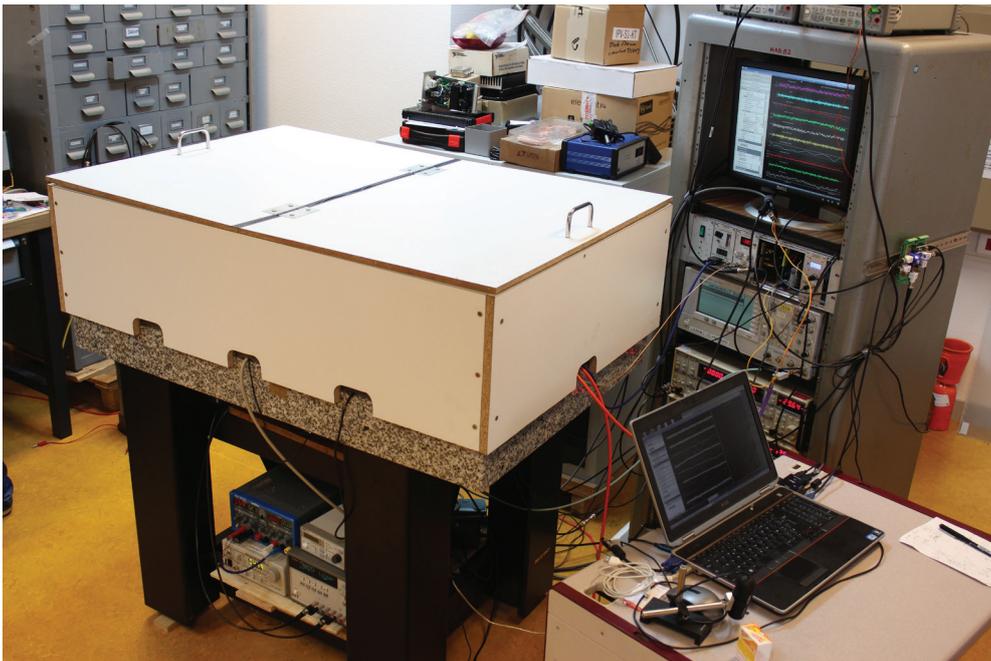Figure 4.2: Schematic of the DFB+EOM setup.

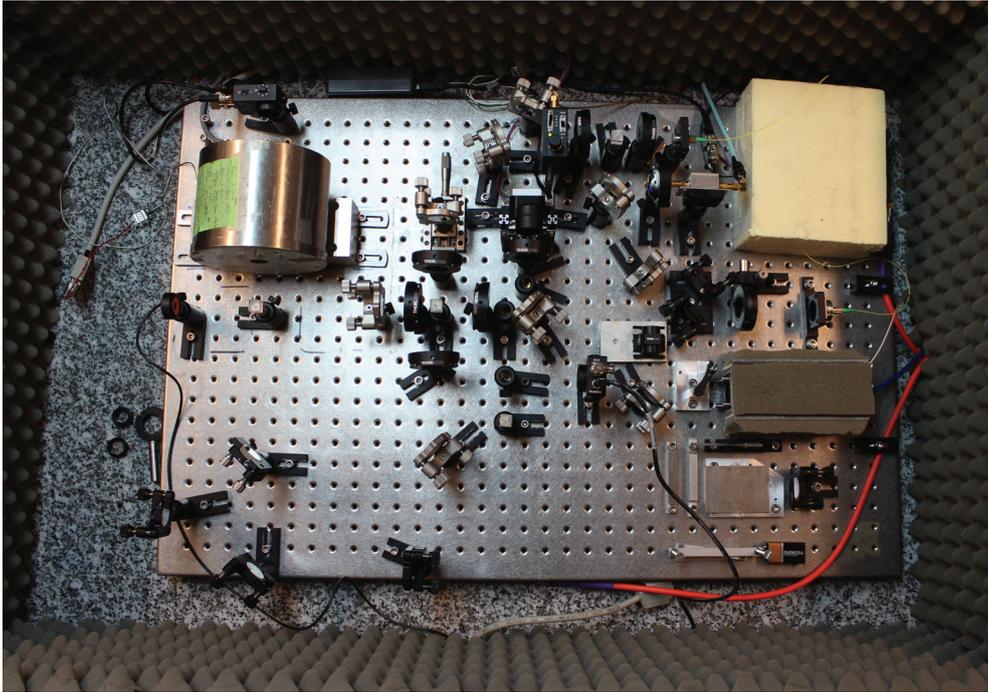Figure 4.3: Picture of the DFB+EOM setup.

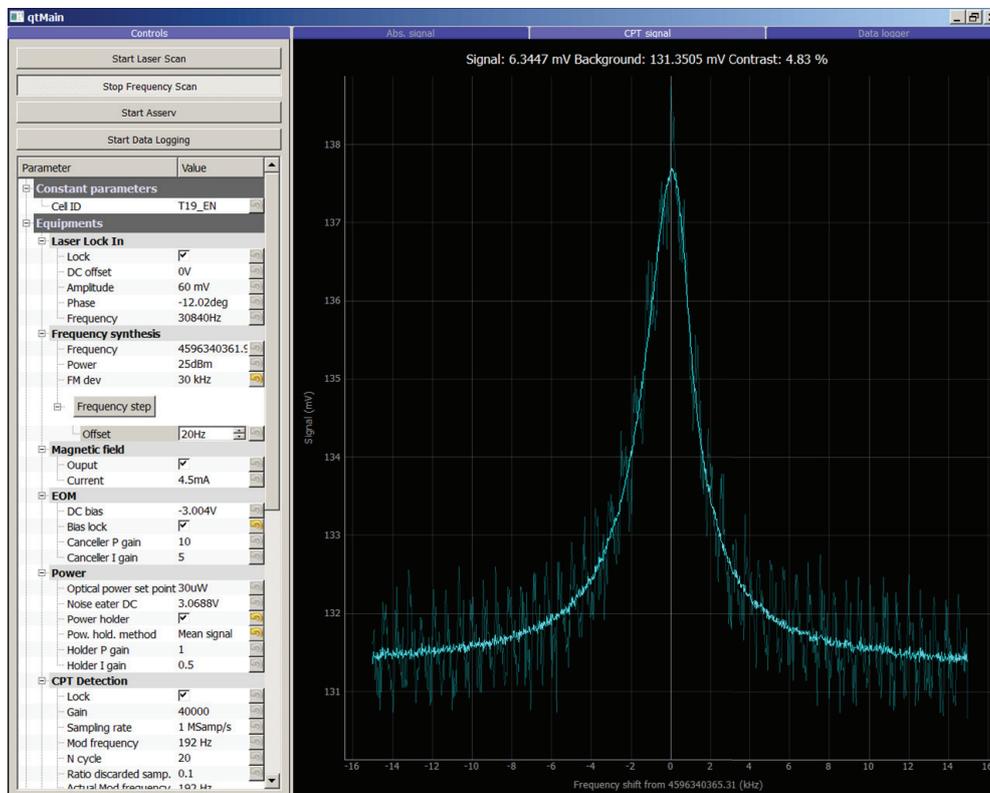Figure 4.4: Picture of the optical breadboard (DFB+EOM setup).

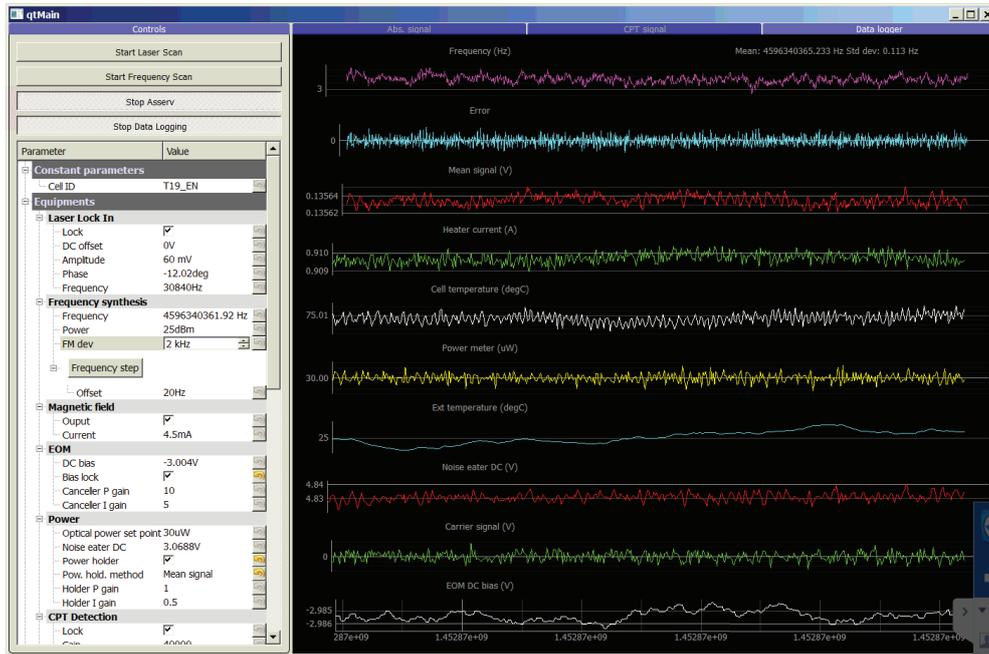Figure 4.5: Control software GUI (CPT spectroscopy).

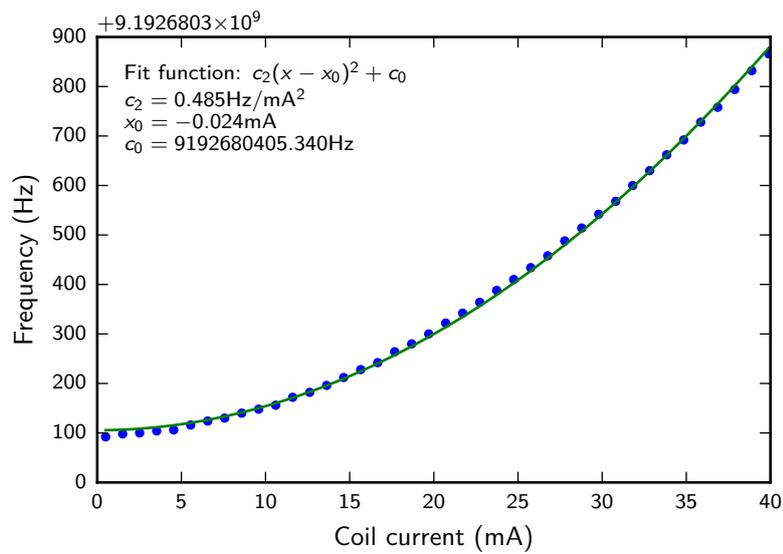Figure 4.6: Control software GUI (monitoring).

Figure 4.7: Frequency of the 0-0 clock transition in function of the Helmholtz coil (blue dots: data points, green line: quadratic fit).
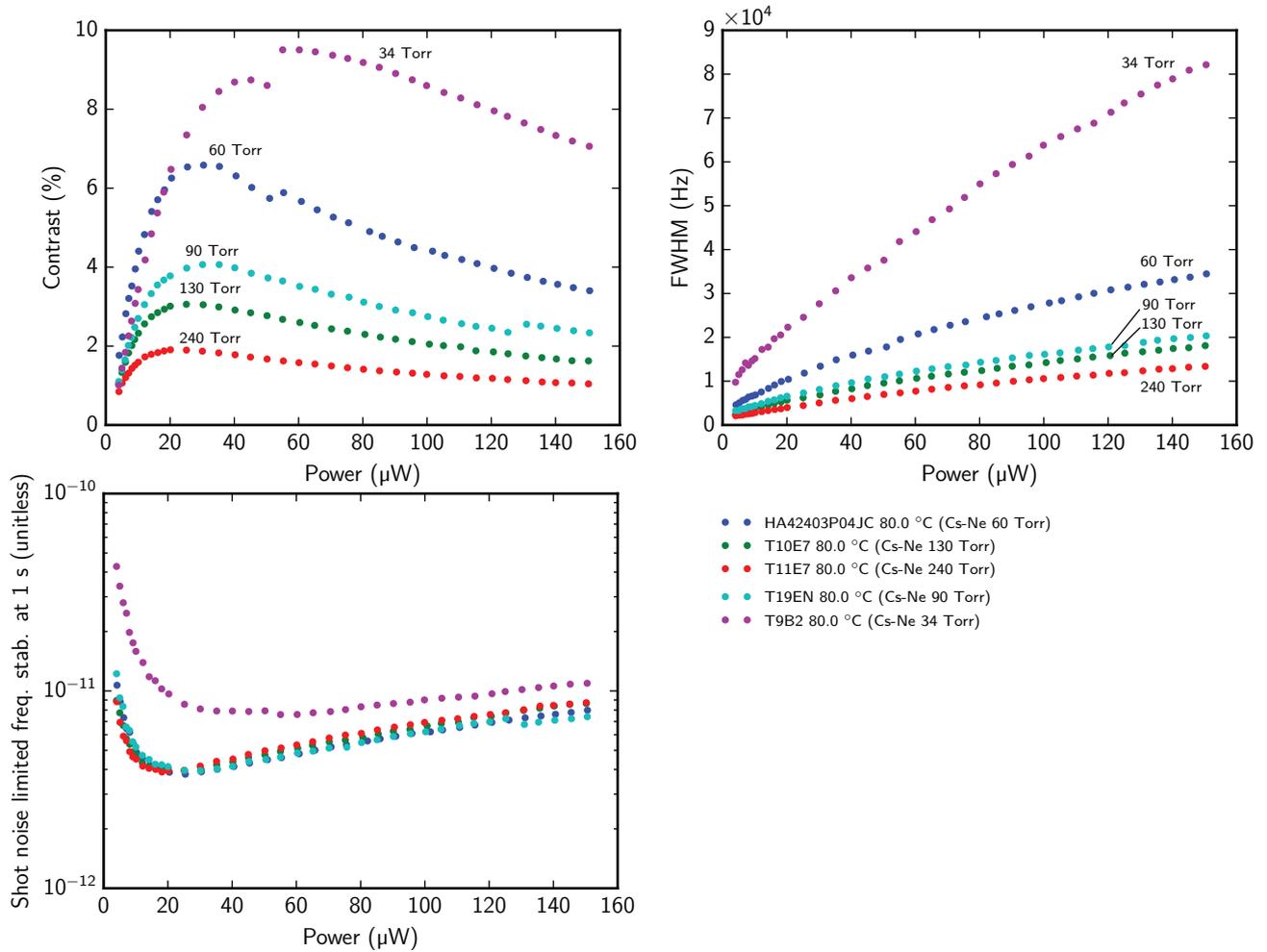
Figure 4.8: Characteristics of the CPT signals against optical power for Cs-Ne cells with different buffer gas pressure, measured with the DFB+EOM setup (circular polarization). Discontinuities result from range changes of the oscilloscope, which was used instead of the DAQ to acquire data at this time.

frequency stability can be estimated from these characteristics using Eq. (2.42) and Eq. (2.43). The estimated short-term frequency stability as a function of the optical power is also shown in Fig. 4.8. Despite the different contrasts and FWHMs, the estimated stability seems rather insensitive to buffer gas pressure from 60 Torr to 240 Torr. This theoretical limit is found to be around 4×10^{-12} at 1 s on this range of pressures. The best stability is obtained at an optimal optical power of 20 µW. Therefore, the reduced resonance linewidth seems to compensate for the reduced contrast.

Figure 4.9 shows the maximum contrast and the FWHM at 150 µW as a function of buffer gas pressure. The evolution of the stability estimation at the optimal optical power along with neon pressure is shown in Fig. 4.10.

This trend must still be confirmed by direct frequency stability measurements with a VCSEL, where contrasts are usually lower. If confirmed with VCSELs, this relatively flat dependence of the frequency stability with optical power around 20 µW may provide some flexibility in the choice of laser injection current, which could help either to find a light-shift cancellation working point or, in an industrial context, compensate would-be dispersions in the VCSELs characteristics.

The mid and long-term frequency stability of the clock is also affected by the light shift. Therefore, even if those measurements do not bring a strong constraint on the neon pressure, we should also consider the effect of buffer gas pressure on the light-shift slope to refine the acceptable pressure range. Indeed, the buffer gas pressure for which we can easily cancel the light shift may place a stronger constraint.
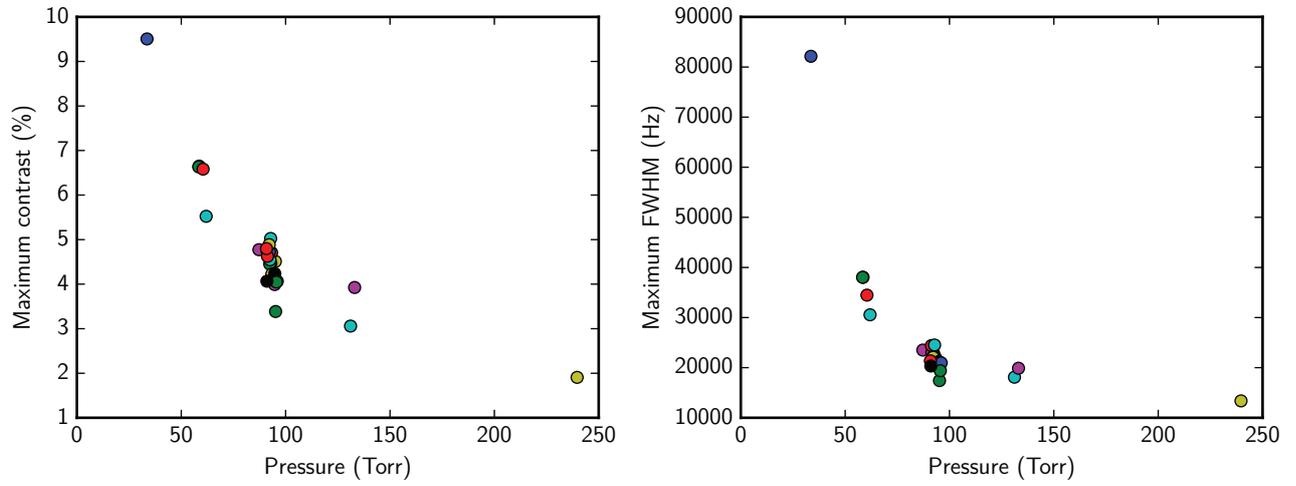
Figure 4.9: Contrast and FWHM maxima of the CPT signals on the 0 to 150 µW optical power range according to neon pressure.
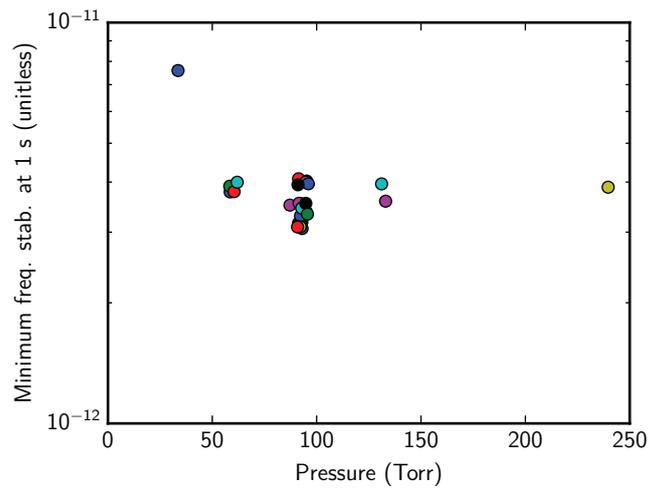
Figure 4.10: Stability estimation at the optimal optical power range according to neon pressure.
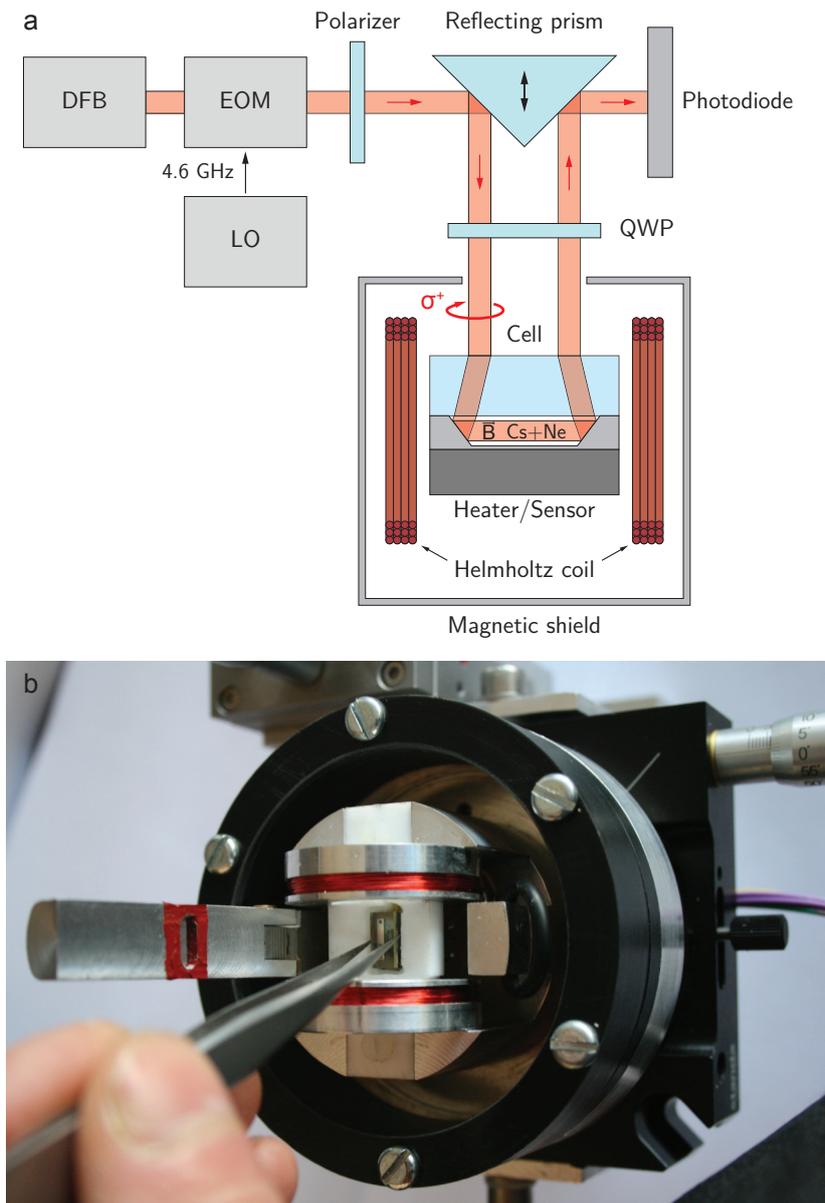
Figure 4.11: Reflective cell characterization physics package (Philippe Abbé).

4.2.2 Reflective cells

Reflective cells were characterized through CPT spectroscopy using the DFB setup. Here again, the setup slightly differs from the setup described earlier. Here, the light at the EOM output is reflected by a prism coated with an aluminum layer and directed toward the cell under test, contained in a physics package. The prism can be translated to adjust the spacing between the input and the output beams according to the length of the cell under test. Before the cell, the linear polarization of the light is converted into circular polarization thanks to a QWP (push-pull is not used). The output light from the cell is reflected by the prism toward a photodiode (Fig. 4.11a). The cell is inserted into a custom bench-top physics package (Fig. 4.11b) where the cell is heated at 75 °C in order to increase the alkali density and the CPT signal. This temperature is stabilized within a range of 100 µK. A small homogeneous longitudinal magnetic field of 20 µT flux density is applied using a Helmholtz coil to lift the degeneracy of the ground-state Zeeman manifold. This assembly is surrounded by a single-layer mu-metal shield to protect the atoms from environmental electromagnetic perturbations. A 1 cm diameter hole in the shield provides optical access to the cell. The local oscillator signal frequency is swept in order to detect the CPT resonance.

The equations detailed in Chapter 2 were used to compute the expected performances of those cells. Figure 4.12(a) reports the CPT linewidth at null laser intensity according to the cell diameter and length for a cell temperature of 75 °C and a neon pressure of 100 Torr. It is assumed that the laser beam diameter equals the cell

diameter. For a cell diameter between 0.2 mm and 2 mm, increasing the cell length over 2 mm does not reduce the linewidth significantly. For a 600 µm cell diameter, a 3.5 kHz linewidth is thus expected. This linewidth is 2.5 times higher than for a cell with a 1.5 mm diameter and 1.5 mm length, which are the typical dimensions of our usual transmissive microfabricated cells. The amplitude of the CPT signal is proportional to the number of atoms interacting with the field and therefore to the atomic density of cesium n_{Cs} and to the volume V of the cell. Figure 4.12(b) reports the CPT signal amplitude according to the dimensions of the cell at a laser intensity of 100 µW mm^{-2} (same temperature and pressure). The CPT signal increases along with the volume. Hence, some geometries with reduced widths may take advantage of an increased length to compensate for the larger linewidth. The evolution of the amplitude-to-linewidth ratio according to the cell dimensions is shown in Figure 4.12(c). It appears that a cell with a 600 µm diameter and a 9 mm length could provide about the same short-term frequency stability as a cell featuring a 1.5 mm diameter and a 1.5 mm length.

Cells with different lengths were fabricated. The beam diameter was set to 600 µm, which is defined by the gratings and apertures size. Cells A and B are filled with a Ne pressure of 100 Torr and feature lengths of 6 and 8 mm, respectively. Cell C is 7 mm long and is filled with 200 Torr. Figure 4.13(a) reports the CPT signals in cell C for different laser powers. For clarity, the background, measured to increase linearly with laser power at a rate of 0.025 V µW^{-1}, is removed. CPT resonances are correctly approximated by a Lorentzian fit function from which the linewidth, the signal amplitude and the contrast are extracted. Figure 4.13(b) reports the linewidth, contrast and contrast-to-linewidth ratio obtained in the different cells at different powers. Cells A, B and C exhibit null power linewidths of 5.87 kHz, 5.07 kHz and 2.23 kHz, respectively. As expected, close values are obtained for cells A and B, showing that a longer cell hardly improves the linewidth. In agreement with Eq. (2.19) and Eq. (2.20), the higher buffer gas pressure in cell C reduces the null power linewidth and the laser power broadening. The null power linewidth in cell C is close to the expected value (2 kHz). For all cells, the CPT resonance contrast increases with the laser power until saturation occurs at high laser intensities. Cell B exhibits a higher contrast than cell A, which shows that the contrast is improved as the length is increased. In particular, cell B reaches contrasts up to 17 %, which is remarkable for a microfabricated cell. In all cells, the contrast-to-linewidth ratio is maximized for a laser power lower than 60 µW. By comparing cell A and B, a longer cell tends to provide a higher contrast-to-linewidth ratio. In cell C, this figure of merit reaches 1.25 % kHz^{-1} at the optimum laser power (about 30 µW) with a contrast of 5.2 % and a FWHM of 4.17 kHz. Despite the stringent beam diameter reduction, this figure of merit shows a two-fold improvement compared to the reported values for microfabricated cells of this scale (Lutwak, 2011, DeNatale *et al.*, 2008, Boudot *et al.*, 2011a).

This elevated contrast is not well understood, but we suspect that a model taking into account an optically dense medium would be more adequate to describe the behavior of those cells where both the temperature and the cavity length is high. Several models have been proposed in the literature and are cited in Section 2.2.2.

4.3   Frequency inversion temperature measurement

As we have seen in Section 2.2.3.1, the buffer gas must be appropriately chosen to cancel the temperature dependence of the clock transition frequency around the desired operating temperature. The collisional shift coefficients that can be found in the literature are not always accurate or available, especially for predicting the behavior of this dependence at high temperatures. For instance, an helium buffer gas was found to provide an inversion temperature around 80 °C (Miletic *et al.*, 2010), which could not be forecast from the coefficients already published at that time. Determining the collisional shift coefficients of a buffer gas requires a rather long characterization, since the clock frequency must be measured for numerous combinations of optical powers and cell temperatures. We expect to speed up considerably those measurements thanks to an automated measurement sequence developed for the benches.

4.3.1   Neon

We first employed this automated measurement method on the DFB setup in a Cs-Ne cell with a pressure around 70 Torr. The clock frequency extrapolated at null optical power for temperatures between 50 °C and 90 °C is shown in Fig. 4.14. Surprisingly, instead of the expected quadratic behavior with an inversion point around 80 °C, the curve exhibits two inversion points around 65 °C and 75 °C. Above 75 °C, the frequency increases with temperature and no other inversion point could be observed before the maximum temperature was reached. A potential impact of the increased heating current on the static magnetic field could be eliminated. This
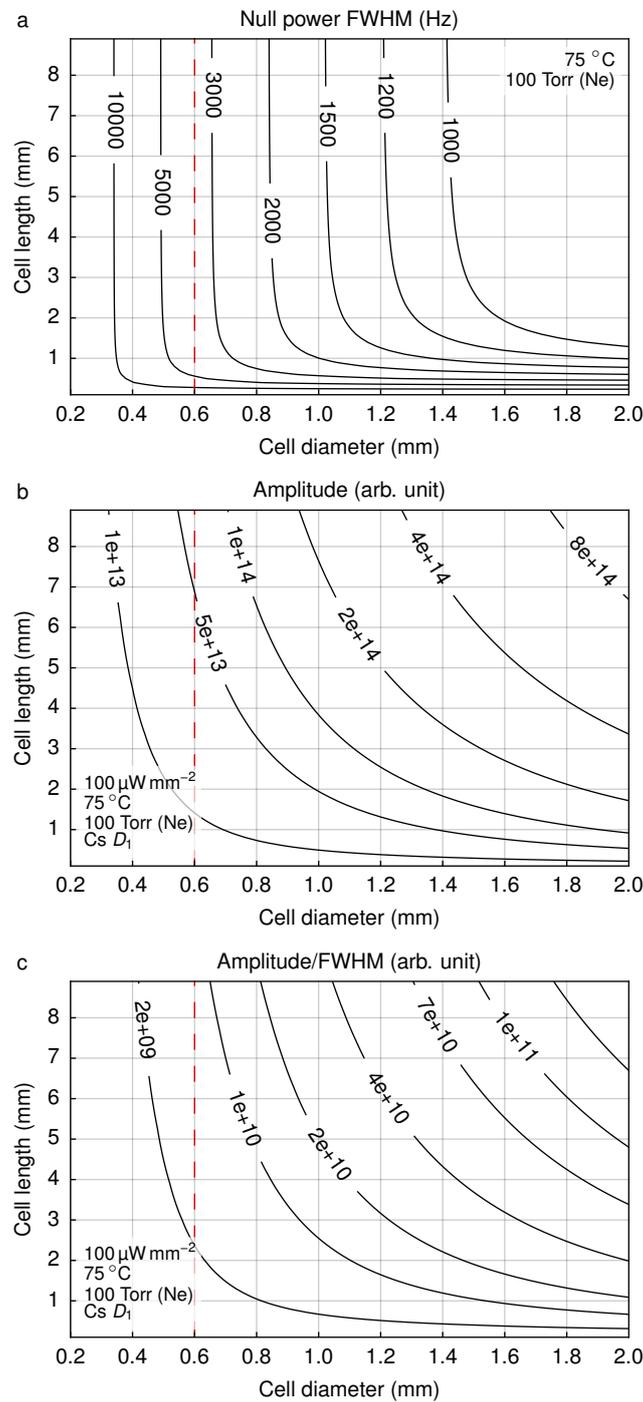
Figure 4.12: Computed (a) CPT linewidth at null power, (b) amplitude and (c) resulting amplitude-to-linewidth ratio of CPT signals for different cell dimensions. The cell temperature is 75 °C and the buffer gas (neon) pressure is 100 Torr.
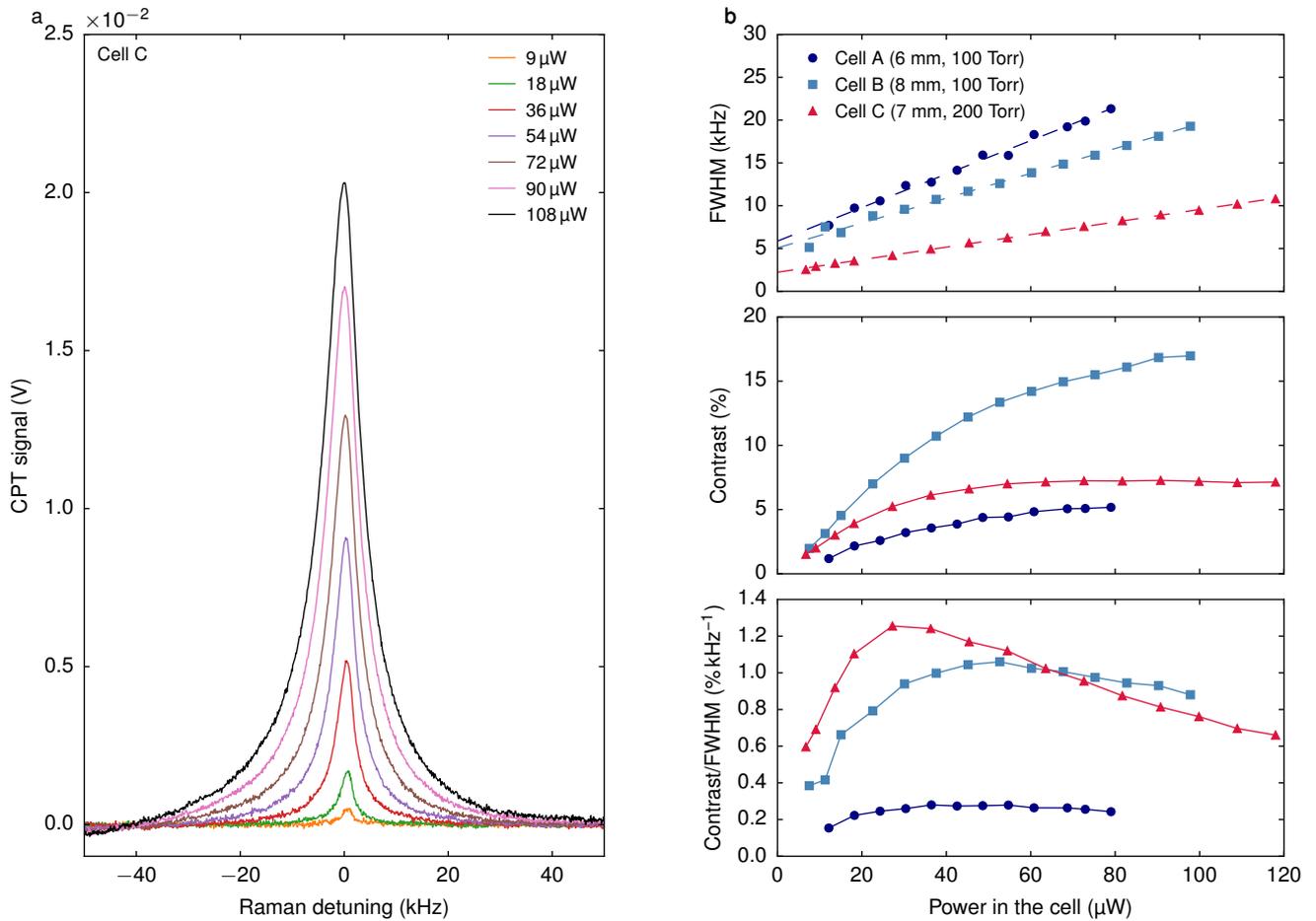
Figure 4.13: (a) CPT signals in cell C for different powers. The cell temperature is 75 °C and the magnetic field magnitude is 20 µT. The background is removed for clarity. (b) Linewidth, contrast and contrast-to-linewidth ratio in different cells.
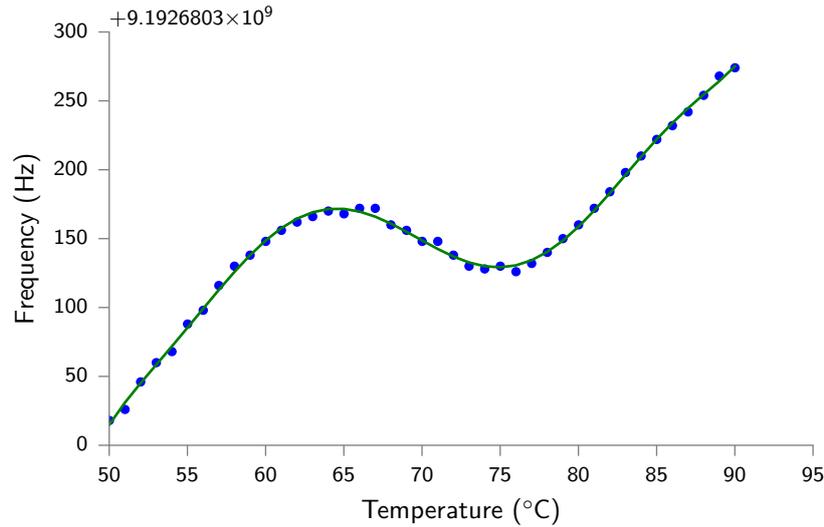
Figure 4.14: Frequency shift of the clock transition extrapolated at null optical power versus cell temperature in a Cs-Ne cell (T19) with buffer gas pressure around 70 Torr. This measurement was performed automatically on the DFB setup. The green line is a 7th order polynomial fit.
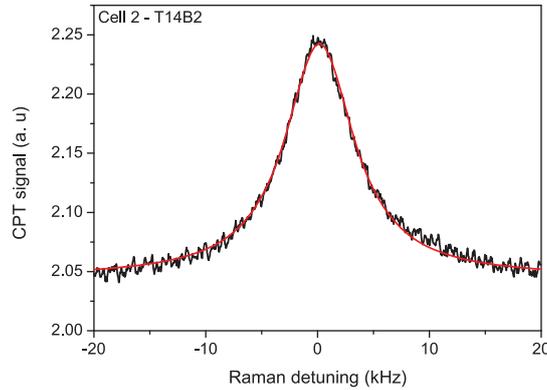
Figure 4.15: CPT resonance detected in a Cs-Ne-He vapor microcell (cell 2) heated at 87 °C. The laser power at the input of the cell is 82 µW. The dashed line is a Lorentzian fit to the experimental data.

behavior remains unexplained and further characterization is planned to address this issue. In can be noted that Masian *et al.* (2015) observed similar thermal dependencies with two inversion points, but the reasons could be different.

4.3.2 Neon-helium mixture

As a neon buffer provides an inversion temperature around 80 °C, which is not enough for many applications, investigations have been pursued to find a buffer gas mixture compliant with dispenser pills and increasing this temperature (Kroemer, 2015). A mixture of neon and helium seemed appropriate as they are both noble gases, inert with the Zr-Al getter alloy contained in dispensers.

A batch of cells with a mixture of neon and helium has been fabricated. The DFB based experimental setup was used to characterize the cells (with a push-pull optical pumping scheme). Different cells (cell 1 to cell 4) coming from the same wafer were measured. The characterization of those cells was performed by Moustafa Abdel Hafiz (the automated bench was not developed at that time). The results were published by Kroemer *et al.* (2015) and led to a patent application (Boudot *et al.*, 2016).

4.3.2.1 Basic CPT spectroscopy

Figure 4.15 reports an example of a CPT resonance detected in a Cs-Ne-He microcell (cell 2) heated at 87 °C. The laser power at the input of the cell is 82 µW. The CPT resonance is well-fitted by a Lorentzian function
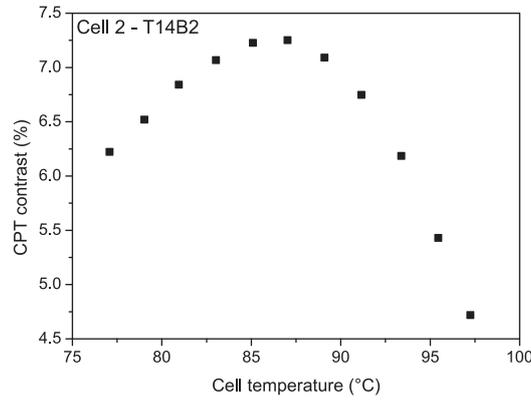
Figure 4.16: Contrast of the CPT resonance versus the cell temperature (cell 2). The laser power is $55\,\mu W$.
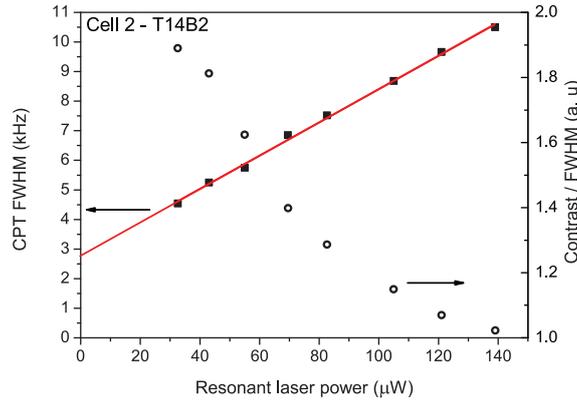
Figure 4.17: Linewidth (filled squares) and contrast/linewidth (circles) of the CPT resonance versus the laser input power (cell 2). The cell temperature is $87\,°C$. The solid line is a linear fit to the CPT linewidth-laser power dependence curve.

with a FWHM of $7.5\,kHz$. The contrast of the resonance, defined as the ratio between the height and the dc background is measured to be $9.6\,\%$. Figure 4.16 shows the contrast of the CPT resonance versus the cell temperature for the cell 2. The laser power at the input of the cell is $55\,\mu W$. As observed by Knappe *et al.* (2001) and Boudot *et al.* (2011a), the CPT signal is increased with atomic density up to a maximum before decreasing because of the increased optical thickness of the atomic vapor (Knappe *et al.*, 2002). The CPT contrast is found to be maximized for a temperature of about $87\,°C$. For comparison, this is around $5\,°C$ higher than in a Cs-Ne cell with a pressure of $79\,Torr$ (Boudot *et al.*, 2012). A similar optimum temperature for CPT contrast was found for other cells. Figure 4.17 plots the CPT linewidth and the CPT contrast/FWHM ratio versus the laser power P_l for the cell 2 heated at $87\,°C$. The linewidth-laser power dependence is well fitted by a linear function such as $\Delta\nu = 2.8 + 0.05 P_l$, in kHz. The ratio contrast/FWHM is found to be maximized for $P_l < 35\,\mu W$. This indicates that the clock short-term frequency stability should be optimized for relatively low laser powers as already observed in numerous references (Knappe *et al.*, 2001, Boudot *et al.*, 2011a).

4.3.2.2 Frequency shift versus cell temperature

Figure 4.18 shows the measured frequency shift of the clock transition from the unperturbed cesium atom frequency ($9.192\,631\,770\,GHz$) versus the cell temperature for cells 2 to 4. Results for all cells are summarized in Table 4.1. All tested cells exhibit an inversion temperature point higher than $85\,°C$ at which the frequency temperature dependence is canceled at the first order. The inversion temperature T_i is measured to be $89.7\,°C$, $89.6\,°C$, $91.0\,°C$ and $94.6\,°C$ for cells 1 to 4 respectively. The frequency shift at the inversion temperature is measured to be $30\,260\,Hz$, $30\,129\,Hz$, $31\,250\,Hz$ and $31\,072\,Hz$ for cells 1 to 4 respectively. From these data, we estimated the actual total buffer gas pressure in the cells and partial pressures. The temperature dependence of the frequency shift vanishes at the inversion temperature T_i for the pressure ratio $a = P_2/P_1$ is given in Eq. (2.38). Buffer gas coefficients reported by Strumia *et al.* (1976) for He and by Kozlova *et al.* (2011) for Ne were used.
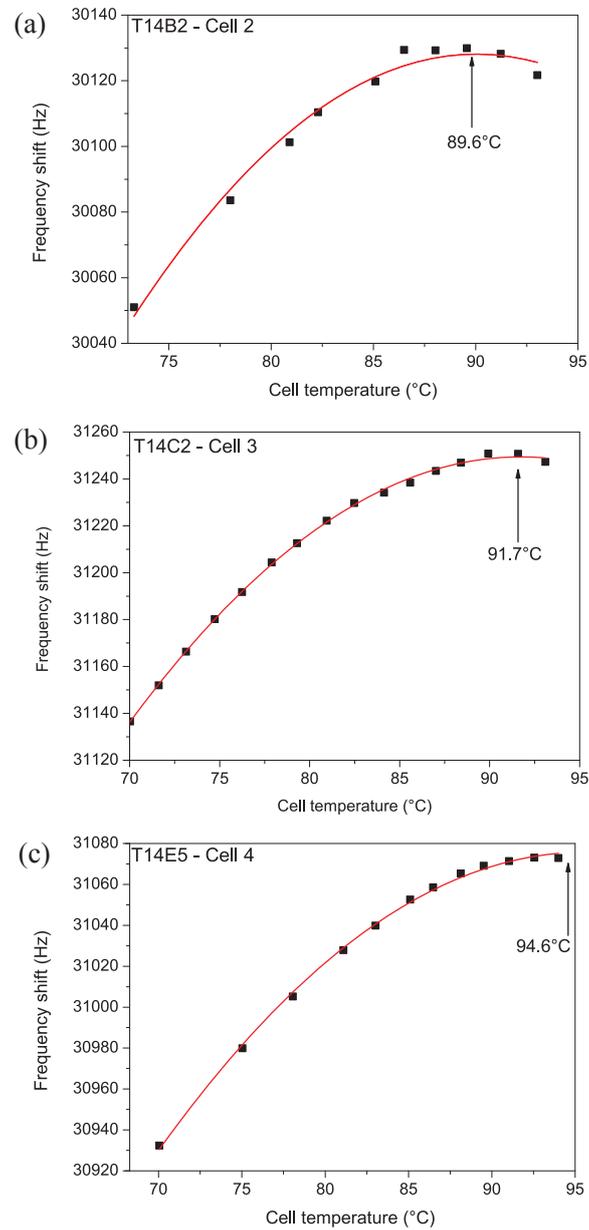
Figure 4.18: Frequency shift of the clock transition with respect to the unperturbed cesium atom frequency (9.192 631 770 GHz) versus the cell temperature. (a): Cell 2, (b): Cell 3, (c): Cell 4.

#	Cell ID	T_i (°C)	$\Delta\nu_{bg}$ at T_i (Hz)	P_{meas} at 0 °C (Torr)	Ne (%)	He (%)
1	T14??	89.7	30 260	42.6	97.6	2.4
2	T14B2	89.6	30 129	42.4	97.6	2.4
3	T14C2	91.7	31 250	43.8	97.2	2.8
4	T14E5	94.6	31 072	43.2	96.7	3.3

Table 4.1: Measured characteristics of the tested Cs-Ne-He microcells. The uncertainty on T_i, $\Delta\nu_{bg}$, P_{meas} and partial pressures are estimated to $\pm 3\,°C$, $\pm 5\,Hz$, $\pm 0.2\,Torr$ and ± 0.2, respectively.

Results from Table 4.1 show that the homogeneity of the cells contents among the wafer is correct. For information, cells 1 to 3 were close to each other on the wafer whereas cell 4 was located at the periphery of the wafer. This could explain that content of cell 4 is slightly different from other cells. It is important to note that inversion points at higher temperatures could be obtained by increasing the partial pressure of helium in the cell, as described in Section 2.2.3.1 (see Fig. 2.9).

For information, we observed in cell 4 an important drift of the clock resonance frequency of about $-2\,Hz\,h^{-1}$ (around $-5 \times 10^{-9}\,d^{-1}$ in terms of fractional frequency). This drift is huge compared to drift values generally reported in vapor cell based clocks (Vanier and Audoin, 1989). This phenomenon could be explained by losses of He gas or Ne gas from the cell induced by microleaks, imperfect anodic bonding at the silicon-glass interface or gas permeation through the cell windows. If attributed to a loss of He gas, the measured frequency drift would correspond to a change of He pressure of about $-1.6\,mTorr\,h^{-1}$. We point out that the use as a buffer gas of He, known to be extremely light, volatile and to exhibit high permeation rate through glass (Norton, 1953, Harding, 1981), will require a cell fabrication process and technology that ensures a long-term stable cell inner atmosphere. Since this drift is supposed to be constant and deterministic, we could envision to implement a drift compensation mechanism to the final device. However, this drift rate seems too high and the rapid loss of helium would quickly displace the temperature inversion point, making the clock more sensitive to temperature fluctuations.

4.3.2.3   Conclusion

We developed Cs vapor microcells filled with Ne-He buffer gas mixture and studied them in a laboratory-prototype CPT clock setup. Basic spectroscopy of the CPT resonance (linewidth, contrast) was reported. We pointed out that this buffer gas mixture allows to cancel the temperature dependence of the Cs clock frequency at temperatures higher than 80 °C, typically around 95 °C when the atmosphere contains around 3.3 % of helium. The presence of such an inversion temperature point is very important for the development of a CPT atomic clock with high mid and long-term frequency stability. Compared to single Ne buffer gas filled Cs vapor microcells, this buffer gas mixture solution is interesting for miniature atomic clocks operating in high-temperature external environment, as specified in defense systems for example. The observation of a clock frequency drift, potentially due to buffer gas diffusion out of a cell, was noted and briefly discussed. We can envision to replace the borosilicate glass by ASG, as discussed in Section 2.4, but Dellis *et al.* (2015) showed that although helium permeation is strongly reduced, a relative frequency drift of $3.7 \times 10^{-11}\,h^{-1}$ remains. ASG will soon be tested with cells containing a Ne-He mixture and the possibility to compensate this drift will then be evaluated. For now, the solution based on microfabricated make-seals exposed in Section 3.6 remains a promising research pathway to answer this issue.

4.4   Frequency aging

We can call the "intrinsic" frequency of the cell, the clock frequency only affected by the collisional shift due to the cell atmosphere. As we have seen in Section 2.4, several factors can entail a long-term drift on the clock frequency. In order to measure such drifts, the characterization bench must be properly stabilized and kept unchanged over extended periods of time. Indeed, we have noticed that several factors such as the settings of the frequency synthesis, the synchronous detection modulation amplitude, the presence of a summing amplifier or even the fact of plugging in an additional USB device on the computer can cause parasitic frequency offsets. Performing measurements with a sufficient repeatability to measure precisely a drift can be challenging. Figure 4.19 shows long-term frequency measurements in a standard Cs-Ne cell done at FEMTO-ST during MAC-TFC and presented by Hasegawa *et al.* (2011b). Even though longer and finer tests are required to
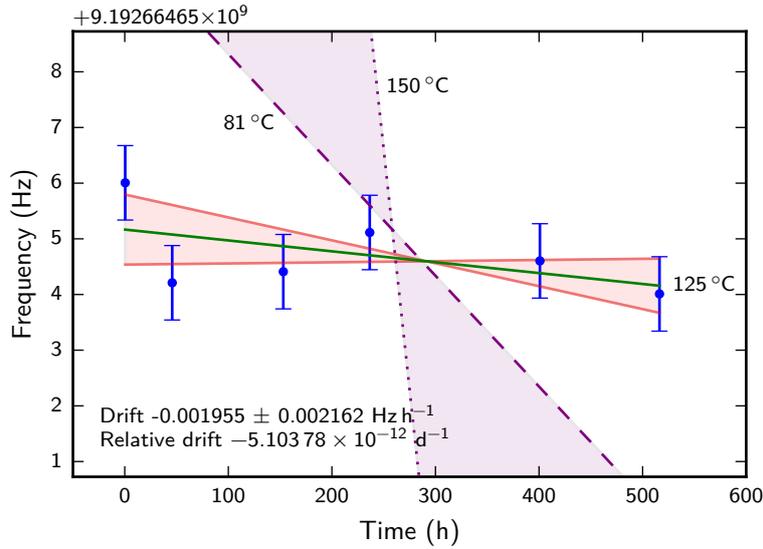
Figure 4.19: Frequency aging data of a Cs-Ne cell with Borofloat33 windows from Hasegawa *et al.* (2011b). The cell was kept in an oven at 125 °C between each measurement. Each of those measurements were performed at a cell temperature of 60 °C. The laser power was 20 µW and the magnetic field was 10 µT. The green line is a linear fit of the data points (slope $a = -1.955 \times 10^{-3}$ Hz h^{-1}), the red lines represents the 2σ error margins on the slope of the linear fit (with slopes $a \pm SE_a$, where $SE_a = 2.162 \times 10^{-3}$ Hz h^{-1} is the standard error of a). The purple dashed and doted lines represents the drift reported by Abdullah *et al.* (2015) for similar cells at 81 °C and 150 °C, respectively.

measure finely the frequency aging of this cell, we can roughly estimate a drift rate around -5.1×10^{-12} d^{-1} ($\pm -5.6 \times 10^{-12}$ d^{-1}) for a cell with a pressure of 6.4 kPa kept at 125 °C. We can confidently claim that the drift rate does not exceed 1×10^{-11} d^{-1} in absolute value, which clearly contradicts the observations of Abdullah *et al.* (2015) in a similar cell. The drifts for cells kept at two different temperatures measured by Abdullah *et al.* are represented on the same graph (Figure 4.19, dashed line: -5.2×10^{-11} d^{-1} at 81 °C, dotted line: -4.5×10^{-10} d^{-1} at 150 °C). According to those measurements, we should have seen a drift comprised between those two lines for a cell at 125 °C. Therefore, we cannot agree on this analysis implying neon permeation and we suspect that other effects may have altered this drift measurement.

As Abdullah *et al.* (2015) reported, it is common to cancel the contribution of the light shift by measuring the clock frequency at different optical powers and extrapolating at a zero power. If no other effect contributes significantly to the measured shift, we obtain an estimate of the "intrinsic" frequency of the cell.

In order to refine the previous long-term drift measurement and evaluate the cell technology developed at FEMTO-ST, a similar measurement was carried out using the VCSEL setup. For this purpose, a dedicated program was created to measure repeatedly the CPT resonance center frequency at different optical powers (from 8 µW to 40 µW) in an automated manner at regular time intervals (typically every minute). Each set of results was extrapolated at null power in order to evaluate the intrinsic frequency. For instance, Fig. 4.20 shows the frequency measured at different optical powers. A fairly linear dependence is observed. The null power frequency is obtained by a linear fit with a standard error (1σ) around 0.2 Hz.

A cell with a neon pressure of 70 Torr kept at 80 °C was thereby measured for 460 h. Figure 4.21 shows how the light shift slope changes through time while the null power frequency changes less significantly. The null power frequency and the light shift slope over time are plotted on Fig. 4.22. Unfortunately, data is missing because the laser frequency lock failed during the laboratory closing period and the setup did not permit to reestablish it remotely at this time. A relative frequency drift around -3.8×10^{-12} d^{-1} is found. It is very likely that the drift is overestimated and a longer and continuous measurement should be performed but it confirms the drift rate measured in Fig. 4.19. This result confirms that the cells are compatible with the targeted specifications regarding the long-term frequency stability of the clock.

In Section 4.3.2, we have shown that using a mixture of neon and helium to shift the operating point of the cell to higher temperatures was not adequate with the current technology because of the drift attributed to helium permeation through the borosilicate glass windows. In order to confirm this phenomenon, the drift of a cesium cell with pure helium as buffer gas was measured over 90 h. At 65 °C and with an initial pressure of
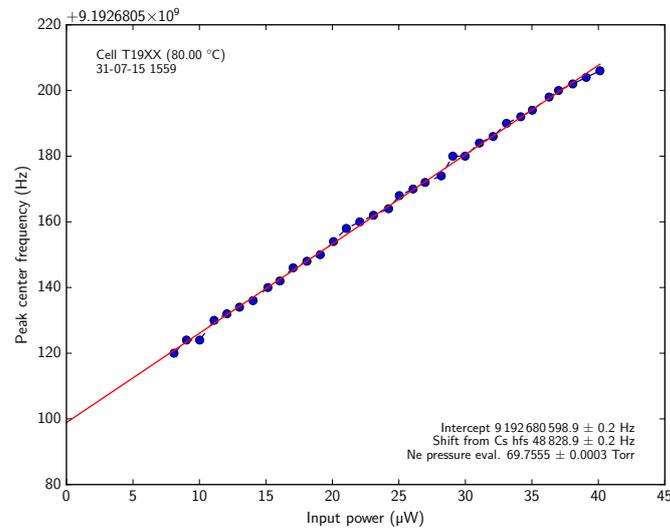
Figure 4.20: CPT resonance center frequency measured for different optical powers and linear extrapolation at null power in cell T19EN.
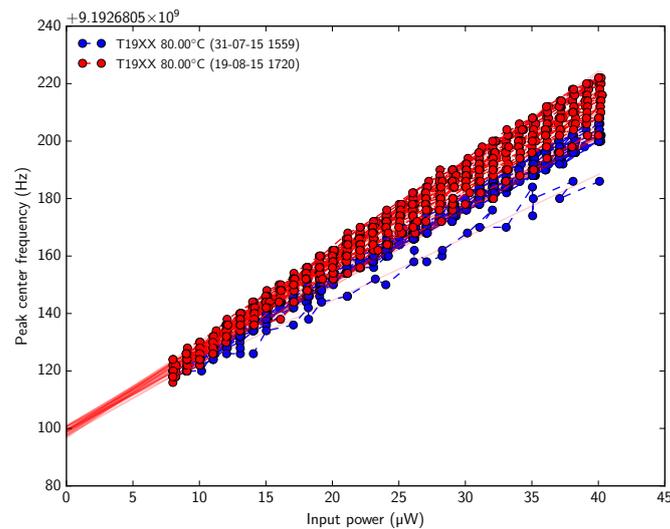

Figure 4.21: Evolution of the resonance frequency dependence on optical power in cell T19EN over a time period of 460 h. The cell is kept at 80 °C throughout the whole period.
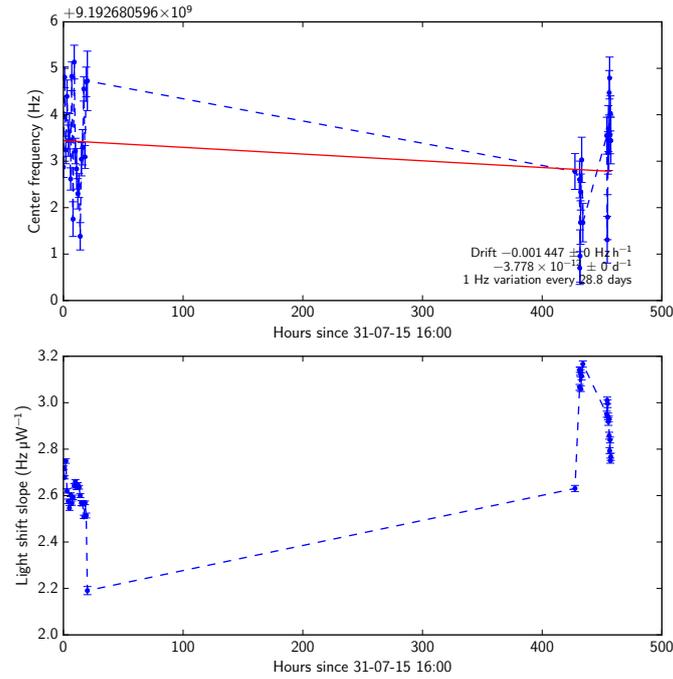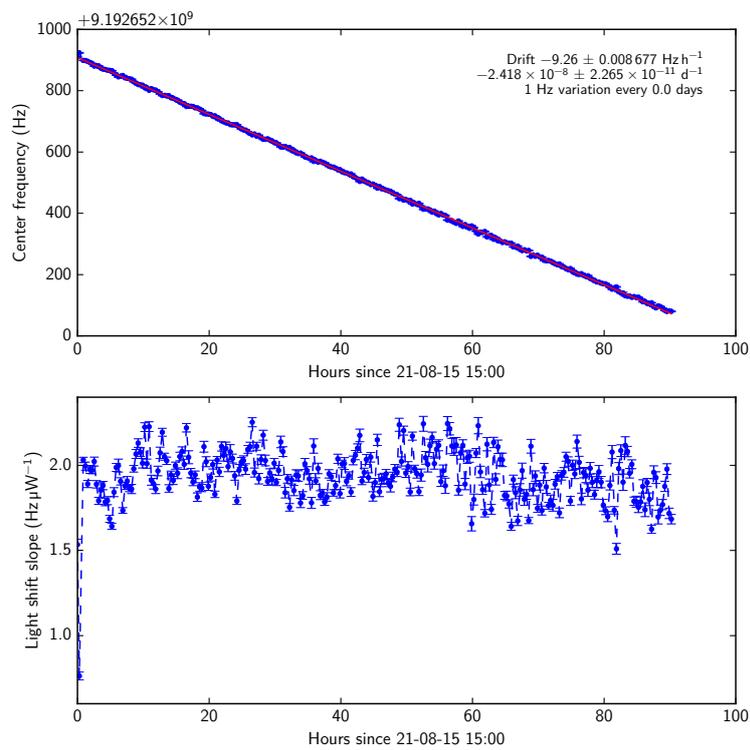
Figure 4.22: CPT resonance frequency extrapolated at null power and light shift slope evolution through a period of 460 h in a Cs-Ne cell (T19EN). Data is missing due a default of the laser frequency lock. The error bars correspond to the standard error resulting from the linear fit used for extrapolating at null optical power.

16 Torr, a drift rate of $-9.26\,\mathrm{Hz\,h^{-1}}$ was observed (Fig. 4.23). Considering a collisional shift coefficient around $1280\,\mathrm{Hz\,Torr^{-1}}$ for cesium in helium, this drift would indicate an helium pressure decrease rate of $7.2\,\mathrm{mTorr\,h^{-1}}$. The drift of $-2\,\mathrm{Hz\,h^{-1}}$ observed in the Cs-Ne-He cell (T14) is five times smaller then this value probably due to the temperature difference of their respective measurements and their different initial helium partial pressures.

Figure 4.23: CPT resonance frequency extrapolated at null power and light shift slope evolution through a period of 90 h in a Cs-He cell (T18B1). The initial pressure was around 16 Torr and the cell was kept at 65 °C. The error bars correspond to the standard error resulting from the linear fit used for extrapolating at null optical power.

Chapter conclusion

This chapter covered the characterization of microfabricated cells. The VCSEL and DFB benches mostly preexisted before this thesis. However, they were modified to perform measurement tasks automatically and a dedicated control software was developed. In particular, the cell temperature and the optical power are now controlled by the computer, allowing temperature dependences to be established autonomously. The impact of buffer gas pressure on the characteristics of the CPT signal was observed with the DFB setup. Those preliminary results tend to show that there is no precise optimum and pressures ranging from 60 Torr to 240 Torr yield equivalent figures of merit regarding the expected short-term stability, since the decreased contrast is compensated by a thiner linewidth as pressure increases. This behavior must still be confirmed in an actual clock configuration on the VCSEL setup. Solutions aiming at reducing light-shift contributions to the long-term instabilities may impose a more specific pressure value.

Reflective cells, presented in Section 3.3, have been characterized through CPT spectroscopy with the DFB setup. Despite a reduced cell volume, figures of merit almost twice as large as in transmissive cells could be observed. Remarkable contrasts up to 17 % were measured.

In order to increase the operating temperature of the cell and broaden the range of applications, a buffer gas mixture composed of neon and helium was characterized. The inversion temperature, initially limited to 80 °C with a single neon buffer gas, was increased up to 95 °C. However, a phenomenon of helium permeation was identified, leading to an important frequency drift rate. Finally, the long-term frequency drift of Cs-Ne cells was estimated by monitoring the clock frequency at null power over an extended period of time. A maximum relative frequency drift around $-3.8 \times 10^{-12}\,\mathrm{d}^{-1}$ was found, corroborating previous drift measurements. This value complies with the targeted long-term frequency stability.

Chapter 5

Wall coatings

5.1 Introduction

While the main technique to extend the lifetime of the hyperfine coherence is to confine alkali atoms in a buffer gas, the use of antirelaxation wall coatings, which are commonly used in hydrogen masers (Kleppner *et al.*, 1962), remains appealing for several reasons for millimeter-scale cells.

First, wall coatings are expected to counter the increased relaxation due to wall collisions, which is exacerbated at millimeter-scales. Indeed, it is common to use higher buffer gas pressures to reduce sufficiently this effect as cells are made smaller. However, this comes at the price of a reduced excited state lifetime, resulting in broadened optical absorption lines and lower pumping efficiencies. As a result, a higher laser power is required.

In addition, a coating would ideally sustain long hyperfine coherence relaxation times while ensuring that the excited state manifold stays resolved, which would allow to increase significantly the signal amplitude, for instance by using closed lambda or double lambda pumping schemes (Shah, 2007, Taichenachev *et al.*, 2005).

Besides, in an evacuated and wall-coated cell, atoms average effectively the magnetic field and the light field as they span the entire cell volume. Consequently, broadenings due to an inhomogeneous light-shift or magnetic field gradients could be attenuated, making the physics package design more tolerant to light intensity or magnetic field inhomogeneities. The laser beam could be made smaller without necessarily degrading the resonance figure of merit thanks to motion induced Ramsey narrowing (Breschi *et al.*, 2010). Even if the long-term frequency aging induced by coatings remains unclear, Budker *et al.* (2005) and Corsini *et al.* (2013) showed low frequency changes over several years in alkane-coated cells.

5.1.1 Literature survey

Paraffin-coatings such as polyethylene, Paraflint ($CH_3(CH_2)_nCH_3$), or tetracontane ($CH_3(CH_2)_{38}CH_3$), formed by long-chain alkane molecules, were pioneerly proposed by Ramsey (1957), first demonstrated by Robinson *et al.* (1958), studied by Brewer (1963), and later extensively by Bouchiat and Brossel (1966). These coatings have demonstrated to support up to 1×10^4 atom-wall collisions, leading to observed linewidths in centimeter-scale cells of a few hertz on either Zeeman (Budker *et al.*, 2002) or hyperfine transitions (Robinson and Johnson, 1982). More recently, Balabas *et al.* reported exceptional anti-relaxation properties of alkene-based coatings (C_nH_{2n+1}). Indeed, polarized alkali-metal vapor with minute-long transverse Zeeman population and coherence lifetimes were demonstrated in a $3\,cm$ diameter cell, which corresponds to about 1×10^6 polarization preserving bounces (Balabas *et al.*, 2010b,a). For clock applications, it has to be noted that comparable microwave hyperfine frequency shifts and linewidths have been recently measured between paraffin-coated and alkene-coated Rb cells (Corsini *et al.*, 2013, Budker *et al.*, 2005). However, a drawback of paraffin and alkene-based coatings, recently studied and investigated in detail using surface science techniques (Seltzer *et al.*, 2010), is their relatively low-temperature melting point of about $85\,°C$ and $35\,°C$ to $100\,°C$, respectively (Balabas *et al.*, 2010b,a). This feature prevents them from being used in microfabricated vapor cells because of the high temperature of the anodic bonding process. In addition, cell temperatures higher than $80\,°C$ are usually required in miniature atomic clocks.

On the other hand, chemisorbed molecules can withstand much higher temperatures than physisorbed molecules. In this respect, self-assembled monolayers, formed when organosilanes chemically bond to silanols on silica surfaces, have therefore been envisioned and OTS layers appeared as particularly interesting candidates.

In the presence of rubidium, multilayer and monolayer OTS were found to withstand 170 °C and 190 °C, respectively (Seltzer and Romalis, 2009). Seltzer *et al.* (2007) reported the measurement of up to 2100 collisions before the population relaxes (T_1) in a potassium vapor cell with OTS multilayers and typically 25 bounces with OTS monolayers in rubidium vapor (Seltzer *et al.*, 2008). Through measurements of hyperfine resonance linewidths and frequency shifts, Yi *et al.* (2008) demonstrated in a 8 mm side cubic vapor cell that rubidium atoms collide up to 40 times with the cell walls before coherence relaxation and estimated their adsorption energy to be 0.065 eV. By measuring relaxation rates in rubidium vapor cells, Camparo *et al.* (1987) reported about 5 collisions with other silane materials. More recently, Straessle *et al.* (2014) reported a microfabricated vapor cell with OTS anti-relaxation coating. It was demonstrated that the coherence was preserved after 11 collisions with the walls in a double resonance rubidium clock setup (more details can be found in Straessle (2013)).

5.1.2   Adaptation to microfabricated cells

In FEMTO-ST, we proposed an original buffer-gas filled Cs vapor microcell fabrication and filling technology (Hasegawa *et al.*, 2011b) that uses post-activation of Cs vapor in the hermetically sealed cell through local laser heating of a Cs pill dispenser. Since no alkali vapor is present during the anodic bonding process and according to Fedchak *et al.* (1997), we can expect the OTS coating to survive a temperature of 350 °C under vacuum. This procedure could be well-adapted for the development of OTS-coated microcells since anodic bonding process could be operated in optimal conditions at such elevated temperatures. In that sense, we investigate here the use of OTS coatings in cesium vapor cells for compact CPT-based atomic clocks applications and potentially for miniature atomic clocks or atomic devices. Interactions between an OTS coating and cesium atoms have only been reported once, by Stephens *et al.* (1994).

First attempts to deposit silane coatings in microcells have been performed during the MAC-TFC project (Hasegawa *et al.*, 2008, Gorecki *et al.*, 2009, Douahi *et al.*, 2008). Octadecyltrimethoxysilane (OTMS) was used as precursor reagent. Methoxysilane is less reactive to humidity than chlorosilane and potentially easier to use than OTS. The layers were characterized by contact angle measurements and spectroscopic ellipsometry. Preliminary studies seemed to indicate that the coating could indeed withstand the temperature of anodic bonding.

Pursuing this study, our approach consisted in developing a coating procedure in classical centimeter-scale cells, before applying it to microfabricated cells. We produced 5 OTS-coated centimeter-scale Cs vapor cells and several wafers of OTS-coated microfabricated cells. This chapter summarizes the coating fabrication and filling procedures, and details the characterization of these cells.

These characterization steps include CPT spectroscopy, hyperfine clock frequency shift measurements, T_1 and T_2 relaxation times measurements and measurements of the coating adsorption energy. The detection of Ramsey fringes in a Cs-OTS cell is reported. The potential of Cs-OTS cells in atomic clocks applications is finally discussed.

5.2   Experiments with centimeter-scale cells

5.2.1   Cell fabrication and coating procedures

This section reports on the coating processes employed for the realization of the centimeter-scale cells. In a first batch, two cells (Cs-OTS1 and Cs-OTS2) were coated using a vapor phase technique. Three cells (Cs-OTS3, Cs-OTS4 and Cs-OTS5) were coated using a liquid phase technique, in a second batch. The cells were made of borosilicate glass[1].

5.2.1.1   Vapor phase coated cells (Cs-OTS1 and Cs-OTS2)

Cell preparation.   Empty commercial cells[2] with a diameter of 15 mm and a length of 15 mm were used. The stem of the cells was reworked by glass-blowing techniques to reduce its section down to 600 μm so as to reduce the stem effect. The cells were cleaned with piranha solution (H_2SO_4/H_2O_2) and rinsed with deionized water. The cleaned cells were dried in an oven at 150 °C for 20 min. Since the inner diameter of the capillary linking the cell to its sidearm is narrow, the introduction of any liquid inside the cell is impeded by capillary

---

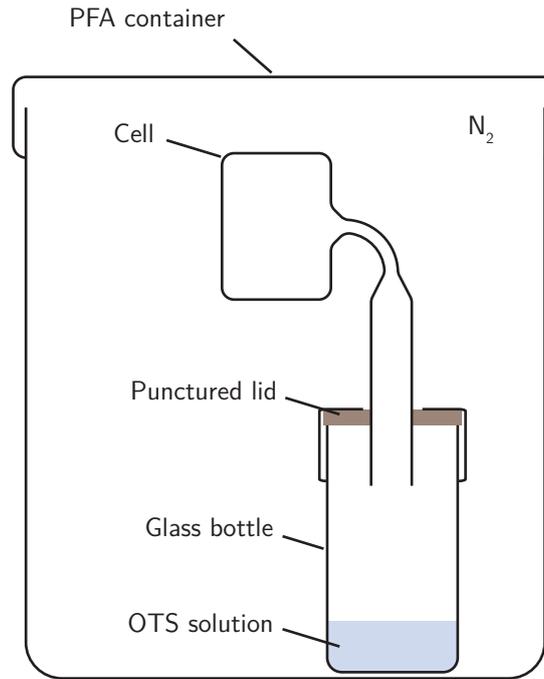[1]Borofloat33 from Schott, Inc.

[2]from Hellma, Inc.

Figure 5.1: Vapor phase OTS coating process

action. Consequently, the sidearm of the cell was immersed in the solution and the pressure in the glovebox was alternatively decreased and increased to allow the gas contained in the cell to be gradually replaced by the solution.

Coating. Each cell was hermetically connected to a small glass bottle containing a few microliters of OTS [3]. This step was performed in a glovebox under a dry nitrogen (N_2) atmosphere to prevent OTS oxidation. Still connected to the bottle, the assembly was enclosed in a PFA (a perfluoroalkoxy polymer) container. In this container, the cell was taken out of the glovebox and baked in an oven at 150 °C for 4 h to let OTS evaporate and polymerize on the cell inner surface. A schematic representation of the setup is shown in Fig. 5.1. The cell was later returned to the glovebox, disconnected from the bottle, rinsed with acetone, and dried. After this preparation done at FEMTO-ST, the cells were packaged under ambient air and sent to SYRTE for sealing.

Filling and sealing. The cells were connected to a glass manifold evacuated with a turbomolecular pump below 1×10^{-7} mbar. Cesium (from Alfa Aesar, Inc.) was distilled in the sidearms of the cells before being finally sealed off. The setup was similar to the one described by Kozlova (2012). During this step, 2 coated cells and 1 uncoated reference cell were fabricated. An additional cell, named Cs-N_2-Ar, was filled with a N_2-Ar buffer gas mixture of total pressure 15 Torr and pressure ratio $r = P_{Ar}/P_{N_2} = 0.4$. The diameter and the length of this last cell are 10 mm.

Figure 5.2 shows a photograph of the OTS-coated cell. The presence of "milky" patches, layers, or thin droplets on the cell inner walls of the coating material seem to indicate the OTS has indeed been deposited.

5.2.1.2 Liquid phase coated cells (Cs-OTS3, Cs-OTS4 and Cs-OTS5)

Cells Cs-OTS3, 4 and 5 are cylindrical, 2 cm long with a diameter of 2 cm. The coating procedure for cells Cs-OTS3, 4 and 5 followed a procedure close to the one described by Seltzer *et al.* (2008). To introduce the different solutions in the cells more easily than the previous method, thin PTFE capillaries[4] were used (400 μm outer diameter) to pull out the air from the cell and let the solution, in which it was immersed, fill the cell. The liquid was then removed by flowing N_2 through the capillary. Wasted liquids were retained in a glass bottle, which sustains under or over-pressurization. The entire coating process is detailed in Table 5.2. After the coating process, the glass that have been in contact with the solution exhibits a pronounced hydrophobic

---

[3]from Sigma-Aldrich, Inc.
[4]from Bola, Bohlender GmbH

Figure 5.2: Photograph of the OTS-coated cell

1.	Cell cleaning in piranha (H_2SO_4/H_2O_2)
2.	Rinsing with deionized water
3.	Drying in an oven at $150\,°C$ for $20\,min$
4.	Connection of the cell to a bottle containing OTS
5.	Enclosure in a PFA container (under N_2 atmosphere, in a glove box)
6.	Heating in an oven at $150\,°C$ for $4\,h$
7.	Rinsing with acetone and drying
8.	Packing under ambient air (2013-06-20)
9.	Cesium filling and off-sealing (2013-09-30)

Table 5.1: Summary of the coating procedure in vapor phase (Cs-OTS1 and 2).

behavior. The liquid phase setup is shown on Fig. 5.3 and Fig. 5.4. This time, the period between coating and sealing was minimized. Special care was taken to avoid a potential contamination from ambient air by transporting the cells to SYRTE in a desiccator under rough vacuum. To provide a reference, we produced two additional evacuated cells without coating with the same dimensions in the same batch.

5.2.2   Characterization of cells Cs-OTS1 and Cs-OTS2

Spectroscopy of Cs-OTS1 and Cs-OTS2 cells was performed by Moustafa Abdel Hafiz. Through linear absorption measurement and CPT measurements, we noted that Cs-OTS1 and Cs-OTS2 gave similar results. The following is focused on results of the cell Cs-OTS2, called Cs-OTS for short.

1.	Cell cleaning in piranha (H_2SO_4/H_2O_2)
2.	Rinsing with deionized water ($\times 3$)
3.	Methanol rinsing
4.	DI water rinsing
5.	Drying at $150\,°C$ under vacuum for $1\,h$
6.	Preparation of $100\,mL$ of OTS solution (hexanes/chloroform 4:1 + $100\,µL$ of OTS)
7.	Cell filling of OTS solution ($5\,min$)
8.	Ambient air flow ($5\,min$)
9.	Chloroform rinsing ($\times 3$)
10.	Drying under vacuum for $14\,h$ at $170\,°C$
11.	Transportation to SYRTE under rough vacuum (within a few hours)
12.	Connection to filling station and baking at $170\,°C$ for $24\,h$
13.	Cesium filling and off-sealing (2014-10-08)

Table 5.2: Summary of the coating procedure in liquid phase (Cs-OTS3, 4 and 5).
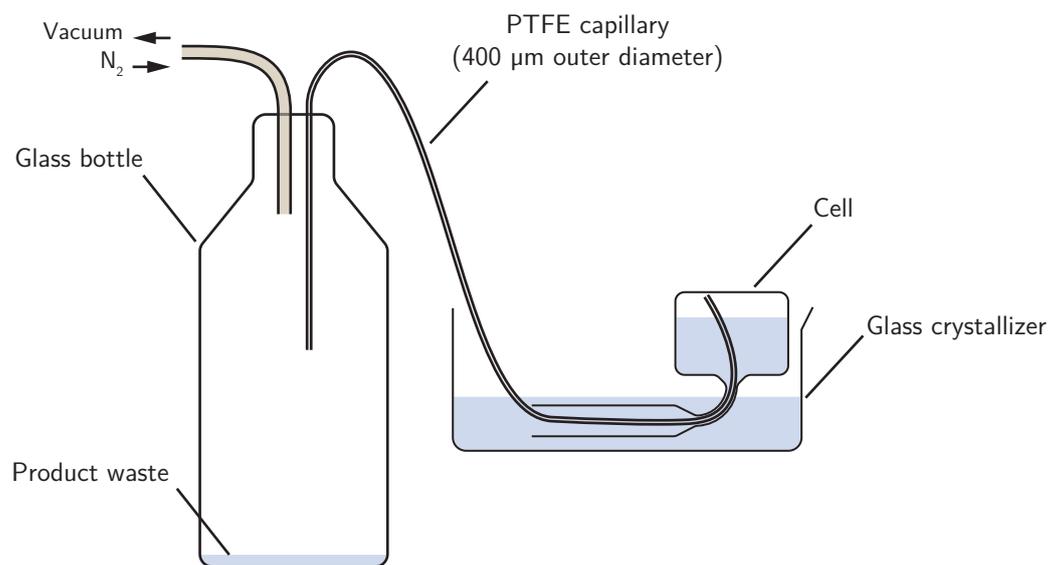
Figure 5.3: Liquid phase OTS coating process
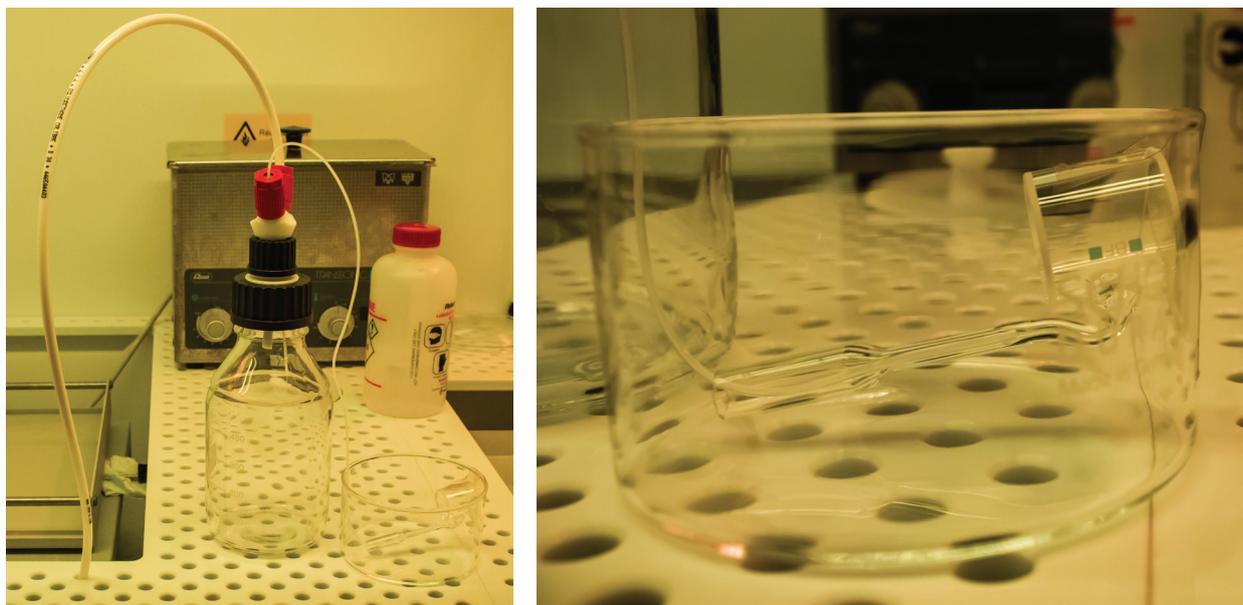
Figure 5.4: Liquid phase OTS coating setup
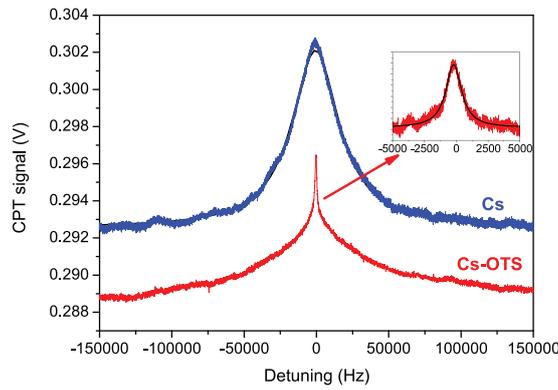
Figure 5.5: CPT clock resonance in the Cs-OTS cell compared to the one detected in the evacuated Cs cell. The laser power incident on the cell is $100\,\mu W$. The cell temperature is $35\,°C$. Experimental data for the evacuated Cs cell are approximated by a Lorentzian fit function. The narrow structure of the resonance in the Cs-OTS cell (figure inset) is approximated by a Lorentzian fit function. The laser beam diameter is $15\,mm$. For the Cs-OTS cell, the slight asymmetry of the CPT resonance is attributed to a minor thermal transient of the clock set-up table during the scan of the CPT resonance.
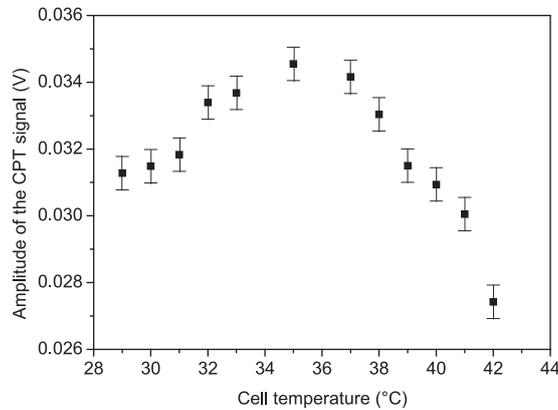
Figure 5.6: Amplitude of the CPT signal (narrow structure) in the Cs-OTS cell versus the cell temperature. The laser power is $600\,\mu W$. The static magnetic field is $892\,mG$.

5.2.2.1   Continuous regime CPT spectroscopy

Figure 5.5 reports, for identical experimental conditions, the CPT clock resonance in the Cs-OTS cell and in the evacuated Cs cell for a total incident laser power of $100\,\mu W$. Both cells exhibit about the same off-resonance background level, i.e., the same laser power absorption. The CPT resonance in the pure Cs cell is well approximated by a Lorentzian function. The dual-structure of the dark resonance, signature of the anti-relaxation effect, is obvious in the OTS-coated cell. The pedestal of the resonance is characterized by a Doppler-broadened structure, whereas the top of the resonance is narrowed thanks to the coating material. As shown in the figure inset, the narrow structure is well approximated by a Lorentzian function with a linewidth of $1486\,Hz$.

Figure 5.6 shows the signal of the CPT resonance (narrow structure) in the Cs-OTS cell versus the cell temperature. The amplitude of the CPT signal is found to be maximized for a cell temperature of about $35\,°C$. The same behavior was observed for the broad structure signal. The contrast of the narrow structure was found to increase from $1.4\,\%$ to $2.6\,\%$ from $29\,°C$ to $42\,°C$. Note that the CPT linewidth of both narrow and broad structures was measured to be reduced very slightly from $30\,°C$ to $50\,°C$. The CPT signal-to-linewidth ratio is optimized at $35\,°C$, and most of the following results are obtained at this temperature.

For further investigation, Fig. 5.7 shows the linewidth of the CPT resonance in the three different Cs vapor cells versus the total laser power P for a cell temperature of $35\,°C$. In an evacuated Cs cell, the main effects contributing to the CPT resonance linewidth are the Doppler broadening, the power broadening, the atom-light limited transit time, and the Cs-Cs spin-exchange collisions.

In a Doppler-broadened system, as explained by Javan *et al.* (2002) for a similar experiment of electromagnetically induced transparency (EIT) and by Radonjić *et al.* (2009), it can be shown that the CPT linewidth is
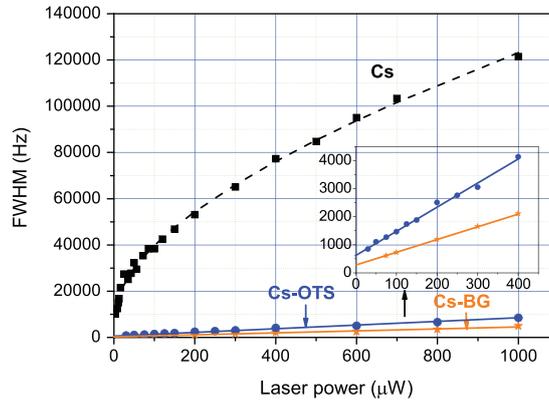
Figure 5.7: Linewidth of the CPT resonance in vapor cells versus the laser power for: evacuated Cs cell (squares), Cs-OTS cell narrow structure (circles), and Cs-N$_2$-Ar cell (stars). Error bars are covered by data points. The cell temperature is 35 °C. Data of the evacuated Cs cell are fitted by the function $a + b\sqrt{P} + cP$ (dashed line, P the laser power, a, b, and c are constants). Experimental data in the Cs-OTS cell and the buffer-gas filled cell are fitted by a linear function. The figure inset is a zoom for Cs-OTS and Cs-N$_2$-Ar cells

proportional to the square root of intensity for low laser intensity of the driving field and is independent of the Doppler width. This is an effect similar to the laser-induced line narrowing effect (Kazakov *et al.*, 2007). At higher laser intensities, the usual power broadening effect is recovered with a CPT linewidth proportional to the laser intensity. This behavior is clearly demonstrated in our measurement, where the CPT linewidth-laser power dependence curve shows two distinct regimes with a sudden linewidth decrease for laser powers lower than about 50 µW. In this laser power region, the contribution of the Doppler broadening is gradually reduced as the laser intensity is decreased. For a cell temperature of 35 °C, the CPT linewidth extrapolated at null laser power in the evacuated Cs cell is measured to be 7 kHz, in excellent agreement with theoretical calculations yielding a total linewidth of 7.07 kHz (sum of spin-exchange and transit-time contributions). The transit time contribution is given by $1/\pi t_t$ where t_t is the mean time of flight between two wall collisions. We note $t_t = \ell/v_m = 45\,\mu s$ with $v_m = \sqrt{8kT/(\pi m)} = 222\,\text{m s}^{-1}$ being the mean atomic velocity, T the cell temperature, k the Boltzmann constant and m the mass of the Cs atom. We note $\ell = 10\,\text{mm}$ the mean free path between two wall collisions in a cylindrical cell of radius R and length L such as $1/\ell = (1/R + 1/L)/2$ (Vanier and Audoin, 1989). The transit time limited linewidth is 7.05 kHz. The spin exchange relaxation term is calculated at 35 °C using Eq. (2.26):

$$\Delta\nu_{\text{SE}} = \frac{1}{\pi\gamma_{\text{SE}}} = \frac{11}{16}n_{\text{Cs}}v_r\sigma_{\text{SE}}\frac{1}{\pi}, \qquad (5.1)$$

Here, n_{cs} is the cesium density (1.2×10^{11} atom/cm^3, Taylor and Langmuir, 1937), v_r is the average relative velocity of cesium atoms, $v_r = \sqrt{2}v_m = 313\,\text{m s}^{-1}$, and σ_{SE} is the Cs spin-exchange cross-section (2.18×10^{-14} cm^2, Vanier and Audoin, 1989), yielding $\Delta\nu_{\text{SE}} = 18\,\text{Hz}$. For the Cs-OTS cell and the buffer-gas filled Cs cell, experimental widths in hertz are well fitted by linear functions $634 + 8.6P$ and $268.9 + 4.6P$, respectively, with P in µW. The CPT linewidth extrapolated at null laser power is about 10 times narrower in the Cs-OTS cell compared to the pure Cs cell but 2.4 wider than in the buffer-gas filled Cs cell. In the Cs-OTS cell, the laser power broadening is about 13 times smaller than in the evacuated Cs cell and 2 times bigger than in the Cs-N$_2$-Ar cell. In a cell coated with an anti-relaxation material, atoms collide with the surface, stick to it for a characteristic time τ_s, and eventually return to the vapor. Attraction of the atom to the cell walls is mainly dominated by the long-range van der Walls force F that depends on the dielectric constant ε of the wall and the electric dipole operator D of the atom such as $F \propto (\varepsilon - 1)/(\varepsilon + 1)D^2$ (Stephens *et al.*, 1994). The cesium energy levels are shifted during the atom-surface interaction, so that the phase of the hyperfine coherence of escaping atoms is shifted by a mean amount ϕ at each collision, which depends on the surface characteristics. Reducing the wall surface attraction through the choice of a surface with low polarizability and choosing a coating material with low dielectric constant will help to reduce the atom-wall interaction time and to make the collision more elastic. This physisorption process can be characterized by an adsorption energy E_a, related to the sticking time τ_s, which translates the kinetic energy an atom must have to escape the coating surface attraction and in turn the period the alkali atoms spend physically adsorbed on the wall of the cell. The adsorption energy can be estimated from the measurement of the clock frequency shift δ_ν,
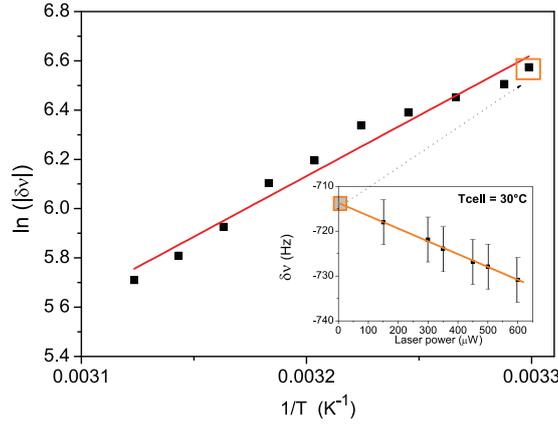
Figure 5.8: Logarithm of the frequency shift $|\delta_\nu|$ versus the inverse of the cell temperature $1/T$ with T in kelvins. Experimental data are fitted by a linear function from which is extracted the value of E_a. In the main figure, error bars are covered by data points. The inset figure shows an example for a cell temperature of $30\,°C$ of light-shift measurement used to extract the temperature frequency shift at null laser power.

defined as the difference between the actual clock frequency and the exact unperturbed cesium atom frequency (9.192 631 770 GHz), versus the cell temperature T as: (Goldenberg *et al.*, 1961, Vanier *et al.*, 1974)

$$|\delta_\nu| \propto E_a \exp\left(\frac{E_a}{kT}\right). \tag{5.2}$$

We measured the clock frequency versus the cell temperature (from $30\,°C$ to $47\,°C$) to extract the value of E_a. The temperature of the cesium reservoir was kept slightly lower than the temperature of the cell wall to prevent deposition of cesium onto the wall coating. For each cell temperature, the clock frequency is measured for different values of laser intensity and extrapolation to null laser intensity is performed as shown on the inset of Fig. 5.8.

A negative frequency shift of a few hundreds of hertz is measured as usually observed on wall-coated cells (Corsini *et al.*, 2013, Yi *et al.*, 2008). At high temperatures, an atom spends less time on the wall and is found to experience a smaller frequency shift magnitude. The shift rate is measured to be $+24.6\,\mathrm{Hz\,K^{-1}}$. According to Eq. (5.2), the plot of $\ln|\delta_\nu|$ against $1/T$ (see Fig. 5.8) is a straight line of slope E_a/k. The fitting data of Fig. 5.8 leads to $E_a = 0.42\,\mathrm{eV}$ with a statistical uncertainty of $0.03\,\mathrm{eV}$. This value corresponds to a sticking time of the atom on the surface $\tau_s = \tau_0 \exp\left(E_a/kT\right) \approx 29\,\mu s$, where $\tau_0 \approx 1 \times 10^{-12}\,s$ (Stephens *et al.*, 1994). The value of E_a is in good agreement with the value $0.40(3)\,\mathrm{eV}$ reported by Stephens *et al.* (1994), the only one we could find in the literature for Cs-Pyrex-OTS. It is worth noting that the measurement of Stephens *et al.* is based on a completely independent method, namely, the atomic number density measurement. For Cs-Paraflint interaction, E_a was estimated to be $0.8\,\mathrm{eV}$ (Goldenberg *et al.*, 1961). This value remains higher than the typical value of about $0.1\,\mathrm{eV}$ reported by other researchers in rubidium vapor cells coated with paraffin (Brewer, 1963, Bouchiat and Brossel, 1966) or even $0.065\,\mathrm{eV}$ in OTS-coated Rb cells (Yi *et al.*, 2008).

The frequency shift of the clock transition is related to the mean phase shift per wall collision ϕ as: (Budker *et al.*, 2005, Goldenberg *et al.*, 1961, Vanier *et al.*, 1974)

$$\delta_\nu = \frac{\phi}{2\pi t_t}. \tag{5.3}$$

The phase shift values, computed from data of Fig. 5.8, are shown in Fig. 5.9 as a function of the cell temperature. On the limited experimental temperature range around $39\,°C$, the phase shift can be fitted by a straight line of equation:

$$\phi = -0.138(2) + 0.0074(3)(T_{cell} - 39), \tag{5.4}$$

with T_{cell} the cell temperature in degree Celsius. $\phi = -168(2)\,\mathrm{mrad/collision}$ at $35\,°C$ and $-94(2)\,\mathrm{mrad/collision}$ at $45\,°C$. For comparison, ϕ was measured to be $-90(10)\,\mathrm{mrad/collision}$ for Cs-Paraflint coating at an unspecified temperature (Goldenberg *et al.*, 1961), $-19\,\mathrm{mrad/collision}$ (Straessle *et al.*, 2014) and $-65\,\mathrm{mrad/collision}$ (Yi *et al.*, 2008) in Rb-OTS cells of smaller dimensions heated at $60\,°C$. ϕ is proportional to $E_a \exp\left(E_a/kT\right)$ and E_a is proportional to the polarizability of the atom (Goldenberg *et al.*, 1961). As cesium has the largest
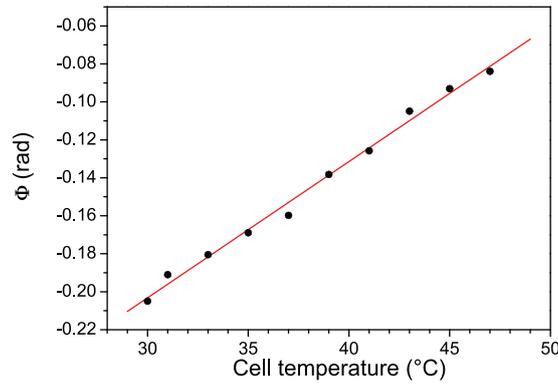
Figure 5.9: Phase shift per wall collision as a function of the cell temperature. The solid line is a linear fit. Error bars are covered by data points.

polarizability, a larger phase shift is expected for cesium than for rubidium or potassium. The actual phase shift experienced by an atom colliding the wall (adiabatic collision) is assumed to follow a Gaussian distribution of mean ϕ and of variance ϕ^2 (Budker *et al.*, 2005, Goldenberg *et al.*, 1961). Here, we do not take into account the atomic velocity distribution and t_t is considered as a constant. After n collisions, the accumulated phase shift distribution $G(n, \phi)$ is also Gaussian of mean $n\phi$ and of variance $n\phi^2$. The probability of experiencing n collisions during a time t is assumed to obey a Poisson distribution $p(n,t) = \exp\left(-t/t_t\right)(t/t_t)^n/n!$ (Budker *et al.*, 2005). As a result, the mean and the variance of the phase shift after a time t are:

$$\phi_m = \sum_{n=0}^{\infty} p(n,t)n\phi = \phi\frac{t}{t_t}, \tag{5.5}$$

$$\sigma_\phi^2 = \langle \phi^2 \rangle - \phi_m^2 = 2\phi\frac{t}{t_t} \tag{5.6}$$

The lineshape L_S of the CPT resonance is given by the weighted sum of detuned Lorentzian profiles $L(\delta, \gamma)$:

$$L_S(\delta, \gamma) = \sum_{n=0}^{\infty} \left(p(n,t) \int_{-\infty}^{+\infty} L(\delta - \phi/t_t, \gamma)G(n, \phi)d\phi \right) \tag{5.7}$$

with δ as the angular frequency Raman detuning and γ as the half-width of the resonance. We have no analytical expression for L_S, which is a weighted sum of Voigt profiles. Nevertheless, as shown in Fig. 5.5, the lineshape is well fitted by a Lorentzian profile. Budker *et al.* (2005) have shown that the contribution of the phase dispersion to the line width of a "classical" microwave transition is (in hertz): (Rahman and Robinson, 1987)

$$\Delta\nu_\phi = \frac{\phi^2}{\pi t_t}. \tag{5.8}$$

At null laser intensity, the width of a CPT resonance or a "classical" resonance is given by the same coherence relaxation terms, thereby we can assume that Eq. (5.8) is valid in our case. The FWHM $\Delta\nu$ can be written as the sum of different contributions as in Eq. (2.34):

$$\Delta\nu = \Delta\nu_{\text{WC}} + \Delta\nu_\phi + \Delta\nu_{\text{SE}} + \Delta\nu_{\text{ST}}. \tag{5.9}$$

Here, these terms are evaluated for a cell temperature of 35 °C. $\Delta\nu_{\text{ST}}$ is the relaxation term due to atoms incoming in the stem. We assume that an atom impacting the stem region, of radius r, is lost and that this probability is proportional to the stem fractional area with respect to the whole cell area. It follows (from Eq. (2.33)):

$$\Delta\nu_{\text{ST}} = \frac{1}{\pi t_t}\frac{r^2}{2R(R+L)}. \tag{5.10}$$

We estimate $r \approx 0.8$ mm and $\Delta\nu_{\text{ST}} = 13$ Hz. The spin-exchange term $\Delta\nu_{\text{SE}}$ is about 18 Hz. The dephasing term of Eq. (5.8) is 200 Hz. The $\Delta\nu_{\text{WC}}$ term takes into account other relaxation contributions induced by wall collisions, e.g., population and hyperfine coherence relaxations or velocity changes such that the atoms go out
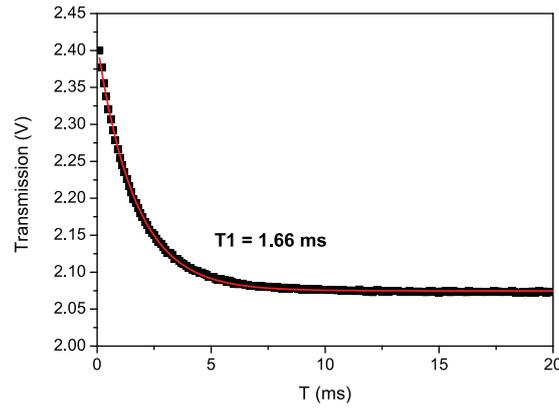
Figure 5.10: Measurement of the T_1 relaxation time in the Cs-OTS cell. The total laser power incident on the cell is $500\,\mu\text{W}$. The actual power seen by the atoms (power of one sideband) is about one half of the total laser power. The cell temperature is $35\,°\text{C}$. The static magnetic field is $900\,\text{mG}$. Squares: data, solid line: fitted exponential function.

of optical resonance by Doppler effect and are lost for the signal. As $\Delta\nu = 634\,\text{Hz}$ at null laser intensity, $\Delta\nu_{\text{WC}}$ is estimated to be about $400\,\text{Hz}$. The coating can be characterized by a mean number n of useful bounces before the loss of the atom or the loss of atomic phase memory. n is equal to the ratio of the relaxation term due to a single wall collision to the relaxation term due to wall collisions in the coated cell:

$$n \approx \frac{1/t_t}{\pi(\Delta\nu_{\text{WC}} + \Delta\nu_\phi)} \tag{5.11}$$

We get $n \approx 12$ bounces. This result is of the same order of magnitude as the one (11 bounces) reported by Straessle *et al.* (2014) in Rb-OTS cells and as those (20–30 bounces) reported by Yi *et al.* (2008), and much smaller than results obtained with paraffin or alkenes.

5.2.2.2   Measurements of population lifetime T_1

Additional characterization of the OTS-coated cell was realized through measurements of T_1 relaxation time in the dark using the Franzen's technique (Franzen, 1959). Atoms interact with a sequence of optical pulse trains. Atoms are first optically pumped during a constant τ_p duration pulse ($\tau_p = 3\,\text{ms}$) in the hyperfine ground state ($F = 4$) with a single laser frequency. Then, light is switched off and atoms relax (($F = 4$) population) in the dark during a dark time T. Each cycle, the duration of the time T is slightly incremented. The next light pulse allows to detect the atomic signal by measuring the laser power transmitted through the cell. The signal is measured $20\,\mu\text{s}$ after the beginning of the pulse. It is defined as the average value of 25 successive measurements realized in a $25\,\mu\text{s}$ duration measurement window of the same light pulse. This study allows to measure how the atomic system, initially prepared in a determined initial state, evolves to the Boltzmann equilibrium. It is a measure of the hyperfine population relaxation performed on all Zeeman sublevels. Figure 5.10 reports, for an incident laser power of $500\,\mu\text{W}$, the measurement of the relaxation time T_1 in the dark of the hyperfine level ($F = 4$) population. A single laser frequency is obtained by detuning the carrier frequency of $9\,\text{GHz}$, tuning consequently a single sideband to the atomic resonance. For information, we noted that the polarization scheme (circularly polarized beam or push-pull optical pumping) and the static magnetic value had a negligible impact on the measured value of the T_1 relaxation time. Experimental data are well fitted by an exponential decay function with a time constant $T_1 = 1.660(7)\,\text{ms}$. Such a time constant corresponds to about 37 useful bounces. Figure 5.11 shows the evolution of the measured T_1 value function of the laser power. For laser power higher than $300\,\mu\text{W}$, the value of T_1 is measured to increase slightly with the laser power before saturation above $1\,\text{mW}$. On the opposite, below $300\,\mu\text{W}$, the T_1 value increases with decreasing laser power. Clearly, there are two opposite phenomena that are not yet identified and need further investigations.

5.2.2.3   Motion-induced Ramsey narrowing and Ramsey spectroscopy in Cs-OTS cells

In a wall-coated cell without buffer gas, the ballistic transport mechanism is distinct from the diffusive behavior in buffer gas-filled cells. Atoms move randomly from wall to wall with constant velocity and direction. For
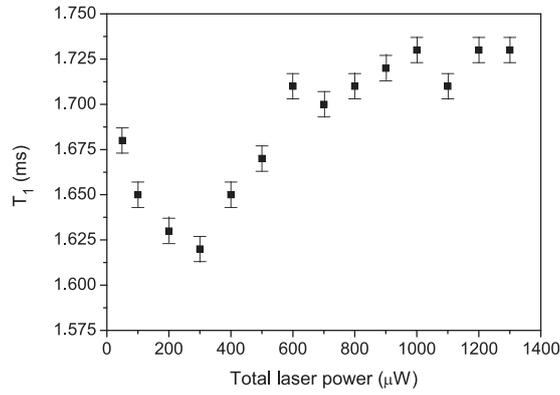
Figure 5.11: Measurement of the T_1 relaxation time in the Cs-OTS cell versus the total laser power incident on the cell. The actual power seen by the atoms is about one half of the total laser power. The cell temperature is $35\,°C$. The static magnetic field is $900\,mG$.

small beam diameters compared to the cell diameter, repeated interactions of atoms with the light fields are equivalent to a sequence of randomly spaced Ramsey pulses in which the two optical fields are turned on and off. The free motion of the polarized atomic spins in and out of the optical interaction region before spin relaxation induces a well-known Ramsey narrowing of the CPT resonance, well studied and described in paraffin-coated cells (Breschi *et al.*, 2010, Klein *et al.*, 2011). Additionally, in our experiments, the residual Doppler effect on the clock transition is reduced by a Dicke-type narrowing, the cell characteristic length ($1.5\,cm$) being smaller than the Cs atom ground-state microwave wavelength ($3.2\,cm$). We investigated the CPT resonance lineshape for different beam diameters in Cs-OTS cells. Figure 5.12(a) shows a CPT resonance in the Cs-OTS cell for a beam diameter of $8\,mm$ and a laser power of $100\,µW$. The lineshape has a Doppler-broadened structure of linewidth $43\,kHz$, in correct agreement with the atom transit time through the interaction volume. The narrow central peak exhibits a width of $1924\,Hz$. Figure 5.12(b) shows the linewidth of the CPT resonance narrow structure versus the laser intensity for different laser beam diameters ($8\,mm$, $10\,mm$ and $12\,mm$). For low laser intensities, which are the case for each experimental data point of the figure, the width of the narrow structure increases linearly with laser intensity. Most significantly, we observe a decrease of the linewidth with the volume of the interaction region at constant optical intensity. Indeed, smaller beams allow longer phase evolution of atoms in the dark, making the CPT narrow structure lineshape narrower. Simultaneously, as observed by Breschi *et al.* (2010), we measured an increase of the CPT resonance amplitude with the laser beam radius. This can be explained qualitatively as an increase of the number of interacting atoms in the interrogation volume. On the contrary, we observed that the broad structure linewidth is increased with smaller beam diameter, which corresponds to a reduced atom-light interaction time. The Ramsey picture of bright and dark times also indicates that the narrow structure linewidth should saturate with increasing intensity, rather than continue power broadening as it would in most vapor-cell systems. This occurs because, for sufficient intensity, light fields optically pump atoms into the dark state in a single pass through the beam. This behavior was clearly observed by Klein *et al.* (2011). Additionally, the experimental setup described above was used to detect CPT-Ramsey fringes in the Cs-OTS cell. Figure 5.13 shows a CPT-Ramsey fringe detected in the Cs-OTS cell. Atoms interact with light in a pulsed CPT sequence where the CPT pumping time τ_p is $3\,ms$ and the free evolution time in the dark T_R is $0.2\,ms$. The laser power is $650\,µW$. Figure 5.14 shows the evolution of the central Ramsey fringe amplitude versus the Ramsey time T_R. Experimental data are well fitted by an exponential decay function with a time constant of $0.46(5)\,ms$. This value can be interpreted as an experimental estimation of the CPT hyperfine coherence lifetime T_2. This value of T_2 is in correct agreement and slightly smaller than the one extracted from the zero-intensity CPT linewidth measurement of $634(50)\,Hz$ reported in Fig. 5.7, which yields a T_2 time of $T_2 = 1/(\pi\Delta\nu) = 0.50(4)\,ms$. Note that the contribution of the phase shift dispersion term to the relaxation rate of the Ramsey fringes is the same as in the CW interrogation case. When the phase distribution is Gaussian of variance σ_ϕ^2, it can be shown that the fringe amplitude scales as $e^{\sigma_\phi^2/2}$. Here, $\sigma_\phi^2 = (t/t_t)\phi^2$ (see Eq. (5.6)), which is equivalent to a time constant t_t/ϕ^2, i.e., the same as the one of the continuous measurement deduced from Eq. (5.8).
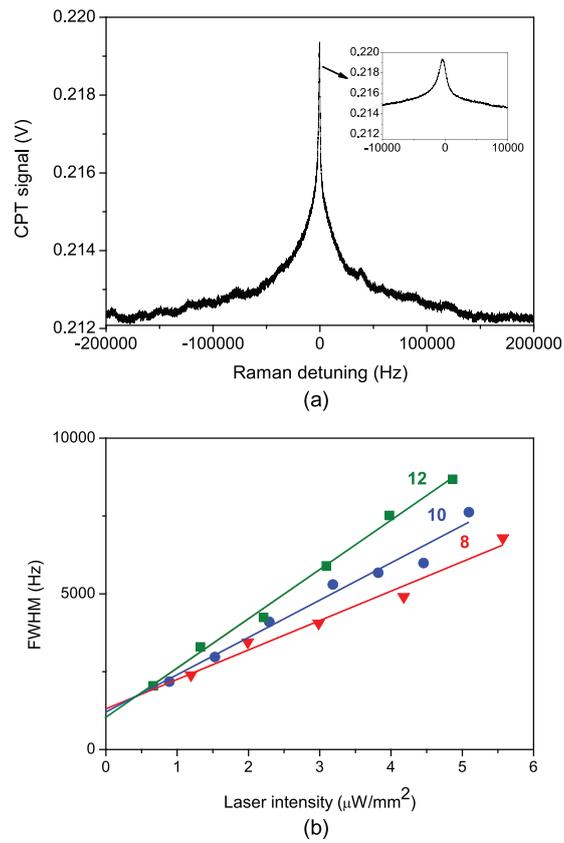
Figure 5.12: (a) CPT resonance in the Cs-OTS cell for a beam diameter of 8 mm. The laser power is 100 μW. (b) Linewidth of the CPT resonance narrow structure versus the laser intensity for different laser beam diameters (8 mm, 10 mm and 12 mm). Error bars are covered by data points.
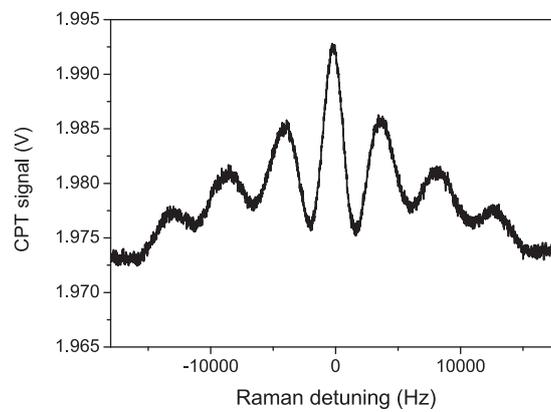

Figure 5.13: CPT-Ramsey fringe detected in a Cs-OTS cell. $\tau_p = 2\,\text{ms}$, $T_R = 0.2\,\text{ms}$. The laser power is 650 μW. The cell temperature is 35 °C. The beam diameter covers the whole cell diameter.
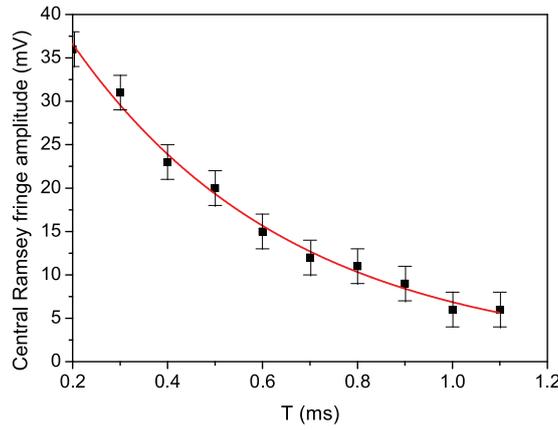
Figure 5.14: Amplitude of the central CPT-Ramsey fringe detected in a Cs-OTS cell versus the Ramsey time T_R. The laser power is 1.4 mW. Experimental data are fitted by an exponential decay function of time constant $T_2 = 0.46$ ms.

5.2.2.4 Applications to atomic clocks

Figure 5.15(a-b) shows the signal and the contrast (defined as the ratio between the CPT signal amplitude and the off-resonance dc background) of the CPT resonance in CW regime for different values of the laser power in the Cs-OTS cell, when the beam diameter covers the whole cell diameter. The signal amplitude shows a quadratic dependence for laser power below 50 µW, while the dependence is linear above this value. This behavior is in good agreement with the CPT signal expression derived by Vanier *et al.* (1998). As observed in buffer-gas filled Cs vapor cells using push-pull optical pumping technique, the resonance contrast is measured to increase with the laser power while a saturation value is expected to be observed at higher intensities (Liu *et al.*, 2013b).

The short-term relative frequency stability of an atomic clock, in terms of Allan deviation $\sigma_y(\tau)$, is given in Eq. (2.42)

Figure 5.15(c) shows the expected shot-noise limited clock frequency Allan deviation in CW regime versus the laser power from measurements of $\Delta\nu$ and C reported in Fig. 5.7, Fig. 5.15(a) and (b). The best frequency stability result, at the level of 6×10^{-13} at 1 s, is obtained for a laser power of about 300 µW. This result is about 3 times worse than the expected relative frequency stability of a clock using a buffer-gas filled Cs vapor cell of slightly smaller dimensions (10 mm length and 10 mm diameter) (Liu *et al.*, 2013b).

Narrowing the linewidth through the motion-induced Ramsey narrowing process could improve the frequency stability, but Breschi *et al.* (2010) have shown that the gain on the shot-noise limited frequency stability does not follow the gain on the resonance linewidth reduction. Actually, the same short-term relative frequency stability can be obtained with a large beam diameter at small laser intensity and a smaller beam diameter at higher laser intensity (i.e., higher clock signal). With the Ramsey technique, the optimum clock short-term frequency stability is expected to be obtained when the free evolution time T_R equals the microwave coherence relaxation time T_2 (Liu *et al.*, 2013a, Micalizio *et al.*, 2012, Guérandel *et al.*, 2007). In the present study, the free evolution time is limited to $T_2 \approx 0.50$ ms, yielding a central fringe width of about 1 kHz. The shot-noise limited frequency stability is given by: (Liu *et al.*, 2013a)

$$\sigma_y(\tau) \approx \frac{\Delta\nu}{\nu_0} \frac{1}{C} \sqrt{\frac{h\nu}{P}} \sqrt{\frac{T_c}{t_m}} \tau^{-1/2}, \tag{5.12}$$

with T_c as the length of an interrogation cycle and t_m as the length of the signal measurement. The stability limit in our case is about 3.5×10^{-12} at 1 s, worse than a CW interrogation, showing that a Ramsey interrogation is not the most appropriate in the case of a fast signal decay.

Eventually, from Fig. 5.8, we note that for a cell temperature of 30 °C, the light shift slope is measured to be -0.029 Hz µW^{-1}, i.e., -50.9 Hz/(mW/cm^2), which yields relatively to the clock frequency 5.5×10^{-9} /(mW/cm^2). This value is of the same order of magnitude than light-shift coefficients measured by Breschi *et al.* (2010) in paraffin-coated cells. Moreover, we note in Fig. 5.8 that the temperature dependence of the clock transition in the Cs-OTS cell is roughly 24 Hz °C^{-1}, which yields relatively to the clock frequency 2.7×10^{-9} K^{-1}. This sensitivity is about 10 times higher than the one measured (2.7×10^{-10} K^{-1}) in a laser-pumped paraffin-coated
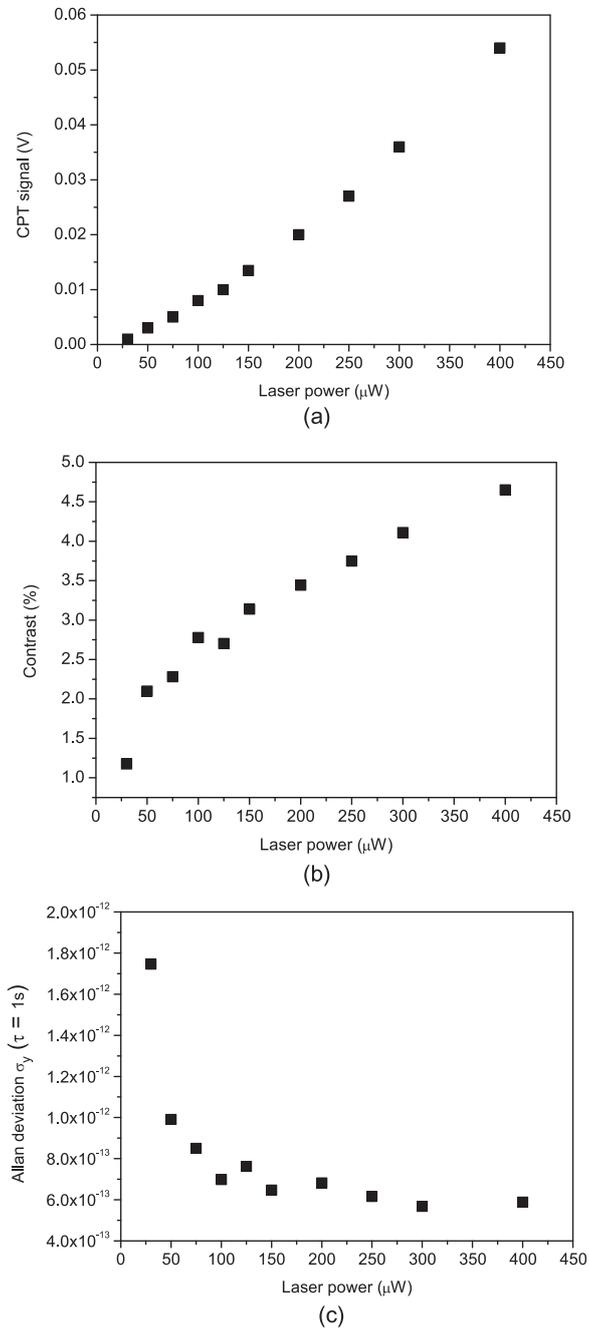
Figure 5.15: (a): CPT resonance signal, (b) CPT resonance contrast, (c) calculated shot-noise limited clock frequency Allan deviation versus the laser power incident on the cell. The cell temperature is 35 °C. The laser beam diameter equals the cell diameter. Error bars are covered by data points.

cell rubidium frequency standard (Bandi *et al.*, 2012) and is huge compared to typical sensitivities that can be achieved in optimized buffer-gas filled vapor cells (Kozlova *et al.*, 2011, Vanier *et al.*, 1982, Miletic *et al.*, 2010). This high temperature sensitivity could be a serious drawback for the use of OTS-coatings towards the development of high-performance compact atomic clocks.

5.2.2.5 Conclusion

We reported the realization of a centimeter-scale Cs vapor cell wall-coated with OTS using a simple vapor phase deposition technique. The coating properties were characterized by means of CPT spectroscopy of the Cs ground state hyperfine transition, in view of application to vapor cell atomic clocks. The presence of a narrow peak Lorentzian structure on the top of a broad structure is a relevant signature of the OTS anti-relaxation coating. Experimental results are given for a cell temperature of 35 °C, which maximizes the CPT signal. Using clock frequency shift measurements, the adsorption energy of Cs atoms on OTS surface was measured to be $E_a = 0.42(3)$ eV, in agreement with the value reported in the literature for Cs-OTS-Pyrex (Stephens *et al.*, 1994) by a completely different method. A clock frequency shift rate of 24.6 Hz °C^{-1} was measured. The phase shift per collision with the OTS surface was estimated to $-168(2)$ mrad, with a shift rate of 7.4 mrad °C^{-1}. Measurements of hyperfine population lifetime (T_1) and microwave coherence lifetime (T_2) of about 1.6 ms and 0.5 ms were reported, corresponding to about 37 and 12 useful bounces, respectively. For comparison, Seltzer *et al.* (2007) reported a number of bounces (for the lifetime T_1) for four OTS-coated K cells ranging from 20 to 2100. Using a Rb cell coated with an OTS monolayer, Yi *et al.* (2008) reports 31 bounces (at 82 °C) and 41 bounces (at 102 °C) for Zeeman coherences, and 21 (at 102 °C) and 30 (at 170 °C) for hyperfine coherence. Straessle *et al.* (2014) reports for a Rb-OTS cell 11 bounces for the hyperfine coherence at a temperature not clearly specified, probably 60 °C. It appears that the number of useful bounces is smaller for hyperfine coherence than for Zeeman coherences, decreases at lower temperatures and decreases for atoms with higher polarizability. In that sense, the relatively low number of bounces (12) reported here for the hyperfine coherence of Cs at 35 °C is reasonable and gives us confidence in the quality of the coating.

Motion-induced Ramsey narrowing (Breschi *et al.*, 2010, Klein *et al.*, 2011) where atoms alternately spend bright and dark time intervals inside and outside the laser beam was observed in the Cs-OTS cell in continuous interaction regime by reducing the laser beam diameter. Raman-Ramsey CPT fringes were detected in the Cs-OTS cell using a temporal Ramsey-like pulsed interrogation scheme. Applications to atomic clocks were discussed. The best calculated shot-noise limited frequency stability was obtained for a CW interrogation.

As a matter of fact, the high Cs-OTS adsorption energy leads to a large atom-wall collision induced phase shift, a high temperature sensitivity of the clock transition frequency, 2.7×10^{-9} °C^{-1} in fractional frequency, and a limited number (about 12) of bounces preserving the hyperfine coherence. We consider these aspects as serious drawbacks for the development of high-performance Cs-OTS atomic clocks compared to the buffer gas technique. Nevertheless, OTS coatings could remain of interest in microfabricated cells and miniature atomic clocks applications. Miniaturized cells usually work at higher temperature (80 °C to 100 °C) than centimeter-sized cells in order to increase the Cs density and the signal. As shown in Fig. 5.9, the module of the phase shift per collision decreases when the temperature increases. If the microcell operates at a temperature where the phase shift value is reduced or canceled, the broadening term $\Delta\nu_\phi$ can be reduced and consequently the number of useful bounces increased. On the other hand, the temperature-related shift will certainly be reduced but not canceled. The use of OTS coatings will be compliant with miniature atomic clocks applications if both the sensitivity of the clock frequency to cell temperature variations and cell temperature control are compatible with typical clock relative frequency stability performances objectives at the level of 1×10^{-11} at 1 h and 1 d averaging time. Those results have recently been published (Abdel Hafiz *et al.*, 2015b,a).

5.2.3 Characterization of cells Cs-OTS3, Cs-OTS4 and Cs-OTS5

The characterization of cells Cs-OTS3, 4 and 5 was performed by Moustafa Abdel Hafiz using the same CPT setup.

5.2.3.1 Linear absorption spectroscopy

Once sealed, we measured absorption lines of cells Cs-OTS3, 4 and 5 by comparison with those in a pure Cs cell of similar dimensions. We observe that the absorption is similar for all the cells and close to the pure Cs cell (Fig. 5.16).
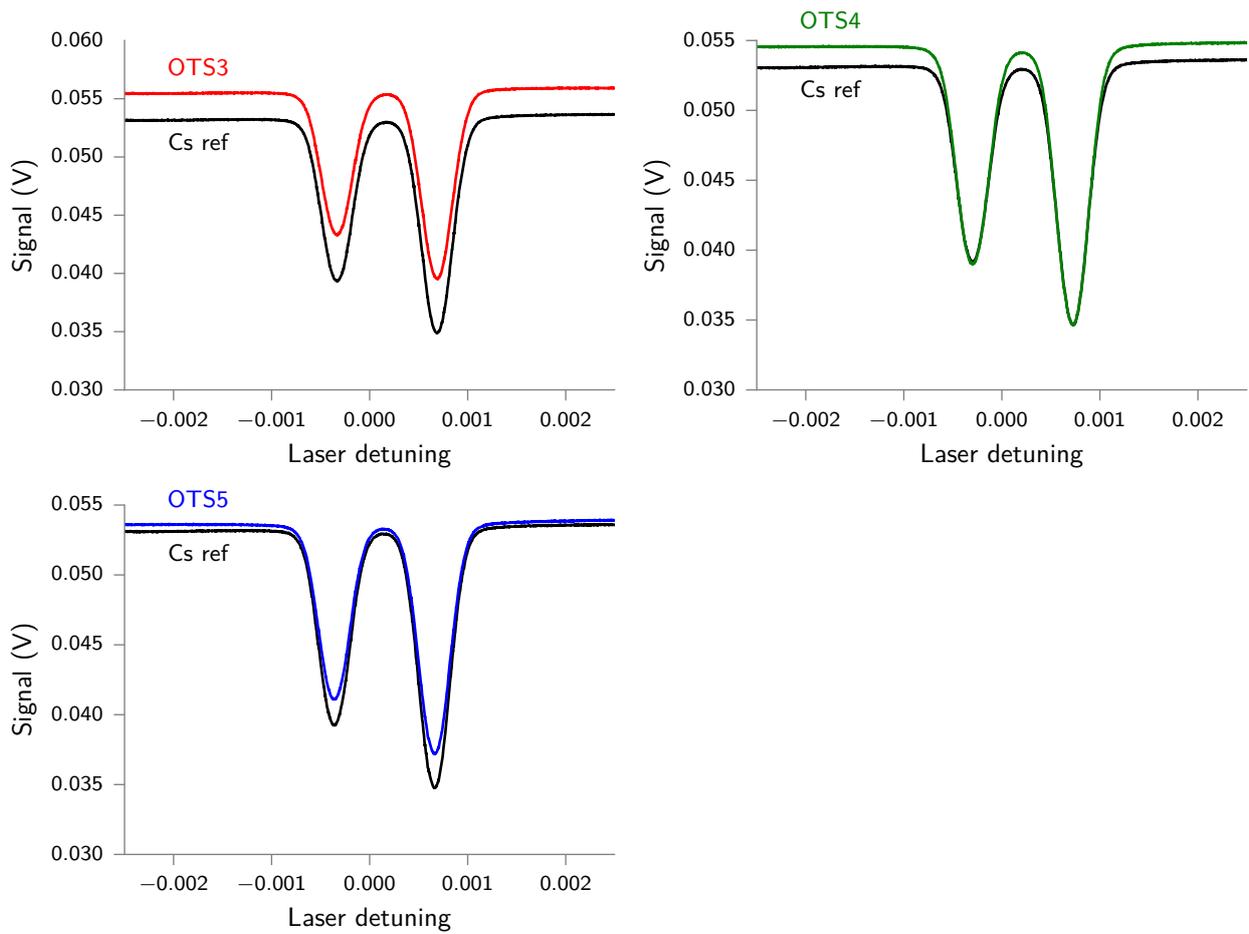
Figure 5.16: Absorption lines in cells OTS3, 4 and 5 compared to a pure Cs cell.
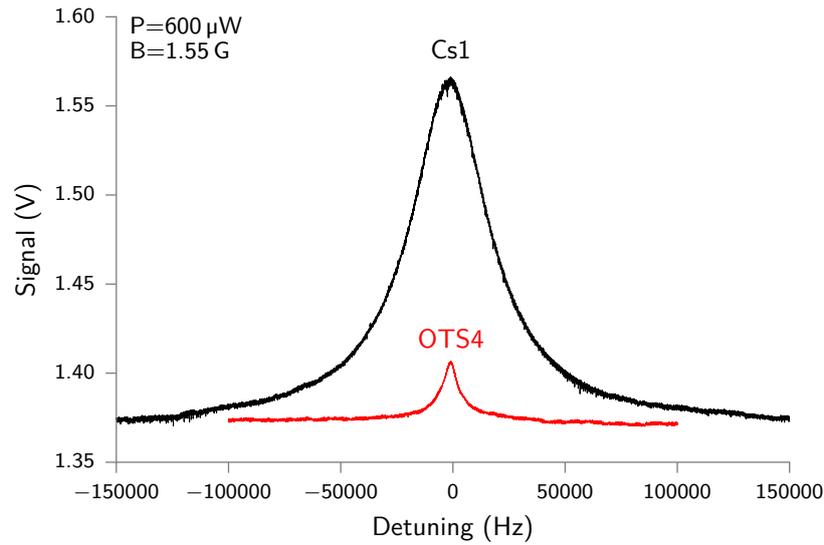
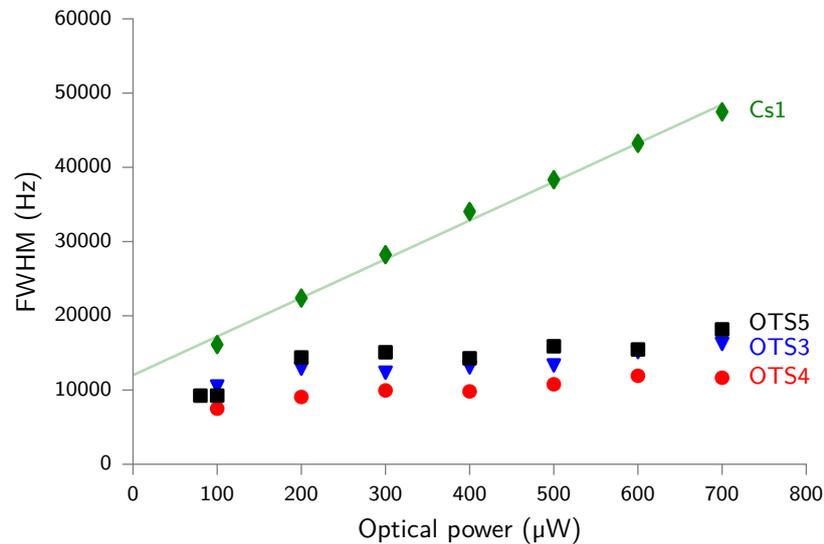Figure 5.17: CPT resonance in the cell Cs-OTS4, by comparison with a pure Cs cell.

Figure 5.18: CPT linewidth versus the laser power for cells Cs-OTS3, 4 and 5. Comparison with a pure Cs cell.

5.2.3.2 CPT spectroscopy

Figure 5.17 shows a CPT resonance in cell Cs-OTS4, by comparison with a pure Cs cell. The laser power is 600 μW. We observe that the dip signal in the OTS cell is surprisingly small. This behavior is not clearly understood. It was found similar in cells Cs-OTS3, 4 and 5.

For further information, we measured the CPT linewidth (Fig. 5.18) and the CPT signal (Fig. 5.19) in the three OTS-cells as a function of the laser power. All the OTS-cells gave similar results. The CPT linewidth at null laser power for OTS cells is in the order of 6 kHz to 7 kHz, i.e. a factor 10 higher than for cells Cs-OTS1 and Cs-OTS2. We conclude that results are not satisfying for cells Cs-OTS3, 4 and 5. In these cells, the anti-relaxation effect of the OTS coating exists but is not significant. We observed that, contrary to cells Cs-OTS1 and 2, it was not possible to detect any Ramsey fringe in this cell, proving that the anti-relaxation effect of the coating is not sufficient. It remains interesting to note that all cells give similar results, proving the reproducibility of the coating and filling process. For these reasons, we did not investigate more characterization of these cells. These cells should be tested again in a few months to observe if any evolution occurred.
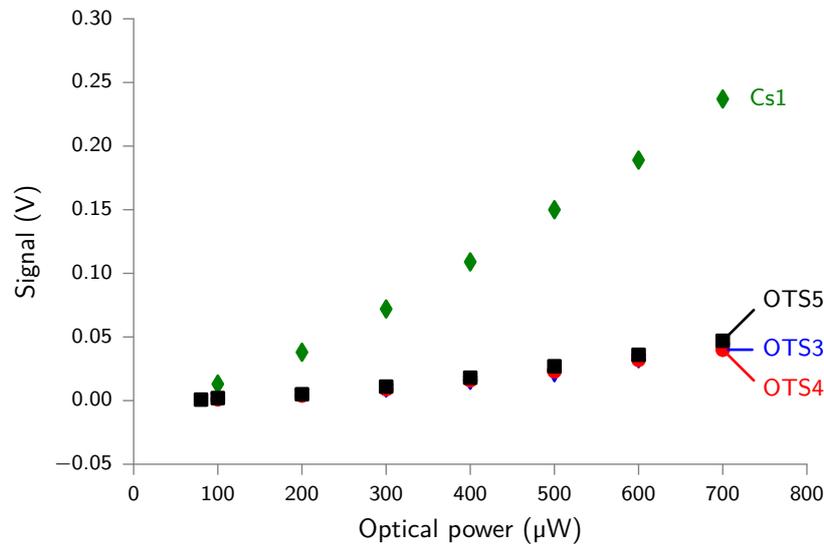
Figure 5.19: CPT signal amplitude versus the laser power for cells Cs-OTS3, 4 and 5. Comparison with a pure Cs.

5.3   Experiments with microfabricated cells

5.3.1   Fabrication process and coating procedure

The initial fabrication process is described on Fig. 5.20. The wafers are first cleaned with a solution of H_2O_2 heated at $110\,°C$ for 30 to 60 minutes. In this process, OTS is deposited with the vapor-phase procedure described in Section 5.2.1.1, as it provided the best results in centimeter-scale cells. In this process, a glass cup containing a few microliters of OTS is introduced in a PFA container along with the preform and the cap wafer. The container is then placed in an oven at $150\,°C$ for several hours (following the procedure described by Sugimura *et al.* (2000)). The whole surfaces of the preform and the cap wafer are coated. Contact angles are measured to provide a rough evaluation of the quality of the coating[5]. Static contact angles around 110° are typically achieved, in accordance with the literature. OTS may prevent anodic bonding and it may be necessary to remove it where a good bonding is to be obtained. It is know that OTS can be removed and patterned by exposure to UV light (Lee *et al.*, 2003). This solution was chosen over O_2 plasma cleaning, which would require additional wet treatments (such as resist coating, development, resist stripping, etc.) to protect the OTS layer with resist. We use a UV+O cleaning process[6], which consists in using short-wavelength UV radiation around $185\,nm$ and $254\,nm$ to dissociate organic contaminants and oxidize the exposed surfaces. After this treatment, water tends to spread on the surface and a contact angle near 0° is observed. This hydrophilic behavior is associated with a high density of hydroxyl groups on the surface (Grundner and Jacob, 1986), which is favorable for anodic bonding. As a matter of fact, this process can also be used to prepare the surface before OTS coating, as a high density of OH groups have also been found to improve the coverage of such coatings, as they act as bonding sites for OTS molecules (Le Grange *et al.*, 1993). The process is illustrated on Figure 5.21. The mask used for OTS patterning is made of $100\,nm$ thick chromium disk sputtered on a quartz substrate, which is sufficiently transparent to those wavelengths. Because the UV light in the UVO-Cleaner is not very directional, a large overlapping area is used to cover the optical cavities of the cells.

5.3.1.1   Fabrication of wafer T26

A first batch (T26) was fabricated from the regular cell design composed of cavities and channels etched in a single DRIE step. After etching, the cavities were polished in a $HF/HNO_3/CH_3COOH$ solution, which is supposed to be isotropic. The resulting surface is shown in Fig. 5.22. In addition, to evaluate the effect of the OTS on the bonding and to assess for the need for OTS patterning, a part of the wafer was protected from UVs to keep OTS at the bonding interface. The bonding was performed using the usual parameters: a temperature of $350\,°C$ and a voltage of $900\,V$. During this bonding, the preform and the cap wafer are aligned in situ thanks

---

[5]with a MCAT Digidrop goniometer from GBX, Inc.
[6]using a UVO-Cleaner from Jelight Company, Inc.
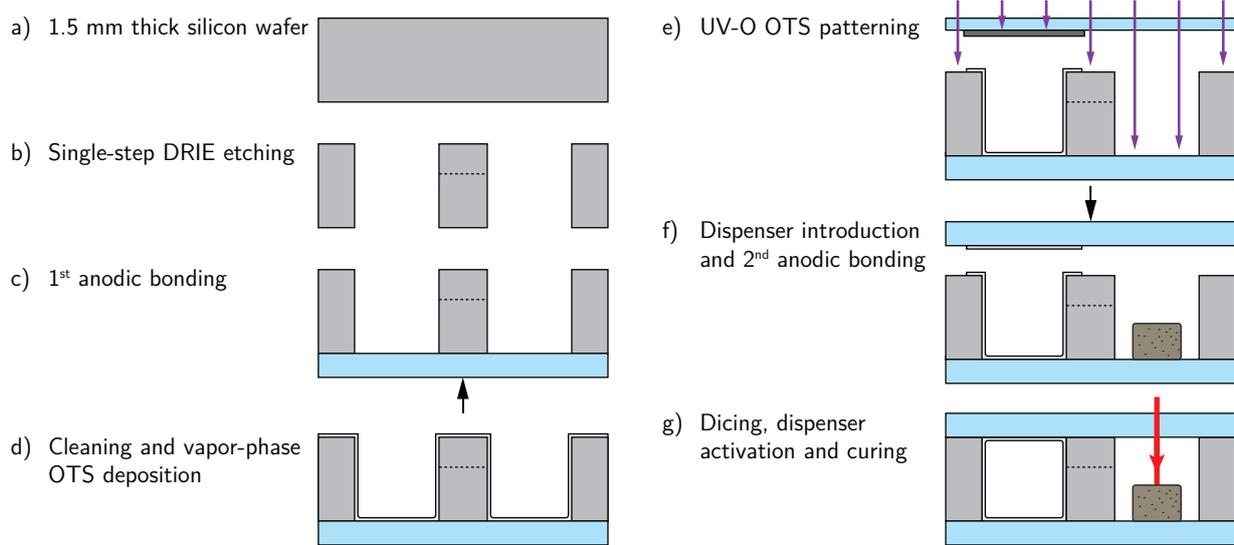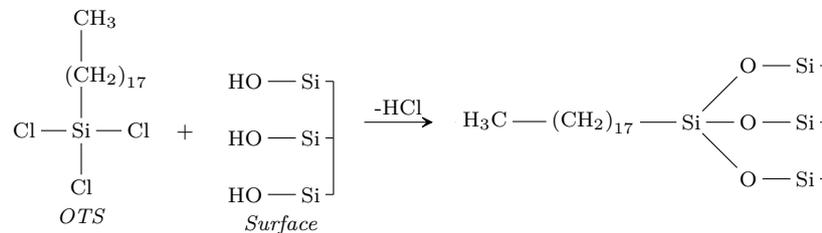
Figure 5.20: Fabrication process

Figure 5.21: OTS molecule and deposition on a silica surface.

to windows which allow to see inside the bonder's chamber. Despite a short outgassing step, a bluish plasma could be seen in the cavities when the voltage was above $700\,\text{V}$. With those parameters, the bonding was not significantly affected by the OTS. Only a few unbounded spots could be seen were OTS was preserved at the interface (Fig. 5.23).

After dicing, the cells were activated. As it is known that cells without buffer gas activate much faster, the selected laser intensities were lower than usual. However, despite this low intensity, a large quantity of liquid cesium was released and could not be kept out of the optical cavities. The cells were then placed on a hot plate at $70\,°\text{C}$ to speed up the curing, meanwhile the evolution of the condensation was recorded by a microscope. Figure 5.24 and Fig. 5.25 show two typical behaviors observed among the cells. While cell T26EC sees its condensation increasing, it is decreasing in cell T26EE before completely disappearing. In all cases, liquid cesium is in contact with the coating at some point, which should be avoided to prevent the degradation of the coating (Seltzer *et al.*, 2013).

Unfortunately, no antirelaxation effect could be observed by CPT spectroscopy and those cells behaved as uncoated pure Cs cells (compared to uncoated microcells T8). However, this first experiment led us to envision several improvements for the second batch of fabrication.

5.3.1.2 Fabrication of wafer T27

As we have seen in Section 2.2.2.3, the section of the channels used to link the cell cavities acts as an uncoated area and can significantly reduce the effect of the coating. The inner area of a cell with a $2\,\text{mm}$ diameter and a $1.5\,\text{mm}$ length is about $16\,\text{mm}^2$. Therefore, the uncoated surface, including the cross-sectional area of the channels, should be less than $0.016\,\text{mm}^2$ in order to reach 1000 non-relaxing bounces. The usual design, used for the previous batch, does not allow to control the depth of the channels, which typically reaches several hundreds of microns. In addition, the polishing step enlarges them further. For this batch, a different process was therefore used to allow the channels to be etched separately at the desired depth after polishing the cavities. In this way, the polishing step would not enlarge further the channel. A specific design featuring a single elongated and meandered channel was adopted to reduce the chances for cesium condensation to reach the optical cavity by
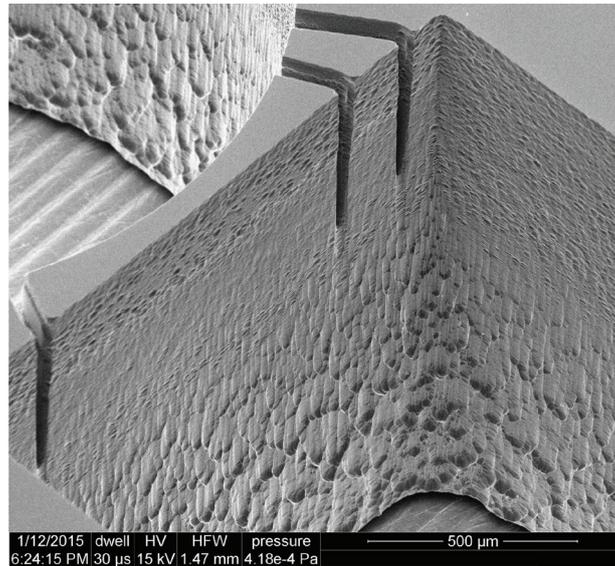
Figure 5.22: SEM image of the cavities after etching (T26).
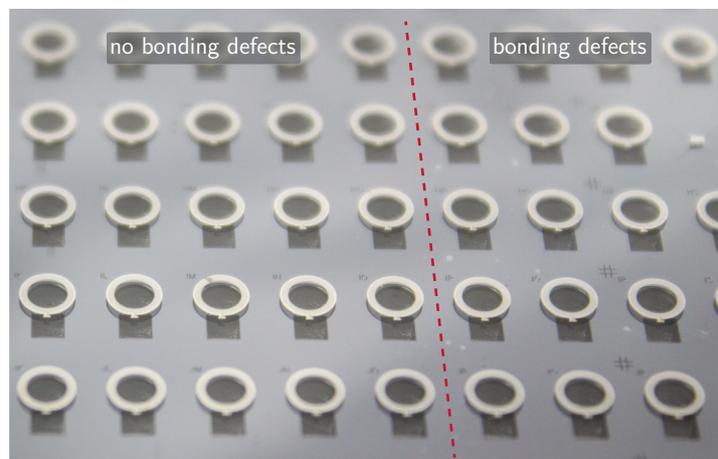
Figure 5.23: Picture of the wafer T26 after the second anodic bonding. OTS was kept on the right of the red line.

Figure 5.24: Evolution of the condensation in cell T26EC over several hours at 70 °C.

Figure 5.25: Evolution of the condensation in cell T26EE over several hours at 70 °C.
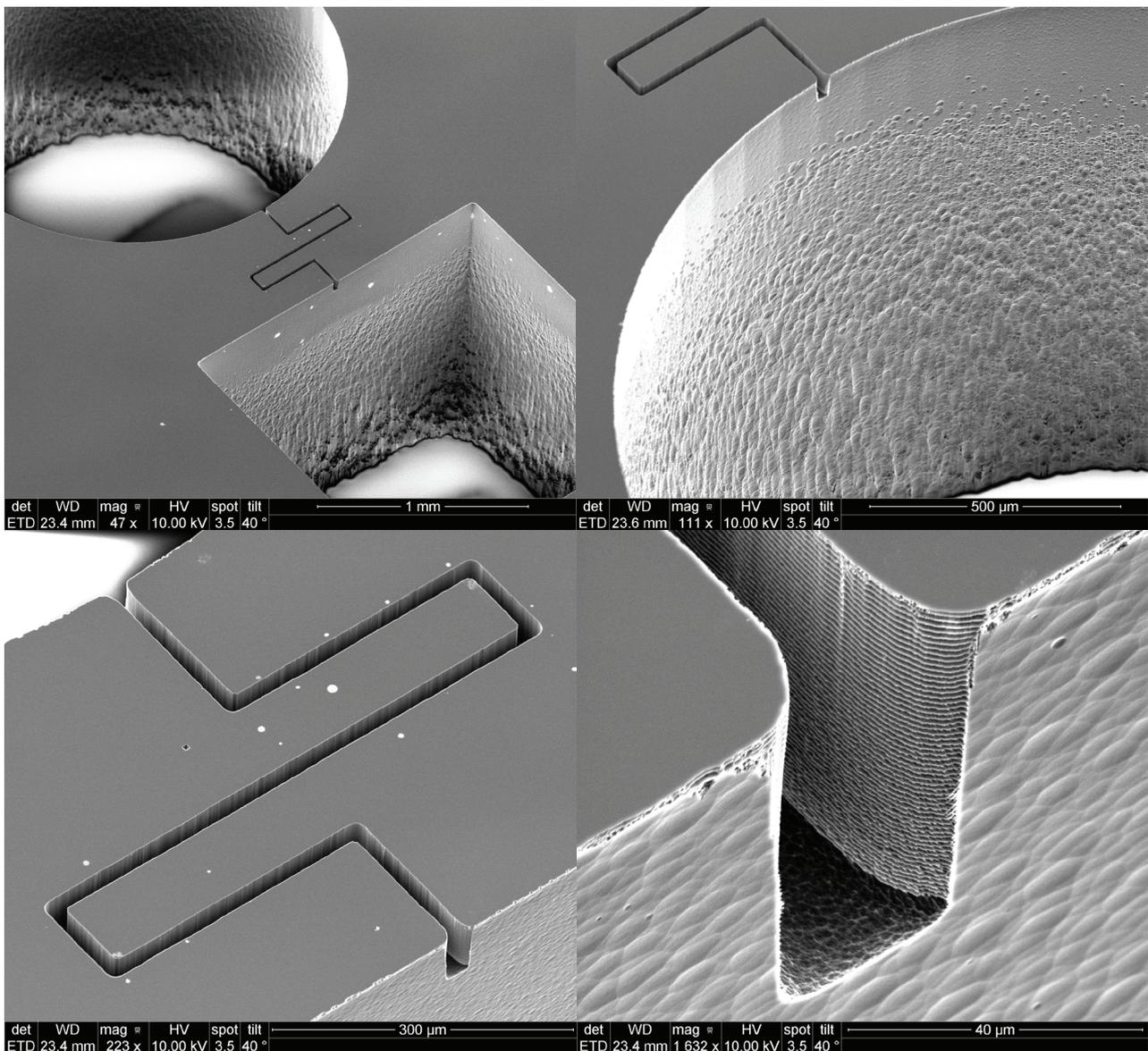
Figure 5.26: SEM images of the cavities after etching. A specific design is used (wafer T27).

capillary action during activation (Fig. 5.26). The channel section was reduced to $20\,\mu m \times 50\,\mu m$.

Besides, it was also preferred to reduce the anodic bonding voltage. Indeed, the bluish plasma that could be seen with the previous batch was not clearly identified and optical emission spectroscopy of the emitted light should be performed to give us some information about the content of the cell at this stage (experiment to be performed). Yet, if it was an oxygen plasma, which also has a bluish color, it may have destroyed the coating. For this second batch, the voltage was therefore limited to $700\,V$ during the bonding to avoid a potential discharge through would-be O_2 traces. The bonding temperature was also reduced to $300\,°C$. The anodic bonding parameters were not ideal and led to a large unbonded area (Fig. 5.27). In this case, areas where the coating was kept at the bonding interface did seem to prevent the anodic bonding. This is particularly visible on the edges of the wafer, where OTS was preserved: the bonded area clearly ends where the area with OTS at the interface begins. Thus, patterning OTS layers may be useful to achieve sufficient bonding when the bonding voltage is reduced. Dicing was particularly difficult due to the weak bonding. Fortunately, a large part of the cells containing dispensers could be diced successfully. Activation was performed using low laser intensities. The intensities at which condensation appeared in each cell were quite different. The cells had to be backed overnight at $70\,°C$ before cesium absorption could be observed. This channel design seems to effectively slow down the migration of cesium condensation, as can be seen in Fig. 5.28. The OTS layer at the interface of the overlapping area around the optical cavity is clearly visible.
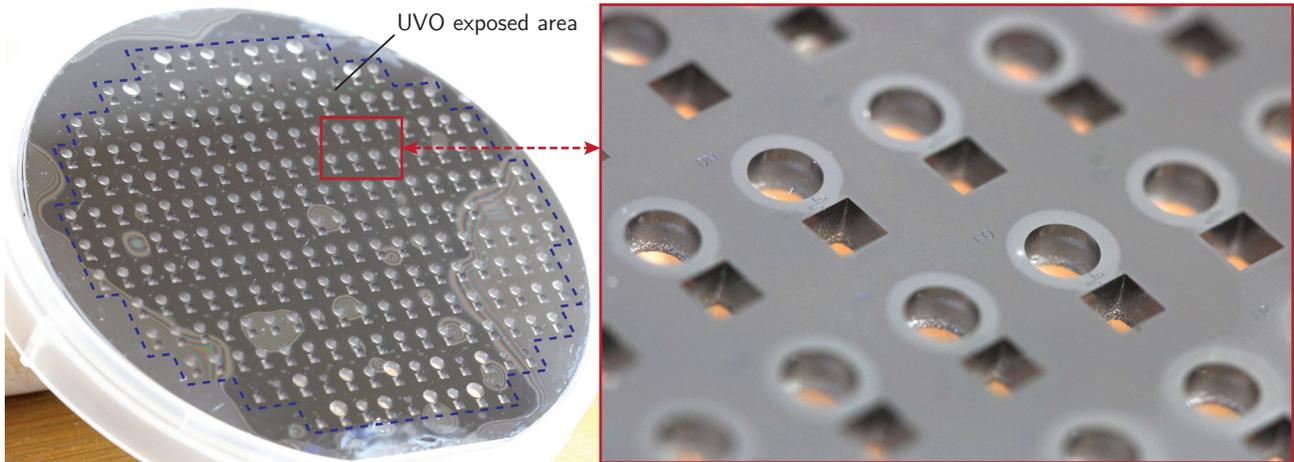
Figure 5.27: Picture of the wafer T27 after the second anodic bonding.
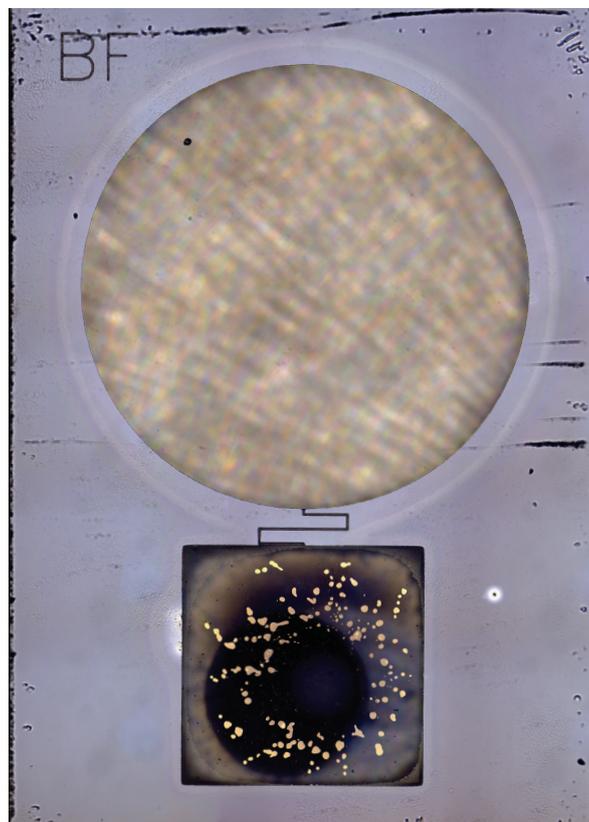
Figure 5.28: Microscope image of a microfabricated OTS-coated cell (T27BF).
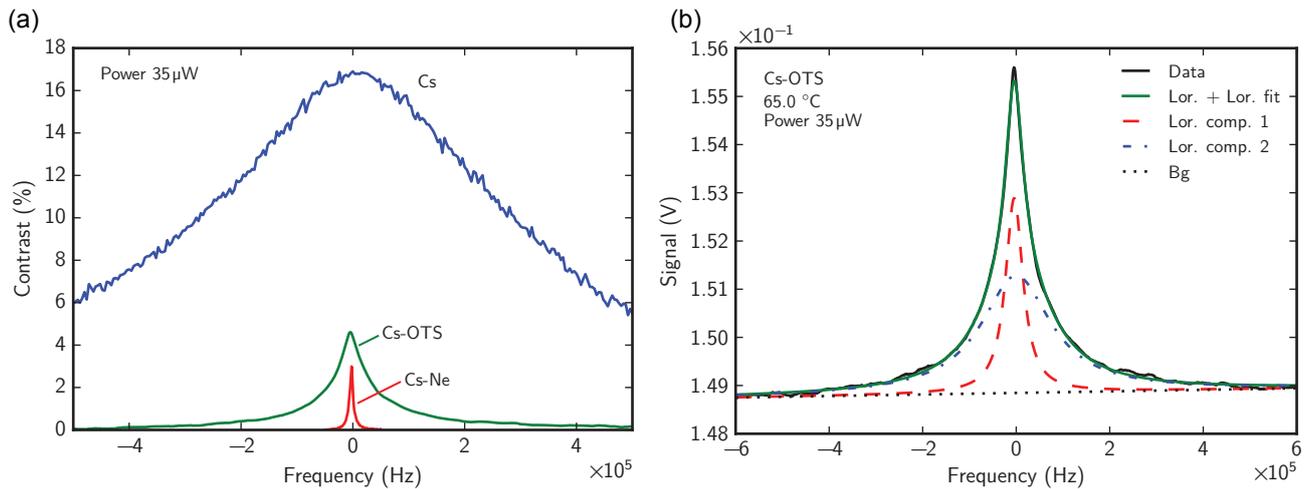
Figure 5.29: (a) CPT signal observed in cell T27BF (Cs-OTS) compared with the evacuated Cs cell (T8D5) and a Cs-Ne cell (T10E7). (b) CPT signal observed in cell T27BF (Cs-OTS) fitted by the sum of two Lorentzian components.

5.3.2 Characterization

CPT spectroscopy was performed using the DFB + EOM setup. Here, the output of the electro optic modulator is circularly polarized and sent to the physics package containing the microcell. A magnetic field flux density between 200 µT (for the uncoated evacuated cell) and 800 µT (for the cell with buffer gas) is applied in order to separate and discriminate correctly Doppler-broadened ground-state microwave Zeeman transitions. CPT signals observed in an evacuated OTS-coated cell (T27BF), an uncoated evacuated cell (T8D5) and a cell filled with neon buffer gas (T10E7) are shown on Fig. 5.29(a). The pressure of neon in the Cs-Ne cell is 17 kPa (130 Torr).

As can be seen on Fig. 5.29(b), the line shape for the Cs-OTS cell presents a narrow structure and is better approximated by the sum of two Lorentzian functions than just a single Lorentzian component. This could result from the LILN effect, which was previously observed in uncoated and evacuated microcells (Kozlova, 2012). However, in our case, the uncoated cell exhibited a line shape closer to a Lorentzian (so does a buffer gas filled cell). This narrowed line shape is therefore attributed to the antirelaxation effect of the coating, despite its lower magnitude compared to the lineshape of the OTS-coated centimeter-scale cell reported above. At a laser power of 35 µW (corresponding to an intensity of $1.1\,\mathrm{mW\,cm^{-2}}$), the FWHM of the fine Lorentzian component is 45 kHz in the OTS-coated cell, whereas it is 672 kHz and 8 kHz in the Cs and the Cs-OTS cells, respectively. Thus, the linewidth of the Cs-OTS cell is divided by a factor 15 compared to the Cs cell. Figure 5.30 gathers the properties of the CPT signals observed in different OTS-coated microcells from the batch T27 for different laser powers. It also shows the computed shot noise limit of the short term frequency stability resulting from those values. The cell T27BF exhibits the narrowest signal and, as a result, the best contrast-to-linewidth ratio. In Fig. 5.31, the FWHM for this cell is extrapolated to zero light intensity and compared to an evacuated uncoated cell (T8D5) and an uncoated cell containing a neon buffer atmosphere (T10E7). This zero intensity FWHM is found to be around 50 kHz, which is nearly 6 times narrower than the evacuated cell but still about 20 times larger than the buffer gas cell. The properties of the CPT signals from those three cells are shown in Fig. 5.32. The expected shot-noise limited short-term fractional frequency stabilities (at 1 s) in cells T8D5, T27BF and T10E7 are 9.0×10^{-11}, 2.2×10^{-11} and 3.6×10^{-12}, respectively.

5.3.3 Conclusion and future improvements

Although those values look positive, the possibility that a background gas is present in those cells cast doubts on those results. Indeed, even if no significant shift or broadening was observed in the coated cells by linear absorption spectroscopy, we were unable to observe saturated absorption peaks, which may indicate that a small background pressure exists. A cell that did not contain a dispenser and that seemed correctly sealed was analyzed by RGA at SAES Getters. The results are reported in Table 5.3. A non-negligible background pressure of 4.4 mbar is measured. The atmosphere is mainly composed of CO_2, H_2, CO and O_2. A bonding defect does not seem likely as the partial pressure of N_2 would be higher. Instead, we suspect that OTS molecules oxidized
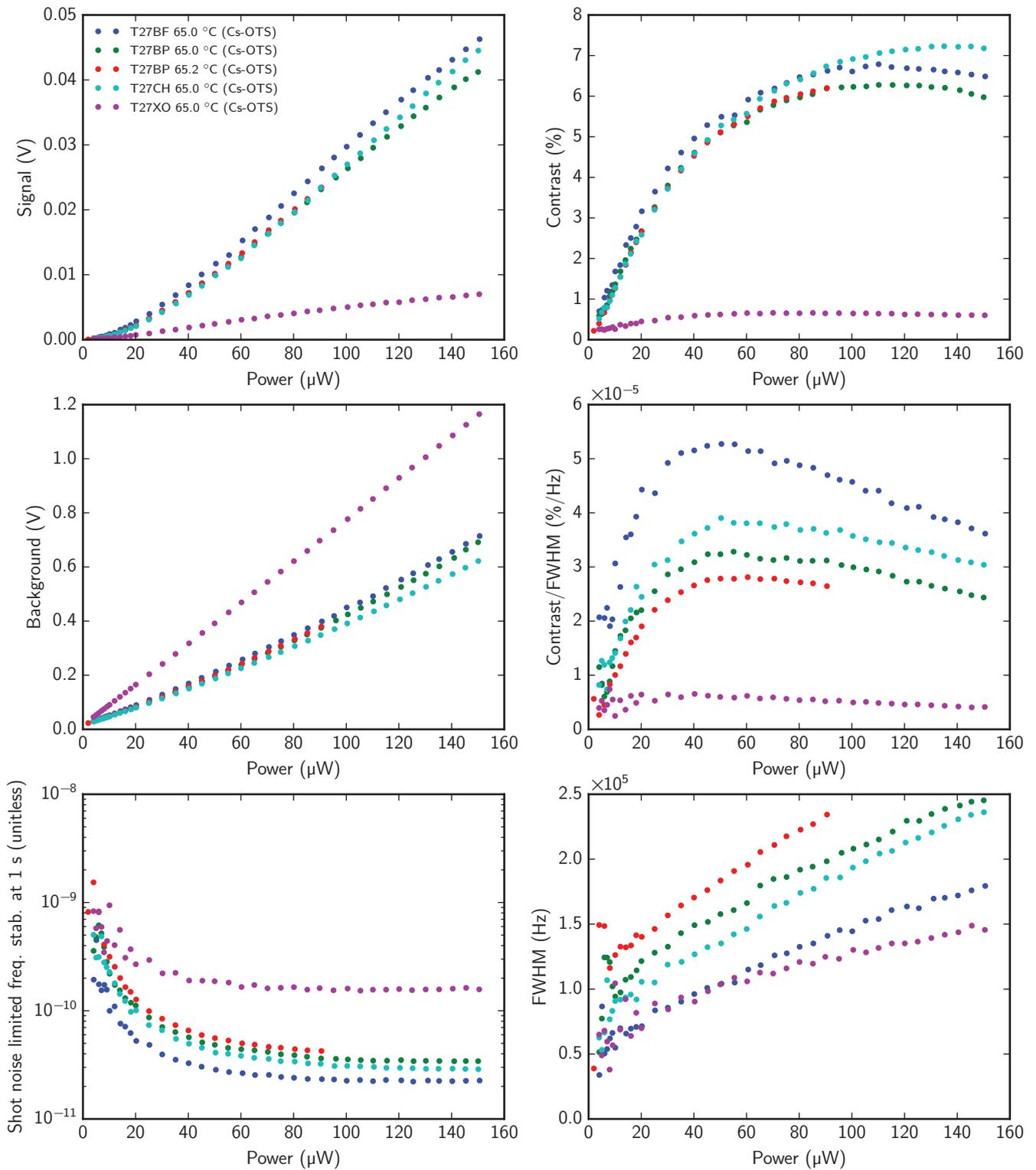
Figure 5.30: CPT signal characteristics and expected shot-noise limited frequency stabilities for different laser powers in OTS-coated microcells. The FWHM corresponds to the width of the single Lorentzian fit function.
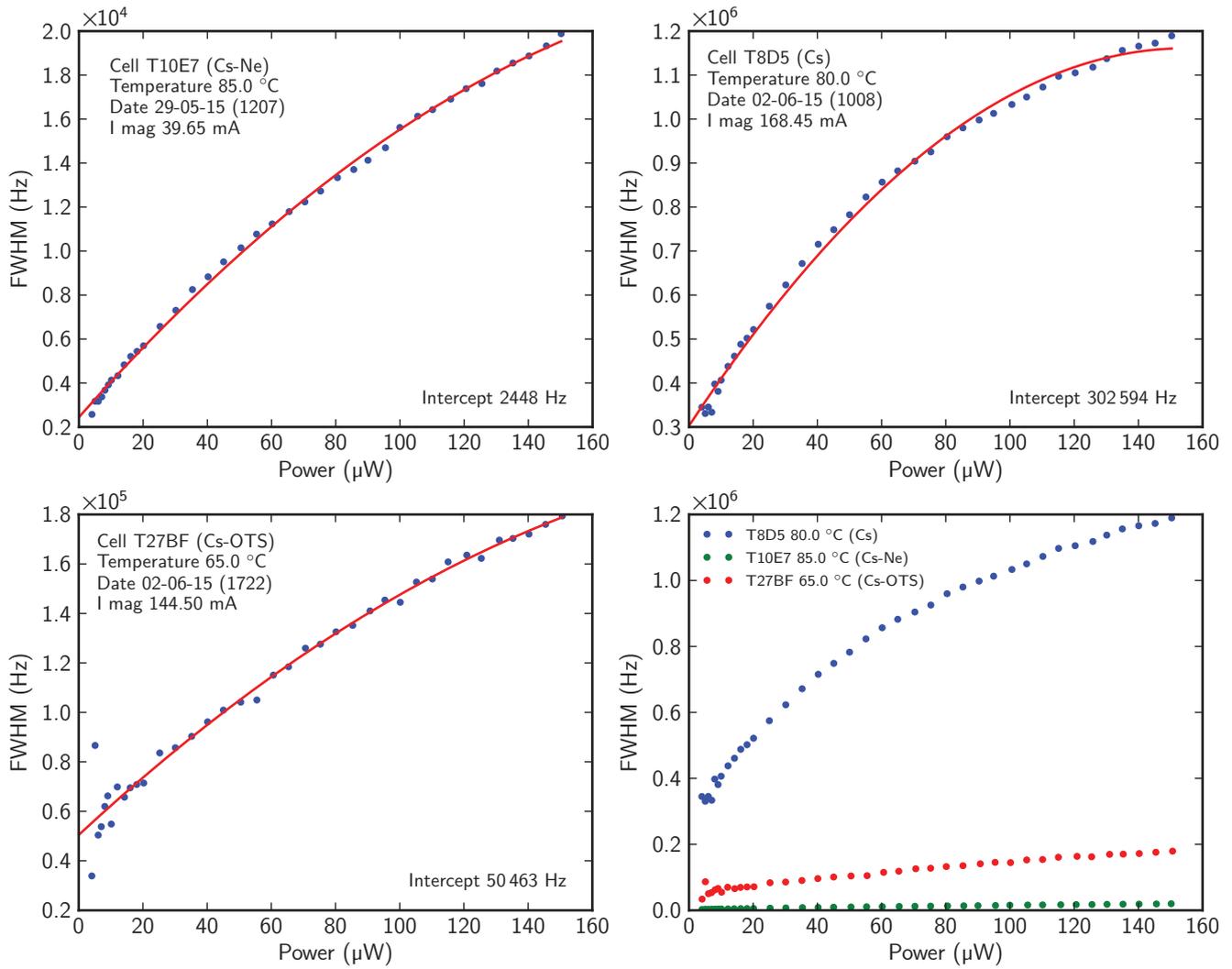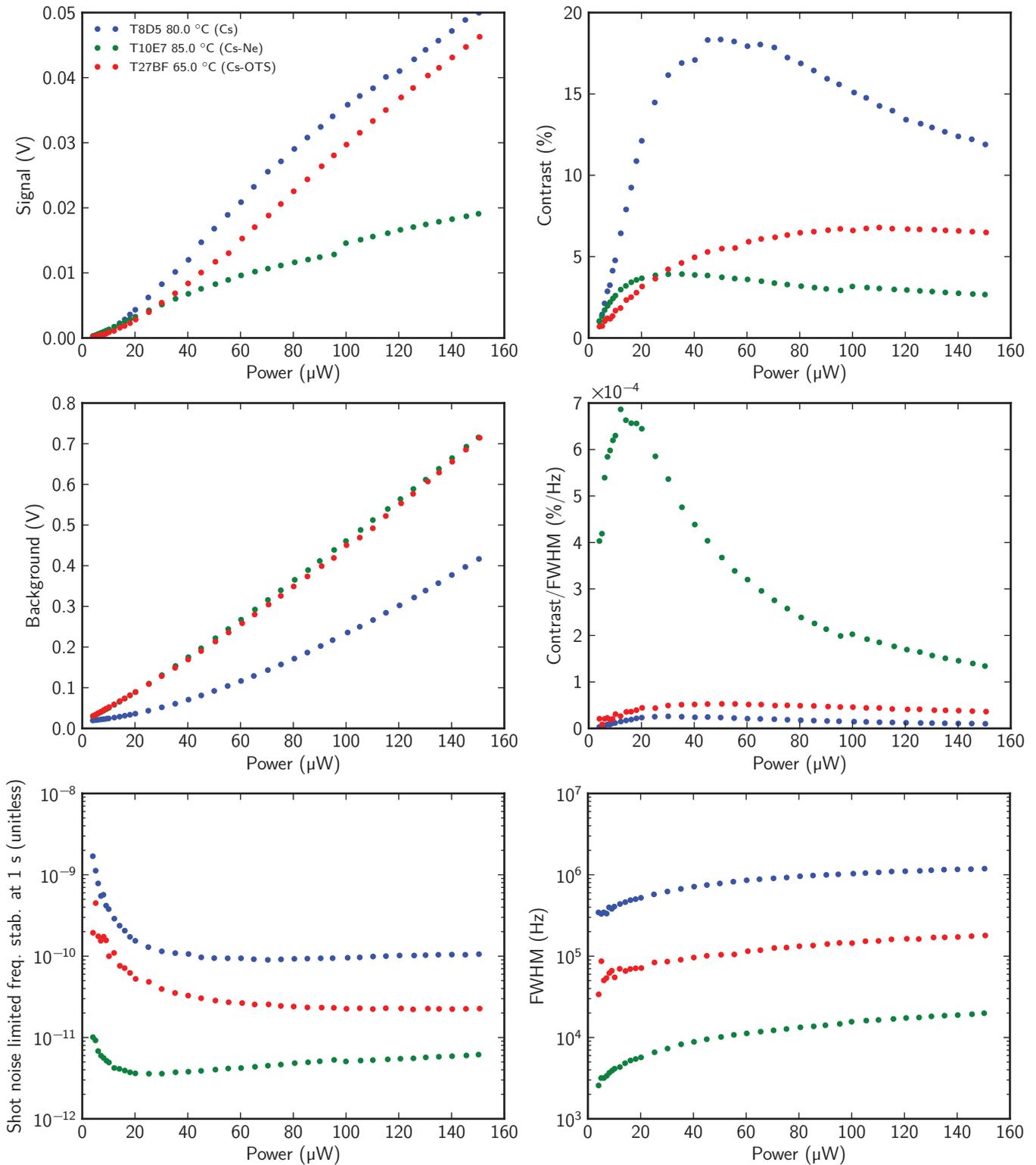
Figure 5.31: FWHM of the CPT signals observed in cells T10E7, T8D5 and T27BF.

| Gas | T28BE OTS (no dispenser) | |
	Pressure (mbar)	Ratio (%)
H_2	1.1	24.73
He	2.0×10^{-3}	0.04
CO	8.9×10^{-1}	20.01
N_2	-	-
CH_4	4.0×10^{-2}	0.90
H_2O	2.0×10^{-3}	0.04
Ne	-	-
O_2	5.1×10^{-1}	11.47
HCs[*]	3.9×10^{-3}	0.09
Ar	1.0×10^{-4}	< 0.01
CO_2	1.9	42.72
Total	4.4	100

[*] HCs = hydrocarbons.

Table 5.3: RGA results from an OTS-coated cell from the wafer T27.

Figure 5.32: CPT signal characteristics and expected shot-noise limited frequency stabilities for different laser powers in cells T27BF (Cs-OTS), T8D5 (Cs) and T10E7 (Cs-Ne).
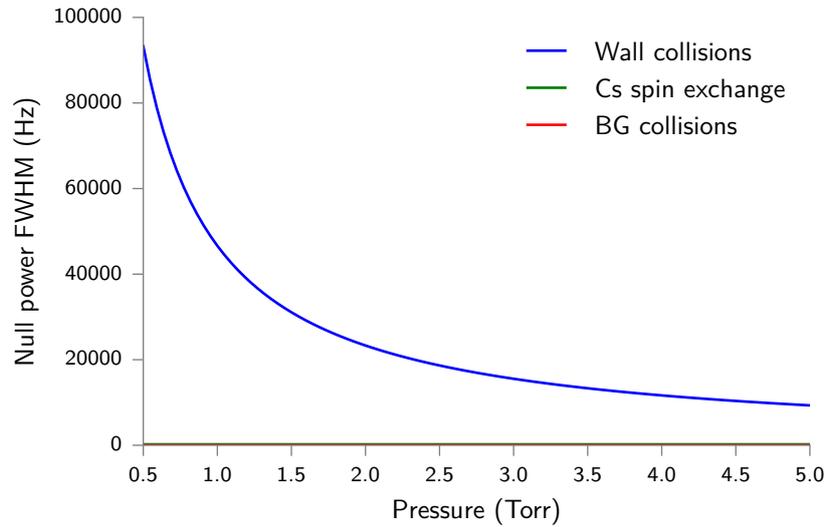
Figure 5.33: Computed null-power FWHM of the CPT signal for low buffer gas pressures according to the model described in Section 2.2.2.2. A temperature of 65 °C and a neon buffer gas are assumed.

in contact with anodic bonding by-products during the process or that gases resulting from OTS molecules cross-linking are emitted. Insufficient outgassing is also possible. However, the cell tested by RGA was free of dispenser. In dispenser-equipped cells, this background gas should be at least partially absorbed by the getter material present in the dispenser or cesium vapor itself. We can thus expect lower background pressure but some species may remain. Indeed, unlike the other main contaminants, H_2 does not react with cesium vapor and its absorptions by the getter can be impeded due to its high diffusivity. Yet, H_2 may not be the only contaminant since additional gases may be emitted during the curing of the coating in presence of cesium vapor. Indeed, background gas pressure in coated cells have been found to increase throughout the ripening process (Camparo *et al.*, 1987, Sekiguchi and Hatakeyama, 2015, 2016). However, the pressures involved are much lower than here. Unfortunately, the collisional shift induced by H_2 on cesium hyperfine transition has never been reported so extracting a potential H_2 residual pressure from hyperfine frequency shift is not possible. Figure 5.33 shows what would be the impact of a low pressure buffer gas on the null-power FWHM of the CPT signal in a cell without coating, according to Eq. (2.30). Relaxation due to wall collisions is dominant, but it seems that a 1 Torr residual pressure of neon would be sufficient to reduce the null-power FWHM below 50 kHz.

As things stand at present, the obtained results cannot be attributed confidently to the OTS properties only. Further investigations are required and, for this purpose, several improvements will be brought to the process for the next experiments. In particular, next cells should benefit from an improved surface quality that can be achieved by optimizing further DRIE and chemical polishing. To ensure that no condensation excess is present in the cell, we could use a gradual activation as proposed earlier. Maintaining a temperature gradient across the cell to prevent cesium condensation from entering the optical cavity might be necessary. New attempts to deposit coatings should be performed using the make-seal technique described earlier, when it is experimentally validated.

Chapter conclusion

According to the literature, OTS coatings can withstand much higher temperatures under vacuum than in presence of an alkali vapor. Since dispensers allow to perform the cell sealing under vacuum, the technology employed at FEMTO-ST seems readily compatible with such coatings. Early experiments aiming at coating microfabricated cells with OTS were performed during MAC-TFC. In this thesis, we undertook further studies to evaluate the benefits of coatings, first in centimeter-scale cells, then in microfabricated cells.

OTS coatings were first deposited in centimeter-scale cells by two different methods: with OTS in liquid phase and in vapor phase. Coatings deposited in vapor phase exhibited a pronounced antirelaxation effect, with a typical dual-structure lineshape. The cells were characterized extensively through CPT spectroscopy and relaxation time measurements. The coating provided a relatively low number of non-relaxing bounces and the clock transition frequency was excessively dependent on the cell temperature. Coatings could still improve the performances of millimeter-scale cells, in which wall-collisions are the dominant factor of relaxation at low buffer gas pressures.

The cell microfabrication process was adapted to allow anodic bonding despite the presence of a coating. A UV+O cleaning process was used to selectively remove OTS at the interface before bonding. Cells with a visible coating layer were thereby fabricated and characterized. Results concerning the observed anti-relaxation effect remain doubtful as a buffer gas contamination, which could explain the effect, could not be excluded.

Chapter 6

Physics package

6.1 Overview

In the framework of miniature atomic clock projects, several generations of bench-top and compact physics package prototypes have been designed and built under the supervision of Serge Galliou and thanks to the constant commitment of Philippe Abbé at FEMTO-ST. Since the early prototype proposed by Dziuban (2011), functionalities have been gradually integrated, in particular to apply a static magnetic field and provide thermal isolation to regulate the cell temperature. Efforts are ongoing to integrate components at the wafer-level, reduce the physics package size and power consumption, and reduce sensitivities to external parameters, which can limit the mid and long-term frequency stability of the clock.

This section presents the design, fabrication and characterization of a compact physics package, which result from the collaboration of several persons. This package integrates resistors fabricated at the wafer-level for heating and sensing the temperature of the cell. Although many developments remain to reach a small-size and low-power device, it represents an additional step toward this goal.

Resistive heating is the widest spread technique and resistors can be deposited either on the cell holding substrates, on a dedicated substrate bonded thereafter or directly on the stack of substrates composing the cell. Here, we chose to deposit the resistors directly on the glass cap wafer composing the cell.

These developments aimed at validating a design able to minimize the emission of parasitic magnetic fields and elaborate the fabrication process. The promotion of a temperature gradient across the cell was intended to address the problem of a possible obstruction of the optical cavity by alkali metal condensation. Additionally, in wall-coated cells, it is particularly important to prevent cesium condensation from covering the coated surfaces, which could cause irreversible damages. These developments were also intended for microfabricated cells with wall coatings.

6.2 Wafer-level integration of heaters and temperature sensors

Design. Heaters ideally have to be placed on the optical windows (Knappe, 2008) and therefore must preferably be transparent. Indium tin oxide (ITO) is often used to this end, however this material was not commonly available at MIMENTO at this time. Mescher *et al.* (2005) and Braun *et al.* (2007) demonstrated physics packages where metallic resistors are placed around the optical cavity, on the substrate holding the cell, without obstructing the light path.

We adopted the same design rule with $10\,\mu m$ wide traces and interleaves. We designed several layouts with various parameters as shown in Fig. 6.1. Layouts were generated thanks to parametric scripting, allowing to produce a set of designs with slight variations very quickly. The parameters of interest that were tested include the spacing between the traces, the relative position of the heater and sensor traces and the overall area surrounded by the traces. Traces are patterned in parallel with alternating current directions so that the magnetic field from each pair of wires is canceled (or minimized). The fabrication process is simplified if both heating and sensing resistors are fabricated in a single lithography and deposition step. This means that the materials and the thickness of both traces are the same, leaving only the possibility to adapt their resistance by playing on their width and length. Since resistors ideally have to be located on both sides of the cell, symmetric masks were designed to ensure that the same resistor layout ends up on both sides of the cell even though the same mask is used for the top and bottom glass wafers.
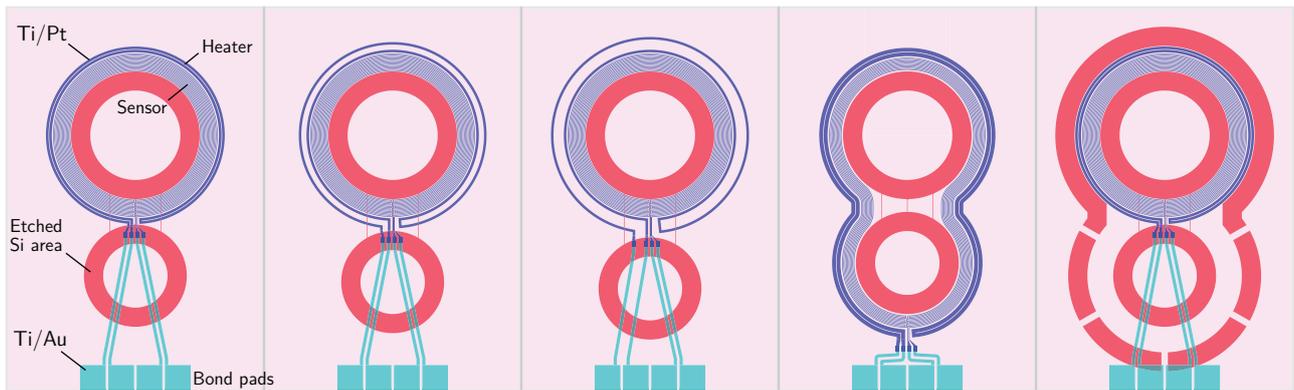
Figure 6.1: Examples of cell layouts integrating resistors generated by parametric scripting.

1. Dry baking of a 500 µm thick Borofloat33 wafer
2. LOR 10A resist spin coating (1 µm)
3. S1813 resist spin coating (1 µm)
4. Exposure and development (1 µm lateral under-etching of LOR)
5. Argon plasma cleaning
6. Titanium sputtering (15 nm)
7. Platinum sputtering (100 nm)
8. Lift-off in acetone or remover 1165
9. Ultrasonic and piranha cleaning

Table 6.1: Fabrication process of the resistors.

Concerning materials, platinum is chosen for its stability, and is widely used for temperature sensors. A titanium layer is used to ensure adhesion on glass. Gold is chosen for bond pads and routing traces for its good electrical conductivity and its compliance with wire bonding.

Fabrication.   Since platinum is rather hard to etch, lift-off process was preferred to pattern the resistors. Table 6.1 describes the deposition process of the resistors.

Sputtering leads to a conformal deposition, which is usually inadequate for lift-off because the solvent can not easily reach the resist and dissolve it. A special resist (LOR 10A) was then applied before the S1813 photoresist. This layer is under-etched during the development of the photoresist providing an undercut, which will be protected from metal deposition by the overlying resist to ensure access to the solvent during the lift-off. The under-etched areas appear clearly in green in Fig. 6.2(a). The resulting resistors after cleaning are shown in Fig. 6.2(b).

The same process was used to deposit a 200 nm thick gold layer for the traces and bonding pads. The picture of the glass wafer after deposition of the resistors in shown in Fig. 6.3(a). After the two deposition steps, the wafer was aligned and directly bonded to the silicon wafer during the cell sealing step. Figure 6.3(b) shows the wafer stack after bonding. For this first test, resistors were only present on one side of the cells.

6.3   Integration in a compact prototype

Cell integration   Several epoxy (FR4) PCBs were designed and patterned by CNC milling by Philippe Abbé. Their role is to hold and thermally isolate the cells . The layout is composed of a small square frame of 12 mm × 12 mm. This frame features bridges to provide enough thermal isolation to the cell so that it can be heated at the desired temperature with realistic currents. This square frame is surrounded by a larger disk-shaped frame with an outer diameter of 25 mm. Depending on the needs, the inner square frame can be detached to be integrated in a compact prototype, but the entire frame can be more convenient to work with, in a larger-scale setup.

The copper traces of the host PCB were electrolytically gold plated. A UV-curable glue was used to bond the cell to the PCB. During bonding, the cell and the holder are maintained and aligned by a dural baseplate (Fig. 6.4). The pads were then wire bonded with a 25 µm thick gold wire. The cell assembly after bonding is shown in Fig. 6.5.
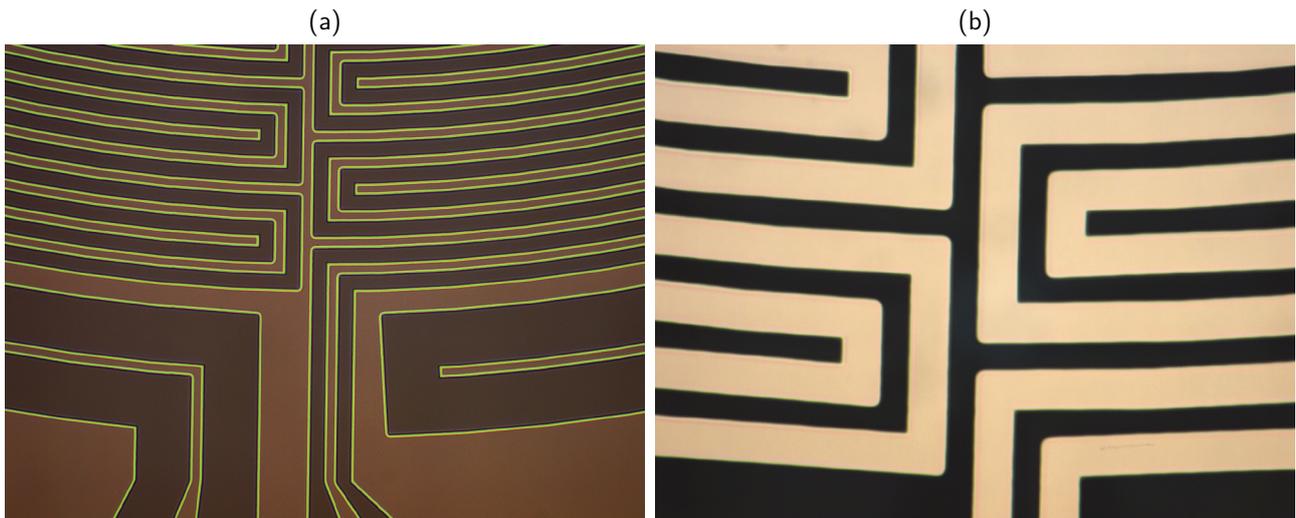
Figure 6.2: Microscope images after photolithography of the resistor patterns (a) and after Ti/Pt deposition, lift-off and cleaning (b). The under-etched areas appear in green lines around the dark developed areas.
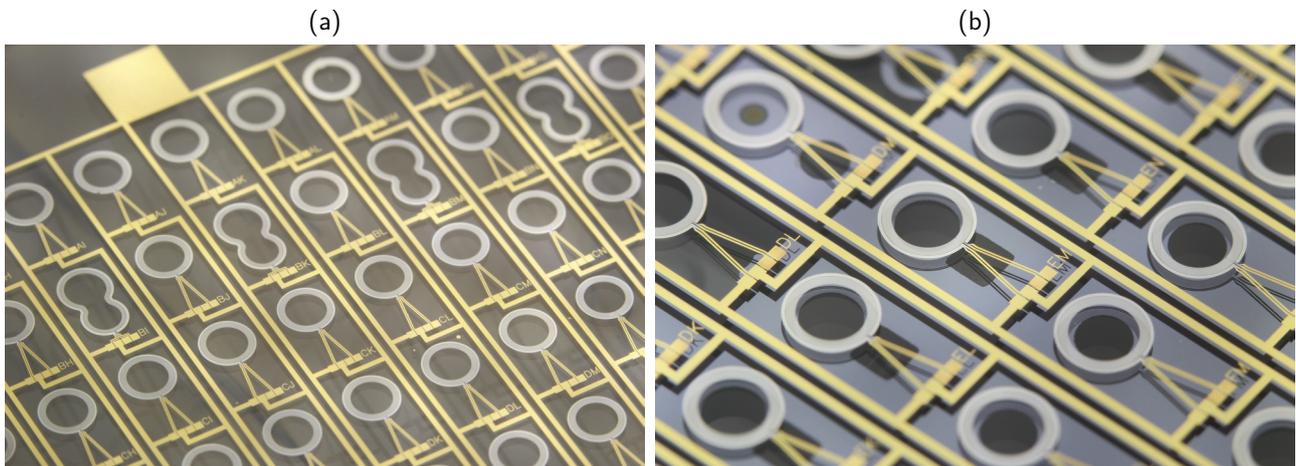

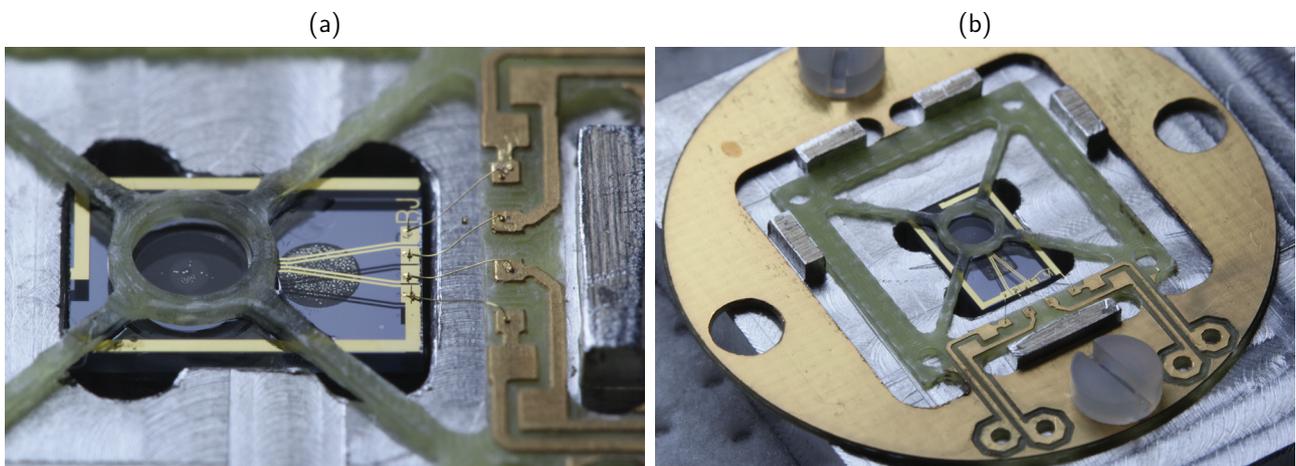Figure 6.3: (a) Picture of a glass wafer with resistors. (b) Picture of the cell wafer stack after bonding.

Figure 6.4: Pictures of the assembly during wire bonding. The dural baseplates and the PCBs were made by Philippe Abbé. Wire bonding was done by Franck Lardet-Vieudrin.
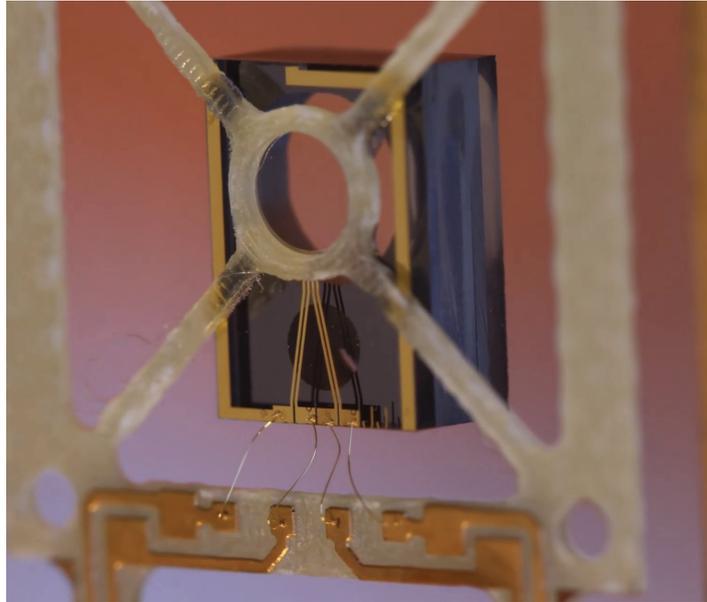
Figure 6.5: Picture of a cell mounted and wire bonded to an FR4 host frame.
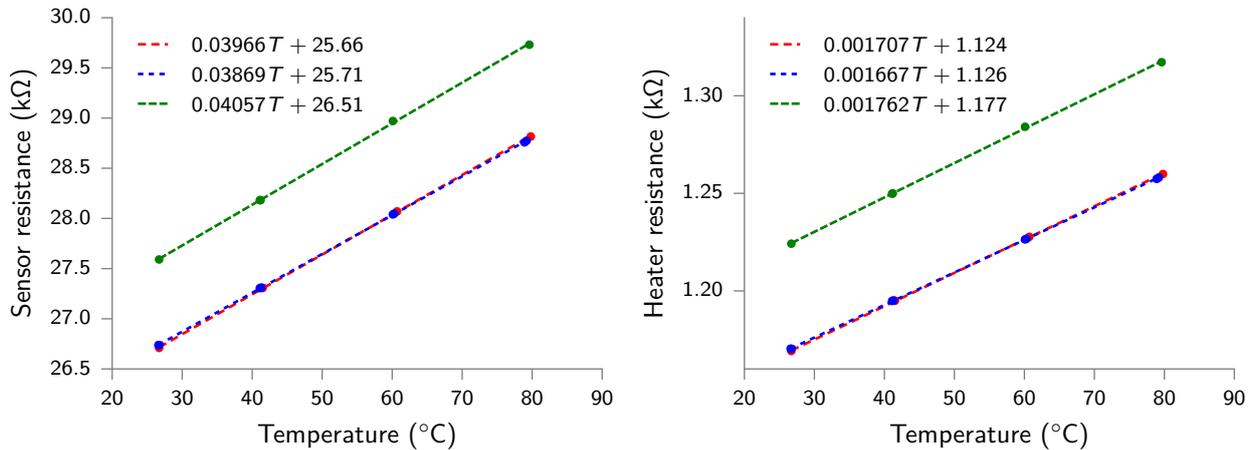
Figure 6.6: Heating and temperature sensing resistors characteristics. Dashed lines are linear fits.

Preliminary characterization.   Preliminary characterizations of the sensing resistors have been conducted by Axel Olivier. The temperature-resistance characteristics were measured by placing the cells in an oven at different temperatures. Those characteristics for three cells are shown in Fig. 6.6. The difference of 3% between those characteristics is not yet explained. The sensitivity of the sensing resistors is around $40\,\Omega\,°C^{-1}$. In addition, heater resistors were tested on unmounted cells, in a configuration where heat was dissipated though a large metal plate at ambient temperature. The heating resistors were found to withstand more than $30\,mA$, dissipating up to $1\,W$, which is more than enough since the targeted power consumption is under $100\,mW$.

Compact physics package prototype.   A compact physics package prototype was designed and fabricated by Rémy Vicarini and Philippe Abbé (Vicarini, 2014). The assembly is composed of a stack of two 3D printed structures interleaved with the FR4 frame holding the cell. Each structure features a slot to host a copper solenoid and forms, together, a Helmholtz coil, which provides a uniform magnetic field in the optical cavity of the cell. A neutral density filter and a QWP can be fitted in a recess of the structure, located on the laser beam path. This assembly is inserted in a cylindrical mu-metal magnetic shield. An additional enclosure made of polyoxymethylene is designed to hold the magnetic shield closed and anchor a VCSEL and a photodiode in standard TO46 packages. Those packages are made of Kovar alloy, which contains ferromagnetic metals likely to induce parasitic magnetic fields. They were therefore kept outside the magnetic shield. The picture of the components composing this prototype can be seen in Fig. 6.7 and a CAD model of the assembly is shown in
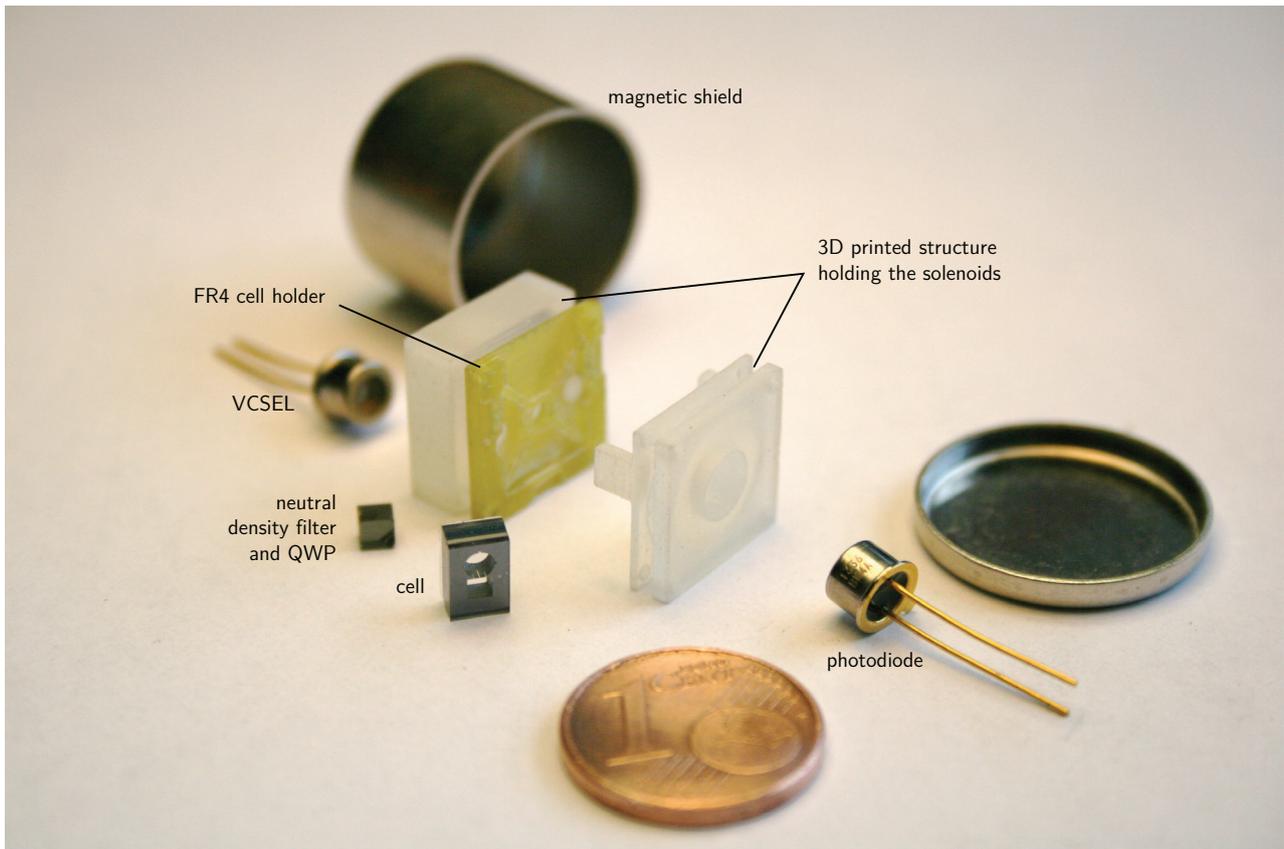
Figure 6.7: Exploded view of the core components composing the compact physics package prototype (Rémy Vicarini).

Fig. 6.8.

6.4 Performance evaluation

Electronic interfacing and CPT spectroscopy. This physics package was interfaced with two host PCBs attached on each side of the polyoxymethylene enclosure. The PCBs were designed and assembled by Jarosław Rutkowski. The VCSEL[1] and the photodiode[2] are soldered directly on each host PCB, along with an operational amplifier[3] used as transimpedance amplifier to amplify the photodiode signal and a CMS bias-tee[4]. Two arrays of pin headers allow the package to be plugged directly on a mother board. Pictures of the host PCBs and the final physics package are shown in Fig. 6.9.

CPT spectroscopy data was provided by Jarosław Rutkowski. CPT signals were measured for different optical powers, which was varied by adjusting the injection current of the VCSEL jointly with its temperature to remain at the same wavelength[5]. The optical power and the laser thermistor resistance for different laser currents are shown in Fig. 6.10, while the CPT signals can be seen in Fig. 6.11.

The characteristics of the CPT signals are summarized in Fig. 6.12. The contrast/FWHM figure of merit is maximized around $47\,\mu W$, where it reaches $0.34\,\%\,kHz^{-1}$, where the FWHM is $1.4\,kHz$ and the contrast is $0.48\,\%$ (Fig. 6.13). The shot-noise limited relative short-term frequency stability is estimated at $7.6 \times 10^{-12}\ \tau^{-1/2}$. In addition, the detection noise was measured (Fig. 6.14). At, $f = 1\,kHz$, the detection noise is $-119\,dBV^2/Hz$, which would lead to a short-term frequency stability of $1.49 \times 10^{-11}\ \tau^{-1/2}$ according to Eq. (2.42). This short-term stability would be close to what we typically expect in cells of this size with Cs D_1 lines. The real frequency stability in a clock configuration will be measured soon.

---

[1] 895S-0000-BC92 from Vixar, Inc. resonant with Cs D_1 transitions. The package includes a thermoelectric element.
[2] TEMD5020 from Vishay, Inc. The initial TO46 component was replaced by this CMS component.
[3] AD820 from Analog Devices, Inc.
[4] TCBT-14R from Mini-Circuits, Inc.
[5] The wavelength depends on the current with a rate of $0.60\,nm\,mA^{-1}$ and it depends on the temperature by $0.06\,nm\,K^{-1}$
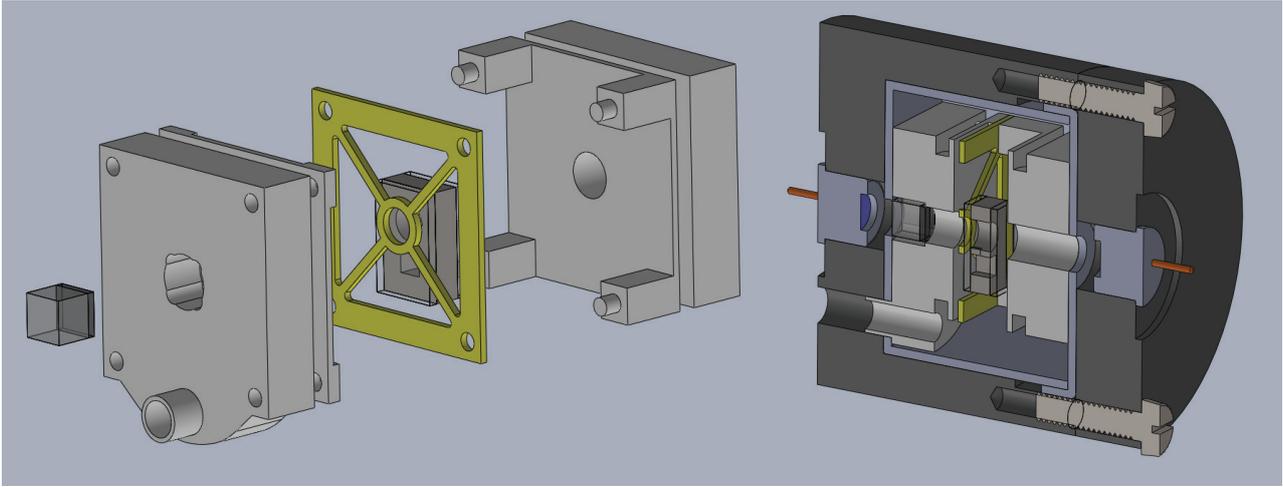
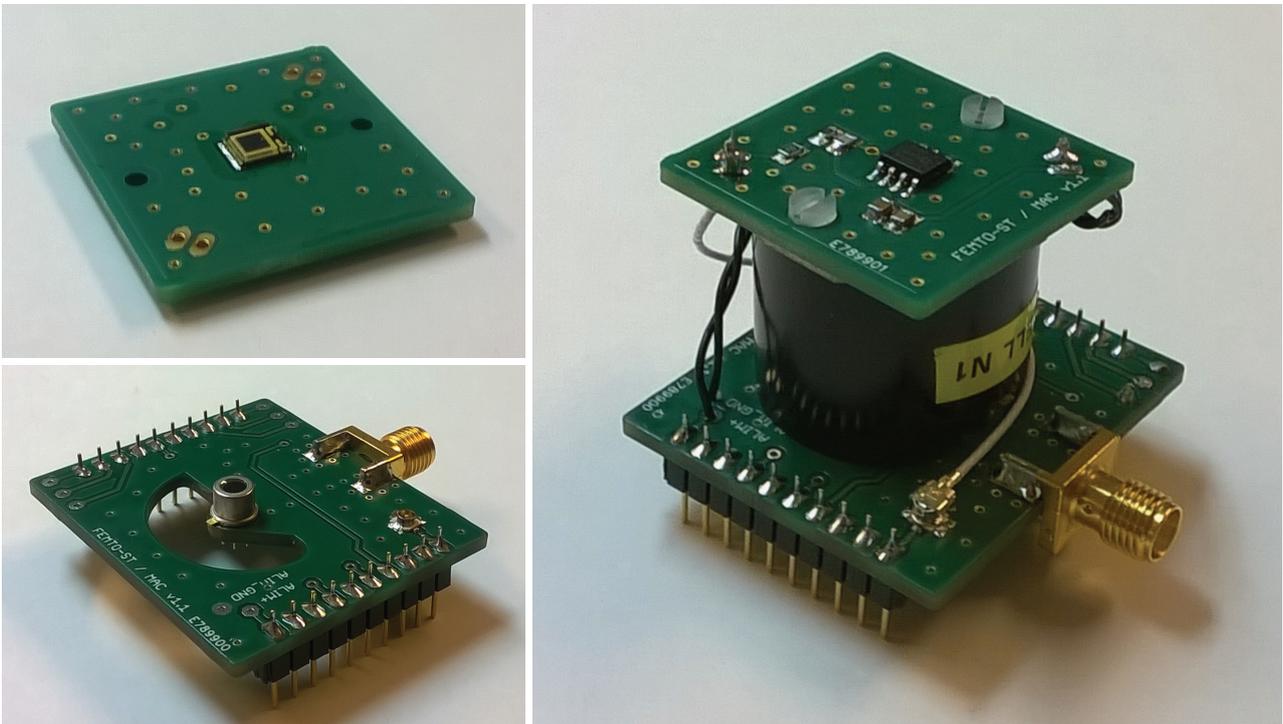Figure 6.8: CAD model of the compact physics package prototype (Rémy Vicarini).

Figure 6.9: Pictures of the photodiode (top left) and VCSEL (bottom left) host PCBs and final physics package (right). The bottom PCB dimensions are $40\,\mathrm{mm} \times 35\,\mathrm{mm}$. Pictures and assembly by Jarosław Rutkowski.
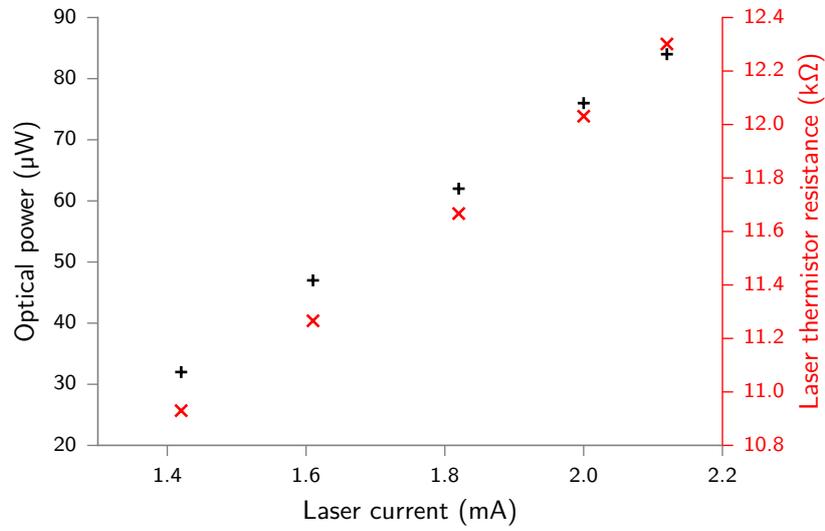
Figure 6.10: Optical power as a function of laser current. The laser temperature is tunned to remain resonant with the cesium D_1 line. The laser thermistor resistance, image of the laser temperature, is shown on the right y-axis.
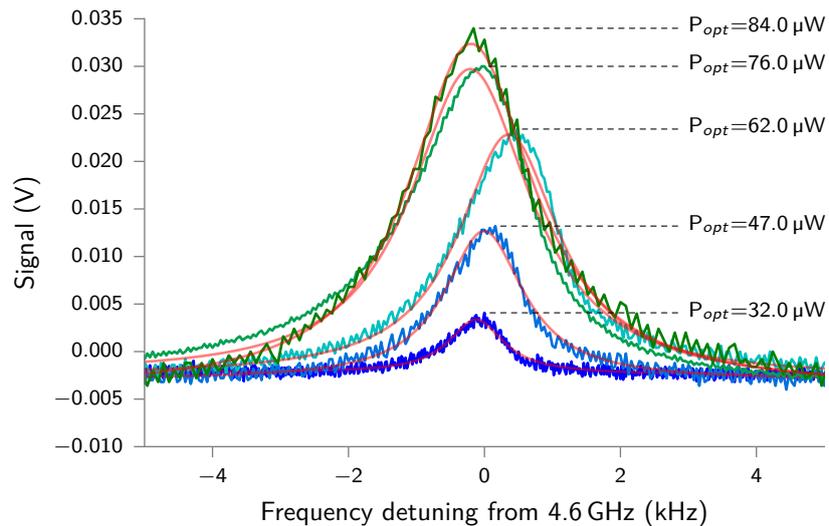
Figure 6.11: CPT signals obtained with the compact physics package at different optical powers. Red lines are Lorentzian fits. The cell temperature is around $80\,°C$.
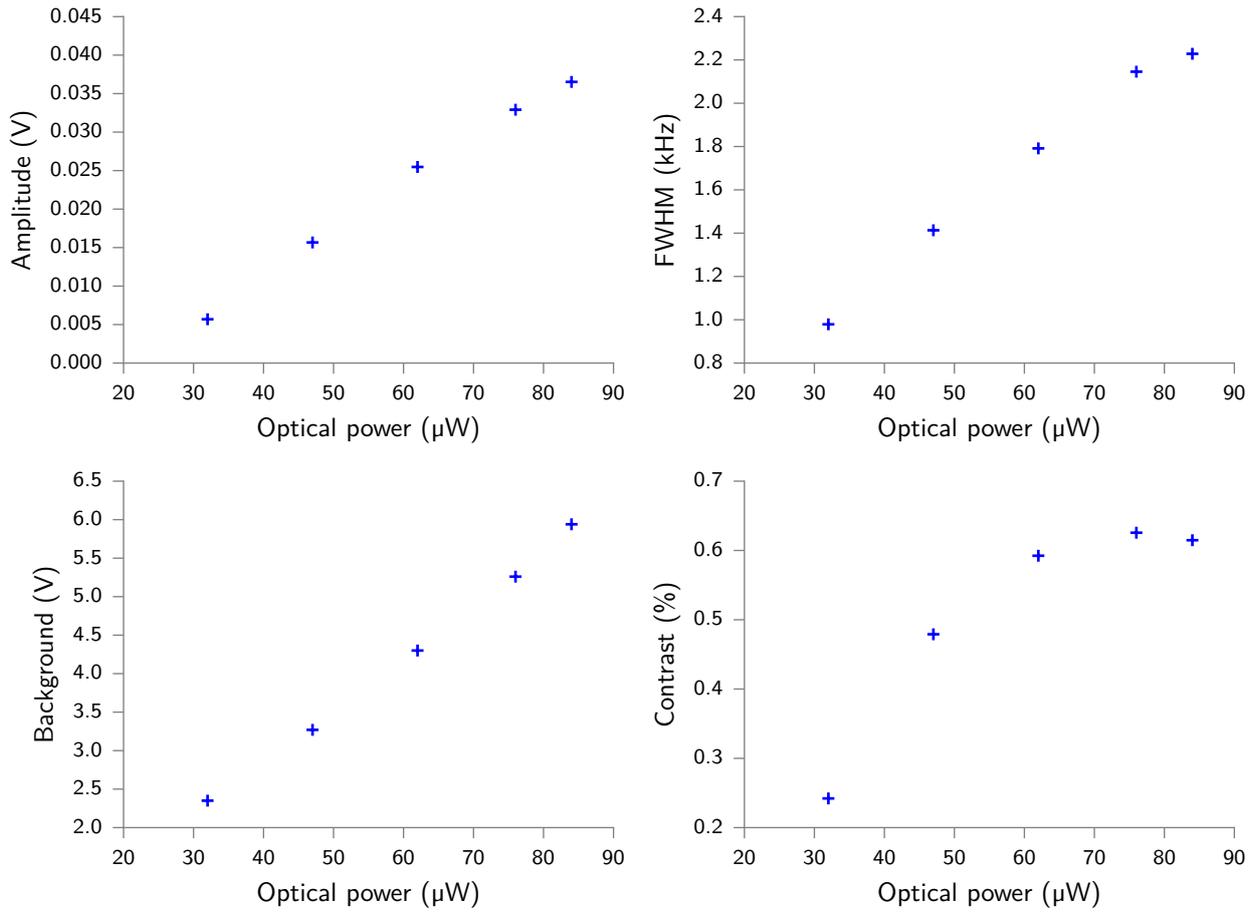
Figure 6.12: Amplitude, FWHM, background level and contrast of the CPT signals at different optical powers. The cell temperature is around 80 °C.
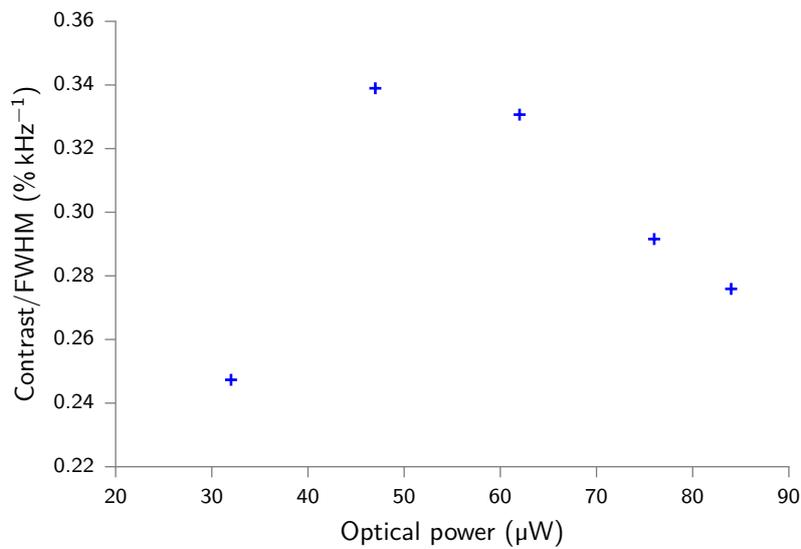
Figure 6.13: Contrast to FWHM ratio of the CPT signals at different optical powers. The cell temperature is around 80 °C.
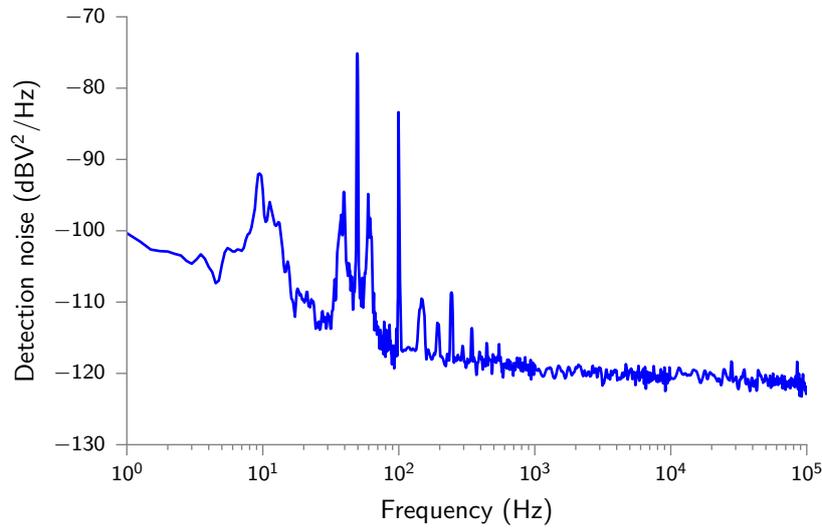
Figure 6.14: Detection noise.
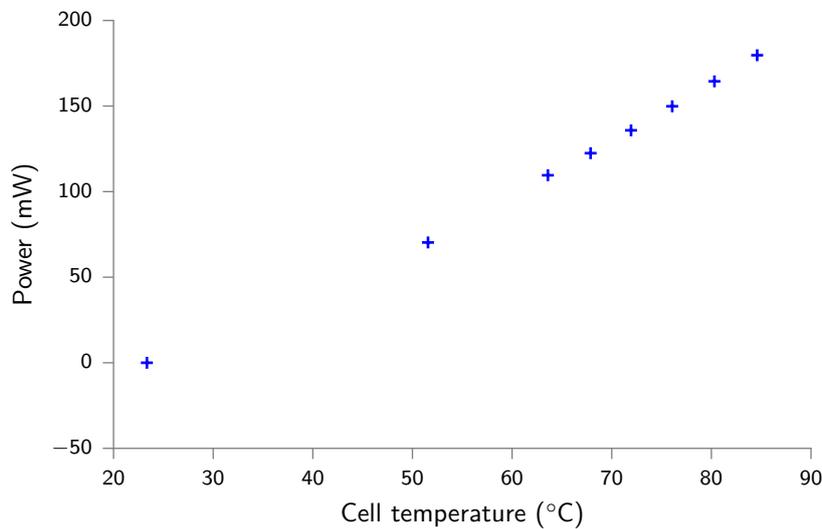
Figure 6.15: Power consumed by the cell heater at different temperatures at an ambient temperature of $22\,°C$.

Power consumption and parasitic magnetic field evaluation.   The power consumed for heating the cell at different temperatures is reported in Fig. 6.15. It reaches $180\,mW$ at $85\,°C$ when the ambient temperature is $22\,°C$. This consumption is primarily due to air conduction and we expect to reduce it significantly by employing vacuum packaging in future designs.

Figure 6.16 shows CPT signals with and without additional magnetic field from the Helmholtz coils. For each configuration, the signal is acquired when the heating current is applied and just after being turned off, while the temperature has not dropped significantly. Without applying any static magnetic field, the lineshape appears broadened, which may indicate the presence of a parasitic static field. However, it does not originate from the heating resistor current. The magnitude of the magnetic field generated by the Helmholtz coils can be estimated by measuring the spacing between the transition from Zeeman levels (-1,-1) and (+1,+1): $\Delta\nu_{-1-1|+1+1} = 2\alpha B$ with $\alpha = 700.84\,kHz\,G^{-1}$. Here, $\Delta\nu_{-1-1|+1+1} = 24.8\,kHz$, and $B = 17.7\,mG$ for a current of $2.25\,mA$. The magnetic field magnitude per current unit generated by the Helmholtz coils is therefore $7.85\,mG\,mA^{-1}$. The frequency of the peaks, corresponding to transitions between different Zeeman sublevels pairs, are estimated by a peak detection algorithm based on continuous wavelet transform, provided by the SciPy[6] library for Python. The maximum contribution to $\Delta\nu_{-1-1|+1+1}$ due to the heater current is estimated at $18\,Hz$, corresponding to a maximum magnetic field around $1.2 \times 10^{-5}\,G$. Assuming that a $100\,mG$ magnetic field is imposed by
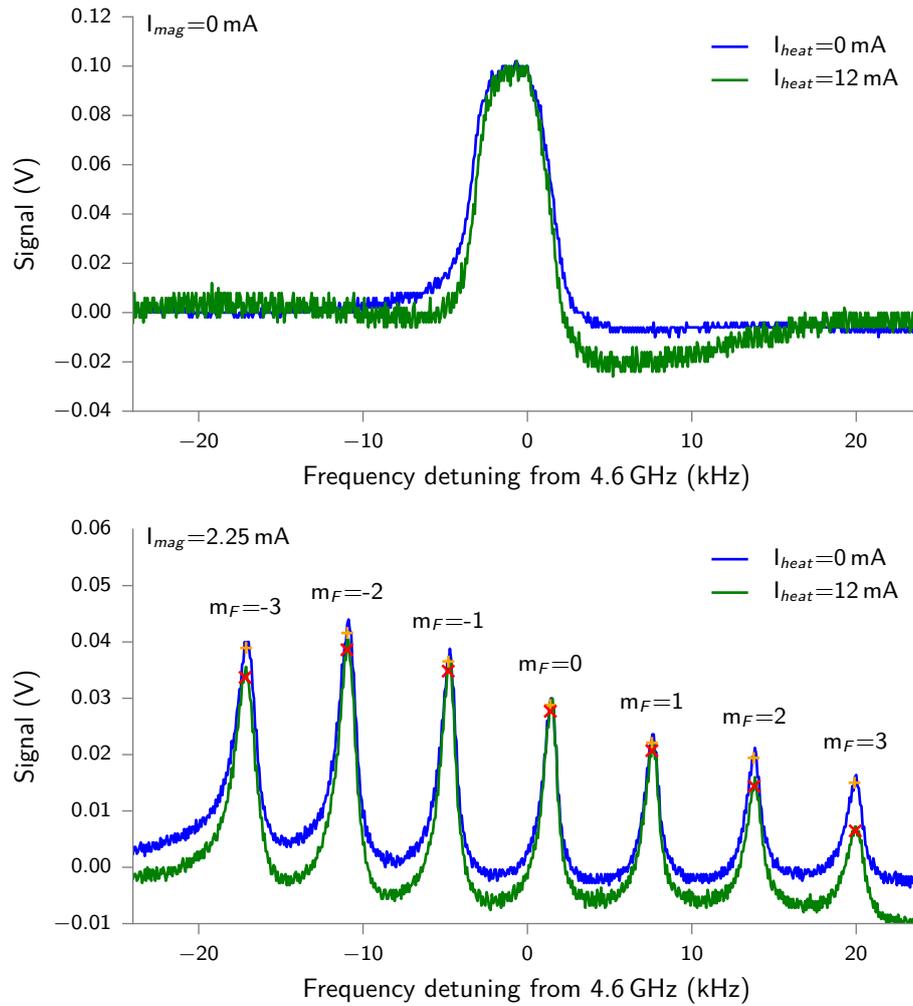
---

[6]http://scipy.org/

Figure 6.16: Influence of the heater current on the magnetic field without static magnetic field (top) and with static magnetic field (bottom). The red and orange crosses mark the position of the detected peaks. The cell temperature is around 85 °C. At steady-state, a current of 12 mA allows to maintain the cell at this temperature when the ambient temperature is 22 °C.

the Helmholtz coil, the additional shift produced by the heater current (12 mA) on the clock frequency (0-0) would be around 1 mHz (1.1×10^{-13} in terms of fractional frequency), which is negligible compared to other instability sources.
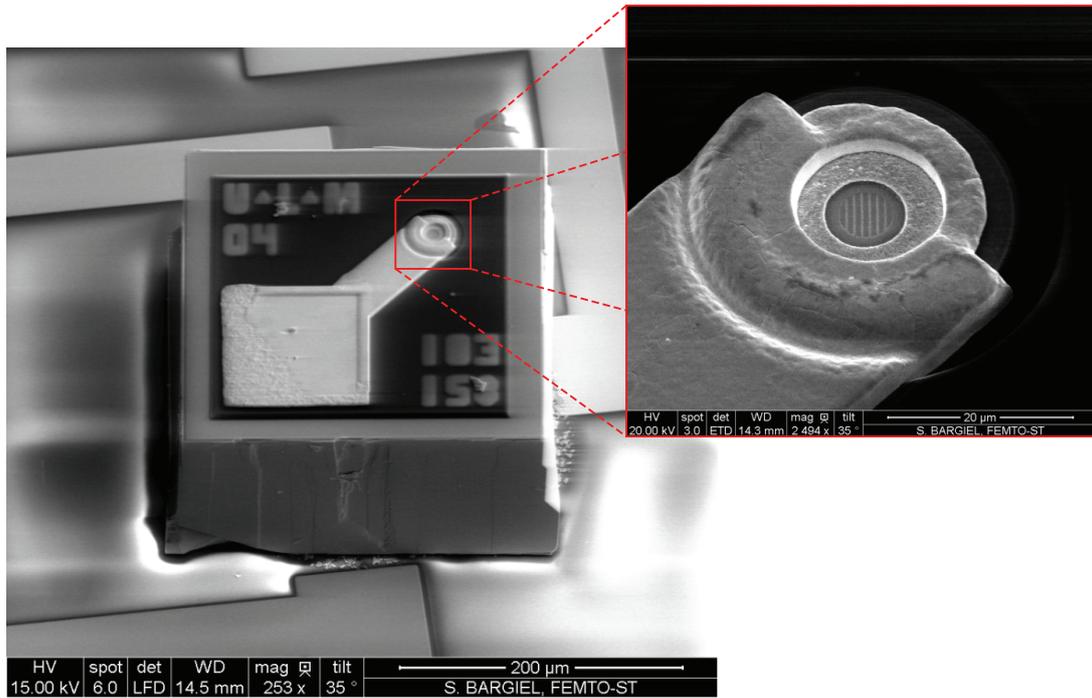
Figure 6.17: SEM image of a VCSEL bonded by solder paste (Sylwester Bargiel).

6.5   Outlooks

The frequency stability obtained with this physics package will soon be evaluated in clock operation. Future developments will consist in reducing further the size and power consumption of the package, while simplifying its assembly. In addition to the problems presented so far, several points will have to be addressed. Indeed, packaging the components in a vacuum enclosure appears mandatory in order to reach a power consumption below 10 mW. The design will have to rely on materials compliant with a vacuum atmosphere, i.e. with low outgassing rates. In order to reduce radiative losses, the non-transparent areas of the cell could be coated with a low emissivity material such as aluminum, silver or gold, as proposed by Mescher *et al.* (2005). The packaging should benefit from a reduced cell size, which would reduce the warm-up time, ease the reduction of the conductivity through the frame bridges and reduce radiative losses.

Bonding the cell by flip-chip and a ball grid array would advantageously replace wire bonding, allowing to attach mechanically the cell to the frame and provide the electrical connections to the resistors.

Using bare VCSEL chips could significantly reduce the size of the package. The distance imposed by the presence of the ferromagnetic TO46 enclosure is detrimental and the integrated thermoelectric element is excessively power-consuming. Like the cell, the VCSEL should be able to operate at a temperature higher than the maximum ambient temperature, so that no cooling is required. The integration of a bare VCSEL chip remains a delicate process as a chip typically measures less than $200\,\mu m \times 200\,\mu m$ and its top surface is fragile. MIMENTO has recently acquired tools to manipulate such components and a procedure to bond VCSEL chips is currently being developed by Sylwester Bargiel. Figure 6.17 shows a SEM image of a VCSEL test die bonded by solder paste on a gold pad deposited on a glass substrate (Bargiel *et al.*, 2016).

Chapter conclusion

Designing a compact physics package requires the integration of a maximum of functions at the wafer-level. Here, we developed a fabrication process to embed heating and sensing resistors directly on the cell. The resistor fabrication process was described in details.

The integration of cells with embedded resistors in a compact physics package and its characterization results from teamwork between several persons, whose respective contributions have been presented. The achieved physics package prototype requires a relatively low power to heat the cell at the desired temperature ($\approx 180\,\mathrm{mW}$ at $22\,°\mathrm{C}$), given that the air conduction losses remain dominant as it does not operate under vacuum. The effect of the heating resistor current on the static magnetic field in the vicinity of the cell was negligible and no significant frequency shifts could be measured. Finally, early CPT spectroscopy and detection noise measurement tend to indicate a promising short-term frequency stability.

Conclusion and perspectives

Driven by strong expectations, the development of miniature atomic clocks has tremendously progressed over the past dozen years, and a commercial device has already appeared on the market. Yet, bringing down their cost below $100 and improving further their reliability and their performances in desirable operating conditions remains challenging and still prevents a wide market acceptance, particularly for telecommunication applications.

Background experience. This work benefited from the experience acquired over the past years by many researchers in the framework of several projects at FEMTO-ST. The work done by Douahi (2009), Dziuban (2011), Chutani (2011) during their PhD thesis can notably be underlined. The past European project MAC-TFC (2008-2012) brought forth important contributions and many aspects investigated in this work initially originated from this project.

It most notably allowed the development of a robust microfabricated cell technology based on solid dispensers, which can easily and safely be employed without complex equipments. The reflective architecture, paste dispensers and antirelaxation coatings were also first considered during this project.

Context. The investigations presented in this thesis were done in the frame of several projects initiated after MAC-TFC and funded by the Direction Générale de l'Armement. Among them, ISIMAC (2012-2015) was specifically oriented toward the reflective architecture and antirelaxation coatings. The HABAC project (2014-2016), conducted in partnership with two industrial partners, aims at transferring the technology know-hows developed at FEMTO-ST to the industry.

Contributions. In this context, the current technology was studied further in order to evaluate its adequacy for large-scale production (Chapter 3). Several improvements have been proposed to reach a high yield consistently. The fabrication process was consolidated and scaled-up by increasing the cell density and employing a custom vacuum pen to handle dispensers more conveniently. A standard anodic bonding equipment has been equipped with dedicated gas lines to provide better buffer gas purities. Buffer gas atmospheres composed of a gas mixture can thereby be prepared with better control. The dispenser laser activation process was found more reliable than what previous experiments foreshadowed. It was notably shown that a baking step of a few hours after the activation was highly beneficial as it speeds up the establishment of the atomic density. After baking, most cells exhibit a saturated cesium vapor. With this respect, a much higher success rate than initially observed was obtained. Concerns about a potential condensation excess, which could lead to light obstruction, have been partially alleviated as dispensers seem to draw condensation away from the optical cavities.

Long-term frequency measurements have shown that the maximum relative frequency drift in cells fabricated with the current technology is lower than $-3.8 \times 10^{-12}\,\mathrm{d}^{-1}$, which complies with the targeted specifications (Section 4.4).

Several limitations on the cell operating temperature, fabrication cost and size were identified and solutions to tackle some of those problems were investigated.

First, a single neon buffer gas, which cancels the thermal frequency dependence around $79\,^\circ\mathrm{C}$, imposes a limit on the maximum ambient temperature the clock can operate at. However, many applications require the device to operate up to $85\,^\circ\mathrm{C}$. This entails that the cell must operate at even higher temperatures. A buffer gas mixture of neon and helium was found to displace the inversion point of the frequency-temperature dependency at higher temperatures, up to $95\,^\circ\mathrm{C}$ (Section 4.3.2). Such an atmosphere could answer this need, but the high permeation rate of helium through borosilicate glass limits its applicability with the current technology.

Alternatively, microfabricated make-seal and break-seal components inspired from classical glass-blown fabrication techniques have been proposed and first experiments have been presented (Section 3.6). After longer-

term developments, they could eliminate the need for incorporating a dispenser in each cell, and would allow any buffer gas to be introduced in the cells, in particular a mixture of nitrogen and argon, which allows to select freely the cell operating temperature and limits radiation trapping. With the ability to share alkali metal from only a few dispensers per wafer, a drastic fabrication cost reduction is expected. The cell dimensions are favorably reduced, which could lower the power consumption of the final device thanks to reduced radiative losses.

Dispensers under a form of paste could also significantly lower the unit cell price, which is currently severely affected by the dispenser cost and its relatively large size (Section 3.5). A first batch of cells has been fabricated and their atomic density has been stable for several months. Compared to make-seal components, which will require further developments, we expect that paste-like dispensers could be applied to a large-scale production relatively soon. As it appeared necessary to monitor cells in parallel through linear absorption spectroscopy over long time periods, a dedicated setup combining activation and linear absorption has been developed. This bench will facilitate further studies and help improving the repeatability of the activation process.

The reflective architecture has been presented, along with its design and fabrication (Section 3.3). A physics package based on such architecture could potentially be fabricated at the wafer-level and significantly lower the associated assembly costs. The characterization of reflective cells was reported (Section 4.2.2). Remarkable contrasts could be measured despite their reduced inner volume with a DFB laser.

As an alternative the buffer gases, wall-coatings could relax some of the constraints imposed on the physics package and could allow high contrast closed-lambda pumping schemes to be employed. In these respects, OTS antirelaxation wall coatings have been studied in centimeter-scale cells and in millimeter-scale cells (Chapter 5). An antirelaxation effect could be observed through the specific dual-structure CPT lineshape. However, the coating performances remain insufficient and the large temperature dependency induced on the clock frequency still precludes their use in clock applications. As we expect the effect of coatings to be exacerbated in millimeter-scale cells, the coating procedure was adapted to microfabricated cells. OTS is supposed to withstand high temperatures under vacuum. The process based on dispensers seems therefore adequate since no alkali vapor is present in the cell when the cell is heated at high temperature during bonding. A method to selectively remove OTS at the bonding interface was identified. Coated microfabricated cells could be fabricated and were characterized through CPT spectroscopy. An antirelaxation effect has seemingly been observed but the effect of a potential buffer gas background pressure could not be excluded.

Finally, aiming at integrating additional functions at the wafer-level, cells with integrated heating and sensing resistors were designed and fabricated (Chapter 6). In a collaborative effort, the cells were integrated in a compact physics package prototype. The deposited resistors were characterized and found particularly robust even for high currents. The physics package was further characterized through CPT spectroscopy and detection noise measurements. A promising short-term frequency stability of $1.49 \times 10^{-11} \; \tau^{-1/2}$ can be expected. The effect of the heating resistor current on the static magnetic field was negligible and no stability degradation is expected with this heater design.

Future work. This thesis outlines at multiple occasions the remaining points that should be studied further, notably, regarding the fabrication processes.

The activation and curing processes can be studied for a larger number of cells, which could allow us to derive statistics and quantify more precisely the potential production yield.

In particular, paste-like dispensers will soon be tested in cells with buffer gas, which will allow to characterize more finely their atmosphere stability.

The development of make-seal and break-seal structures has only began. After the preliminary experiments exposed here, complete structures will be fabricated. It is worth noting that this technique opens the path to other alkali metal sources, in particular ^{87}Rb, which could help to reach high operating temperatures without degrading the short-term stability.

In order to prevent helium permeation, other types of glass, such as aluminosilicate glass could be envisioned.

Wall-coatings could be developed further and could notably be used in combination with buffer gas. A filling technique based on make-seal components could help to deposit the coating through microfluidic means.

As far as the physics package is concerned, investigations are ongoing to integrate bare VCSEL dies and incorporate additional functions at the wafer-level. The compact physics package prototype presented here, will be tested in a clock setup. The package could be particularly convenient to measure the long-term frequency evolution of several cells in parallel.

Beyond atomic clocks. In addition to atomic clocks, the spectroscopy of atoms in small devices can be exploited in a wide variety of applications. In a recent review, Kitching *et al.* (2011b) presents different atomic sensors. In particular, optical magnetometers with sensitivities exceeding those of superconducting quantum interference devices (SQUIDs) have recently been demonstrated. A small form-factor magnetometer can be made with a physics package almost identical to a CSAC. Indeed, it did not take long after the demonstration of the first CSAC for a chip-scale atomic magnetometer to be demonstrated (Schwindt *et al.*, 2004). Instead of probing a transition whose frequency is invariant with the magnetic field, the frequency of two transitions sensitive to the magnetic field are measured and subtracted to cancel the magnetic-field-invariant component of the frequency.

Shah *et al.* (2007), Schwindt *et al.* (2007), Mhaskar *et al.* (2012), Rutkowski *et al.* (2014) reported excellent sensitivities and in vivo medical applications have already been reported (Sander *et al.*, 2012, Alem *et al.*, 2014, Corsi, 2015).

Appendix A

Cell list

Wafer/Cell ID	Cesium source	Atmosphere	Note
T8	Cs pills	Evac.	
T9	Cs pills	Ne 20 Torr	
T10	Cs pills	Ne 150 Torr	
T11	Cs pills	Ne 250 Torr	
T12	Cs pills	Ne 350 Torr	
T14	Cs pills	Ne + He 50 Torr	
T16	Cs pills	Ne + He 50 Torr	
T18	Cs pills	He 20 Torr	
T19	Cs pills	Ne 70 Torr	Integrated heater
T21	Cs pills	Evac.	Break seal
T26	Cs pills	Evac.	OTS
T27	Cs pills	Evac.	OTS
T28	Cs pills	Evac.	OTS
R1xx	Cs pills	Evac.	
R2xx	Cs pills	Ne 100 Torr	
R3xx	Cs pills	Ne 200 Torr	
R4xx	Cs pills	Ne 100 Torr	
HABW6	Cs pills	Ne 80 Torr	Getters
HABW7	Cs paste and pills	Evac.	
HABW8	Cs pills	He 80 Torr	HOYA SD2
Cs1	Pure Cs	Evac.	
Cs2	Pure Cs	Evac.	
Cs-OTS1	Pure Cs	Evac.	OTS vapor phase
Cs-OTS2	Pure Cs	Evac.	OTS vapor phase
Cs-OTS3	Pure Cs	Evac.	OTS vapor phase
Cs-OTS4	Pure Cs	Evac.	OTS liquid phase
Cs-OTS5	Pure Cs	Evac.	OTS liquid phase

Table A.1: List of wafers of microfabricated cells and centimeter scale glass-blown cells.

Bibliography

M. Abdel Hafiz and R. Boudot. A coherent population trapping Cs vapor cell atomic clock based on push-pull optical pumping. *Journal of Applied Physics*, 118(12):124903, 2015. doi: 10.1063/1.4931768. □

M. Abdel Hafiz, V. Maurice, R. Chutani, N. Passilly, C. Gorecki, S. Guérandel, E. de Clercq, and R. Boudot. Spectroscopy and hyperfine clock frequency shift measurements in Cs vapor cells coated with octadecyl-trichlorosilanes (OTS). In *2015 Joint Conference of the IEEE International Frequency Control Symposium the European Frequency and Time Forum*, pages 33–36, 2015a. doi: 10.1109/FCS.2015.7138787. □

M. Abdel Hafiz, V. Maurice, R. K. Chutani, N. Passilly, C. Gorecki, S. Guérandel, E. de Clercq, and R. Boudot. Characterization of Cs vapor cell coated with octadecyltrichlorosilane using coherent population trapping spectroscopy. *Journal of Applied Physics*, 117(18):184901, 2015b. doi: 10.1063/1.4919841. □

S. Abdullah, C. Affolderbach, F. Gruet, and G. Mileti. Aging studies on micro-fabricated alkali buffer-gas cells for miniature atomic clocks. *Applied Physics Letters*, 106(16):163505, 2015. doi: 10.1063/1.4919009. □

C. Affolderbach, A. Nagel, S. Knappe, C. Jung, D. Wiedenmann, and R. Wynands. Nonlinear spectroscopy with a vertical-cavity surface-emitting laser (VCSEL). *Applied Physics B*, 70(3):407–413, 2000. doi: 10.1007/s003400050066. □

A. Al-Samaneh, M. Bou Sanayeh, M. J. Miah, W. Schwarz, D. Wahl, A. Kern, and R. Michalzik. Polarization-stable vertical-cavity surface-emitting lasers with inverted grating relief for use in microscale atomic clocks. *Applied Physics Letters*, 101(17):171104, 2012. doi: 10.1063/1.4764010. □

O. Alem, A. M. Benison, D. S. Barth, J. Kitching, and S. Knappe. Magnetoencephalography of epilepsy with a microfabricated atomic magnetrode. *The Journal of Neuroscience*, 34(43):14324–7, 2014. doi: 10.1523/JNEUROSCI.3495-14.2014. □

D. W. Allan. Statistics of Atomic Frequency Standards. In *Proceedings of the IEEE*, volume 54, pages 221–230. IEEE, 1966. doi: 10.1109/PROC.1966.4634. □

D. W. Allan, N. Ashby, and C. Hodge. *The Science of Timekeeping.* Application note 1289. Hewlett-Packard, 1997.

G. Alzetta, A. Gozzini, L. Moi, and G. Orriols. An experimental method for the observation of RF transitions and laser beat resonances in oriented Na vapour. *Il Nuovo Cimento B*, 36(1):5–20, 1976. doi: 10.1007/BF02749417. □

A. Andalkar and R. Warrington. High-resolution measurement of the pressure broadening and shift of the Cs $D1$ and $D2$ lines by N_2 and He buffer gases. *Physical Review A*, 65(3):1–7, 2002. doi: 10.1103/PhysRevA.65.032708. □

M. V. Balabas, K. Jensen, W. Wasilewski, H. Krauter, L. S. Madsen, J. H. Müller, T. Fernholz, and E. S. Polzik. High quality anti-relaxation coating material for alkali atom vapor cells. *Optics Express*, 18(6):5825–30, 2010a. doi: 10.1364/OE.18.005825. □

M. V. Balabas, T. Karaulanov, M. P. Ledbetter, and D. Budker. Polarized Alkali-Metal Vapor with Minute-Long Transverse Spin-Relaxation Time. *Physical Review Letters*, 105(7):070801, 2010b. doi: 10.1103/PhysRevLett.105.070801. □

T. Bandi, C. Affolderbach, and G. Mileti. Laser-pumped paraffin-coated cell rubidium frequency standard. *Journal of Applied Physics*, 111(12):124906, 2012. doi: 10.1063/1.4729570. □

T. Bandi, C. Affolderbach, C. Stefanucci, F. Merli, A. K. Skrivervik, and G. Mileti. Compact high-performance continuous-wave double-resonance rubidium standard with $1.4 \times 10^{-13} \tau^{-1/2}$ stability. *IEEE Transactions on Ultrasonics, Ferroelectrics and Frequency Control*, 61(11):1769–78, 2014. doi: 10.1109/TUFFC.2013.005955. ☐

K. A. Barantsev, E. N. Popov, and A. N. Litvinov. Influence of the finite linewidth of the laser radiation spectrum on the shape of the coherent population trapping resonance line in an optically dense medium with a buffer gas. *Journal of Experimental and Theoretical Physics*, 121(5):758–769, 2015. doi: 10.1134/S1063776115110011. ☐

S. Bargiel, V. Petrini, and F. Lardet-Vieudrin. Flip-chip machine (Suss Microtec FC-250). MIMENTO technical report, 2016. ☐

M. Bartek, J. A. Foerster, and R. F. Wolffenbuttel. Vacuum sealing of microcavities using metal evaporation. *Sensors and Actuators A: Physical*, 61(1–3):364–368, 1997. doi: 10.1016/S0924-4247(97)80290-7. ☐

E. Bernabeu and J. Alvarez. Shift and broadening of hyperfine components of the first doublet of cesium perturbed by foreign gases. *Physical Review A*, 22(6):2690–2695, 1980. doi: 10.1103/PhysRevA.22.2690. ☐

N. Beverini, P. Minguzzi, and F. Strumia. Foreign-gas-induced cesium hyperfine relaxation. *Physical Review A*, 4(2):550–555, 1971. doi: 10.1103/PhysRevA.4.550. ☐

M. Bloch, O. Mancini, and T. McClelland. Performance of rubidium and quartz clocks in space. In *Proceedings of the 2002 IEEE International Frequency Control Symposium and PDA Exhibition (Cat. No.02CH37234)*, pages 505–509. IEEE, 2002. doi: 10.1109/FREQ.2002.1075936. ☐

R. L. Borwick, J. F. DeNatale, C. Tsai, P. A. Stupar, and Y.-C. Chen. System for heating a vapor cell. United States Patent US 8,319,156 B2, 2012. ☐

M.-A. Bouchiat. *Etude par pompage optique de la relaxation d'atomes de rubidium.* PhD thesis, Université de Paris, 1964. ☐

M.-A. Bouchiat and J. Brossel. Relaxation of optically pumped Rb atoms on paraffin-coated walls. *Physical Review*, 147(1):41–54, 1966. doi: 10.1103/PhysRev.147.41. ☐

M.-A. Bouchiat, J. Guéna, P. Jacquier, M. Lintz, and A. V. Papoyan. Electrical conductivity of glass and sapphire cells exposed to dry cesium vapor. *Applied Physics B*, 68(6):1109–1116, 1999. doi: 10.1007/s003400050752. ☐

R. Boudot, P. Dziuban, M. Hasegawa, R. K. Chutani, S. Galliou, V. Giordano, and C. Gorecki. Coherent population trapping resonances in Cs-Ne vapor microcells for miniature clocks applications. *Journal of Applied Physics*, 109(1):014912, 2011a. doi: 10.1063/1.3530951. ☐

R. Boudot, P. Dziuban, X. Liu, M. Hasegawa, R. K. Chutani, S. Galliou, V. Giordano, and C. Gorecki. Dark line resonances in Cs-Ne vapor microcells for chip scale atomic clocks. *2011 Joint Conference of the IEEE International Frequency Control and the European Frequency and Time Forum FCS Proceedings*, pages 1–5, 2011b. doi: 10.1109/FCS.2011.5977774. ☐

R. Boudot, X. Liu, P. Abbe, R. K. Chutani, N. Passilly, S. Galliou, C. Gorecki, and V. Giordano. A high-performance frequency stability compact CPT clock based on a Cs-Ne microcell. *IEEE Transactions on Ultrasonics, Ferroelectrics and Frequency Control*, 59(11):2584–2587, 2012. doi: 10.1109/TUFFC.2012.2493. ☐

R. Boudot, C. Gorecki, V. Maurice, E. Kroemer, and B. Fouilland. Caesium atomic micro-clock microcell buffer gas mixture. United States Patent Application US 2016/0109859 A1, 2016. ☐

Y. Bourgin, Y. Jourlin, O. Parriaux, A. Talneau, S. Tonchev, C. Veillas, P. Karvinen, N. Passilly, A. R. Md Zain, R. M. De La Rue, J. Van Erps, and D. Troadec. 100 nm period grating by high-index phase-mask immersion lithography. *Optics Express*, 18(10):10557–10566, 2010. doi: 10.1364/OE.18.010557. ☐

A. M. Braun, T. J. Davis, M. H. Kwakernaak, J. Michalchuk, W. K. Chan, J. H. Abeles, Z. Shellenbarger, Y.-Y. Jau, W. Happer, T. McClelland, H. Fruehauf, R. Drap, W. Weidemann, and M. Variakojis. RF-interrogated end-state chip-scale atomic clock. In *39th Annual Precise Time and Time Interval (PTTI) Meeting*, pages 233–248, 2007. ☐

E. Breschi, G. A. Kazakov, C. Schori, G. Di Domenico, G. Mileti, A. N. Litvinov, and B. G. Matisov. Light effects in the atomic-motion-induced Ramsey narrowing of dark resonances in wall-coated cells. *Physical Review A*, 82(6):063810, 2010. doi: 10.1103/PhysRevA.82.063810. ☐

R. G. Brewer. Study of Atom—Wall Collisions by Optical Pumping. *The Journal of Chemical Physics*, 38(12): 3015, 1963. doi: 10.1063/1.1733636. ☐

J. Brossel, J.-L. Mosser, and M. Winter. Absorption du sodium par des parois de verre chauffées à 120 °C. *J. Phys. Radium*, 16(10):814–815, 1955. doi: 10.1051/jphysrad:019550016010081401. ☐

D. Budker, W. Gawlik, D. F. Kimball, S. M. Rochester, V. V. Yashchuk, and A. Weis. Resonant nonlinear magneto-optical effects in atoms. *Reviews of Modern Physics*, 74(4):1153–1201, 2002. doi: 10.1103/RevModPhys.74.1153. ☐

D. Budker, L. Hollberg, D. F. J. Kimball, J. Kitching, S. Pustelny, and V. V. Yashchuk. Microwave transitions and nonlinear magneto-optical rotation in anti-relaxation-coated cells. *Physical Review A*, 71(1):012903, 2005. doi: 10.1103/PhysRevA.71.012903. ☐

L. Cacciapuoti and C. Salomon. Space clocks and fundamental tests: The ACES experiment. *The European Physical Journal Special Topics*, 172(1):57–68, 2009. doi: 10.1140/epjst/e2009-01041-7. ☐

J. C. Camparo. Frequency equilibration and the light-shift effect for block IIR GPS rubidium clocks. *36th Annual Precise Time and Time Interval (PTTI) Meeting*, pages 393–410, 2004. ☐

J. C. Camparo, R. Frueholz, and B. Jaduszliwer. Alkali reactions with wall coating materials used in atomic resonance cells. *Journal of Applied Physics*, 62(2):676, 1987. doi: 10.1063/1.339741. ☐

L. Cattaneo, C. Maeda, and R. Petersen. AlkaMax SAES Solution for Alkali Metal Dispensing in OLED Display Manufacturing. Application note, SAES Getters, 2004. ☐

R. K. Chutani. *Conception, technologie et packaging de cellules à vapeur de césium pour les horloges atomiques de type MEMS*. PhD thesis, Université de Franche-Comté, Besançon, 2011. ☐

R. K. Chutani, S. Galliou, N. Passilly, C. Gorecki, A. Sitomaniemi, M. Heikkinen, K. Kautio, A. Keränen, and A. Jornod. Thermal management of fully LTCC-packaged Cs vapour cell for MEMS atomic clock. *Sensors and Actuators A: Physical*, 174:58–68, 2012. doi: 10.1016/j.sna.2011.11.025. ☐

R. K. Chutani, N. Passilly, J. Albero, M. Baranski, and C. Gorecki. Deep Wet-Etched Silicon Cavities for Micro-Optical Sensors: Influence of Masking on Sidewalls Surface Quality. *Journal of Microeletromechanical Systems*, 23(3):585–591, 2013. doi: 10.1109/JMEMS.2013.2285575. ☐

R. K. Chutani, M. Hasegawa, V. Maurice, N. Passilly, and C. Gorecki. Single-step deep reactive ion etching of ultra-deep silicon cavities with smooth sidewalls. *Sensors and Actuators A: Physical*, 208:66–72, 2014. doi: 10.1016/j.sna.2013.12.031. ☐

R. K. Chutani, V. Maurice, N. Passilly, C. Gorecki, R. Boudot, M. Abdel Hafiz, P. Abbé, S. Galliou, J.-Y. Rauch, and E. de Clercq. Laser light routing in an elongated micromachined vapor cell with diffraction gratings for atomic clock applications. *Scientific Reports*, 5:14001, 2015. doi: 10.1038/srep14001. ☐

M.-C. Corsi. *Magnétomètres à pompage optique à Hélium 4 : développement et preuve de concept en magnéto-cardiographie et en magnétoencéphalographie*. PhD thesis, Université Grenoble Alpes, 2015. ☐

E. Corsini, T. Karaulanov, M. V. Balabas, and D. Budker. Hyperfine frequency shift and Zeeman relaxation in alkali-metal-vapor cells with antirelaxation alkene coating. *Physical Review A*, 87(2):022901, 2013. doi: 10.1103/PhysRevA.87.022901. ☐

A. H. Couture, T. B. Clegg, and B. Driehuys. Pressure shifts and broadening of the Cs D_1 and D_2 lines by He, N_2, and Xe at densities used for optical pumping and spin exchange polarization. *Journal of Applied Physics*, 104(9):094912, 2008. doi: 10.1063/1.3018181. ☐

N. Cyr, M. Têtu, and M. Breton. All-optical microwave frequency standard: a proposal. *IEEE Transactions On Instrumentation And Measurement*, 42(2):640–649, 1993. doi: 10.1109/19.278645. ☐

J.-M. Danet. *Horloge atomique à piégeage cohérent de population du césium en cellule : limitations à la stabilité de fréquence.* PhD thesis, Université Pierre et Marie Curie - Paris VI, 2014. ☐

J.-M. Danet, O. Kozlova, P. Yun, S. Guérandel, and E. de Clercq. Compact atomic clock prototype based on coherent population trapping. *EPJ Web of Conferences*, 77:00017, 2014. doi: 10.1051/epjconf/20147700017. ☐

J. A. Davis, J. Adachi, C. R. Fernández-Pousa, and I. Moreno. Polarization beam splitters using polarization diffraction gratings. *Optics Letters*, 26(9):587–589, 2001. doi: 10.1364/OL.26.000587. ☐

T. J. Davis, S. E. McBride, A. M. Braun, and W. Happer. System and method for modulating pressure in an alkali-vapor cell. United States Patent US 7,902,927 B2, 2011. ☐

E. de Clercq, M. de Labachellerie, G. Avila, P. Cerez, and M. Têtu. Laser diode optically pumped caesium beam. *Journal de Physique*, 45(2):239–247, 1984. doi: 10.1051/jphys:01984004502023900. ☐

A. Dellis, S. Knappe, E. A. Donley, and J. Kitching. Low He Permeation Cells for CSACs. In *8th Symposium on Frequency Standards and Metrology*, Postdam, 2015.

J. F. DeNatale, R. L. Borwick, C. Tsai, P. A. Stupar, Y.-H. Lin, R. A. Newgard, R. W. Berquist, and M. Zhu. Compact, low-power chip-scale atomic clock. In *Proceedings of the Position Location and Navigation Symposium (PLANS)*, pages 67–70, Monterey, CA, 2008. IEEE/ION. doi: 10.1109/PLANS.2008.4570007. ☐

J. F. DeNatale, R. L. Borwick, P. A. Stupar, and C. Tsai. Compact optical assembly for chip-scale atomic clock. United States Patent US 7,619,485 B2, 2009. ☐

R. Dicke. The effect of collisions upon the Doppler width of spectral lines. *Physical Review*, 89(2):472–473, 1953. doi: 10.1103/PhysRev.89.472. ☐

A. Douahi. *Contributions au développement d'une microhorloge CPT : étude des microcellules à vapeur de césium.* PhD thesis, Université de Franche-Comté, 2009. ☐

A. Douahi, L. Nieradko, and J.-C. Beugnot. Vapour microcell for chip scale atomic frequency standard. *Electronics Letters*, 43(5):34–35, 2007. doi: 10.1049/el:20070147. ☐

A. Douahi, M. Hasegawa, L. Nieradko, J. Boy, C. Gorecki, and V. Giordano. Advanced Vapor Cell Technologies for Chip Scale Atomic Clock. In *22nd european frequency and time forum*, pages 1–5, Toulouse, 2008. ☐

P. Dziuban. *La micro horloge atomique : étude et caractérisation métrologique de microcellules.* PhD thesis, 2011. ☐

E. J. Eklund and A. M. Shkel. Glass blowing on a wafer level. *Journal of Microeletromechanical Systems*, 16 (2):232–239, 2007. doi: 10.1109/JMEMS.2007.892887. ☐

H. Elfström, M. Kuittinen, T. Vallius, B. H. Kleemann, J. Ruoff, and R. Arnold. Fabrication of blazed gratings by area-coded effective medium structures. *Optics Communications*, 266(2):697–703, 2006. doi: 10.1016/j.optcom.2006.05.042. ☐

H. Failache, L. Lenci, and A. Lezama. Raman-Ramsey multizone spectroscopy in a pure rubidium vapor cell. *Physical Review A*, 81(2):023801, 2010. doi: 10.1103/PhysRevA.81.023801. ☐

J. Fedchak, P. Cabauy, W. Cummings, C. Jones, and R. Kowalczyk. Silane coatings for laser-driven polarized hydrogen sources and targets. *Nuclear Instruments and Methods in Physics Research Section A*, 391(3): 405–416, 1997. doi: 10.1016/S0168-9002(97)00571-8. ☐

M. Feld and A. Javan. Laser-induced line-narrowing effects in coupled Doppler-broadened transitions. *Physical Review*, 177(2):540–562, 1969. doi: 10.1103/PhysRev.177.540. ☐

O. Firstenberg, M. Shuker, A. Ben-Kish, D. Fredkin, N. Davidson, and A. Ron. Theory of Dicke narrowing in coherent population trapping. *Physical Review A*, 76(1):013818, 2007. doi: 10.1103/PhysRevA.76.013818. ☐

F. Franz. Enhancement of alkali optical pumping by quenching. *Physics Letters*, 27A(7):457–458, 1968. doi: 10.1016/0375-9601(68)90858-X. ☐

W. Franzen. Spin relaxation of optically aligned rubidium vapor. *Physical Review*, 115(4):850–856, 1959. doi: 10.1103/PhysRev.115.850. ☐

S. Gateva, L. Gurdev, E. Alipieva, E. Taskova, and G. Todorov. Narrow structure in the coherent population trapping resonances in rubidium and Rayleigh scattering. *Journal of Physics B: Atomic, Molecular and Optical Physics*, 44(3):035401, 2011. doi: 10.1088/0953-4075/44/3/035401. ☐

A. Godone, F. Levi, S. Micalizio, and J. Vanier. Dark-line in optically-thick vapors: inversion phenomena and line width narrowing. *The European Physical Journal D - Atomic, Molecular, Optical and Plasma Physics*, 18(1):5–13, 2002. doi: 10.1140/e10053-002-0001-z. ☐

M. Godun, R. B. R. Nisbet-Jones, P. M. Jones, J. A. King, S. A. M. Johnson, L. S. Margolis, H. K. Szymaniec, N. Lea, S. K. Bongs, and P. Gill. Frequency Ratio of Two Optical Clock Transitions in ^{171}Yb$^+$ and Constraints on the Time Variation of Fundamental Constants. *Physical Review Letters*, 113(21):210801, 2014. doi: 10.1103/PhysRevLett.113.210801. ☐

H. M. Goldenberg, D. Kleppner, and N. F. Ramsey. Atomic Beam Resonance Experiments with Stored Beams. *Physical Review*, 123(2):530–537, 1961. doi: 10.1103/PhysRev.123.530. ☐

F. Gong, Y.-Y. Jau, K. Jensen, and W. Happer. Electrolytic fabrication of atomic clock cells. *Review of Scientific Instruments*, 77(7):076101, 2006. doi: 10.1063/1.2219730. ☐

C. Gorecki, M. Hasegawa, N. Passilly, R. K. Chutani, P. Dziuban, S. Galliou, and V. Giordano. Towards the realization of the first European MEMS atomic clock. In *2009 IEEE/LEOS International Conference on Optical MEMS and Nanophotonics*, volume 1, pages 47–48, Clearwater, FL, 2009. IEEE. doi: 10.1109/OMEMS.2009.5338604. ☐

F. Gori. Measuring Stokes parameters by means of a polarization grating. *Optics Letters*, 24(9):584–586, 1999. doi: 10.1364/OL.24.000584. ☐

M. B. Gornyi, B. G. Matisov, and Y. V. Rozhdestvenskii. Coherent population trapping in an optically dense medium. *Soviet Physics - JETP (English Translation)*, 68(4):728–731, 1989. ☐

M. Graf, D. F. J. Kimball, S. M. Rochester, K. Kerner, C. Wong, D. Budker, E. B. Aleksandrov, M. V. Balabas, and V. V. Yashchuk. Relaxation of atomic polarization in paraffin-coated cesium vapor cells. *Physical Review A*, 72(2):023401, 2005. doi: 10.1103/PhysRevA.72.023401. ☐

F. Gruet, A. Al-Samaneh, E. Kroemer, L. Bimboes, D. Miletic, C. Affolderbach, D. Wahl, R. Boudot, G. Mileti, and R. Michalzik. Metrological characterization of custom-designed 894.6 nm VCSELs for miniature atomic clocks. *Optics Express*, 21(5):5781–92, 2013. ☐

M. Grundner and H. Jacob. Investigations on hydrophilic and hydrophobic silicon (100) wafer surfaces by X-ray photoelectron and high-resolution electron energy loss-spectroscopy. *Applied Physics A*, 39:73–82, 1986. doi: 10.1007/BF00616822. ☐

T. Grzebyk, A. Górecka-Drzazga, and J. A. Dziuban. Glow-discharge ion-sorption micropump for vacuum MEMS. *Sensors and Actuators A: Physical*, 208:113–119, 2014. doi: 10.1016/j.sna.2014.01.011. ☐

J. Guéna, M. Abgrall, D. Rovera, P. Rosenbusch, M. E. Tobar, P. Laurent, A. Clairon, and S. Bize. Improved tests of local position invariance using ^{87}Rb and ^{133}Cs fountains. *Physical Review Letters*, 109(8):1–5, 2012. doi: 10.1103/PhysRevLett.109.080801. ☐

S. Guérandel, T. Zanon-Willette, N. Castagna, F. Dahes, E. de Clercq, and A. Clairon. Raman–Ramsey interaction for coherent population trapping Cs clock. *IEEE Transactions on Instrumentation and Measurement*, 56(2):383–387, 2007. doi: 10.1109/TIM.2007.891124. □

J. Haesler, L. Balet, J.-A. Porchet, T. Overstolz, J. Pierer, R. J. James, S. Grossmann, D. Ruffieux, and S. Lecomte. The Integrated Swiss Miniature Atomic Clock. In *2013 Joint European Frequency and Time Forum & International Frequency Control Symposium (EFTF/IFC)*, pages 579–581, Prague, 2013. doi: 10.1109/EFTF-IFC.2013.6702125. □

K. Harasaka, K. Adachi, H. Shouji, A. Itoh, S. Sato, and S. Satoh. Alkali metal cell, atomic oscillator, and alkali metal cell fabricating method. United States Patent Application US 2014/0139294 A1, 2014. □

G. L. Harding. Helium permeation in all-glass tubular evacuated solar energy collectors. *Solar Energy Materials*, 5(2):141–147, 1981. doi: 10.1016/0165-1633(81)90025-3. □

M. Hasegawa, P. Dziuban, L. Nieradko, A. Douahi, C. Gorecki, and V. Giordano. Fabrication of wall-coated Cs vapor cells for a chip-scale atomic clock. In *Optical MEMs and Nanophotonics, 2008 IEEE/LEOS International Conference on*, pages 162–163. IEEE, 2008. doi: 10.1109/OMEMS.2008.4607879. □

M. Hasegawa, R. K. Chutani, and C. Gorecki. Microfabrication and thermal behavior of miniature cesium-vapor cells for atomic clock operations. In *24th International Conference on Micro Electro Mechanical Systems (MEMS)*, pages 712–715, Cancun, 2011a. IEEE. doi: 10.1109/MEMSYS.2011.5734524. □

M. Hasegawa, R. K. Chutani, C. Gorecki, R. Boudot, P. Dziuban, V. Giordano, S. Clatot, and L. Mauri. Microfabrication of cesium vapor cells with buffer gas for MEMS atomic clocks. *Sensors and Actuators A: Physical*, 167(2):594–601, 2011b. doi: 10.1016/j.sna.2011.02.039. □

M. Hasegawa, R. K. Chutani, R. Boudot, L. Mauri, C. Gorecki, X. Liu, and N. Passilly. Effects of getters on hermetically sealed micromachined cesium–neon cells for atomic clocks. *Journal of Micromechanics and Microengineering*, 23(5):055022, 2013. doi: 10.1088/0960-1317/23/5/055022. □

E. Hasman, Z. 'ev Bomzon, A. Niv, G. Biener, and V. Kleiner. Polarization beam-splitters and optical switches based on space-variant computer-generated subwavelength quasi-periodic structures. *Optics Communications*, 209(1-3):45–54, 2002. doi: 10.1016/S0030-4018(02)01598-5. □

S. Herbulock, C. Klimcak, A. Presser, J. Milne, and J. C. Camparo. Investigations of vapor-cell clock equilibration following initial activation: A progress report. *35th Annual Precise Time and Time Interval (PTTI) Meeting*, 2004. □

M. Hirashima and M. Asano. Reaction of Caesium Vapour with Gold. In J. McGee, D. McMullan, and E. Kahan, editors, *Photo-Electronic Image Devices, Proceedings of the Third Symposium*, volume 22 of *Advances in Electronics and Electron Physics*, pages 643–650. Academic Press, 1966. doi: 10.1016/S0065-2539(08)61693-5. □

M. Honma and T. Nose. Twisted nematic liquid crystal polarization grating with the handedness conservation of a circularly polarized state. *Optics Express*, 20(16):18449–18458, 2012. doi: 10.1364/OE.20.018449. □

J. F. Hulbert, K. B. Hurd, B. T. Carroll, A. R. Hawkins, B. Wu, and H. Schmidt. Versatile approach to Rb vapor cell construction. *Journal of Vacuum Science & Technology A*, 29(3):033001, 2011. doi: 10.1116/1.3568954. □

J. D. Hunter. Matplotlib: A 2D graphics environment. *Computing In Science & Engineering*, 9(3):90–95, 2007. doi: 10.1109/MCSE.2007.55.

N. Ishihara. Atomic cell, manufacturing method for atomic cell, quantum interference device, atomic oscillator, electronic apparatus, and moving object. United States Patent Application US 2015/0244382 A1, 2015. □

N. Ishihara. Atomic cell, atomic cell manufacturing method, quantum interference device, atomic oscillator, electronic device, and moving object. United States Patent Application US 2016/0072439 A1, 2016. □

Y.-Y. Jau, E. Miron, A. B. Post, N. N. Kuzma, and W. Happer. Push-Pull Optical Pumping of Pure Superposition States. *Physical Review Letters*, 93(16):1–4, 2004. doi: 10.1103/PhysRevLett.93.160802. □

A. Javan, O. Kocharovskaya, H. Lee, and M. O. Scully. Narrowing of electromagnetically induced transparency resonance in a Doppler-broadened medium. *Physical Review A*, 66(1):013805, 2002. doi: 10.1103/PhysRevA.66.013805. ☐

Y. Kamada, T. Osabe, S. Suzuki, A. Kandori, and R. Kawabata. Magnetic field measuring apparatus and method for manufacturing same. United States Patent Application US 2014/0306700 A1, 2014. ☐

P. Karioja, K. Kautio, J. Ollila, K. Keränen, M. Karppinen, V. Heikkinen, T. Jaakola, and M. Lahti. MEMS , MOEMS , RF-MEMS and photonics packaging based on LTCC technology. In *Electronics System-Integration Technology Conference (ESTC)*, Helsinki, 2014. doi: 10.1109/ESTC.2014.6962731. ☐

G. A. Kazakov, B. G. Matisov, A. N. Litvinov, and I. E. Mazets. Coherent population trapping in a finite-size buffer-less cell. *Journal of Physics B: Atomic, Molecular and Optical Physics*, 40(19):3851–3860, 2007. doi: 10.1088/0953-4075/40/19/006. ☐

G. A. Kazakov, A. N. Litvinov, and B. G. Matisov. Narrowing of the coherent population trapping resonance under zone pumping in cells with different characteristics of the wall coating. *Quantum Electronics*, 42(2): 185–188, 2012. doi: 10.1070/QE2012v042n02ABEH014744. ☐

J. Kitching, L. Hollberg, S. Knappe, and R. Wynands. Compact atomic clock based on coherent population trapping. *Electronics Letters*, 37(24):1449–1451, 2001. doi: 10.1049/el:20010959. ☐

J. Kitching, S. Knappe, and L. Hollberg. Miniature vapor-cell atomic-frequency references. *Applied Physics Letters*, 81(3):553–555, 2002. doi: 10.1063/1.1494115. ☐

J. Kitching, E. A. Donley, E. Hodby, A. M. Shkel, and E. J. Eklund. Compact atomic magnetometer and gyroscope based on a diverging laser beam. United States Patent US 7,872,473 B2, 2011a. ☐

J. Kitching, S. Knappe, and E. A. Donley. Atomic Sensors – A Review. *IEEE Sensors Journal*, 11(9):1749–1758, 2011b. doi: 10.1109/JSEN.2011.2157679. ☐

M. Klein. *Slow and Stored Light in Atomic Vapor Cells*. PhD thesis, Harvard University, 2009. ☐

M. Klein, M. Hohensee, D. Phillips, and R. L. Walsworth. Electromagnetically induced transparency in paraffin-coated vapor cells. *Physical Review A*, 83(1):013826, 2011. doi: 10.1103/PhysRevA.83.013826. ☐

D. Kleppner, H. Goldenberg, and N. F. Ramsey. Theory of the Hydrogen Maser. *Physical Review*, 126(2): 603–615, 1962. doi: 10.1103/PhysRev.126.603. ☐

S. Knappe. MEMS Atomic Clocks. In Y. Gianchandani, O. Tabata, and H. Zappe, editors, *Comprehensive Microsystems*, volume 3, pages 571–612. Elsevier B.V., 2008. doi: 10.1016/B978-044452190-3.00048-3. ☐

S. Knappe, R. Wynands, J. Kitching, H. G. Robinson, and L. Hollberg. Characterization of coherent population-trapping resonances as atomic frequency references. *Journal of the Optical Society of America B*, 18(11): 1545, 2001. doi: 10.1364/JOSAB.18.001545. ☐

S. Knappe, J. Kitching, L. Hollberg, and R. Wynands. Temperature dependence of coherent population trapping resonances. *Applied Physics B*, 74(3):217–222, 2002. doi: 10.1007/s003400200800. ☐

S. Knappe, V. L. Velichansky, H. G. Robinson, J. Kitching, and L. Hollberg. Compact atomic vapor cells fabricated by laser-induced heating of hollow-core glass fibers. *Review of Scientific Instruments*, 74(6):3142, 2003a. doi: 10.1063/1.1575925. ☐

S. Knappe, V. L. Velichansky, H. G. Robinson, L.-A. Liew, J. Moreland, J. Kitching, and L. Hollberg. Atomic vapor cells for miniature frequency references. In *IEEE International Frequency Control Symposium and PDA Exhibition Jointly with the 17th European Frequency and Time Forum*, pages 31–32. IEEE, 2003b. doi: 10.1109/FREQ.2003.1274981. ☐

S. Knappe, P. D. D. Schwindt, V. Shah, L. Hollberg, and J. Kitching. Microfabricated atomic frequency references. *2004 IEEE International Ultrasonics, Ferroelectrics, and Frequency Control Joint 50th Anniversary Conference*, 00:87–91, 2004a. ☐

S. Knappe, V. Shah, P. D. D. Schwindt, L. Hollberg, J. Kitching, L.-A. Liew, and J. Moreland. A microfabricated atomic clock. *Applied Physics Letters*, 85(9):1460–1462, 2004b. doi: 10.1063/1.1787942. ☐

S. Knappe, V. Gerginov, P. D. D. Schwindt, V. Shah, H. G. Robinson, L. Hollberg, and J. Kitching. Atomic vapor cells for chip-scale atomic clocks with improved long-term frequency stability. *Optics Letters*, 30(18): 2351–2353, 2005a. doi: 10.1364/OL.30.002351. ☐

S. Knappe, P. D. D. Schwindt, V. Shah, L. Hollberg, J. Kitching, L.-A. Liew, and J. Moreland. A chip-scale atomic clock based on ^{87}Rb with improved frequency stability. *Optics Express*, 13(4):1249–1253, 2005b. doi: 10.1364/OPEX.13.001249. ☐

S. Knappe, H. G. Robinson, and L. Hollberg. Microfabricated saturated absorption laser spectrometer. *Opt. Express*, 15(10):6293–6299, 2007. doi: 10.1364/OE.15.006293. ☐

O. Kozlova. *Caractérisation d'une horloge à piégeage cohérent de population dans une vapeur thermique de césium.* PhD thesis, Université Paris VI Pierre et Marie Curie, 2012. ☐

O. Kozlova, S. Guérandel, and E. de Clercq. Temperature and pressure shift of the Cs clock transition in the presence of buffer gases: Ne, N$_2$, Ar. *Physical Review A*, 83(6):62714, 2011. doi: 10.1103/PhysRevA.83.062714. ☐

E. Kroemer. *Étude du déplacement collisionnel de la fréquence d'horloge du césium en présence du gaz tampon hélium ou xénon. Applications pour microcellules à haute température.* PhD thesis, Université de Franche-Comté, 2015. ☐

E. Kroemer, M. Abdel Hafiz, V. Maurice, B. Fouilland, C. Gorecki, and R. Boudot. Cs vapor microcells with Ne-He buffer gas mixture for high operation-temperature miniature atomic clocks. *Optics Express*, 23(14): 18373, 2015. doi: 10.1364/OE.23.018373. ☐

M. H. Kwakernaak, S. A. Lipp, and S. E. McBride. Components for Batch-Fabricated Chip-Scale Atomic Clocks. In *36th Annual Precise Time and Time Interval (PTTI) Meeting*, pages 355–368, Washington, DC, 2004. ☐

A. Lal and S. Radhakrishnan. Alkali metal-wax micropackets for alkali metal handling. United States Patent US 7,666,485 B2, 2010. ☐

P. Lalanne, S. Astilean, P. Chavel, E. Cambril, and H. Launois. Blazed binary subwavelength gratings with efficiencies larger than those of conventional échelette gratings. *Optics Letters*, 23(14):1081–1083, 1998. doi: 10.1364/OL.23.001081. ☐

P. Lalanne, S. Astilean, P. Chavel, E. Cambril, and H. Launois. Design and fabrication of blazed binary diffractive elements with sampling periods smaller than the structural cutoff. *Journal of the Optical Society of America A*, 16(5):1143–1156, 1999. doi: 10.1364/JOSAA.16.001143. ☐

S.-Y. Lan, P.-C. Kuan, B. Estey, D. English, J. M. Brown, M. A. Hohensee, and H. Müller. A Clock Directly Linking Time to a Particle's Mass. *Science*, 339(6119):554–557, 2013. doi: 10.1126/science.1230767. ☐

J. D. Le Grange, J. Markham, and C. R. Kurkjian. Effects of Surface Hydration on the Deposition of Silane Monolayers on Silica. *Langmuir*, 9(7):1749–1753, 1993. doi: 10.1021/la00031a023. ☐

C. Lee, H. Guo, S. Radhakrishnan, and A. Lal. A batch fabricated rubidium-vapor resonance cell for chip-scale atomic clocks. page 23, Hilton Head Island, South Carolina, 2004.

J. P. Lee, H. K. Kim, C. R. Park, G. Park, H. T. Kwak, S. M. Koo, and M. M. Sung. Photocatalytic Decomposition of Alkylsiloxane Self-Assembled Monolayers on Titanium Oxide Surfaces. *Journal of Physical Chemistry B*, 107(34):8997–9002, 2003. doi: 10.1021/jp030077k. ☐

F. Levi, A. Godone, and J. Vanier. The light shift effect in the coherent population trapping cesium maser. *IEEE Transactions on Ultrasonics, Ferroelectrics, and Frequency Control*, 47(2):466–470, 2000. doi: 10.1109/58.827437. ☐

L.-A. Liew, S. Knappe, J. Moreland, H. G. Robinson, L. Hollberg, and J. Kitching. Microfabricated alkali atom vapor cells. *Applied Physics Letters*, 84(14):2694–2696, 2004. doi: 10.1063/1.1691490. ☐

L.-A. Liew, J. Moreland, and V. Gerginov. Wafer-level fabrication and filling of cesium vapor cells for chip-scale atomic devices. In *Proceedings of the 20th Eurosensors Conference*, Göteborg, 2006. □

L.-A. Liew, J. Moreland, and V. Gerginov. Wafer-level filling of microfabricated atomic vapor cells based on thin-film deposition and photolysis of cesium azide. *Applied Physics Letters*, 90(11):114106, 2007. doi: 10.1063/1.2712501. □

S. A. Lipp, J. H. Abeles, A. M. Braun, S. E. McBride, J. P. Riganati, R. D. Whaley, and P. J. Zanzucchi. Anodically bonded cell, method for making same and systems incorporating same. United States Patent US 7,400,207 B2, 2008. □

X. Liu, J.-M. Mérolla, S. Guérandel, E. de Clercq, and R. Boudot. Ramsey spectroscopy of high-contrast CPT resonances with push-pull optical pumping in Cs vapor. *Optics Express*, 21(10):12451–12459, 2013a. doi: 10.1364/OE.21.012451. □

X. Liu, J.-M. Mérolla, S. Guérandel, C. Gorecki, E. de Clercq, and R. Boudot. Coherent-population-trapping resonances in buffer-gas-filled Cs-vapor cells with push-pull optical pumping. *Physical Review A*, 87(1): 013416, 2013b. doi: 10.1103/PhysRevA.87.013416. □

M. A. Lombardi. Fondamentals of Time and Frequency. In *Mecatronics Handbook*. Taylor & Francis (CRC Press), Boca Raton, 2002. □

S. S. Losev, D. I. Sevostianov, V. V. Vassiliev, and V. L. Velishansky. Production of Miniature Glass Cells with Rubidium for Chip Scale Atomic Clock. *Physics Procedia*, 71:242–246, 2015. doi: 10.1016/j.phpro.2015.08.357. □

L. M. Lust and D. W. Youngner. Chip scale atomic gyroscope. United States Patent US 7,359,059 B2, 2008. □

R. Lutwak. The SA. 45s Chip-Scale Atomic Clock - Early Production Statistics. In *43rd Annual Precise Time and Time Interval Systems and Applications Meeting*, pages 207–220, Long Beach, CA, 2011. □

R. Lutwak, D. Emmons, T. English, W. J. Riley, A. Duwel, M. Varghese, D. K. Serkland, and G. M. Peake. The chip-scale atomic clock-recent development progress. In *35th Annual Precise Time and Time Interval (PTTI) Meeting*, pages 467–478, San Diego, California, 2003. □

R. Lutwak, J. Deng, W. J. Riley, and M. Varghese. The chip-scale atomic clock-low-power physics package. In *36th Annual Precise Time and Time Interval (PTTI) Meeting*, pages 339–354, Washington, D.C., 2004. □

R. Lutwak, A. Rashed, M. Varghese, G. Tepolt, J. LeBlanc, M. J. Mescher, D. K. Serkland, K. M. Geib, G. M. Peake, and S. Römisch. The Chip-Scale Atomic Clock-Prototype Evaluation. In *39th Annual Precise Time and Time Interval (PTTI) Meeting*, pages 269–290, Long Beach, CA, 2007a. □

R. Lutwak, A. Rashed, M. Varghese, G. Tepolt, J. Leblanc, M. J. Mescher, D. K. Serkland, and G. M. Peake. The Miniature Atomic Clock - Pre-Production Results. In *2007 IEEE International Frequency Control Symposium Joint with the 21st European Frequency and Time Forum*, pages 1327–1333, 2007b. doi: 10.1109/FREQ.2007.4319292. □

J. Ma, A. Kishinevski, Y.-Y. Jau, C. Reuter, and W. Happer. Modification of glass cell walls by rubidium vapor. *Physical Review A*, 79(4):042905, 2009. doi: 10.1103/PhysRevA.79.042905. □

S. Mack, H. Baumann, U. Gösele, H. Werner, and R. Schlögl. Analysis of Bonding-Related Gas Enclosure in Micromachined Cavities Sealed by Silicon Wafer Bonding. *Journal of the Electrochemical Society*, 144(3): 1106–1111, 1997. doi: 10.1149/1.1837540. □

Y. Maki and T. Nakajima. Atom cell, quantum interference device, atomic oscillator, electronic apparatus, and moving object. United States Patent Application US 2015/0270844 A1, 2015. □

Y. Masian, A. Sivak, D. Sevostianov, V. Vassiliev, and V. Velichansky. Study and Optimization of CPT Resonance Parameters in 87 Rb/Ar/Ne Microcells Aimed for Application in Metrology. *Physics Procedia*, 71:252–256, 2015. doi: 10.1016/j.phpro.2015.08.359. □

A. Mathis, F. Courvoisier, L. Froehly, L. Furfaro, M. Jacquot, P. A. Lacourt, and J. M. Dudley. Micromachining along a curve: Femtosecond laser micromachining of curved profiles in diamond and silicon using accelerating beams. *Applied Physics Letters*, 101(7):071110, 2012. doi: 10.1063/1.4745925. □

L. Mauri, A. Gallitognotta, and A. Coda. Organic-inorganic composition for the vapour release of alkali or alkali-earth metals. United States Patent US 9,175,184 B2, 2015. □

M. J. Mescher, R. Lutwak, and M. Varghese. An ultra-low-power physics package for a chip-scale atomic clock. *The 13th International Conference on Solid-State Sensors, Actuators and Microsystems, 2005. Digest of Technical Papers. TRANSDUCERS '05.*, 1:311–316, 2005. doi: 10.1109/SENSOR.2005.1496419. □

R. R. Mhaskar, S. Knappe, and J. Kitching. A low-power, high-sensitivity micromachined optical magnetometer. *Applied Physics Letters*, 101(24):241105, 2012. doi: 10.1063/1.4770361. □

S. Micalizio, A. Godone, F. Levi, and J. Vanier. Spin-exchange frequency shift in alkali-metal-vapor cell frequency standards. *Physical Review A*, 73(3):1–5, 2006. doi: 10.1103/PhysRevA.73.033414. □

S. Micalizio, C. E. Calosso, A. Godone, and F. Levi. Metrological characterization of the pulsed Rb clock with optical detection. *Metrologia*, 49(4):425, 2012. doi: 10.1088/0026-1394/49/4/425. □

J. Migdalek and Y.-K. Kim. Core polarization and oscillator strength ratio anomaly in potassium, rubidium and caesium. *Journal of Physics B: Atomic, Molecular and Optical Physics*, 31(9):1947, 1998. doi: 10.1088/0953-4075/31/9/011. □

D. Miletic, P. Dziuban, R. Boudot, M. Hasegawa, R. K. Chutani, G. Mileti, V. Giordano, and C. Gorecki. Quadratic dependence on temperature of Cs 0–0 hyperfine resonance frequency in single Ne buffer gas microfabricated vapour cell. *Electronics Letters*, 46(15):1069, 2010. doi: 10.1049/el.2010.0891. □

D. Miletic, C. Affolderbach, M. Hasegawa, R. Boudot, C. Gorecki, and G. Mileti. AC Stark-shift in CPT-based Cs miniature atomic clocks. *Applied Physics B*, 109(1):89–97, 2012. doi: 10.1007/s00340-012-5121-7. □

J. Mueller, S. Vargo, J. Forgrave, D. Bame, I. Chakraborty, and W. Tang. Development of a Micro-Isolation Valve. In *35th AIAA/ASME SAE/ASEE Joint Propulsion Conference and Exhibit*, Los Angeles, CA, 1999. □

J. Mueller, E.-H. Yang, A. A. Green, V. White, I. Chakraborty, and R. H. Reinicke. Design and fabrication of MEMS-based micropropulsion devices at JPL. In *Proceedings of SPIE*, volume 4558, pages 57–71, San Francisco, CA, 2001. doi: 10.1117/12.443018. □

Muquans. Muquans.com - MuClock product description. http://www.muquans.com/, 2016.

T. Nakajima. Atom cell, quantum interference device, atomic oscillator, electronic apparatus, and moving object. United States Patent Application US 2015/0349791 A1, 2015. □

T. Nakajima and Y. Maki. Atomic cell, quantum interference device, atomic oscillator, electronic device and moving object. United States Patent Application US 2015/0270843 A1, 2015. □

K. Nasyrov, S. Gozzini, A. Lucchesini, C. Marinelli, S. Gateva, S. Cartaleva, and L. Marmugi. Antirelaxation coatings in coherent spectroscopy: Theoretical investigation and experimental test. *Physical Review A*, 92(4):043803, 2015. doi: 10.1103/PhysRevA.92.043803. □

L. Nieradko, C. Gorecki, J. Dziuban, A. Douahi, V. Giordano, J.-C. Beugnot, S. Guérandel, and M. Moraja. From the Implementation to the Characterisation and Assembling of Microfabricated Optical Alcali Vapor Cell for MEMS Atomic Clocks. In *Solid-State Sensors, Actuators and Microsystems Conference, 2007. TRANSDUCERS 2007. International*, pages 45–48, Lyon, 2007. doi: 10.1109/SENSOR.2007.4300067. □

L. Nieradko, C. Gorecki, A. Douahi, V. Giordano, J.-C. Beugnot, J. Dziuban, and M. Moraja. New approach of fabrication and dispensing of micromachined cesium vapor cell. *Journal of Micro/Nanolithography, MEMS and MOEMS*, 7(3):033013, 2008. doi: 10.1117/1.2964288. □

S. N. Nikolić, M. Radonjić, A. J. Krmpot, N. M. Lučić, B. V. Zlatković, and B. M. Jelenković. Effects of a laser beam profile on Zeeman electromagnetically induced transparency in the Rb buffer gas cell. *Journal of Physics B: Atomic, Molecular and Optical Physics*, 46(7):075501, 2013. doi: 10.1088/0953-4075/46/7/075501. ☐

F. J. Norton. Helium Diffusion Through Glass. *Journal of the American Ceramic Society*, 36(3):90–96, 1953. doi: 10.1111/j.1151-2916.1953.tb12843.x. ☐

T. Overstolz, J. Haesler, G. Bergonzi, A. Pezous, P.-A. Clerc, S. Ischer, J. Kaufmann, and M. Despont. Wafer scale fabrication of highly integrated rubidium vapor cells. In *27th International Conference on Micro Electro Mechanical Systems (MEMS)*, pages 552–555, San Francisco, CA, 2014. IEEE. doi: 10.1109/MEMSYS.2014.6765700. ☐

R. Parsa and W. French. Microfabricated atomic clocks (MFAC) & magnetometers (MFAM): high sensitivity vapor cell structure with internal condensation site. United States Patent Application US 2015/0378316 A1, 2015. ☐

R. Parsa and P. J. Hopper. Microfabricated atomic clocks (MFAC) & magnetometers (MFAM): self-condensing silicon vapor cell cavity structure. United States Patent Application US 2015/0372686 A1, 2015. ☐

N. Passilly, C. Gorecki, R. Chutani, and R. Boudot. Alkali-Metal Vapour Cell, Especially for an Atomic Clock, and Manufacturing Process. United States Patent Application US 2015/0277386 A1, 2015. ☐

B. Patton, K. Ishikawa, Y.-Y. Jau, and W. Happer. Intrinsic Impurities in Glass Alkali-Vapor Cells. *Physical Review Letters*, 99(2):027601, 2007. doi: 10.1103/PhysRevLett.99.027601. ☐

M. A. Perez, U. Nguyen, S. Knappe, E. A. Donley, J. Kitching, and A. M. Shkel. Rubidium vapor cell with integrated Bragg reflectors for compact atomic MEMS. *Sensors and Actuators A: Physical*, 154(2):295–303, 2009. doi: 10.1016/j.sna.2009.06.001. ☐

M. A. Perez, S. Knappe, and J. Kitching. MEMS techniques for the parallel fabrication of Chip Scale Atomic Devices. In *Sensors*, pages 2155–2158, Kona, HI, 2010. IEEE. doi: 10.1109/ICSENS.2010.5690546. ☐

Y. Pétremand, C. Schori, and R. Straessle. Low temperature indium-based sealing of microfabricated alkali cells for chip scale atomic clocks. In *Proc. European Frequency and Time Forum (EFTF)*, pages 2–4, Noordwijk, 2010. IEEE. doi: 10.1109/EFTF.2010.6533683. ☐

Y. Pétremand, C. Affolderbach, R. Straessle, M. Pellaton, D. Briand, G. Mileti, and N. F. de Rooij. Microfabricated rubidium vapour cell with a thick glass core for small-scale atomic clock applications. *Journal of Micromechanics and Microengineering*, 22(2):025013, 2012. doi: 10.1088/0960-1317/22/2/025013. ☐

G. A. Pitz, D. E. Wertepny, and G. P. Perram. Pressure broadening and shift of the cesium D_1 transition by the noble gases and N_2, H_2, HD, D_2, CH_4, C_2H_6, CF_4, and ^{3}He. *Physical Review A*, 80(6):062718, 2009. doi: 10.1103/PhysRevA.80.062718. ☐

G. A. Pitz, C. Fox, and G. P. Perram. Pressure broadening and shift of the cesium D_2 transition by the noble gases and N_2, H_2, HD, D_2, CH_4, C_2H_6, CF_4, and ^{3}He with comparison to the D_1 transition. *Physical Review A*, 82(4):1–9, 2010. doi: 10.1103/PhysRevA.82.042502. ☐

A. B. Post, Y.-Y. Jau, N. N. Kuzma, A. M. Braun, S. A. Lipp, J. H. Abeles, M. V. Romalis, E. Miron, and W. Happer. End Resonances for Atomic Clocks. *35th Annual Precise Time and Time Interval (PTTI) Meeting*, 2004. ☐

S. Radhakrishnan and A. Lal. Alkali metal-wax micropackets for chip-scale atomic clocks. *The 13th International Conference on SolidState Sensors Actuators and Microsystems 2005 Digest of Technical Papers TRANSDUCERS 05*, pages 23–26, 2005. doi: 10.1109/SENSOR.2005.1496349. ☐

I. S. Radojičić, M. Radonjić, M. M. Lekić, Z. D. Grujić, D. Lukić, and B. Jelenković. Raman–Ramsey electromagnetically induced transparency in the configuration of counterpropagating pump and probe in vacuum Rb cell. *Journal of the Optical Society of America B*, 32(3):426, 2015. doi: 10.1364/JOSAB.32.000426. ☐

M. Radonjić, D. Arsenović, Z. Grujić, and B. M. Jelenković. Coherent population trapping linewidths for open transitions: Cases of different transverse laser intensity distribution. *Physical Review A*, 79(2):1–9, 2009. doi: 10.1103/PhysRevA.79.023805. □

C. Rahman and H. G. Robinson. Rb 0-0 hyperfine transition in evacuated wall-coated cell at melting temperature. *IEEE Journal of Quantum Electronics*, 23(4):452–454, 1987. doi: 10.1109/JQE.1987.1073365. □

N. F. Ramsey. Resonance Experiments in Successive Oscillatory Fields. *Review of Scientific Instruments*, 28 (1):57–58, 1957. doi: 10.1063/1.1715708. □

W. J. Riley. The physics of the environmental sensitivity of rubidium gas cell atomic frequency standards. *IEEE Transactions on Ultrasonics, Ferroelectrics and Frequency Control*, 39:232–240, 1992. doi: 10.1109/58.139119. □

W. J. Riley and R. Lutwak. Miniature gas cell with folded optics. United States Patent US 7,064,835 B2, 2006. □

H. G. Robinson. Evacuated, wall-coated, sealed, alkali atom cell for an atomic frequency standard. United States Patent US 4,596,962, 1986. □

H. G. Robinson and C. E. Johnson. Narrow ^{87}Rb hyperfine-structure resonances in an evacuated wall-coated cell. *Applied Physics Letters*, 40(9):771, 1982. doi: 10.1063/1.93279. □

H. G. Robinson, E. Ensberg, and H. Dehmelt. Preservation of spin state in free atom-inert surface collisions. *Bulletin of the American Physical Society*, 3(9), 1958.

M. D. Rotondaro and G. P. Perram. Collisional broadening and shift of the rubidium D_1 and D_2 lines ($5^2S_{1/2} \rightarrow 5^2P_{1/2}, 5^2P_{3/2}$) by rare gases, H_2, D_2, N_2, CH_4 and CF_4. *Journal of Quantitative Spectroscopy and Radiative Transfer*, 57(4):497–507, 1997. doi: 10.1016/S0022-4073(96)00147-1. □

D. Ruffieux, J. Haesler, L. Balet, T. Overstolz, J. Pierer, R. J. James, and S. Lecomte. Towards Portable Miniature Atomic Clocks. In A. Baschirotto, K. A. Makinwa, and P. Harpe, editors, *Frequency References, Power Management for SoC, and Smart Wireless Interfaces*. Springer International Publishing, Cham, 2014. doi: 10.1007/978-3-319-01080-9_6. □

J. Rushton, M. Aldous, and M. Himsworth. Contributed Review: The feasibility of a fully miniaturized magneto-optical trap for portable ultracold quantum technology. *Review of Scientific Instruments*, 85(12): 121501, 2014. doi: 10.1063/1.4904066. □

J. Rutkowski. *Investigation of thermal activation of caesium dispensers for micro-atomic clock*. Master's thesis, Politechnika Wrocławska, 2010. □

J. Rutkowski, W. Fourcault, F. Bertrand, U. Rossini, S. Gétin, S. Le Calvez, T. Jager, E. Herth, C. Gorecki, M. Le Prado, J. M. Léger, and S. Morales. Towards a miniature atomic scalar magnetometer using a liquid crystal polarization rotator. *Sensors and Actuators A: Physical*, 216:386–393, 2014. doi: 10.1016/j.sna.2014.05.003. □

J. Rutman and F. L. Walls. Characterization of frequency stability in precision frequency sources. *Proceedings of the IEEE*, 79(7):952–960, 1991. doi: 10.1109/5.84972. □

SAES Getters. Alkali Metal Dispensers. Datasheet AMD 920630, 2007. □

T. H. Sander, J. Preusser, R. R. Mhaskar, J. Kitching, L. Trahms, and S. Knappe. Magnetoencephalography with a chip-scale atomic magnetometer. *Optics Express*, 3(5):27167–27172, 2012. doi: 10.1364/BOE.3.000981. □

S. Sato, A. Itoh, and Y. Sato. Atomic oscillator and method for fabricating atomic oscillator. United States Patent Application US 2013/0015920 A1, 2013. □

A. B. Scholes. Low helium permeability atomic frequency standard cell and method for forming same. United States Patent US 5,256,995 A, 1993. □

P. D. D. Schwindt, S. Knappe, V. Shah, L. Hollberg, J. Kitching, L.-A. Liew, and J. Moreland. Chip-scale atomic magnetometer. *Applied Physics Letters*, 85(26):6409, 2004. doi: 10.1063/1.1839274. ☐

P. D. D. Schwindt, B. Lindseth, S. Knappe, V. Shah, J. Kitching, and L.-A. Liew. Chip-scale atomic magnetometer with improved sensitivity by use of the M_x technique. *Applied Physics Letters*, 90(8):081102, 2007. doi: 10.1063/1.2709532. ☐

P. D. D. Schwindt, Y.-Y. Jau, H. Partner, A. Casias, A. R. Wagner, M. Moorman, R. P. Manginell, J. R. Kellogg, and J. D. Prestage. A highly miniaturized vacuum package for a trapped ion atomic clock. *Review of Scientific Instruments*, 87(5):053112, 2016. doi: 10.1063/1.4948739. ☐

N. Sekiguchi and A. Hatakeyama. Measurement of background gas in paraffin-coated alkali vapor cells. *arXiv:1510.05744 [physics]*, 2015. ☐

N. Sekiguchi and A. Hatakeyama. Non-negligible collisions of alkali atoms with background gas in buffer-gas-free cells coated with paraffin. *Applied Physics B*, 122(4):1–6, 2016. doi: 10.1007/s00340-016-6352-9. ☐

S. J. Seltzer. *Developments in alkali-metal atomic magnetometry*. PhD thesis, Princeton University, 2008. ☐

S. J. Seltzer and M. V. Romalis. High-temperature alkali vapor cells with antirelaxation surface coatings. *Journal of Applied Physics*, 106(11):114905, 2009. doi: 10.1063/1.3236649. ☐

S. J. Seltzer, P. Meares, and M. V. Romalis. Synchronous optical pumping of quantum revival beats for atomic magnetometry. *Physical Review A*, 75(5):051407, 2007. doi: 10.1103/PhysRevA.75.051407. ☐

S. J. Seltzer, D. M. Rampulla, S. Rivillon-Amy, Y. J. Chabal, S. L. Bernasek, and M. V. Romalis. Testing the effect of surface coatings on alkali atom polarization lifetimes. *Journal of Applied Physics*, 104(10):103116, 2008. doi: 10.1063/1.2985913. ☐

S. J. Seltzer, D. J. Michalak, M. H. Donaldson, M. V. Balabas, S. K. Barber, S. L. Bernasek, M.-A. Bouchiat, A. Hexemer, A. Hibberd, D. F. J. Kimball, C. Jaye, T. Karaulanov, F. A. Narducci, S. A. Rangwala, H. G. Robinson, A. K. Shmakov, D. L. Voronov, V. V. Yashchuk, A. Pines, and D. Budker. Investigation of antirelaxation coatings for alkali-metal vapor cells using surface science techniques. *The Journal of Chemical Physics*, 133(14):144703, 2010. doi: 10.1063/1.3489922. ☐

S. J. Seltzer, M.-A. Bouchiat, and M. V. Balabas. Surface coatings for magnetometry applications (Chapter 11 supplementary material). In D. Budker and D. F. J. Kimball, editors, *Optical Magnetometry*. Cambridge University Press, 2013. ☐

V. Shah. *Microfabricated Atomic Clocks Based on Coherent Population Trapping*. PhD thesis, University of Colorado, 2007. ☐

V. Shah and J. Kitching. Advances in Coherent Population Trapping for Atomic Clocks. In E. Arimondo, P. R. Berman, and C. C. Lin, editors, *Advances In Atomic, Molecular, and Optical Physics*, volume 59, pages 21–74. Elsevier, 2010. doi: 10.1016/S1049-250X(10)59002-5. ☐

V. Shah, V. Gerginov, P. D. D. Schwindt, S. Knappe, L. Hollberg, and J. Kitching. Continuous light-shift correction in modulated coherent population trapping clocks. *Applied Physics Letters*, 89(15):151124, 2006. doi: 10.1063/1.2360921. ☐

V. Shah, S. Knappe, P. D. D. Schwindt, and J. Kitching. Subpicotesla atomic magnetometry with a microfabricated vapour cell. *Nature Photonics*, 1(11):649–652, 2007. doi: 10.1038/nphoton.2007.201. ☐

V. Shah, R. Lutwak, R. Stoner, and M. Mescher. A compact and low-power cold atom clock. In *Frequency Control Symposium (FCS), 2012 IEEE International*, pages 1–6, 2012. doi: 10.1109/FCS.2012.6243691. ☐

L. Shao-Liang, X. Jing, Z. Zhi-Qiang, Z. Lu-Bing, L. Liang, and W. Ya-Ming. Integrated physics package of chip-scale atomic clock. *Chinese Physics B*, 23(7):1–6, 2014. doi: 10.1088/1674-1056/23/7/074302. ☐

F. Shi, R. Yang, F. Nian, Z. Zhang, Y. Cui, H. Zhao, N. Wang, and K. Feng. Portable atomic frequency standard based on coherent population trapping. In *Proceedings of SPIE*, volume 9543, pages 95431R–8, 2015. doi: 10.1117/12.2180549. ☐

G. Singh, P. Dilavore, and C. O. Alley. A Technique for Preparing Wall Coated Cesium Vapor Cells. *Review of Scientific Instruments*, 43(9):1388, 1972. doi: 10.1063/1.1685940. □

M. Stähler, R. Wynands, S. Knappe, J. Kitching, L. Hollberg, A. Taichenachev, and V. Yudin. Coherent population trapping resonances in thermal ^{85}Rb vapor: D_1 versus D_2 line excitation. *Optics Letters*, 27(16): 1472, 2002. doi: 10.1364/OL.27.001472. □

Stanford Research Systems. Thinksrs.com. `http://www.thinksrs.com/`, 2016.

D. Steck. Cesium D line data. *Los Alamos National Laboratory*, 4710(7):1–29, 2003. □

M. Stephens, R. Rhodes, and C. Wieman. Study of wall coatings for vapor-cell laser traps. *Journal of Applied Physics*, 76(6):3479, 1994. doi: 10.1063/1.358502. □

R. Straessle. *Low Temperature Hermetic Wafer Bonding and Microfabrication of Wall-Coated Alkali Vapor Cells for Chip-Scale Atomic Clocks*. PhD thesis, École polytechnique fédérale de Lausanne, 2013. doi: 10.5075/epfl-thesis-5818. □

R. Straessle, M. Pellaton, C. Affolderbach, Y. Pétremand, D. Briand, G. Mileti, and N. F. de Rooij. Low-temperature indium-bonded alkali vapor cell for chip-scale atomic clocks. *Journal of Applied Physics*, 6(113): 064501, 2013. doi: 10.1063/1.4789942. □

R. Straessle, M. Pellaton, C. Affolderbach, Y. Pétremand, D. Briand, G. Mileti, and N. F. de Rooij. Microfabricated alkali vapor cell with anti-relaxation wall coating. *Applied Physics Letters*, 105(4):043502, 2014. doi: 10.1063/1.4891248. □

F. Strumia, N. Beverini, A. Moretti, and G. Rovera. Optimization of the buffer gas mixture for optically pumped Cs frequency standards. In *30th Annual Symposium on Frequency Control*, pages 468–472. IEEE, 1976. doi: 10.1109/FREQ.1976.201353. □

M. A. Sturza. GPS Navigation Using Three Satellites and a Precise Clock. *Navigation*, 30(2):122–132, 1983. doi: 10.1002/j.2161-4296.1983.tb00831.x. □

M. Succi, R. Canino, and B. Ferrario. Atomic absorption evaporation flow rate measurements of alkali metal dispensers. *Vacuum*, 35(12):579–582, 1985. doi: 10.1016/0042-207X(85)90319-7. □

H. Sugimura, K. Ushiyama, A. Hozumi, and O. Takai. Micropatterning of alkyl- and fluoroalkylsilane self-assembled monolayers using vacuum ultraviolet light. *Langmuir*, 16(32):885–888, 2000. doi: 10.1021/la990953e. □

A. V. Taichenachev, V. I. Yudin, V. L. Velichansky, and S. A. Zibrov. On the unique possibility of significantly increasing the contrast of dark resonances on the D1 line of 87 Rb. *JETP letters*, 82(7):398–403, 2005. doi: 10.1134/1.2142864. □

J. B. Taylor and I. Langmuir. Vapor Pressure of Caesium by the Positive Ion Method. *Physical Review*, 51(9): 753–760, 1937. doi: 10.1103/PhysRev.51.753. □

J. H. Taylor. Binary pulsars and relativistic gravity. *Reviews of Modern Physics*, 66(3):711–719, 1994. doi: http://dx.doi.org/10.1103/RevModPhys.66.711. □

J. Tervo and J. Turunen. Paraxial-domain diffractive elements with 100% efficiency based on polarization gratings. *Optics Letters*, 25(11):785–786, 2000. doi: 10.1364/OL.25.000785. □

M. Thomsen, L. Stief, and R. Fallon. Study of the Phenomena Affecting the Composition of Rubidium Vapor Cells. In *22nd Annual Symposium on Frequency Control*, pages 559–572. IEEE, 1968. doi: 10.1109/FREQ.1968.199733. □

W. Thomson and P. G. Tait. *Elements of Natural Philosophy*. Clarendon Press series. University Press, 1879.

K. Tsujimoto, K. Ban, Y. Hirai, K. Sugano, T. Tsuchiya, N. Mizutani, and O. Tabata. On-chip fabrication of alkali-metal vapor cells utilizing an alkali-metal source tablet. *Journal of Micromechanics and Microengineering*, 23(11):115003, 2013a. doi: 10.1088/0960-1317/23/11/115003. □

K. Tsujimoto, Y. Hirai, K. Sugano, T. Tsuchiya, and O. Tabata. Sacrificial microchannel sealing by glass-frit reflow for chip scale atomic magnetometer. *Electronics and Communications in Japan*, 96(5):58–66, 2013b. doi: 10.1002/ecj.10432. □

J. Turunen. Diffraction theory of microrelief gratings. In H. Herzig, editor, *Micro-Optics: Elements, systems and applications*, pages 31–52. Taylor & Francis, 1997.

T. Van Baak. LeapSecond.com. `http://www.leapsecond.com/`, 2015.

J. Vanier. Atomic clocks based on coherent population trapping: a review. *Applied Physics B*, 81(4):421–442, 2005. doi: 10.1007/s00340-005-1905-3. □

J. Vanier and C. Audoin. *The quantum physics of atomic frequency standards*. A. Hilger (Bristol and Philadelphia), 1989.

J. Vanier, J.-F. Simard, and J.-S. Boulanger. Relaxation and frequency shifts in the ground state of Rb^{85}. *Physical Review A*, 9(3):1031–1040, 1974. doi: 10.1103/PhysRevA.9.1031. □

J. Vanier, R. Kunski, N. Cyr, J. Savard, and M. Têtu. On hyperfine frequency shifts caused by buffer gases: Application to the optically pumped passive rubidium frequency standard. *Journal of Applied Physics*, 53 (8):5387, 1982. doi: 10.1063/1.331467. □

J. Vanier, A. Godone, and F. Levi. Coherent population trapping in cesium: Dark lines and coherent microwave emission. *Physical Review A*, 58(3):2345–2358, 1998. doi: 10.1103/PhysRevA.58.2345. □

J. Vanier, M. W. Levine, D. Janssen, and M. Delaney. Contrast and linewidth of the coherent population trapping transmission hyperfine resonance line in ^{87}Rb: Effect of optical pumping. *Physical Review A*, 67 (6):065801, 2003. doi: 10.1103/PhysRevA.67.065801. □

J. Vanier, M. Levine, S. Kendig, D. Janssen, C. Everson, and M. Delaney. Practical realization of a passive coherent population trapping frequency standard. In *Proceedings of the 2004 IEEE International Frequency Control Symposium and Exposition, 2004.*, pages 92–99, Montréal, 2004. IEEE. doi: 10.1109/FREQ.2004.1418434. □

I. Vartiainen, J. Tervo, J. Turunen, and M. Kuittinen. Surface-relief polarization gratings for visible light. *Optics Express*, 18(22):22850–22858, 2010. doi: 10.1364/OE.18.022850. □

F. Vecchio, V. Venkatraman, H. R. Shea, T. Maeder, and P. Ryser. Dispensing and hermetic sealing Rb in a miniature reference cell for integrated atomic clocks. *Sensors and Actuators A: Physical*, 172(1):330–335, 2011. doi: 10.1016/j.sna.2011.03.045. □

R. Vicarini. Démonstrateur et module physique de la micro-horloge atomique au césium. Mémoire de stage de fin d'études, École Nationale Supérieure de Mécanique et des Microtechniques, Besançon, 2014. □

J. R. Vig. Introduction to Quartz Frequency Standards. *Research and Development Technical Report SLCET-TR-92-1*, pages 1–55, 1992. □

J. R. Vig. Military applications of high accuracy frequency standards and clocks. *IEEE Transactions on Ultrasonics, Ferroelectrics and Frequency Control*, 40(5):522–527, 1993. doi: 10.1109/58.238104. □

K. L. Wlodarczyk. *Surface deformation mechanisms in laser smoothing and micromachining of optical glasses*. PhD thesis, Heriot-Watt University, 2011. □

S. Woetzel, V. Schultze, R. IJsselsteijn, T. Schulz, S. Anders, R. Stolz, and H.-G. Meyer. Microfabricated atomic vapor cell arrays for magnetic field measurements. *The Review of scientific instruments*, 82(3):033111, 2011. doi: 10.1063/1.3559304. □

S. Woetzel, F. Talkenberg, T. Scholtes, R. IJsselsteijn, V. Schultze, and H.-G. Meyer. Lifetime improvement of micro-fabricated alkali vapor cells by atomic layer deposited wall coatings. *Surface and Coatings Technology*, 221:158–162, 2013. doi: 10.1016/j.surfcoat.2013.01.044. □

Y. Xiao, I. Novikova, D. F. Phillips, and R. L. Walsworth. Diffusion-Induced Ramsey Narrowing. *Physical Review Letters*, 96(4):3–6, 2006. doi: 10.1103/PhysRevLett.96.043601. □

Y. Xiao, I. Novikova, D. F. Phillips, and R. L. Walsworth. Repeated interaction model for diffusion-induced Ramsey narrowing. *Optics Express*, 16(18):14128, 2008. doi: 10.1364/OE.16.014128. ☐

Y. W. Yi, H. G. Robinson, S. Knappe, J. E. Maclennan, C. D. Jones, C. Zhu, N. a. Clark, and J. Kitching. Method for characterizing self-assembled monolayers as antirelaxation wall coatings for alkali vapor cells. *Journal of Applied Physics*, 104(2):023534, 2008. doi: 10.1063/1.2958329. ☐

D. W. Youngner, L. M. Lust, D. R. Carlson, S. T. Lu, L. Forner, E. M. Chanhvongsak, and T. D. Stark. A manufacturable chip-scale atomic clock. In *Solid-State Sensors, Actuators and Microsystems Conference, 2007. TRANSDUCERS 2007. International*, pages 39–44, Lyon, 2007. IEEE. doi: 10.1109/SENSOR.2007.4300066. ☐

D. W. Youngner, S. T. Lu, T. D. Stark, and E. M. Chanhvongsak. Microcontainer for hermetically encapsulating reactive materials. United States Patent Application US 2008/0057619 A1, 2008. ☐

V. I. Yudin, A. V. Taichenachev, D. I. Sevostianov, V. L. Velichansky, V. V. Vasiliev, A. A. Zibrov, A. S. Zibrov, and S. A. Zibrov. Feedback spectroscopy of atomic resonances. *Physical Review A*, 87(6):063806, 2013. doi: 10.1103/PhysRevA.87.063806. ☐

N. D. Zameroski, G. D. Hager, W. Rudolph, C. J. Erickson, and D. A. Hostutler. Pressure broadening and collisional shift of the Rb D2 absorption line by CH_4, C_2H_6, C_3H_8, n-C_4H_{10}, and He. *Journal of Quantitative Spectroscopy and Radiative Transfer*, 112(1):59–67, 2011. doi: 10.1016/j.jqsrt.2010.08.016. ☐

T. Zanon-Willette. *Développement d'une horloge a piégeage cohérent de population. Etude théorique et expérimentale du régime impulsionnel et continu.* PhD thesis, Université Paris VI, 2005. ☐

Y. Zhao, S. Tanner, A. Casagrande, C. Affolderbach, L. Schneller, G. Mileti, and P.-A. Farine. CPT Cesium-Cell Atomic Clock Operation With a 12-mW Frequency Synthesizer ASIC. *IEEE Transactions on Instrumentation and Measurement*, pages 1–8, 2014. doi: 10.1109/TIM.2014.2329383. ☐

A. S. Zibrov and A. Matsko. Optical Ramsey fringes induced by Zeeman coherence. *Physical Review A*, 65(1): 013814, 2001. doi: 10.1103/PhysRevA.65.013814. ☐

Publications in peer-reviewed journals

- R. K. Chutani, M. Hasegawa, **V. Maurice**, N. Passilly, and C. Gorecki. Single-step deep reactive ion etching of ultra-deep silicon cavities with smooth sidewalls. *Sensors and Actuators A: Physical*, 208: 66–72, 2014. doi: 10.1016/j.sna.2013.12.031. ☐

- M. Abdel Hafiz, **V. Maurice**, R. K. Chutani, N. Passilly, C. Gorecki, S. Guérandel, E. de Clercq, and R. Boudot. Characterization of Cs vapor cell coated with octadecyltrichlorosilane using coherent population trapping spectroscopy. *Journal of Applied Physics*, 117(18):184901, 2015. doi: 10.1063/1.4919841. ☐

- R. K. Chutani, **V. Maurice**, N. Passilly, C. Gorecki, R. Boudot, M. Abdel Hafiz, P. Abbé, S. Galliou, J.-Y. Rauch, and E. de Clercq. Laser light routing in an elongated micromachined vapor cell with diffraction gratings for atomic clock applications. *Scientific Reports*, 5:14001, 2015. doi: 10.1038/srep14001. ☐

- E. Kroemer, M. Abdel Hafiz, **V. Maurice**, B. Fouilland, C. Gorecki, and R. Boudot. Cs vapor microcells with Ne-He buffer gas mixture for high operation-temperature miniature atomic clocks. *Optics Express*, 23(14):18373, 2015. doi: 10.1364/OE.23.018373. ☐

Presentations in international symposiums

- M. Hasegawa, R. K. Chutani, R. Boudot, <u>**V. Maurice**</u>, L. Mauri, C. Gorecki, and N. Passilly. Wafer-level integration of getters in cesium-neon cells for miniature atomic clocks. *Joint UFFC, EFTF and PFM Symposium*, Prague, 2013.

- <u>R. Boudot</u>, N. Passilly, R. K. Chutani, X. Liu, **V. Maurice**, S. Galliou, V. Giordano, and C. Gorecki. A European version of miniature atomic clock prototype. *French-Russian-German Laser Symposium*, Besançon, November 4-7 2013.

- <u>R. Boudot</u>, **V. Maurice**, R. K. Chutani, E. Kroemer, P. Abbé , S. Galliou, N. Passilly, and C. Gorecki. Miniature Cs vapor cell atomic clocks based on Coherent Population Trapping in FEMTO-ST. *Micro- and Millimeter Wave Technology and Techniques Workshop*, ESA-ESTEC, the Netherlands, November 25-27 2014.

- M. Abdel Hafiz, **V. Maurice**, R. Chutani, N. Passilly, C. Gorecki, S. Guérandel, E. D. Clercq, and <u>R. Boudot</u>. Spectroscopy and hyperfine clock frequency shift measurements in Cs vapor cells coated with octadecyltrichlorosilanes (OTS). In *2015 Joint Conference of the IEEE International Frequency Control Symposium the European Frequency and Time Forum*, pages 33–36, 2015a. doi: 10.1109/FCS.2015.7138787. ☐

Patents

- **V. Maurice**, N. Passilly, and C. Gorecki. Dispositifs pour l'introduction de gaz dans des cellules à vapeur alcaline microfabriquées. Patent application deposited with the INPI (1556729), 2015.

- N. Passilly, C. Gorecki and **V. Maurice**. Polariseur circulaire à base de réseaux sub-longueur d'onde pour horloges atomiques miniatures. Patent application deposited with the INPI (1557210), 2015.

- R. Boudot, C. Gorecki, **V. Maurice**, E. Kroemer, and B. Fouilland. Caesium atomic micro-clock microcell buffer gas mixture. United States Patent Application US 2016/0109859 A1, 2016. ☐

Abstract:

Chip-scale atomic clocks (CSACs) provide unprecedented frequency stability within volumes down to a few cubic centimeters and power consumptions as low as 100 mW.
In this work, we determine the optimal parameters regarding the design and the fabrication of cesium vapor cells, one of the key components of a CSAC. For this purpose, cells were characterized on both short and long-term performances in clock setups. In addition, we propose solutions to overcome present limitations including the operating temperature range, the device microfabrication cost and the ease of integration of the physics package.
A novel mixture of buffer-gas composed of neon and helium was found to potentially extend the operating range of the device above 80 °C, meeting the industrial requirements. Unlike the well-known buffer gas compositions, this mixture is compatible with solid cesium dispensers whose reliability is established. As an alternative to buffer gases, wall coatings are known to limit the relaxation induced by sidewalls. Here, we investigated octadecyltrichlorosilane (OTS) coatings. An anti-relaxation effect has been observed in centimeter-scale cells and a process was developed to coat microfabricated cells.
Other cesium sources have been investigated to overcome the drawbacks imposed by solid cesium dispensers. A paste-like dispenser, which can be deposited collectively, was explored and has shown stable atomic densities so far. Single-use zero-leak micro valves were also proposed to hermetically seal and detach cells from a common cesium reservoir.
Eventually, the first steps toward a microfabricated physics package were made. In particular, an original cell design combining diffraction gratings with an anisotropically etched single-crystalline silicon sidewalls was characterized and exhibited remarkable CPT contrasts despite a reduced cavity volume, which could lead to a more compact physics package. Finally, cells with integrated heating and temperature sensing resistors were fabricated and their magnetic field compliance was characterized in a compact physics package prototype.

Keywords: Miniature atomic clocks, alkali vapor cells, microfabrication, buffer gas, antirelaxation coatings.

Résumé :

Les horloges atomiques miniatures présentent des stabilités de fréquence inégalées avec des volumes de quelques centimètres cubes et des consommations inférieures à 100 mW.
Dans cette thèse, les paramètres optimaux concernant la conception et la fabrication des cellules à vapeur de césium, un des composant clés de ce type d'horloges, sont définis. Ainsi, les performances de plusieurs cellules ont été caractérisées en condition d'horloge à court et long terme. En parallèle, des solutions sont proposées pour pallier à certaines limitations telles que la plage de température opérationnelle, le coût de fabrication du dispositif et la facilité d'assemblage du module physique.
Un nouveau mélange de gaz tampon composé de néon et d'hélium peut étendre la plage de fonctionnement au-dessus de 80 °C, en adéquation avec les besoins industriels. A l'inverse des gaz tampon usuels, ce mélange est compatible avec les dispensers de césium solides, dont la fiabilité est établie.
Outre les gaz tampon, les revêtements permettent également de limiter la relaxation induite par les parois de la cellule. Ici, des revêtements d'octadécyltrichlorosilane sont étudiés. Un effet anti-relaxant a été observé dans des cellules centimétriques et un procédé a été développé pour revêtir des cellules micro-fabriquées.
D'autres sources de césium sont présentées pour s'affranchir des inconvénients propres aux dispensers solides. Un dispenser sous forme de pâte, qui peut être déposée collectivement, a été étudié et montre des densités atomiques stables jusqu'à présent. Un concept de vannes hermétiques micro-fabriquées a été proposé pour sceller hermétiquement et séparer des cellules d'un réservoir de césium commun.
Les premières étapes vers un module physique micro-fabriqué sont ensuite présentées. En particulier, un design original de cellule combinant des réseaux de diffraction à une cavité en silicium formée par gravure anisotrope a été caractérisé et a montré des contrastes CPT remarquables malgré un volume de cavité réduit, ce qui permettrait de réaliser un module physique particulièrement compact. Enfin, des cellules intégrant des résistances chauffantes et thermométriques ont été fabriquées et leur compatibilité vis-à-vis du champ magnétique généré a été caractérisée dans un prototype de module physique compact.

Mots-clés : Horloges atomiques miniatures, cellules à vapeur alcaline, microfabrication, gaz tampon, revêtements anti-relaxants.

SPIM

UFC
UNIVERSITÉ
DE FRANCHE-COMTÉ